Function and Assembly of Teneurin-3-positive Retinal Circuits

Antinucci, Paride

Awarding institution:
King's College London

Function and Assembly of Teneurin-3-positive Retinal Circuits

Thesis for the Degree of

Doctor of Philosophy

Paride Antinucci

Supervisors:

Dr. Robert Hindges (Primary Supervisor)

Dr. Martin P. Meyer (Secondary Supervisor)

Submitted: 20 October 2016

Pages: 224 Words: 48,379

MRC Centre for Developmental Neurobiology

Institute of Psychiatry, Psychology & Neuroscience

King's College London, UK

Table of Contents

Figures

Movies

Movie 3.1 – *Supplementary Video 1*. Functional imaging of neural activity in the optic tectum of control and PTU-treated zebrafish larvae.
http://www.nature.com/articles/srep29490#supplementary-information

Movie 3.2 – *Supplementary Video 2*. Whole-brain light-sheet imaging in *nacre* and *crystal* mutant zebrafish.
http://www.nature.com/articles/srep29490#supplementary-information

Movie 3.3 – *Supplementary Video 3*. Functional imaging of neural activity in the retina of *crystal* zebrafish.
http://www.nature.com/articles/srep29490#supplementary-information

Movie 4.1 – *Movie S2. Tenm3*$^{+}$ ACs in the Retina of a 4 dpf Zebrafish Larva.
http://www.sciencedirect.com/science/article/pii/S0960982216304948

Movie 5.1 – *Movie S1.* Functional RGC Responses to Drifting Bars in a Representative 5 dpf WT Zebrafish Larva.
http://www.sciencedirect.com/science/article/pii/S2211124713005688

Movie 5.2 – *Movie S2.* Functional RGC Responses to Drifting Bars in a Representative 5 dpf Control MO-Injected Zebrafish Larva.
http://www.sciencedirect.com/science/article/pii/S2211124713005688

Movie 5.3 – *Movie S3.* Functional RGC Responses to Drifting Bars in a Representative 5 dpf *teneurin-3* Morphant Zebrafish Larva.
http://www.sciencedirect.com/science/article/pii/S2211124713005688

Movie 5.4 – *Movie S1.* RGC Visual Responses to Moving Bars in Control and *tenm3*^{KO} 4 dpf Zebrafish Larvae.
http://www.sciencedirect.com/science/article/pii/S0960982216304948

Movie 6.1 – *Movie S4*. Visual Responses to Moving Gratings of *tenm3*$^{+}$ AC Synaptic Terminals in a 4 dpf Zebrafish Larva.
http://www.sciencedirect.com/science/article/pii/S0960982216304948

Movie 6.2 – *Movie S3*. RGC Visual Responses to Moving Bars in Control and *tenm3*$^{+}$ AC-Ablated 4 dpf Zebrafish Larvae.
http://www.sciencedirect.com/science/article/pii/S0960982216304948

Movie 6.3 – *Movie S5.* Visual Responses to Moving Gratings of BC Ribbon Synapses in a 4 dpf Zebrafish Larva.
http://www.sciencedirect.com/science/article/pii/S0960982216304948

Abstract

The retina is a sensory neural structure formed by multiple classes of excitatory cells (photoreceptors, bipolar and retinal ganglion cells) and inhibitory cells (horizontal and amacrine cells). Its primary role is to detect light stimuli, convert them into electrochemical signals and, subsequently, send the processed information to higher visual nuclei through different types of functionally specialised ganglion cells, the sole output neurons of the retina. Considerable progress has been made in uncovering cellular and molecular mechanisms underlying the assembly and normal functioning of some retinal circuits like, for example, direction-selective circuits. However, little is known about other circuits, such as those generating orientation selectivity in retinal ganglion cells. During my PhD, I started filling this knowledge gap using the larval zebrafish retina as model system. My research focused on circuits composed of neurons that express the transmembrane cell-adhesion protein Teneurin-3. This molecular marker provided a genetic access point to reveal the cellular components and mechanisms of defined retinal circuits. A wide range of techniques, including *in vivo* confocal and two-photon calcium imaging, BAC transgenesis, TALEN-mediated genome editing, single-cell labelling, pharmacology, optogenetics, as well as a newly generated combinatorial pigmentation mutant zebrafish, were used to dissect a neural circuit underlying the emergence of orientation selectivity in the retina. First, neurons expressing Teneurin-3 in the visual system were characterised. Second, by assessing the role played by Teneurin-3 in the assembly of defined retinal circuits, its requirement in the morphological and functional development of the orientation-selective circuit was revealed. Third, a specific class of orientation-selective amacrine cells with elongated dendritic fields was identified. Notably, these cells generate orientation selectivity in retinal ganglion cells by being a source of tuned GABAergic inhibition. Lastly, evidence showing that orientation selectivity is also present in a fraction of bipolar cell presynaptic terminals is provided. In conclusion, these results define a retinal circuit processing orientation-specific information and identify essential molecular and cellular requirements for its development and function.

Acknowledgements

Firstly, I would like to thank my primary supervisor Robert Hindges for taking me in his lab and supporting me as I progressed through being an MSc student, Research assistant and, lastly, PhD student. I am truly grateful to him for all the responsibility, trust and genuine friendship he has given me over the past years. Special thanks also go to my second supervisor Martin Meyer for his help, enthusiasm, encouragement, and for letting me be an integral part of his lab. I am also incredibly grateful to my various PhD advisors, Ian Thompson and Esther Bell first, and Matt Grubb and Anthony Graham later, for their very useful guidance throughout the PhD.

I would also like to thank the following people: Nikolas Nikolaou for his invaluable help in the first months of my project, Oniz Suleyman for teaching me zebrafish embryo microinjections and generating the *tenm3*^{KO} mutant, Clinton Monfries for his molecular biology wisdom, Paul Hunter for advice on imaging and analysis, Andrew Lowe for analysis tools and guidance, Victoria Gonzalez-Sabater for help collecting the data displayed in Fig. 5.14-16, and Andy Symonds for BAC cloning reagents and help. Many thanks to Greta Schachermayer, Ankur Perry, Katherine Trevers, Nadine Brassel, Nicola Maiorano, Fatima Abbas and Tom Ryan for being great lab members to work and have fun with. Thanks also to Elisa Galliano, Federico Grillo and Winnie Wefelmeyer for their useful chats on electrophysiological and pharmacological methods. Of course, I have to say a big thank to all the fantastic and inspiring people I have met at the MRC Centre over five exciting years. Thank you all for your help and friendship!

Many thanks to the Nikon Imaging Centre team at King's College London for support and instrumentation, Vladimir Grigoriev for providing the Nikon D7000 digital SLR camera, Ben Ewins for providing the ZEISS Lightsheet Z.1 microscope, and Leon Lagnado for providing the *Tg(-1.8ctbp2:SyGCaMP6)* zebrafish line. Also, I would like to thank the Medical Research Council for funding my PhD and allowing me undertake this fascinating project.

Last but not least, thanks a lot Cele, mum and dad for the daily support and for being there when I needed you most!

Abbreviations

AC	Amacrine Cell
AF	Arborisation Field
AMPA	α-Amino-3-hydroxy-5-Methyl-4-isoxazolepropionic Acid
Amp	Ampicillin
ANOVA	Analysis of Variance
APV	D-2-Amino-5-Phosphonovaleric acid
AU	Airy Unit
BAC	Bacterial Artificial Chromosome
BC	Bipolar Cell
BCIP	5-Bromo-4-Chloro-3-Indolyl-Phosphate
bp	Base Pair
BSA	Bovine Serum Albumin
CAM	Cell-Adhesion Molecule
Cam^R	Chloramphenicol Resistance
CBC	Cone Bipolar Cell
CCD	Charge-Coupled Device
Cdh	Cadherin
cDNA	Complementary Deoxyribonucleic Acid
ChAT	Choline Acetyltransferase
Cm	Chloramphenicol
Chr	Chromosome
DAC	Dopaminergic Amacrine Cell
ddH_2O	Double-Distilled water
DEPC	Diethylpyrocarbonate
DF	Dendritic Field
$\Delta F/F_0$	Relative change of Fluorescence signal
dKO	Double Knockout
dLGN	Dorsal Lateral Geniculate Nucleus
DLP	Digital Light Processing
DNA	Deoxyribonucleic Acid
dpf	Day Post-Fertilisation

DPI	Direction Preference Index
DS	Direction-Selective
DSCAM	Down Syndrome Cell Adhesion Molecule
DSCAML	Down Syndrome Cell Adhesion Molecule-Like protein
DSGC	Direction-Selective Ganglion Cell
DSI	Direction Selectivity Index
DTN	Dorsal Terminal Nucleus
EGF	Epidermal Growth Factor
eGFP	Enhanced Green Fluorescent Protein
ELFN1	Extracellular Leucine-rich Repeat and Fibronectin type III domain 1
FLRT2	Fibronectin Leucine-rich Repeat Transmembrane 2
GaAsP	Gallium Arsenide Phosphide
GABA	Gamma-Aminobutyric Acid
GC	Ganglion Cell
GCL	Ganglion Cell Layer
GFP	Green Fluorescent Protein
HA	Homology Arm
HC	Horizontal Cell
HEPES	4-(2-Hydroxyethyl)-1-Piperazineethanesulfonic acid
HM	Hybridization Mix
HSD	Honest Significant Difference
Hyg	Hygromycin
IGL	Intergeniculate Leaflet
INL	Inner Nuclear Layer
IPL	Inner Plexiform Layer
ipRGC	Intrinsically Photosensitive Retinal Ganglion Cell
Kan	Kanamycin
kb	Kilo-Base pair
KD	Knockdown
KO	Knockout
LB	Lysogeny Broth
LCD	Liquid Crystal Display
LED	Local Edge Detectors
LSM	Laser Scanning Microscope
mdPPN	Medial Division of the Posterior Pretectal Nucleus

MEGF	Multiple Epidermal Growth Factor-like domains protein
mGluR6	Metabotropic Glutamate Receptor 6
MO	Morpholino Oligonucleotides
MP	Multi-Photon
mRNA	Messenger Ribonucleic Acid
MTNd	Dorsal Medial Terminal Nucleus
MTNv	Ventral Medial Terminal Nucleus
NA	Numerical Aperture
NBQX	2,3-dihydroxy-6-Nitro-7-sulfamoyl-Benzo[f]Quinoxaline-2,3-dione
NBT	Nitro Blue Tetrazolium
NDD	Natural Diamond Detectors
NGL-2	Netrin-G Ligand 2
NHL	NCL-1, HT2A, and Lin-41
NMDA	N-Methyl-D-Aspartate
NOT	Nucleus of the Optic Tract
Np	Neuropil
ns	Non-Significant
NTMT	Alkaline phosphatase buffer
OCT	Optimal Cutting Temperature compound
OE	Overexpression
ONL	Outer Nuclear Layer
OPL	Outer Plexiform Layer
OPN	Olivary Pretectal Nucleus
ORF	Open Reading Frame
OS	Orientation-Selective
OSGC	Orientation-Selective Ganglion Cell
OSI	Orientation Selectivity Index
PBS	Phosphate-Buffered Saline
PBT	Phosphate-Buffered Saline/0.1% Tween-20
Pcdh	Protocadherin
PCR	Polymerase Chain Reaction
PFA	Paraformaldehyde
Plex	Plexin
PO	Preferred Orientation
Pop	Population

PR	Photoreceptor
PRL	Photoreceptor Layer
PSD95	Postsynaptic Density protein 95
PSF	Point Spread Function
PTU	1-Phenyl-2-Thiourea
PV	Parvalbumin
RBC	Rod Bipolar Cell
R-cad	R-cadherin
REAL	Restriction Enzyme And Ligation
RFP	Red Fluorescent Protein
RGC	Retinal Ganglion Cell
RNA	Ribonucleic Acid
R_{null}	Response to Null
ROI	Region Of Interest
R_{orth}	Response to Orthogonal
RPE	Retinal Pigment Epithelium
R_{pref}	Response to Preferred
RT-PCR	Reverse Transcription Polymerase Chain Reaction
s-Off	OFF-Sustained
SAC	Starburst Amacrine Cell
SAC/SPV	Lamina between Stratum Album Centrale and Stratum Periventriculare
SC	Superior Colliculus
SCN	Suprachiasmatic Nucleus
SD	Standard Deviation
SEM	Standard Error of the Mean
Sema	Semaphorin
SFGS	Stratum Fibrosum et Griseum Superficiale
SGC	Stratum Griseum Centrale
Sdk	Sidekick
SIN	Superficial Interneuron
SLR	Single-Lens Reflex
SO	Stratum Opticum
SP	Substance P
SPV	Stratum Periventriculare
SSC	Saline-Sodium Citrate

t-Off	OFF-Transient
TAE	Tris-acetate-EDTA
TALEN	Transcription Activator-Like Effector Nucleases
TCAP	Teneurin C-terminal-Associated Peptide
Tenm	Teneurin
TeNT	Tetanus Toxin light chain
TFP	Teal Fluorescent Protein
Tg	Transgenic
TH	Tyrosine Hydroxylase
Tot	Total
TTL	Transistor–Transistor Logic
TUNEL	Terminal deoxynucleotidyl transferase dUTP Nick End Labeling
UAS	Upstream Activation Sequence
Unc5C	Uncoordinated-5C
URE	Upstream Regulatory Elements
UV	Ultraviolet
V1	Primary Visual cortex
VBA	Visual Background Adaptation
VGluT3	Vesicular Glutamate Transporter 3
vLGN	Ventral Lateral Geniculate Nucleus
WT	Wild Type
YD	Tyrosine-Aspartate

Chapter 1

Introduction

Vision allows animals to effectively interact with their surrounding environment. Visual perception, in particular, arises through sequential steps of image processing at different stages along the visual system (Marr et al., 2010). In vertebrates, the first steps in visual processing take place in the neural retina (Rodieck, 1998). The retina does not simply capture light stimuli, but instead it extracts visual features that are important for the organism and then sends the processed visual information to the rest of the brain. It does so through functionally specialised neural circuits made by multiple classes of excitatory and inhibitory neurons (Masland, 2012a). At the basis of this functional specificity are the stereotyped synaptic connections between several different types of neurons characterised by defined morphological and physiological properties (Masland, 2001; Seung and Sumbul, 2014).

This introductory chapter focuses on the organisation, function and development of the vertebrate retina. Particular emphasis is given to studies in zebrafish and mouse, two model organisms that have allowed to understand fundamental aspects of retinal physiology and development through advanced genetic and imaging techniques. Firstly, a general overview of the neural architecture of the retina is provided. The different types of bipolar, amacrine and ganglion cells – the most heterogeneous retinal cell classes – are presented. Secondly, the main neural mechanisms underlying image processing in the retina are discussed. Two prominent computations performed by retinal circuits – direction and orientation selectivity – are described in detail. Thirdly, known developmental mechanisms underlying the wiring of retinal circuits are presented. Particular focus is given to roles played by cell adhesion molecules, especially Teneurins, in circuit assembly. Lastly, the main aims of my PhD project are outlined. The scope of this chapter is to provide a general introduction setting the stage for the results, which are then further introduced in each chapter.

1.1 The Vertebrate Retina

The retina is a light-sensitive tissue located in the eye (Fig. 1.1A). The primary function of the retina is to detect light stimuli, convert them into electrochemical signals and,

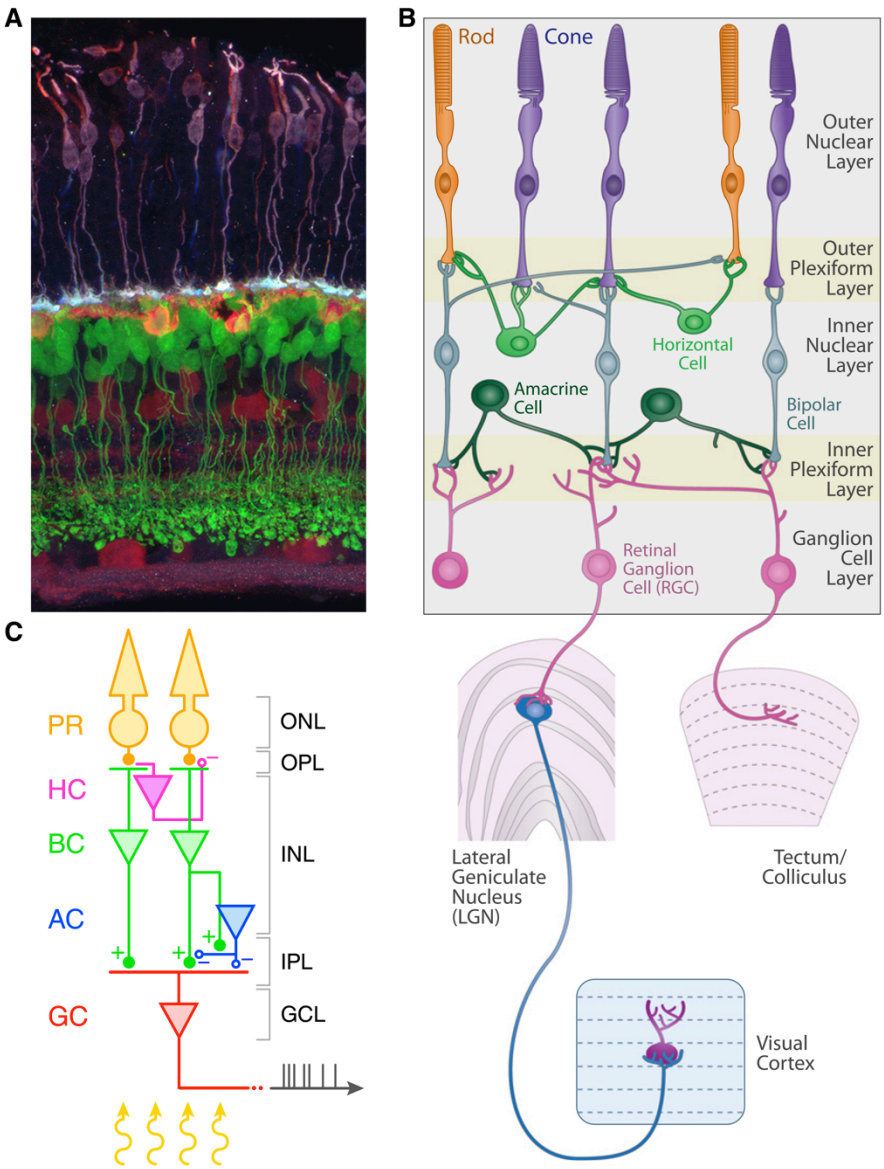

Figure 1.1. Cellular and synaptic organisation of the vertebrate retina. A, Vertical section immunostaining of the mouse retina. Image by Josh Morgan (Rachel Wong Lab). Purple: cones. Orange: horizontal cells. Green: bipolar cells. Dark red: amacrine and ganglion cells. **B,** Mammalian visual system showing retina, dorsal lateral geniculate nucleus, superior colliculus (called optic tectum in lower vertebrates), and primary visual cortex. The names of neural cell types, cellular layers and neuropil layers are reported. Image is from (Sanes and Zipursky, 2010). **C,** Basic neural circuit structure of the vertebrate retina. Cell classes are represented in colours, whereas layers are shown in black. Excitatory synapses are indicated by '+' (filled circles), inhibitory synapses are labelled with '–' (empty circles). PR, photoreceptor; HC, horizontal cell; BC, bipolar cell; AC, amacrine cell; RGC, retinal ganglion cell; ONL, outer nuclear layer; INL, inner nuclear layer; GCL, ganglion cell layer; OPL, outer plexiform layer; IPL, inner plexiform layer.

subsequently, send the processed information to higher visual nuclei through parallel feature-specific neural pathways (Rodieck, 1998; Masland, 2012a). Its neuronal architecture consists of five cell classes – *photoreceptor, horizontal, bipolar, amacrine* and *retinal ganglion cells* – arranged in three cellular layers – *outer nuclear, inner nuclear* and *ganglion cell layers* – and two synaptic layers – *outer* and *inner plexiform layers* (Fig. 1.1B,C), with Müller glial cells providing metabolic and homeostatic

support. The optics of the eye creates an image of the visual scene onto the retina through the cornea and lens. Photons of light are then detected by photoreceptor cells of the retina – *cones* and *rods* – and a cascade of biochemical events, called phototransduction, is triggered (Rodieck, 1998). In high luminance conditions (e.g., sunlight, 10 to 10^8 cd/m^2) vision is mainly mediated by cones (*photopic* vision), whereas during low luminance conditions (e.g., moonlight, 10^{-3} to 10^{-6} cd/m^2) vision is mediated by rods (*scotopic* vision). At intermediate luminance conditions (10^{-3} to 10 cd/m^2), both cones and rods contribute to vision (*mesopic* vision). Additionally, photoreceptors are sensitive to defined ranges of light wavelengths depending on what type/s of light-sensitive proteins (or opsins) they express (Fig. 1.2A,B).

The phototransduction cascade results in either photoreceptor hyperpolarisation (during light increments) or depolarisation (during light decrements), which cause decrease or increase in glutamate release, respectively (Rodieck, 1998). Glutamate neurotransmission has differential effects on bipolar cells depending on what type of glutamate receptors they express. *ON* bipolar cells express the metabotropic glutamate receptor mGluR6 and are therefore inhibited by glutamate (i.e., they respond at light onset), whereas *OFF* bipolar cells express ionotropic glutamate receptors and are excited by glutamate (i.e., they respond at light offset). These two main streams of visual information with opposite response polarities are then transmitted by bipolar cells, which are excitatory, to the inner retina. There, bipolar cells are synaptically connected with amacrine and ganglion cells in a layered neuropil structure called the inner plexiform layer (or IPL). The IPL is where most of the image processing performed by the retina take place. ON and OFF signals can interact in multiple ways in the IPL through different circuit motifs (Fig. 1.2C,D) and, as a result, give rise to emergent response features (Roska and Werblin, 2001; Demb and Singer, 2015). A simple example is the presence of amacrine and ganglion cells that integrate both ON and OFF signals and therefore show *ON-OFF* responses (i.e., they respond at both light onset and offset).

1.1.1 Bipolar Cells

Bipolar cells link the outer portion of the retina to the inner retina by contacting photoreceptors and relaying their signals to the IPL (Fig. 1.1C). Several different types of bipolar cells have been characterised based on their morphology, physiology and synaptic connectivity (Fig. 1.3A) (Euler et al., 2014). In mouse, ~15 bipolar cell types

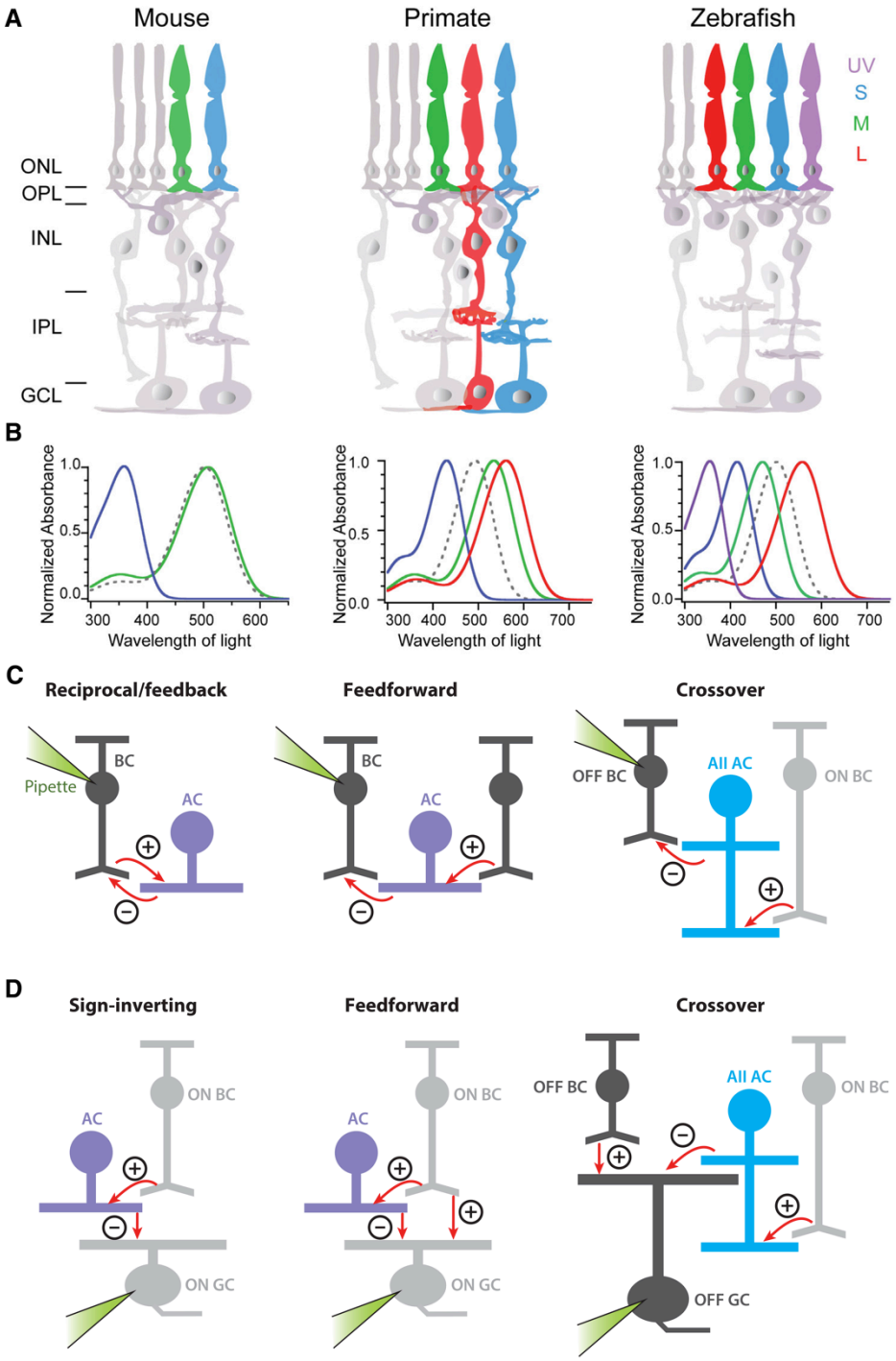

Figure 1.2. Cone composition across vertebrate species and common synaptic motifs. A, The retinae of mouse, primate (macaque) and zebrafish share a common basic architecture, but have some functional variations. In particular, they differ in terms of opsin expression in cone photoreceptors. UV: ultraviolet, S: short, M: medium, L: long wavelength cones. The primate retina has dedicated pathways for colour processing as indicated for L and S cone pathways. ONL, outer nuclear layer; INL, inner nuclear layer; GCL, ganglion cell layer; OPL, outer plexiform layer; IPL, inner plexiform layer. **B,** Absorption spectra of the different cone opsins across species (coloured lines) compared to rhodopsin (dotted line), which is expressed in rod photoreceptors. Images in (**A**) and (**B**) are from (Hoon et al., 2014). **C**|**D,** Common circuit motifs in the inner retina. **C,** Bipolar cell (BC) presynaptic terminals receive inhibitory inputs from amacrine cells (ACs) through multiple synaptic motifs. Excitatory (+) and inhibitory (–) synapses are indicated; feedback and feedforward synapses can occur in both ON and OFF systems, and crossover inhibition acts between ON and OFF systems and vice versa. **D,** Similarly, ganglion cells (GCs) receive inhibitory inputs from ACs via multiple synaptic motifs. Images in (**C**) and (**D**) are from (Demb and Singer, 2015).

are present (Helmstaedter et al., 2013; Franke et al., 2016; Shekhar et al., 2016), including a recently characterised glutamatergic interneuron with atypical monopolar morphology (Della Santina et al., 2016). In zebrafish, up to ~20 types of bipolar cells have been identified (Connaughton, 2011; Li et al., 2012a). The main morphological difference between mammals and teleosts is that mammalian bipolar cells tend to stratify their axon terminals in individual IPL strata, whereas teleost bipolar cell axons often extend vertically rather than laterally, resulting in bi- or tri-stratified bipolar cell types with presynaptic terminals distributed across several IPL strata. In regards to their physiological features, each bipolar cell type transforms the photoreceptor input in a unique way, therefore generating distinct visual streams encoding defined stimulus properties, like luminance polarity, temporal profile and chromatic composition (Fig. 1.3B) (Euler et al., 2014; Franke et al., 2016). Interestingly, the temporal properties of mouse bipolar cell output is linked to the anatomical localisation of bipolar cell axon terminals within the IPL. Briefly, bipolar cell types that show transient responses tend to stratify at intermediate depths of the IPL, whereas sustained bipolar cell types stratify in the outermost or innermost IPL strata (Fig. 1.3B) (Baden et al., 2013). Notably, this 'temporal layering' may play a crucial role in the computation of motion direction selectivity in some retinal circuits (see 1.2.1) (Kim et al., 2014; Greene et al., 2016). In zebrafish larvae, however, transient and sustained bipolar cell signals seem to overlap in the IPL with no clear anatomical segregation across the IPL depth (Nikolaev et al., 2013). Similarly, ON and OFF signals are not restricted to 'ON-only' or 'OFF-only' IPL subregions in zebrafish (Nikolaev et al., 2013), as instead is observed in mammals (Fig. 1.3B) (Baden et al., 2013; Franke et al., 2016).

A key aspect contributing to bipolar cell functional diversity is the fact that amacrine cells can modulate bipolar cell output at the level of their axon terminals. Interestingly, not only the surround inhibition provided by amacrine cells can decorrelate bipolar cell responses across different types thereby broadening the response space of bipolar cells at the population level (Franke et al., 2016), but also the response properties of individual presynaptic terminals belonging to the same bipolar cell appear to be differentially modulated by amacrine cells, which thus expand the effects that activation of a single bipolar cell can have on different postsynaptic ganglion cells (Asari and Meister, 2012, 2014). Additionally, intrinsic properties of individual bipolar cell presynaptic terminals, like their volume, play a role in the temporal filtering of visual signals, with small terminals transmitting high frequency

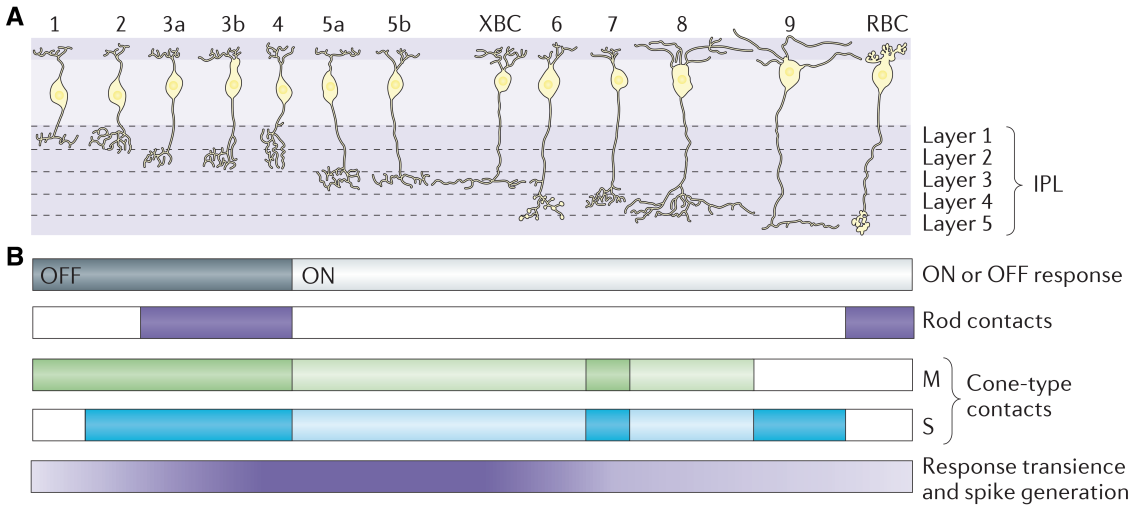

Figure 1.3. Bipolar cell types in the mouse retina. A, Morphological features of the various types of cone bipolar cells and the rod bipolar cell (RBC) in the mouse retina. Note that each bipolar cell type has a characteristic axonal stratification pattern in the inner plexiform layer (IPL). **B,** Functional properties of bipolar cell types. Depending on the polarity of their light responses, bipolar cells are classified as ON and OFF cells. Some bipolar cells relay scotopic light signals from rods. Mice have short (S; blue) and medium (M; green) wavelength-sensitive cone photoreceptors, with many M-cones co-expressing S-opsin. Depending on the cone type (or types) they contact, bipolar cells can be grouped as chromatic or achromatic (light bars indicate likely but not yet experimentally confirmed contacts). Bipolar cells with axon terminals in the central region of the IPL show more transient responses (and often generate action potentials) than those with terminals closer to the IPL borders. Images in (**A**) and (**B**) are from (Euler et al., 2014).

stimuli more effectively than large terminals (Baden et al., 2014). Overall, bipolar cells constitute the first stage where light signals start to markedly segregate within the retina and form separate channels of visual information. Intriguingly, this functional heterogeneity extends to individual bipolar cell presynaptic terminals, which therefore act as elementary computational units in the IPL.

1.1.2 Amacrine Cells

Amacrine cells constitute the most diverse cell class of the retina, not only because they exhibit extremely heterogeneous cell morphologies but also because of their physiology, connectivity and neurotransmitter expression. The main function of amacrine cells is to modulate and shape the responses of ganglion and bipolar cells as well as other amacrine cells, thereby increasing the computational power of the retinal output (Masland, 2012b; Jadzinsky and Baccus, 2013). Consequently, the coding properties of certain ganglion cells can often be linked to the specific amacrine cell types they are connected with. Most amacrine cell types release inhibitory neurotransmitters, generally γ-aminobutyric acid (GABA) or glycine (Zhang and McCall, 2012). However, some amacrine cells also release excitatory neurotransmitters like acetylcholine (Taylor and Smith, 2012) or glutamate (Lee et al., 2014). Interestingly, the

co-release of inhibitory and excitatory neurotransmitters by certain amacrine cell types, like starburst amacrine cells co-releasing GABA and acetylcholine (Sethuramanujam et al., 2016), or VGluT3 amacrine cells co-releasing glycine and glutamate (Lee et al., 2016), appears to have important roles in specific aspects of image processing by retinal circuits. Moreover, amacrine cells often form electrical synapses through gap junctions with bipolar, ganglion or other amacrine cells, further expanding the complexity of amacrine cell signalling (Bloomfield and Volgyi, 2009).

Morphological analyses of amacrine cells in the rabbit retina have characterised ~30 types that can be grouped into narrow-, medium- or wide-field classes depending on the area of their dendritic fields (Fig. 1.4) (MacNeil and Masland, 1998; MacNeil et al., 1999). Another anatomical property used for classification is the stratification pattern of amacrine cell neurites in the IPL (i.e, diffuse, mono- or multistratified neurites). Recently, a 3D electron microscopy connectomic reconstruction of the mouse IPL led to the identification of ~45 morphological types of amacrine cells (Helmstaedter et al., 2013). In zebrafish, ~28 types have been observed through light microscopy (Jusuf and Harris, 2009; Jusuf et al., 2011). These morphological analyses suggest that amacrine cells play a variety of functional roles in image processing, and that their function is likely linked to their morphological properties. Compared to morphological analyses, however, a systematic functional characterisation of amacrine cells is still far from complete (Pang et al., 2002). In a comprehensive characterisation of mouse ganglion cell functional diversity, Baden et al. (2016) have identified ~14 groups of displaced amacrine cells in the ganglion cell layer with stereotypic functional properties, but no analysis has been carried out in the inner nuclear layer. Common functions attributable to multiple amacrine cell types are, for example: (a) *lateral* or *surround inhibition,* typically provided by wide-field monostratified GABAergic amacrine cells; (b) *crossover inhibition,* mediated by narrow-field diffusely stratified glycinergic amacrine cells (Fig. 1.2C,D) (Werblin, 2011). Amacrine cell types with well-described functions include the starburst amacrine cells, which play a central role in the generation of ganglion cell direction selectivity (see 1.2.1) (Taylor and Smith, 2012; Vaney et al., 2012), and the AII amacrine cells, which are essential circuit elements for scotopic vision by linking the rod photoreceptor pathway to the cone pathway (Demb and Singer, 2012). In conclusion, amacrine cells are key players in image processing but their numerous functions have not been fully investigated and characterised yet.

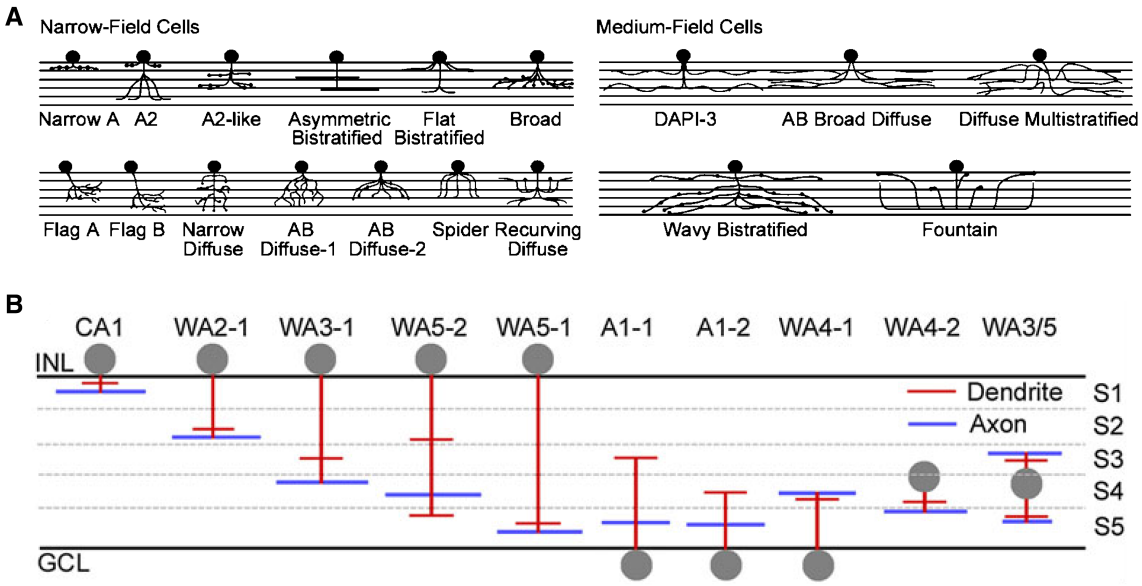

Figure 1.4. Amacrine cell types in the mouse retina. A, Narrow- (left) and medium-field (right) amacrine cells. Schematic representing the morphology and level of neurite stratification of the different amacrine cell types within the IPL. **B,** Polyaxonal amacrine cells in the mouse retina. Dendrites are represented in red and axons in blue. Note that these cells are present in most IPL strata, and that some have axons and dendrites in different strata. The lateral spread of axonal and dendritic processes is not completely represented, except to indicate that the spread of the dendritic field in these cells is narrower than the spread of axons. Images in (**A**) and (**B**) are from (Masland, 2012b).

1.1.3 Retinal Ganglion Cells

Retinal ganglion cells (RGCs) are the sole output neurons of the retina (Fig. 1.1B,C). Therefore, the processed visual information transmitted from RGCs to higher visual areas constitutes what the rest of the brain will ever know about the visual world. By integrating multiple excitatory and inhibitory synaptic inputs from bipolar and amacrine cells, RGCs produce complex outputs forming parallel 'channels' of feature-specific visual information (Wassle, 2004; Gollisch and Meister, 2010). To give some examples, there are RGC types that respond selectively to specific cues present in the visual field, like stimuli moving in a particular direction, approaching stimuli, small stimuli, or elongated stimuli oriented along a certain axis (see 1.2). Over the past years, there have been various attempts to comprehensively classify RGCs according to their anatomical, molecular or physiological features [reviewed in (Seung and Sumbul, 2014) and (Sanes and Masland, 2015)]. In a recent study, Baden et al. (2016) have carried out an unbiased systematic characterisation of all the functional output channels present in the mouse retina. The authors performed calcium imaging while presenting a large set of different visual stimuli to distinguish the various RGC response types, followed by electrophysiological, anatomical and immunohistochemical analyses to further confirm the identified types. This led to the profiling of ~32 groups of

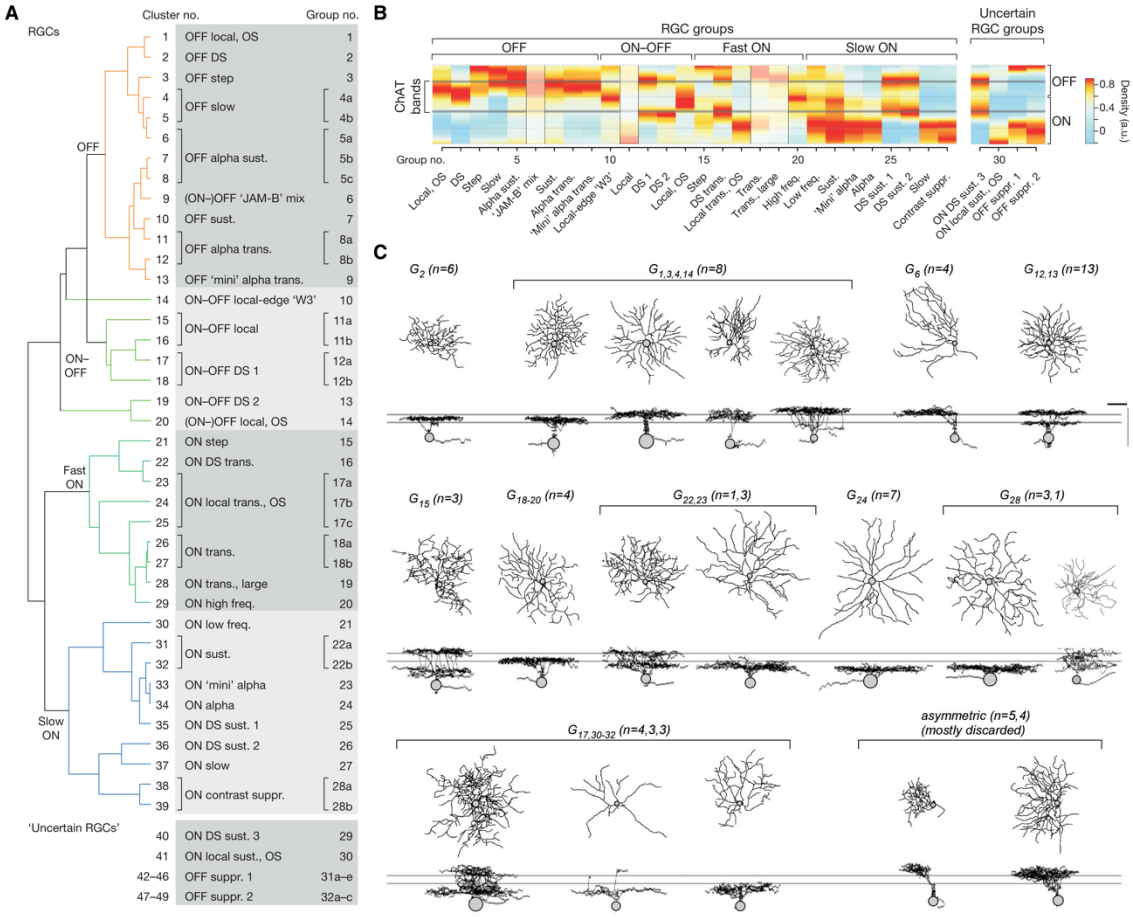

Figure 1.5. Ganglion cell types in the mouse retina. A, Tree diagram representing the different retinal ganglion cell (RGC) types in the mouse retina and how they are functionally related. Each group (1-32) represents RGCs with defined functional properties. DS, direction-selective; OS, orientation-selective; freq., frequency; suppr., suppressed; sust., sustained; trans., transient. **B,** Heat map of estimated dendritic stratification pattern in the inner plexiform layer (IPL) for each RGC group. ON and OFF IPL portions and choline acetyltransferase^{+} (ChAT) bands are indicated. Warmer colours represent higher dendritic densities. a.u., arbitrary units. **C,** Morphology of example RGCs for each identified functional group in (**A**). RGCs at the bottom right corner could not be classified into any functional group. Scale bars are 50 µm. Images in (**A-C**) are from (Baden et al., 2016).

functionally, morphologically, and (in some cases) genetically defined RGC types (Fig. 1.5). Interestingly, the study revealed a higher-than-expected functional diversity of RGC feature channels, thus highlighting the extensive processing of visual scenes performed by the retina. In addition to this vast functional heterogeneity, a different study reported that the responses of some RGCs change qualitatively depending on the level of ambient luminance, suggesting that the functional output channels of the retina dynamically adjust in response to constantly varying environmental lightning conditions (Tikidji-Hamburyan et al., 2015).

The results highlighted above beg the question: how is this diversity generated? Some answers to this question are explored in section 1.2 '*Visual Computations in the Inner Retina*' and 1.3 '*Assembly of Retinal Circuits during Development*'. Briefly, the emergent functional properties observed in the retinal output result from highly specific

and stereotypic synaptic connectivity patterns between defined bipolar, amacrine and ganglion cell types (Briggman et al., 2011; Helmstaedter et al., 2013; Dunn and Wong, 2014). Developmental studies have shown that the wiring of functionally specialised retinal circuits is specified by multiple mechanisms, mostly mediated by molecular cues, operating in parallel over subsequent developmental steps (i.e., neurite extension, arborisation, lamination, synaptic partner matching, synapse stabilisation, etc.) (Sanes and Yamagata, 2009; Lefebvre et al., 2015; Missaire and Hindges, 2015). How the different cell types in the retina are produced through fate determination over development (Cepko, 2014), or to what extent some cell types show different topographic distributions across the retina (Bleckert et al., 2014) are interesting topics that, for brevity reasons, are not discussed here.

1.1.4 Retinal Projection Targets

Several lines of evidence suggest that the different output channels of the retina have distinct roles in downstream visual processing and, therefore, perception and behaviour [reviewed in (Dhande and Huberman, 2014) and (Dhande et al., 2015)]. A first indication comes from various observations showing that RGCs have cell-type-specific axon projection patterns (Fig. 1.6A). In particular, not only RGC types differ in terms of the number of visual brain areas they target (e.g., the superior colliculus is the only retinorecipient area innervated by more than 85% of RGCs in mouse) (Huberman et al., 2008b; Kim et al., 2008; Kay et al., 2011; Ellis et al., 2016), but also they show type-specific axonal arborisations (e.g., columnar or laminar) within retinorecipient nuclei innervated by multiple RGC types (e.g., superior colliculus or lateral geniculate nucleus) (Huberman et al., 2009; Kim et al., 2010). In mouse, for instance, defined types of ON direction-selective RGCs (which respond preferentially to slowly moving stimuli) exclusively innervate nuclei of the accessory optic system, whereas most ON-OFF direction-selective RGC types (tuned to fast moving stimuli) do not target these nuclei and instead preferentially innervate other retinorecipient areas, like the superior colliculus (Dhande et al., 2013; Gauvain and Murphy, 2015). To give another striking example, mouse local edge detector RGCs project exclusively to the superior colliculus, where they stratify their axon terminals in the most superficial layer of the neuropil (Kim et al., 2010; Zhang et al., 2012). A second line of evidence comes from studies in which selective ablations of defined retinal cell types cause specific behavioural impairments. A prominent case is represented by melanopsin-expressing

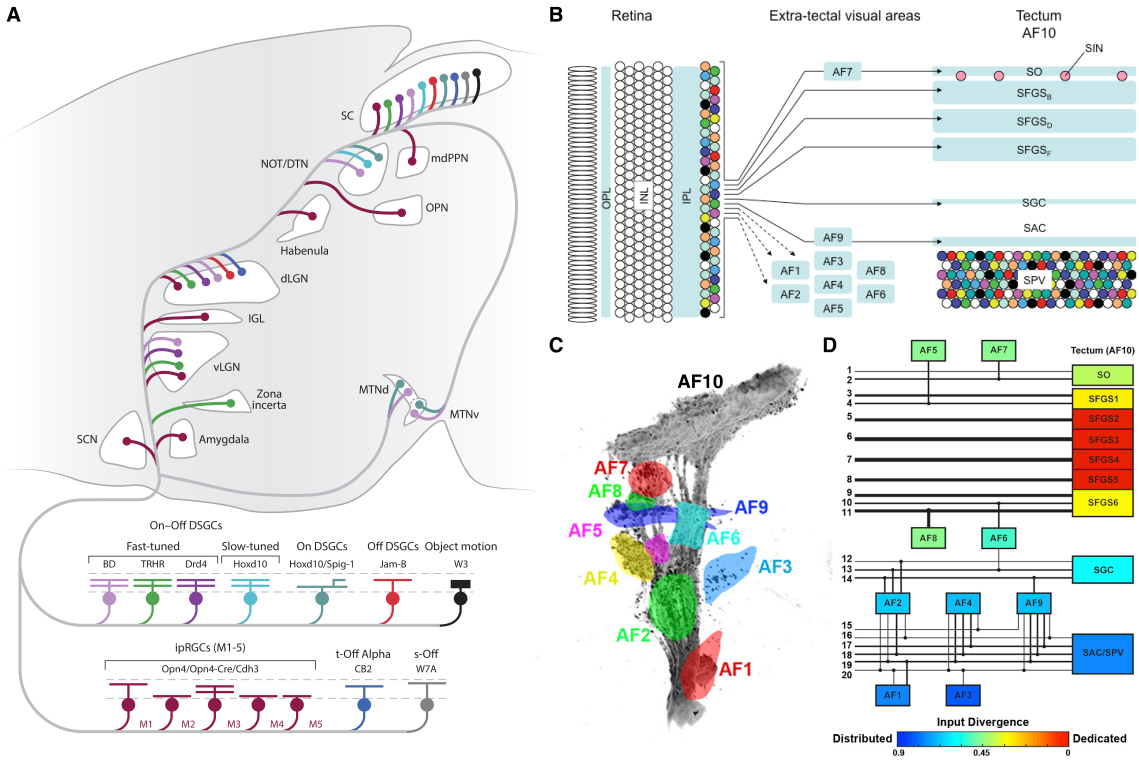

Figure 1.6. RGC projection targets in mouse and zebrafish. A, Schematic showing known projection patterns of the main retinal ganglion cell (RGC) types in mouse. The names of mouse transgenic lines labelling these RGC types are also reported. For simplicity, axonal projections of intrinsically photosensitive RGCs (ipRGCs) are represented as a single population. dLGN, dorsal lateral geniculate nucleus; DSGCs, direction-selective ganglion cells; IGL, intergeniculate leaflet; mdPPN, medial division of the posterior pretectal nucleus; MTNd, dorsal medial terminal nucleus; MTNv, ventral medial terminal nucleus; NOT/DTN, nucleus of the optic tract/dorsal terminal nucleus; OPN, olivary pretectal nucleus; SC, superior colliculus; SCN, suprachiasmatic nucleus; s-Off, Off-sustained; t-Off, Off-transient; vLGN, ventral lateral geniculate nucleus. Image is from (Dhande et al., 2015). **B,** Schematic representing the main retinofugal pathways in the larval zebrafish. Coloured circles indicate diverse cell types. Different RGC types (colours) have defined projections to one or more of ten retinorecipient arborisation fields (AF1-9 plus AF10, which is the optic tectum). INL, inner nuclear layer; IPL, inner plexiform layer; OPL, outer plexiform layer; SAC, stratum album centrale; SFGS, stratum fibrosum et griseum superficiale; SGC, stratum griseum centrale; SIN, superficial interneuron; SO, stratum opticum; SPV, stratum periventriculare. Image from (Nevin et al., 2010). **C,** Pseudocoloured lateral view of the optic tract and arborisation fields in a larval zebrafish. **D,** Schematic of the larval zebrafish optic tract representing the 20 identified RGC projection classes (horizontal lines). Line width indicates relative frequency, and black circles represent axon branching points. The colour of each arborisation field is consistent with the observed input divergence index. Images in (**A**) and (**B**) are from (Robles et al., 2014).

intrinsically photosensitive RGCs, which are the only RGCs projecting to the suprachiasmatic nucleus, the master circadian clock in the brain (Hattar et al., 2002; LeGates et al., 2014). Notably, targeted genetic killing of melanopsin-expressing RGCs led to a full loss of circadian photoentrainment, thus revealing their crucial role in regulating endogenous circadian rhythms (Guler et al., 2008). To provide another key case, the selective ablation of starburst amacrine cells resulted in loss of RGC direction selectivity and, as a consequence, severe impairment in performing the optokinetic eye reflex in response to whole-field visual motion (Yoshida et al., 2001).

In zebrafish, numerous studies have characterised cell-type-specific RGC projections through anatomical, functional and behavioural approaches. Ten retinorecipient brain areas (or arborisation fields – AFs) have been identified in larval zebrafish, the main one being the optic tectum (AF10), which is the teleost homologue of the mammalian superior colliculus (Fig. 1.6B,C) (Burrill and Easter, 1994). The neuropil of the optic tectum is then further subdivided into ten retinorecipient laminae, where individual RGC axon terminals arborise in a planar fashion within a single neuropil lamina (Meek, 1983; Robles et al., 2013). In a comprehensive survey of RGC axonal and dendritic arborisation patterns, Robles et al. (2014) reported the presence of ~20 stereotyped axon projection patterns (Fig. 1.6D), which could be further classified into ~50 structural RGC types with unique combinations of dendritic and axonal morphologies. Notably, it was shown that the optic tectum receives inputs from virtually all morphological RGC types, and most RGC types target other arborisation fields through axon collaterals, therefore creating brain-area-specific visual representations (Fig. 1.6D). Even though a complete functional characterisation of zebrafish RGC output and cell-type-specific projections is not available to date, various studies have started addressing these questions. Nikolaou et al. (2012) and Lowe et al. (2013) found that direction-selective RGCs target the most superficial laminae of the tectal neuropil, whereas orientation-selective RGCs innervate deeper neuropil laminae. Strikingly, this projection specificity extends to the different subtypes of direction- and orientation-selective RGCs, with each subtype (tuned to a particular direction or orientation) stereotypically targeting one or a few anatomically distinct neuropil laminae. Similarly, RGCs tuned to small visual stimuli tend to project to the most superficial tectal neuropil laminae, whereas large-size-selective RGCs preferentially target deeper laminae (Preuss et al., 2014). Interestingly, Semmelhack et al. (2014) showed that morphologically defined RGCs tuned to small visual stimuli (similar in size to prey stimuli) project to superficial tectal neuropil laminae as well as to AF7. The authors also reported that targeted laser ablation of AF7 significantly reduced prey capture behaviour, thus indicating a potential link between defined RGC types projecting to AF7 and an ethologically relevant visual behaviour. Other studies have analysed RGC outputs selective for looming stimuli and found that the optic tectum seems to be the main retinorecipient area capable of integrating this visual information and, subsequently, triggering escape responses (Temizer et al., 2015; Dunn et al., 2016a).

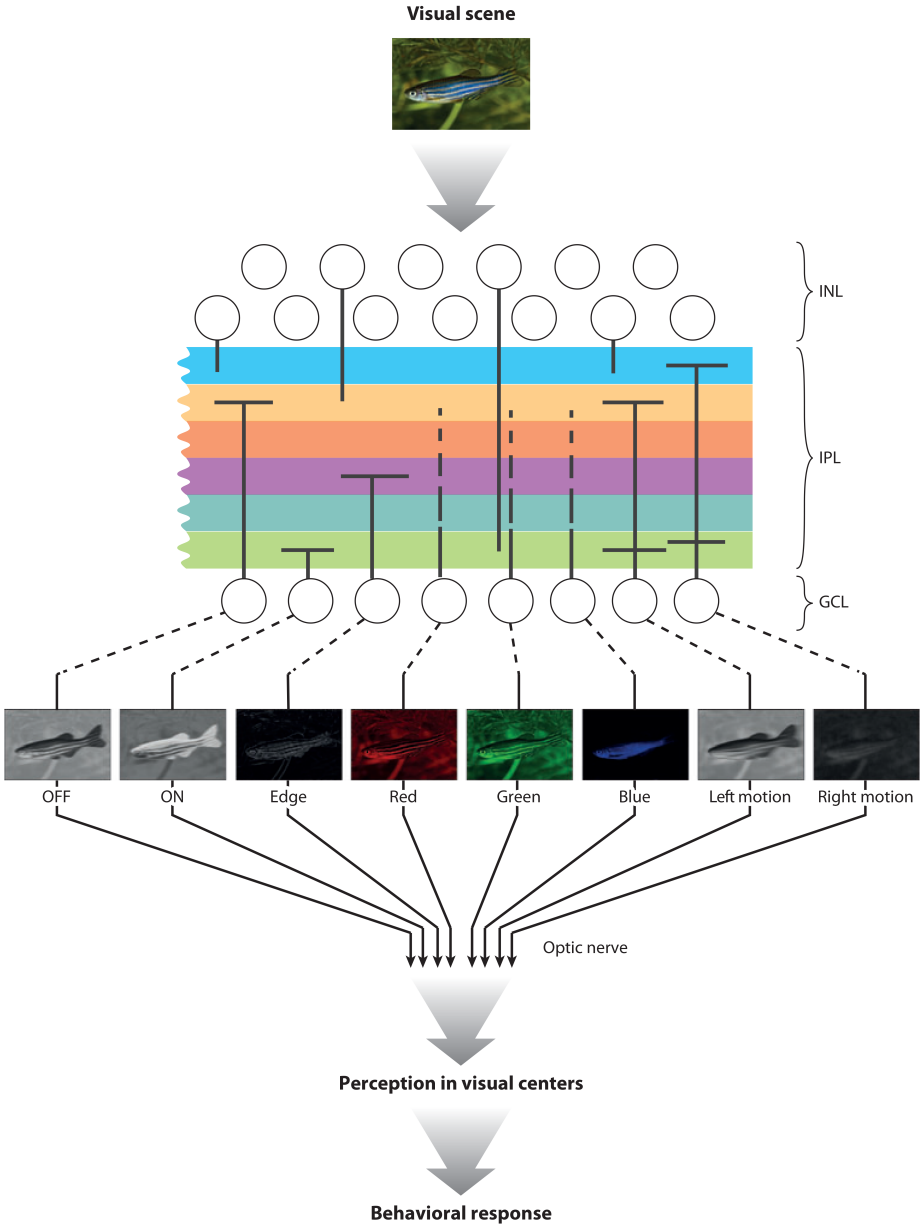

Figure 1.7. Parallel processing of visual features in the retina. Defined features of the visual scene (top), such as increase (ON) or decrease (OFF) of luminance level, high contrast contours (edge), chromatic information (e.g., red, green, and blue), and direction of motion (e.g., left, right) are detected by morphologically and physiologically defined types of retinal ganglion cells (RGCs). This selectivity is the result of specific, lamina-restricted inputs from defined subsets of bipolar and amacrine cells, which contact RGCs in a layered synaptic structure called the inner plexiform layer (IPL). RGCs project axons via the optic nerve to several visual brain areas. The combined activity of these distributed brain areas contributes to the animal's perception and behavioural output (bottom). GCL, ganglion cell layer; INL, inner nuclear layer. Image is from (Baier, 2013).

To conclude, visual scenes are extensively processed in the retina before visual information is transmitted to higher visual centres. Multiple retinal circuits operating in parallel decompose input images into feature-specific output neural channels playing different roles in visual perception and behaviour (Fig. 1.7). Most of the image processing takes place in the IPL and involves morphologically and functionally defined bipolar, amacrine and ganglion cells – the core computational elements of retina.

1.2 Visual Computations in the Inner Retina

In this section, the key circuit building blocks and connectivity patterns generating direction and orientation selectivity in RGCs are described in detail. Other retinal circuits underlying important visual computations, such as object motion selectivity and approach sensitivity, are also discussed.

1.2.1 Direction-selective Circuits

The computation of directional motion is one of the most basic and important processing steps carried out in the early visual system, and is thought to play an essential role in, for example, detecting the direction in which a prey or predator is moving. Direction selectivity is described as the selectivity of neuronal firing for visual stimuli moving in a certain direction (or *preferred direction*), and suppression of firing when stimuli move in the opposite direction (or *null direction*) (Fig. 1.8A). Neurons that exhibit this property are called direction-selective (DS) and were first discovered in the rabbit retina by Barlow and Hill (1963) more than 50 years ago. Since then, a large number of studies have investigated the neural mechanisms generating direction selectivity in several different vertebrate and invertebrate species [reviewed in (Borst and Euler, 2011) and (Borst and Helmstaedter, 2015)]. In vertebrates, especially mammals, the cell types and microcircuitry underlying this neural computation have been uncovered in great detail, thus making retinal DS circuits among the best-understood circuits of the brain [reviewed in (Wei and Feller, 2011) and (Vaney et al., 2012)]. In the mammalian retina, three main types of DS ganglion cells (DSGCs) with different response polarities have been identified: ON DSGCs, OFF DSGCs and ON-OFF DSGCs. All OFF DSGCs are selective to upward motion, whereas ON and ON-OFF types are further subdivided into different subtypes according to their preferred direction of stimulus motion: three ON DSGCs (selective to forward, upward or downward motion) and four ON-OFF DSGCs (selective to forward, backward, upward or downward motion). In zebrafish, three DSGC subtypes selective to forward, upward or downward motion have been found, but their response polarity has not been fully characterised (Nikolaou et al., 2012; Lowe et al., 2013).

Among all DSGC types, ON-OFF DSGCs are the most extensively characterised. They possess a bistratified dendritic morphology, with the ON and OFF dendritic arbours co-stratifying with the neurites of ON and OFF starburst amacrine cells (SACs), respectively (Fig. 1.9A,B). This anatomical feature was initially seen as

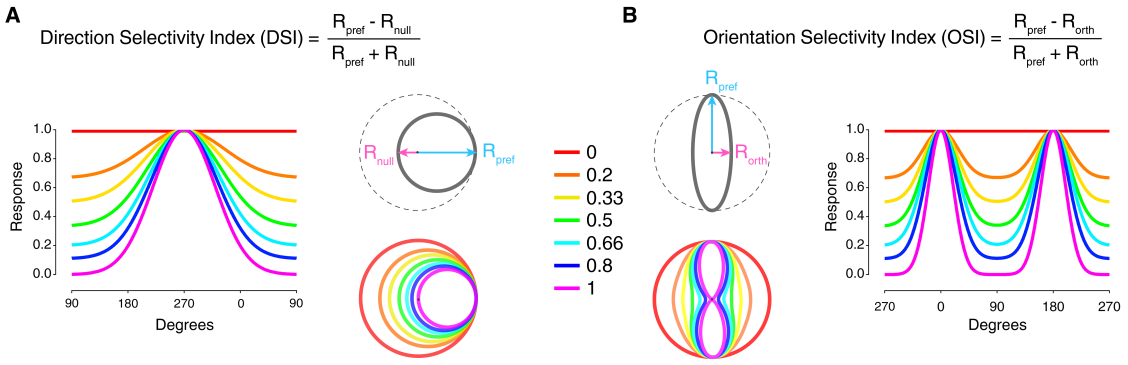

Figure 1.8. Direction and orientation selectivity. A|B, Diagram illustrating the quantification of direction selectivity (**A**) and orientation selectivity (**B**), using the direction selectivity index (DSI) and orientation selectivity index (OSI), respectively. The algorithms used to calculate DSI and OSI of visual responses are reported at the top. For DSI, the responses to the preferred direction of moving bars (R_{pref}) and opposite, or null, direction (R_{null}; 180° angular distance) are used. For OSI, the responses to the preferred axis (R_{pref}) and orthogonal axis (R_{orth}; 90° angular distance) are used. Note that the arrows indicate the motion direction of orthogonally oriented bars or gratings. A single Gaussian or von-Mises distribution is used to fit responses of direction-selective cells and estimate their preferred direction of motion from the centre of the fitted curve. The sum of two Gaussian or von-Mises distributions (180° angular distance apart) is used to fit responses of orientation-selective cells to estimate their preferred axis and stimulus orientation from the centres of the fitted curves. The colour code describes the different levels of direction (**A**) and orientation (**B**) selectivity.

an indication that SACs are crucial circuit players presynaptic to ON-OFF DSGCs (Famiglietti, 1991, 1992). Subsequent studies have further confirmed and extended the role of SACs as necessary cellular components in which direction selectivity is first computed and, subsequently, transmitted to DSGCs. The major findings supporting the central role of SACs in direction selectivity are the following: (a) targeted genetic ablation of SACs leads to a dramatic loss of DS responses in RGCs (Yoshida et al., 2001). (b) SACs release the neurotransmitter GABA and pharmacologically blocking $GABA_A$ receptors completely abolishes direction selectivity in DSGCs (Wyatt and Day, 1976; He and Masland, 1997). Specific genetic disruption of GABA neurotransmission exclusively in SACs further demonstrated the crucial role played by SAC-derived GABAergic inhibition, and also revealed additional excitatory mechanisms (Pei et al., 2015). SACs are the only retinal neurons releasing the excitatory neurotransmitter acetylcholine and, even though early reports did not show a crucial effect of cholinergic transmission on direction selectivity (He and Masland, 1997), GABA/acetylcholine co-release from SACs seems to play an important role in shaping DSGC responses (Sethuramanujam et al., 2016). (c) Individual dendritic branches of SACs are direction-selective as they show higher calcium transients in response to stimuli moving centrifugally (away from the cell soma) than to stimuli moving centripetally (towards the soma) (Fig. 1.9E) (Euler et al., 2002). Responses are only visible in distal regions of the dendritic tree, which contain varicosities corresponding to the synaptic outputs of

SACs (Ding et al., 2016). These observations suggest that individual SAC dendritic branches act as independent processing units constituting subcellular substrates where direction selectivity is computed before being generated in DSGCs. (d) The results described in (c) imply that the preferred direction of a given DSGC is opposite to the preferred direction of the SAC dendrites providing its inhibitory inputs (Fig. 1.9C). Two different lines of evidence demonstrate that this is indeed the case. First, Fried et al. (2002) performed dual electrophysiological recordings revealing that the inhibitory input DSGCs receive from SACs located on their null side is greater than the input received from SACs located on their preferred side. Second, Briggman et al. (2011) combined two-photon population calcium imaging of RGCs with serial block-face scanning electron microscopy followed by connectomic reconstructions, to relate the synaptic inputs ON-OFF DSGCs receive from SACs with their observed directional tuning. Notably, they found that DSGCs form numerous synapses with null-side SACs but few with preferred-side SACs (Fig. 1.9D). This extremely precise wiring pattern results from an asymmetric increase in the number of inhibitory synapses from null-side SACs during the second postnatal week of mouse development (Wei et al., 2011; Yonehara et al., 2011; Morrie and Feller, 2015). Interestingly, this developmental switch depends on molecular cues, at least in DSGCs tuned to forward or backward motion (Yonehara et al., 2016).

The results highlighted above place SACs at the centre of retinal DS circuits, and indicate a crucial role played by SAC dendritic computation in detecting stimulus motion direction. However, how is direction selectivity generated in SAC dendritic branches? Currently, there are two main, non-mutually exclusive models explaining this phenomenon. The first is a dendrite-autonomous mechanism whereby the specific dendritic geometry of SACs and the distribution of excitatory inputs along their dendrites, together with active dendritic conductances, can produce direction selectivity (Hausselt et al., 2007; Vlasits et al., 2016). The second model is based on the observation that the different bipolar cell types show responses with distinct temporal dynamics and that they stratify their presynaptic terminals in a stereotypic fashion across the IPL depth (see 1.1.1) (Baden et al., 2013). Electron microscopy connectomic reconstructions of bipolar cells forming contacts with SAC dendrites showed that slow bipolar cell types with sustained responses connect proximally to the SAC soma, whereas fast bipolar cell types with transient responses connect distally (Fig. 1.9F) (Kim et al., 2014; Ding et al., 2016; Greene et al., 2016). This specific

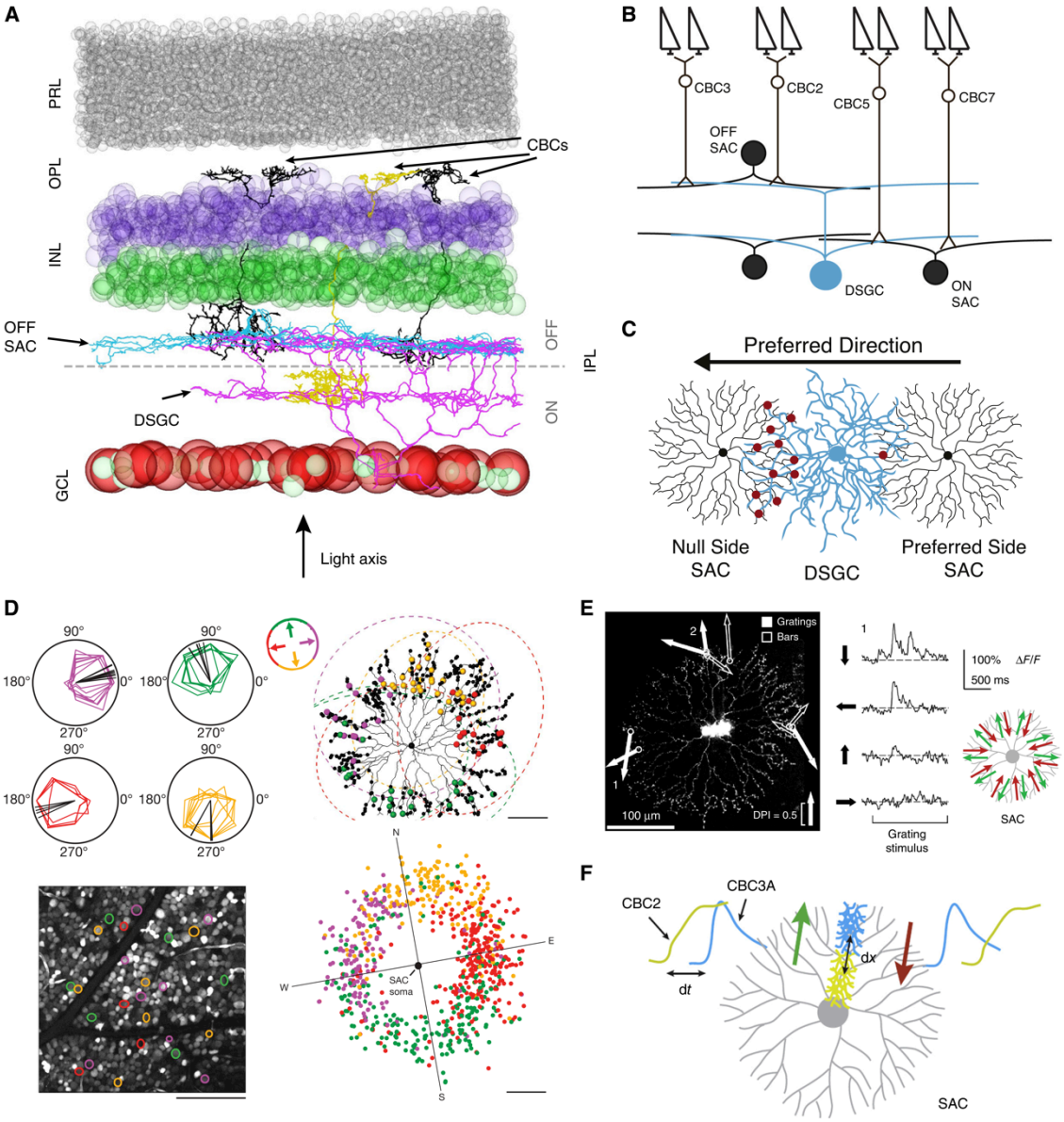

Figure 1.9. Cell types and circuit mechanisms underlying retinal direction selectivity. A, Layout of the cell types involved in directional motion detection obtained from a densely reconstructed electron microscopy data set. Reconstructions of a direction-selective ON-OFF ganglion cell (DSGC, magenta) with dendrites bistratified in ON and OFF strata of the IPL, an OFF starburst amacrine cell (SAC, cyan), and type 2 (black), 3A (black) and 5B/C (yellow) cone bipolar cells (CBCs) are shown. Soma positions of photoreceptors (grey), bipolar cells (blue), ganglion cells (red), and amacrine cells (green) are reported. PRL, photoreceptor layer; OPL, outer plexiform layer; INL, inner nuclear layer; IPL, inner plexiform layer, GCL, ganglion cell layer. **B,** Schematic representing the key cellular components of the direction-selective circuit of the retina. Bipolar cells provide excitatory gluatamatergic input to SACs and DSGCs. Distinct bipolar cell types contact ON or OFF SACs at the subcellular locations shown (proximal vs. distal). SACs provide feedforward GABAergic inhibition to DSGCs. **C,** Diagram showing the circuit wiring underlying directional GABA release onto DSGCs. SACs on the null side of DSGCs form more GABAergic synapses than SACs on the preferred side. **D,** Polar plot response profiles of DSGCs (left) colour-coded according to their preferred motion direction (black lines). Corresponding DSGC soma locations superimposed onto a two-photon image of the recorded region in the GCL. An OFF SAC (right; black skeleton), with varicosities indicated by black dots. DSGC dendritic fields are represented by colour-coded dashed ellipses. Synapses are colour-coded according to the preferred direction of the postsynaptic DSGC. Scale bars are 100 µm (left) and 50 µm (right). **E,** Direction-selective responses in SAC dendrites. A fluorescent dye-filled SAC (left) and calcium responses to gratings moving in four directions (centre) are shown. Each of the radially oriented dendritic branch has its own preferred direction of motion, namely motion from SAC soma to dendrite tip. DPI, direction preference index. **F,** Spatially offset excitatory inputs from different cone bipolar cell types together with their differences in response kinetics likely underlies the detection of directional

motion in individual SAC dendritic branches. Type 2 CBCs (yellow) with slower and longer-latency release contact the OFF SAC dendrite (grey) more proximally, whereas 3A CBCs (cyan) with faster and short-latency responses contact the OFF SAC dendrite more distally, therefore establishing a spatial (dx) and temporal (dt) offset resulting in outward-preferred (green arrow) and inward-suppressed (red arrow) directional responses. Images in (**A**), (**E**) and (**F**) are from (Borst and Helmstaedter, 2015), with left side of (**E**) adapted from (Euler et al., 2002). Images in (**B**) and (**C**) are from (Morrie and Feller, 2016). Images in (**D**) is from (Briggman et al., 2011).

spatial arrangement of bipolar cell presynaptic terminals along SAC dendrites would result in different temporal delays between slow and fast bipolar cell inputs depending on the direction of stimulus motion, thus generating direction selectivity (Kim et al., 2014). Briefly, visual stimuli moving centrifugally (soma to dendrite) would trigger slow inputs before fast ones, which would then reach the SAC dendrite simultaneously, summing to elicit strong depolarisations. Stimuli moving centripetally (dendrite to soma) would instead trigger fast responses before the slow, more proximal ones can kick in, therefore causing small depolarisations (Fig. 1.9F).

Finally, it is worth mentioning that postsynaptic mechanisms can also produce direction selectivity in DSGCs. For example, in a genetically defined subpopulation of ON-OFF DSGCs tuned to forward motion, asymmetric dendritic arbours aligned to the preferred direction of motion enhance DSGC directional tuning through mechanisms working in parallel with SAC-derived DS inhibition (Trenholm et al., 2011). Similarly, the asymmetry of dendritic arbours appears to be an essential requirement for generating upward motion selectivity in OFF DSGCs, which do not receive SAC inputs (Kim et al., 2008). Additionally, it has been shown that active conductances in DSGC dendrites enhance direction selectivity by producing dendritic calcium spikes during preferred direction stimulation, while GABAergic synaptic inhibition prevents the initiation of dendritic spikes during null-direction stimulation (Oesch et al., 2005; Sivyer and Williams, 2013). No direct contribution to DSGC tuning appears to be provided by excitatory inputs from bipolar cell axon terminals, whose responses lack direction selectivity (Yonehara et al., 2013; Park et al., 2014), consistent with the observation that SACs do not form synapses onto bipolar cell terminals (Ding et al., 2016).

1.2.2 Orientation-selective Circuits

Detecting the orientation of elongated visual stimuli is another fundamental image processing step carried out in the early visual system. Orientation selectivity was first discovered in cat primary visual cortex more than 50 years ago by Hubel and Wiesel (1962). They described it as the selectivity of neuronal firing for elongated visual stimuli oriented along a specific axis in the visual field (or *preferred orientation*), and

suppression of firing when stimuli are oriented orthogonally to their preferred axis (or *orthogonal orientation*) (Fig. 1.8B). Shortly afterwards, Levick (1967) identified orientation-selective ganglion cells (OSGCs) in the rabbit retina, suggesting that orientation-specific information is already evident in the output neurons of the retina. Since then, orientation-selective cells have been described in many vertebrate and invertebrate visual systems, including primates (Hubel and Wiesel, 1968), rodents (Niell and Stryker, 2008), fish (Nikolaou et al., 2012) and insects (Fisher et al., 2015). Compared to retinal DS circuits, however, our understanding of the cellular players and microcircuit mechanisms generating orientation selectivity in the retina is still far from complete, mostly due to the lack of specific molecular markers. In mammals, OSGCs have been found in rabbit (Levick, 1967; Caldwell et al., 1978; Amthor et al., 1989; Bloomfield, 1994; He et al., 1998; Venkataramani and Taylor, 2010, 2016), cat (Levick and Thibos, 1980, 1982), mouse (Zhao et al., 2013; Chen et al., 2014; Pearson and Kerschensteiner, 2015; Baden et al., 2016; Nath and Schwartz, 2016), and primates (Passaglia et al., 2002). In lower vertebrates, OSGCs have been described in zebrafish (Nikolaou et al., 2012; Lowe et al., 2013), carp (Damjanovic et al., 2009), and turtle (Sernagor and Grzywacz, 1995).

To date, only few OSGC types in two species have been characterised in terms of their morphology and physiology (Fig. 1.10A,B). In rabbit, Venkataramani and Taylor (2010, 2016) identified two subtypes of OFF OSGCs tuned to horizontal or vertical visual stimuli, and one type of ON OSGCs selective to horizontally oriented stimuli (Fig. 1.10A,B right). In mouse, Nath and Schwartz (2016) found two ON OSGC subtypes tuned to horizontal or vertical stimuli (Fig. 1.10A,B left and 1.10C). Baden et al. (2016) functionally identified also OFF and ON-OFF OSGC types in the mouse retina (both comprising subtypes tuned to different cardinal orientations), but their precise morphology is still unclear. In zebrafish, Lowe et al. (2013) reported the presence of four OSGC subtypes tuned to different cardinal or diagonal orientations, but their response polarity and dendritic stratification in the IPL remain to be described. In mouse, the dendrites of ON OSGCs stratify in both ON and OFF IPL regions (Nath and Schwartz, 2016), while in rabbit they stratify exclusively in the ON region (Fig. 1.10A) (Venkataramani and Taylor, 2016). The IPL dendritic stratification pattern of rabbit OFF OSGCs has not yet been described in detail (Venkataramani and Taylor, 2010). Strikingly, both mouse and rabbit horizontal ON OSGCs cells have elongated dendritic arbours oriented according to their stimulus orientation preference (i.e., horizontally

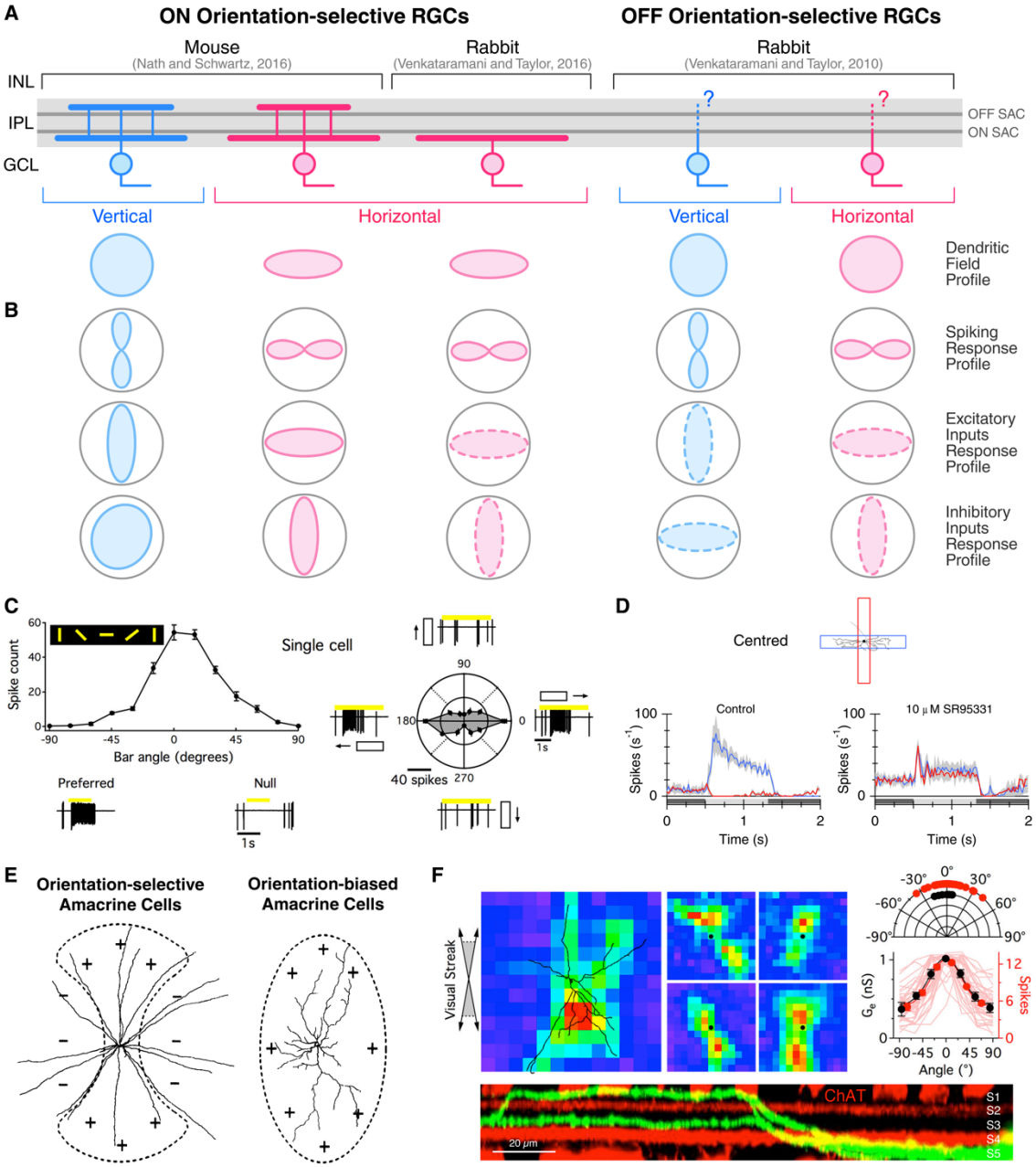

Figure 1.10. Orientation-selective ganglion and amacrine cells in mouse and rabbit. A|B, Schematic summarizing the morphological (**A**) and physiological (**B**) properties of ON OSGCs in mouse (Nath and Schwartz, 2016), and ON and OFF OSGCs in rabbit (Venkataramani and Taylor, 2010, 2016). **A,** Dendritic stratification (top) in the inner plexiform layer (IPL), and dendritic field profiles (bottom) of ON-OSGCs. Dark grey lines in the IPL indicate ON and OFF choline acetyltransferase (ChAT) strata corresponding to ON and OFF starburst amacrine cell (SAC) neurites, respectively. INL, inner nuclear layer; GCL, ganglion cell layer. **B,** Response profiles of OSGC spiking (top), excitatory inputs (middle), and inhibitory inputs (bottom). Dashed lines of excitatory and inhibitory inputs response profiles in rabbit OSGCs indicate estimated profiles from responses recorded during preferred versus orthogonal orientation stimulation. Note the high degree of morphological and physiological homology between mouse and rabbit OSGCs. **C,** Spike responses of an example mouse ON OSGC to static bar stimuli (left). Preferred and null orientation responses are reported. Polar plot of an example mouse ON OSGC responses to moving bar stimuli with responses to preferred and null orientations (right). Error bars indicate SEM across trials. Image is from (Nath and Schwartz, 2016). **D,** Pharmacological block of $GABA_A$ receptors suppresses orientation selectivity in rabbit ON OSGCs. Average spike responses in control and in the presence of 10 μM SR-95531 (Gabazine) to block $GABA_A$ receptors are reported. Image is from (Venkataramani and Taylor, 2016). **E,** Schematic illustration representing proposed receptive-field organisation of the orientation-selective and orientation-biased amacrine cells identified in the rabbit retina. Excitatory inputs are indicated by (+) whereas inhibitory inputs are indicated by (–). Note that orientation tuning in orientation-biased

amacrine cells does not appear to result from spatially anisotropic inhibition like in orientation-selective amacrine cells. Image is from (Bloomfield, 1994). **F,** Morphological and functional features of an ON orientation-selective, wide-field polyaxonal amacrine cell type found in the rabbit retina. Receptive field mapping of the excitatory inputs received by this cell type (top left) revealed its elongated receptive field with orientation coinciding with its preferred stimulus orientation. Black dots indicate cell body position. Average peak excitatory conductances (black) and spike counts (red) versus stimulus angle, with 0° corresponding to the maximal response (top right). Preferred stimulus angle for individual spike tuning curves (red), or dominant orientation of dendritic fields (black) are also reported. Z-stack image of an ON orientation-selective polyaxonal amacrine cell (green) showing its dendritic stratification pattern in laminae S1 and S3 of the IPL (bottom). $ChAT^+$ strata are stained in red. Image is from (Murphy-Baum and Taylor, 2015).

oriented, Fig. 1.10A) (Nath and Schwartz, 2016; Venkataramani and Taylor, 2016). This morphological bias could contribute to the tuning of horizontal ON OSGCs, however, the extent to which this feature is necessary to generate orientation selectivity is unclear because no significant bias was found in rabbit OFF OSGCs or mouse vertically tuned ON OSGCs (Venkataramani and Taylor, 2010; Nath and Schwartz, 2016; Venkataramani and Taylor, 2016).

If morphology alone is an unlikely prerequisite for OSGC tuning, what else could produce their orientation selectivity? Interestingly, presynaptic mechanisms play a crucial role in the emergence of OSGC tuning. In both mouse and rabbit, whole-cell voltage clamp recordings isolating excitatory and inhibitory conductances revealed that OSGCs receive synaptic inputs with highly stereotypical tuning profiles (Venkataramani and Taylor, 2010; Nath and Schwartz, 2016; Venkataramani and Taylor, 2016). Specifically, both mouse and rabbit OSGCs receive excitatory inputs tuned to their preferred orientation, and inhibitory inputs tuned to the orthogonal orientation (i.e., 90° angular distance; Fig. 1.10B). Mouse vertical ON OSGCs appear to be the only exception, since some cells receive inhibitory inputs that are not orthogonally tuned (Fig. 1.10B left) (Nath and Schwartz, 2016). In rabbit, pharmacologically blocking $GABA_A$ receptors showed that GABA-mediated inhibition is crucial in rendering the spiking output of OSGCs orientation-selective (Fig. 1.10D) (Caldwell et al., 1978; Venkataramani and Taylor, 2010, 2016). Notably, the block of GABAergic inhibition markedly reduces the orientation tuning of both excitatory and inhibitory inputs, although some cell subtype-specific differences are present (Venkataramani and Taylor, 2010, 2016). An early study reported that glycine-mediated inhibition is not strictly required to generate OSGC tuning in rabbit (Caldwell et al., 1978). However, a role for glycinergic dis-inhibition in providing orientation-selective excitatory drive has been described in rabbit OFF OSGCs (Venkataramani and Taylor, 2010; Taylor and Smith, 2011). In mouse, individually blocking either $GABA_A$ or glycine receptors does not produce any significant change in the orientation tuning of excitatory or inhibitory

inputs, suggesting that there is a substantial level of redundancy among GABAergic and glycinergic mechanisms (Nath and Schwartz, 2016). Blocking both receptor types simultaneously completely abolishes inhibitory conductances but, surprisingly, does not affect the tuning of excitatory inputs, which thus arises through inhibition-independent mechanisms.

Overall, the results highlighted above indicate that, at least in rabbit, synaptic inhibition from amacrine cells plays a crucial role in generating OSGC tuning. Moreover, in some cell subtypes orientation-tuned inhibition from amacrine cells appears to modulate the tuning of both OSGCs and bipolar cell presynaptic terminals (Venkataramani and Taylor, 2010). Interestingly, orientation-tuned amacrine cell types have been described in the rabbit retina (Bloomfield, 1991, 1994; Murphy-Baum and Taylor, 2015), but the precise extent to which their outputs directly contribute to OSGC tuning remains unclear. Bloomfield (1991, 1994) described two classes of orientation-tuned amacrine cells comprising both ON and OFF types: (1) *orientation-selective* and (2) *orientation-biased* amacrine cells (Fig. 1.10E). Orientation-selective amacrine cells are monostratified wide-field polyaxonal amacrine cells whose selectivity arises from orthogonally tuned inhibitory inputs. Orientation-biased amacrine cells are monostratified medium-field amacrine cells whose tuning appears to result exclusively from their highly elongated dendritic morphology, since no inhibitory input is observed during orthogonal-orientation stimulation. Consistent with this idea, the orientation of their elongated dendritic field corresponds to their preferred stimulus orientation. Similarly, an ON amacrine cell type in which orientation tuning results from an elongated dendritic morphology has been identified by Murphy-Baum and Taylor (2015) in the rabbit retina (Fig. 1.10F). Unlike the orientation-biased amacrine cells described by Bloomfield (1994), however, this cell type is a wide-field polyaxonal amacrine cell with a bistratified dendritic stratification pattern in the IPL, and cell soma displaced in the ganglion cell layer. Notably, both excitatory and inhibitory inputs received by this cell type are tuned to the preferred stimulus orientation, although excitatory inputs are more tuned than inhibitory ones. Furthermore, receptive field mapping revealed that its excitatory receptive field structure coincides with its dendritic arbour morphology, thus reinforcing the idea that its orientation-tuned responses are not produced by inhibition but by the arrangement of excitatory inputs onto its elongated dendritic field (Fig. 1.10F).

Finally, several lines of evidence suggest that orientation-selective circuits operate independently of direction-selective ones, and that the ways these two

computations are implemented in the retina rely on distinct cell types and microcircuits. First, neither OSGCs nor orientation-tuned amacrine cells co-stratify their dendrites with SACs (Fig. 1.10A,F) (Murphy-Baum and Taylor, 2015; Nath and Schwartz, 2016; Venkataramani and Taylor, 2016), an anatomical feature characteristic of most direction-selective circuits (see 1.2.1). Additionally, the tuning of OSGCs shows a different maturation pattern than DSGC tuning during mouse postnatal development (Chen et al., 2014). Another indication that orientation- and direction-selective circuits form distinct retinal output channels comes from the larval zebrafish, in which OSGC and DSGC axonal projections terminate in different, non-overlapping neuropil laminae of the optic tectum (Nikolaou et al., 2012; Lowe et al., 2013).

1.2.3 Additional Computations Performed by Retinal Circuits

Direction and orientation selectivity are two important computations carried out by retinal circuits. Among other features that the retina can extract from visual scenes, two computations have been described in detail: object motion sensitivity and approach sensitivity (Fig. 1.11A,B). Notably, both feature sensitivities rely on defined microcircuit connectivity motifs and specific inputs from distinct amacrine cell types (Fig. 1.11C,D).

Object motion sensitivity was initially discovered in frog RGCs by Lettvin et al. (1959). In their seminal study – *What the frog's eye tells the frog's brain* – they described RGCs capable of responding selectively to small visual stimuli (1-3°) moving across the receptive field centre with a trajectory different from the background, and defined these RGCs as 'bug detectors'. Later, RGC object motion sensitivity has also been found in rabbit (Levick, 1967; van Wyk et al., 2006), cat (Cleland and Levick, 1974), mouse (Zhang et al., 2012), salamander (Olveczky et al., 2003, 2007; Baccus et al., 2008), and zebrafish (Semmelhack et al., 2014). In most species, object motion-sensitive RGCs, often called local edge detectors (LEDs), have compact and densely branched dendritic arbours stratifying near the centre of the IPL depth (van Wyk et al., 2006; Kim et al., 2010; Zhang et al., 2012). Their firing selectivity for local instead of global motion (Fig. 1.11A) is primarily due to a strong inhibitory surround (Fig. 1.11C) (Olveczky et al., 2003; van Wyk et al., 2006; Olveczky et al., 2007; Zhang et al., 2012). Interestingly, the main cellular players providing this inhibitory surround during global motion are wide-field polyaxonal amacrine cells (Baccus et al., 2008), which act on both LEDs and bipolar cell presynaptic terminals (Baccus et al., 2008; Zhang et al., 2012). Importantly, LEDs are selective not only for local motion within the receptive

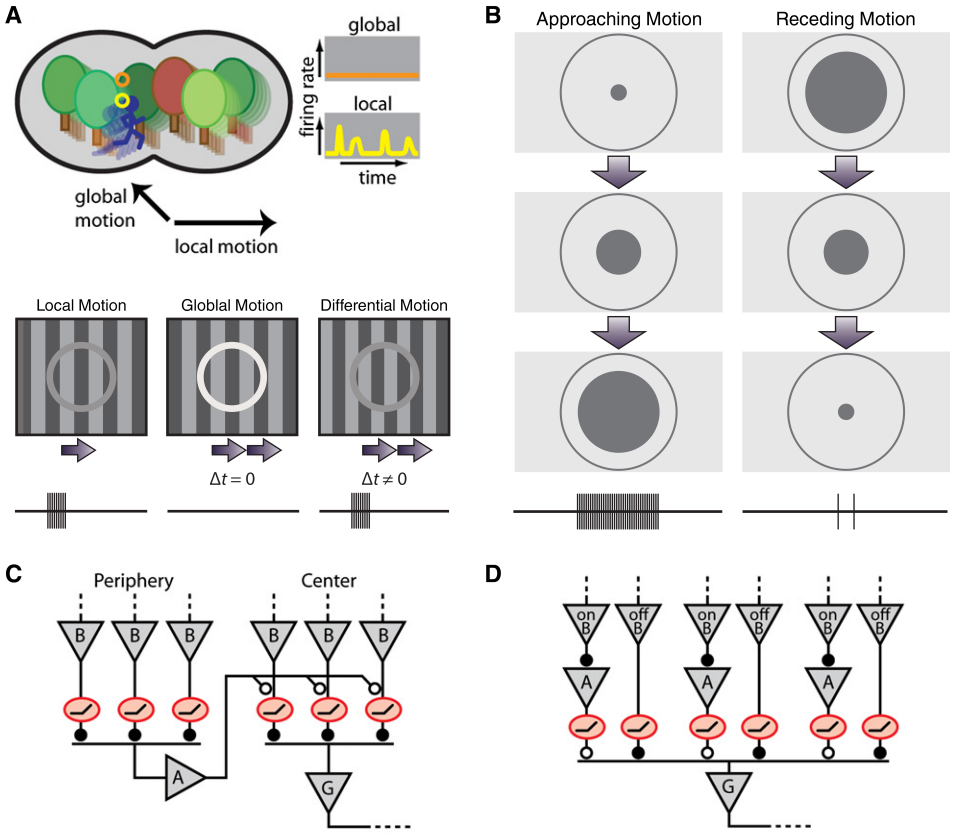

Figure 1.11. Object and approaching motion sensitivity in the retina. A, Detection of differential motion between an object and background. An object motion-sensitive ganglion cell remains silent during global motion of the visual field but fires when the image patch in its receptive field centre moves differently from the background. In particular, when the temporal delay (Δt) between object and background motion is zero, the cell is silent. Whereas, when Δt is different from zero the cell fires action potentials. Note that object motion-sensitive cells are also sensitive to local motion (i.e., an object moving over a static background). **B,** Approaching motion sensitivity. The PV-5 type of parvalbumin-expressing retinal ganglion cell responds strongly to an approaching dark object (i.e, dark stimulus with a continuously expanding contour; left). If the object is receding (i.e., dark stimulus with a continuously contracting contour) or moving laterally, the cell does not respond (right). **C,** Retinal circuitry underlying object motion sensitivity. Polyaxonal amacrine cells (A) in the periphery are excited by motion and send inhibitory inputs to the receptive field centre of the object motion-sensitive ganglion cell (G). If motion in the periphery is synchronous with that in the centre, the excitatory inputs the ganglion cell receives from bipolar cells (B) coincide with the inhibitory ones, and firing is suppressed. **D,** Retinal circuitry underlying approaching motion sensitivity. The approach-sensitive ganglion cell receives excitatory inputs from OFF bipolar cells and inhibitory inputs from ON amacrine cells. These ON amacrine cells are electrically coupled to ON bipolar cells through gap junctions, and can therefore provide rapid inhibition to the approach-sensitive ganglion cell. When a stimulus moves laterally or contracts, the inhibitory ON inputs generated by the light trailing edge of the stimulus supress firing in the ganglion cell. Images in (**A**) and (**B**) are from (Sanes and Masland, 2015). Images in (**A**), (**C**) and (**D**) are from (Gollisch and Meister, 2010).

field centre, but also for differential motion between centre and surround, namely object and background moving in different directions or at different speeds (Fig. 1.11A). How do LEDs perform this computation? A mathematical circuit model suggests that, to detect differential motion, the time course of excitatory inputs in the receptive field centre (reflecting the object motion trajectory) needs to differ from the time course of surround inhibitory inputs provided by polyaxonal amacrine cells (representing the background motion trajectory) (Baccus et al., 2008; Gollisch and Meister, 2010). When

the trajectories of object and background are identical (e.g., during global motion), the time courses of excitatory and inhibitory inputs coincide and, as a consequence, LED firing is suppressed. When instead the object and background motion trajectories differ (e.g., during differential motion), the time courses of excitatory and inhibitory inputs are not synchronised and LED can fire action potentials. Strikingly, recent studies in mouse have revealed that LEDs receive most of their excitatory inputs from glutamatergic VGluT3 amacrine cells (Lee et al., 2014; Krishnaswamy et al., 2015), which are themselves sensitive to differential motion and directly contribute to LED object motion sensitivity (Kim et al., 2015).

Approach sensitivity is described as the capability of some RGCs to respond selectively to dark looming stimuli, and stay silent when stimuli recede or move laterally in the visual field (Fig. 1.11B). Munch et al. (2009) characterised a type of parvalbumin-expressing OFF RGCs (also referred to as PV-5 RGC) that shows approach-sensitive responses. This RGC type is strongly activated by an expanding dark stimulus, even when the global luminance of the visual scene remains constant. On the contrary, its responses are completely suppressed by lateral motion of a dark stimulus. Munch et al. (2009) found that this selective suppression of firing is primarily mediated by AII amacrine cells. In particular, by receiving electrical inputs from ON bipolar cells through gap junctions, AII amacrine cells can provide rapid glycinergic crossover inhibition to PV-5 RGCs. During lateral motion, the bright trailing edge of a dark moving stimulus activates AII amacrine cells through the ON pathway, therefore counteracting the excitatory inputs PV-5 RGCs receive from OFF bipolar cells activated by the dark leading edge of the stimulus (Fig 1.11D). During approaching motion, instead, AII amacrine cells are not activated and PV-5 RGC firing is thus not inhibited. Interestingly, these results highlight the multifunctional roles played by AII amacrine cells, which can also feed rod bipolar cell signals into cone bipolar cells during scotopic 'night' vision (see 1.1.2). Finally, approach-sensitive PV-5 RGCs are potential candidates in triggering looming-evoked escape behaviour, which has been observed in various vertebrate species including mouse (De Franceschi et al.; Yilmaz and Meister, 2013), frog (Ishikane et al., 2005), and zebrafish (Temizer et al., 2015; Dunn et al., 2016a).

In conclusion, different retinal microcircuit motifs formed by defined cell types are capable of performing relatively complex visual computations that, potentially, have direct roles in driving specific visual behaviours. A common recurring theme among the different microcircuits described above is the prominent role amacrine cells play in

generating RGC feature selectivity. This essential function is probably best exemplified by studies in which the firing selectivity of RGCs was dramatically impaired when specific amacrine cell types were ablated (Yoshida et al., 2001) or synaptic connectivity between defined amacrine and ganglion cell types was disrupted (Kim et al., 2015; Krishnaswamy et al., 2015; Pei et al., 2015; Yonehara et al., 2016).

1.3 Assembly of Retinal Circuits during Development

The above sections highlight the remarkable specificity of neural wiring in retinal circuits and how this is required for appropriate visual processing and function. What are the developmental mechanisms generating these complex connectivity patterns? How is appropriate morphology and synapse specificity achieved during development? Several decades of developmental neurobiology research have led to the identification of the main mechanisms and principles underlying circuit wiring in the nervous system [reviewed in (Luo, 2015) and (Sanes and Yamagata, 2009)]. Importantly, the same mechanisms often operate in multiple brain regions and at different developmental stages. Overall, they can be broadly grouped in two classes: (1) mechanisms controlled by molecular cues (Shen and Scheiffele, 2010; Williams et al., 2010; Kolodkin and Tessier-Lavigne, 2011; Yogev and Shen, 2014), and (2) neural activity-mediated mechanisms (Katz and Shatz, 1996; Zhang and Poo, 2001; Kirkby et al., 2013; Okawa et al., 2014b). Among the different types of molecules involved in neural circuit wiring, transmembrane proteins (Fig. 1.12) play crucial roles since they mediate fine-scale cell-cell interaction processes, such as adhesion, repulsion, self-avoidance, and synapse formation (Dalva et al., 2007; Shapiro et al., 2007; de Wit and Ghosh, 2016). A large body of research, not discussed here, has uncovered the developmental processes controlling RGC target selection (Osterhout et al., 2011; Xiao et al., 2011; Osterhout et al., 2014; Osterhout et al., 2015; Sun et al., 2015), as well as topographic map formation and refinement in the visual system (McLaughlin and O'Leary, 2005; Luo and Flanagan, 2007; Huberman et al., 2008a; Feldheim and O'Leary, 2010; Cang and Feldheim, 2013). Here, instead, the mechanisms regulating circuit wiring within the retina are analysed. First, both attractive and repulsive processes controlled by cell-surface molecules are examined. Then, the roles played by neural activity in retinal circuit development are briefly described. Lastly, special focus is given to the transmembrane proteins teneurins and their function in neural circuit wiring, both in vertebrates and invertebrates.

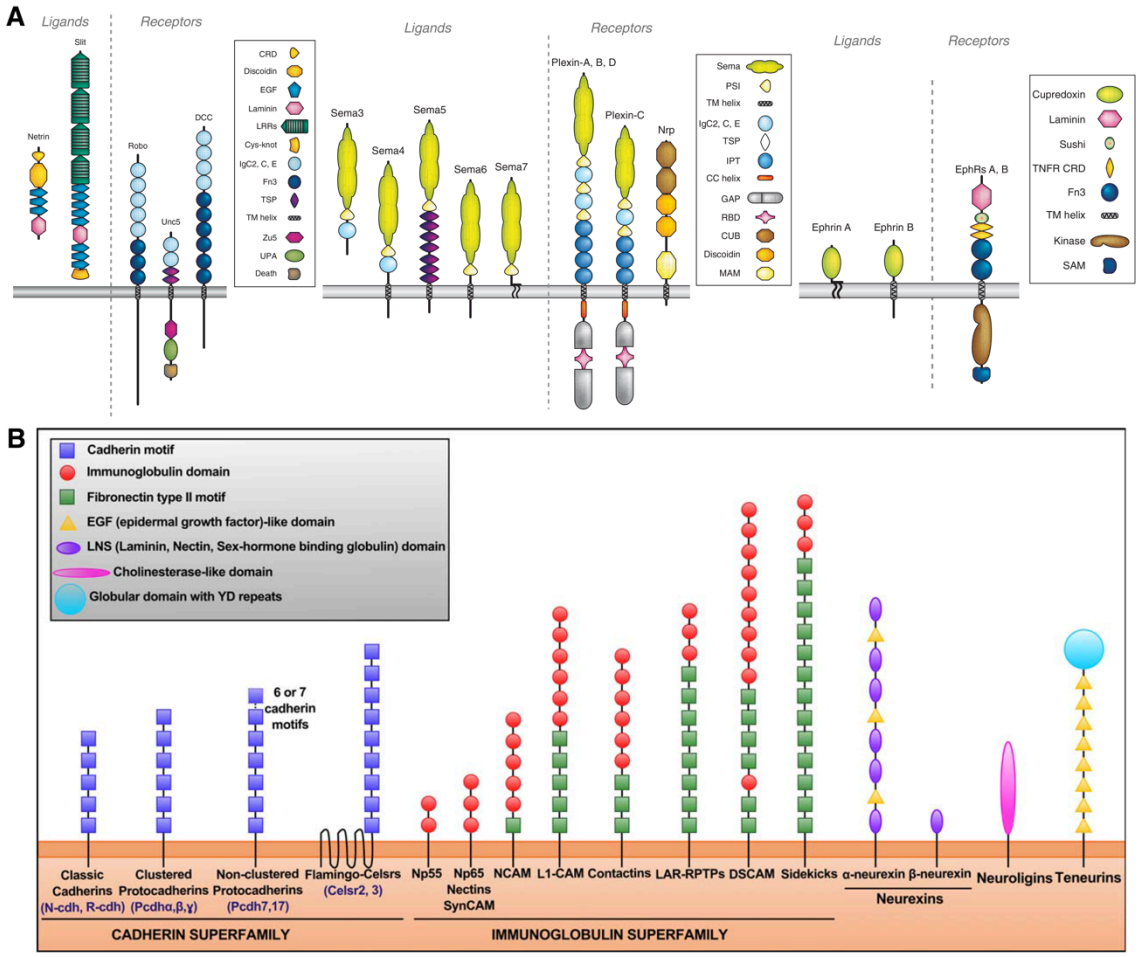

Figure 1.12. Cell-surface molecules involved in neural circuit wiring. A, Netrins, Slits, and their receptors (left), including receptors signalling attraction (DCC) and repulsion (UNC5 for Netrins; Robo for Slits). Semaphorins and their receptors (middle). The five classes of vertebrate Semaphorins and the major holoreceptor complexes required for Semaphorin-mediated repulsive and attractive guidance responses are represented. Ephrins and their receptors (right). Schematic showing the main A and B classes of Ephrins and their EphA and EphB receptors. The distinct protein domains found in these proteins are reported in the legends. Image is from (Kolodkin and Tessier-Lavigne, 2011). **B,** Schematic representing the most important families of cell-adhesion molecules (CAMs) involved in neural circuit wiring. Most of these CAMs mediate cell-cell recognition and adhesion through homophilic interactions in trans, but some do so through trans heterophilic interactions (e.g., neurexins-neuroligins). Some CAMs, such as NCAM and teneurins, form dimers in cis in the plasma membrane. The distinct protein domains found in these proteins are reported in the legend. Image is from (Missaire and Hindges, 2015).

1.3.1 Cell-interaction Molecules Involved in Retinal Circuit Wiring

A common feature of neural circuit wiring is the arrangement of synaptic connections in neuropil laminae (Sanes and Zipursky, 2010; Baier, 2013). This laminar organisation of neurites and synapses is particularly prominent in the retina, where both the IPL and outer plexiform layer (OPL) are characterised by precisely stratified architectures. Studies in which one or more retinal cell classes were completely ablated suggest that no single cell class is essential for the basic formation of the IPL or OPL (Tomita et al., 2000; Kay et al., 2004; Keeley et al., 2013; Randlett et al., 2013). However, the precise organisation of neurites into stereotypic strata requires interactions between different

retinal cells, often between pre- and postsynaptic partners. *In vivo* time-lapse studies in zebrafish have revealed that these stereotypic stratification patterns occur gradually over development and involve highly dynamic neurite rearrangements, such as rapid exploratory filopodial extensions and retractions (Godinho et al., 2005; Mumm et al., 2006; Chow et al., 2015).

The very first steps in the formation of layered neuropil structures in the retina consist in the polarised extension of neurites. Studies in mouse have shown that the atypical cadherin Fat3, which is localised throughout the IPL depth, directs the asymmetric extension of amacrine cell neurites towards the IPL (Deans et al., 2011; Krol et al., 2016). Strikingly, in mice lacking Fat3 some amacrine cells fail to target the IPL and form two additional neuropil laminae in the inner nuclear layer (INL) and ganglion cell layer (GCL). Fat3 loss of function also affects rod bipolar cells, which overshoot ectopic axon processes in the GCL. In zebrafish, the extracellular matrix component Laminin-1 is required for the appropriate emergence, orientation and extension of nascent RGC axons (Randlett et al., 2011).

A subsequent step in retinal neuropil layering consists in the confinement of neurites within the appropriate synaptic lamina/e. Generally, repulsive cell-surface molecules regulate this process in both the IPL and OPL. Extensive work in mouse has demonstrated that repulsive semaphorin signalling through plexin receptors acts in both the IPL and OPL to restrict neurite stratification in defined neuropil laminae (Matsuoka et al., 2011b; Matsuoka et al., 2011a; Matsuoka et al., 2012; Sun et al., 2013). Interestingly, this heterotypic repulsive signalling operates in a cell-type-specific way through selective expression of different semaphorins and plexins in distinct retinal cell types and, therefore, defined cellular layers or neuropil laminae (Fig. 1.13A). Transmembrane Semaphorin-5A and 5B (expressed in the outer portion of the INL) constrain neurites of amacrine, bipolar and ganglion cells within the IPL by signalling through Plexin-A1 and A3 (localised in the IPL) (Matsuoka et al., 2011b). In the absence of these proteins, neurites show severe mistargeting errors into the outer portions of the retina (Fig. 1.13A bottom), which lead to specific defects in RGC response properties. Likewise, Semaphorin-6A and Plexin-A4 are expressed in a complementary fashion in the IPL, with Semaphorin-6A being localised in most ON strata and Plexin-A4 in OFF strata (Matsuoka et al., 2011a). Semaphorin-6A or Plexin-A4 loss of function leads to dramatic stratification defects exclusively in dopaminergic amacrine cells, intrinsically photosensitive RGCs and calbindin-positive cells. These proteins are also required in the OPL where they are both expressed in horizontal cells

and control the confinement within the OPL of their axons that, in Semaphorin-6A or Plexin-A4 null mutant mice, overshoot to the outer nuclear layer (ONL; Fig. 1.13A bottom) (Matsuoka et al., 2012). To give another example, Semaphorin-6A (expressed in ON SACs) signalling through Plexin-A2 (expressed in both ON and OFF SACs) is essential for the segregation of ON and OFF SAC dendrites into distinct, non-overlapping IPL laminae (Fig. 1.13A bottom) (Sun et al., 2013). Additionally, a recent biochemical screen has found that Fibronectin Leucine-Rich Transmembrane 2 (FLRT2) and Uncoordinated-5C (Unc5C) form a repulsive interacting pair and are differentially expressed in the retina (Visser et al., 2015). Specifically, SACs and their postsynaptic partners ON-OFF DSGCs express FLRT2 and are repelled by Unc5C, which is localised in IPL strata not occupied by the dendrites of SACs and ON-OFF DSGCs.

These studies indicate that repulsive interactions restrict neurites of specific retinal cell types within defined neuropil laminae. However, how do synaptic partners recognise each other, co-stratify their neurites and, subsequently, form functional synapses? A substantial body of evidence indicates that synaptic partner matching is mainly mediated by cell-adhesion molecules. Studies in chick have shown that transmembrane proteins of the immunogloblulin superfamily – namely Down Syndrome Cell-adhesion Molecule (DSCAM), DSCAML, Sidekick-1, Sidekick-2, and Contactin-1 to -5 – form a cell-adhesion code that instructs lamina-specific targeting and co-stratification of retinal neurites in the IPL through homophilic interactions (Yamagata et al., 2002; Yamagata and Sanes, 2008, 2012). In particular, these proteins are expressed in largely non-overlapping subsets of bipolar, amacrine and ganglion cells, and exhibit a combinatorial localisation pattern in the IPL (Fig. 1.13B top). Importantly, all of these proteins mediate homophilic cell adhesion *in vitro*. Moreover, knockdown or ectopic overexpression of some of these proteins causes neurite mistargeting to inappropriate laminae or neurite re-direction to the corresponding overexpressed molecule-positive laminae, respectively (Fig. 1.13B bottom). Recently, an elegant study in mouse revealed that Sidekick-2 specifies the synaptic matching between VGluT3 amacrine cells and their postsynaptic partners LEDs through homophilic cell-cell interactions (Krishnaswamy et al., 2015). Notably, loss of function of Sidekick-2 leads to a dramatic decrease in synaptic connectivity between these two cell types as well as impaired object motion sensitivity in LEDs. Nevertheless, only minor dendritic stratification defects have been observed in VGluT3 amacrine cells and LEDs, whose overall morphology appears unaffected in Sidekick-2 mutant mice.

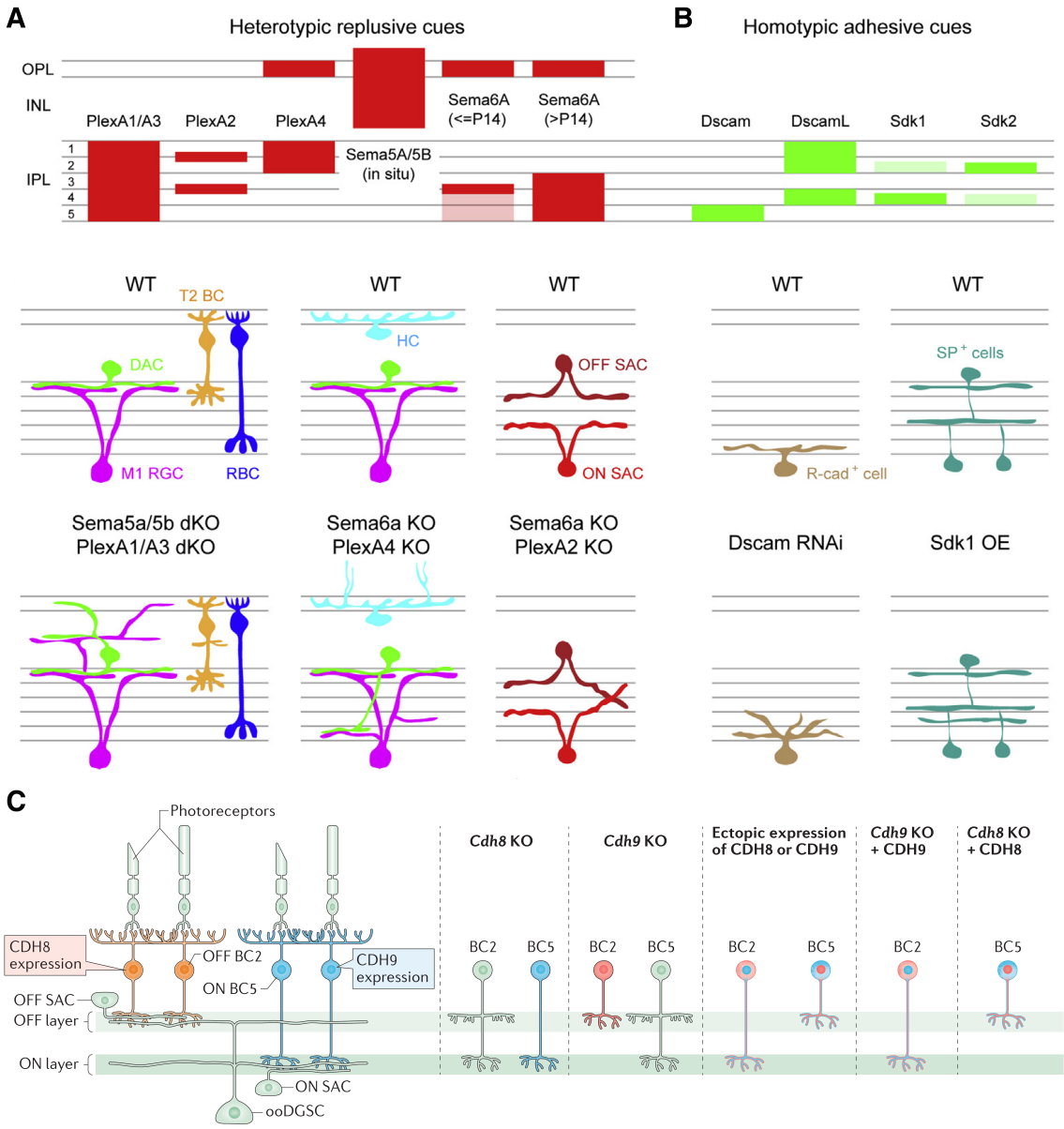

Figure 1.13. Cell-surface molecules instructing neurite lamination in the retina. A, Schematic showing the expression pattern of heterotypic repulsive molecular cues in different neuropil laminae of the mouse retina. Illustration showing abnormal stratification of mouse retinal cell types when semaphorin (Sema)-plexin (Plex) signaling is disrupted compared to wildtype retina (WT). KO, knockout; dKO, double knockout; M1 RGC, Type 1 melanopsin-positive retinal ganglion cell; DAC, dopaminergic amacrine cell; T2 BC, Type 2 OFF-cone bipolar cells; RBC, rod bipolar cell; HC, horizontal cell; SAC, starburst amacrine cell; OPL, outer plexiform layer; INL, inner nuclear layer; IPL, inner plexiform layer. **B,** Schematic showing the expression pattern of homotypic adhesive molecular cues in different neuropil laminae of the chick retina. Illustration showing disrupted dendritic stratification of R-cadherin (R-cad)-positive ganglion cells in the Dscam knockdown retina, and unusual lamination of substance P (SP)-positive amacrine cells in sidekick1 (Sdk1) overexpressing (OE) chick retina. Images in (**A**) and (**B**) are from (Hoon et al., 2014). **C,** Type II cadherins instruct bipolar cell axon lamina targeting in the mouse retina. Two distinct types of bipolar cells (BCs), each expressing a different type II cadherin, target different strata in the IPL. Cadherin 8 (Cdh8)-expressing OFF type 2 BCs (BC2s; orange) target the outer IPL, where they contact the dendrites of OFF SACs and the OFF dendritic portion of bistratified ON-OFF direction-selective ganglion cells (DSGCs). Cdh9-expressing ON BC5s (blue) target the inner IPL, where they contact the dendrites of ON SACs and the ON dendritic portion of ON-OFF DSGCs. Axon mistargeting errors resulting from either cadherin loss-of-function (middle) or ectopic overexpression (right) are also depicted. Image is from (de Wit and Ghosh, 2016).

Also heterophilic cell-adhesion signalling can direct lamina targeting and synaptic partner recognition in the retina. In mouse, type II cadherins acting heterophilically with yet-to-be-determined cues regulate axon terminal positioning and connectivity of defined bipolar cell types (Duan et al., 2014). More specifically, type 2 OFF bipolar cells expressing Cadherin-8 co-stratify their axon terminals with OFF SAC dendrites and the OFF portion of ON-OFF DSGC dendrites, to which they provide excitatory input (Fig. 1.13C). On the other hand, type 5 ON bipolar cells expressing Cadherin-9 co-stratify their axons with ON SAC dendrites and the ON portion of ON-OFF DSGC dendrites, to which they provide excitatory input. Similarly to chick immunoglobulin superfamily transmembrane proteins, loss of function or ectopic overexpression of Cadherin-8 or -9 causes axon terminal mistargeting to inappropriate IPL laminae or axon re-direction to the corresponding Cadherin-positive lamina, respectively (Fig. 1.13C right). Consistent with this, the mistargeting errors resulting from Cadherin-8 or -9 loss-of-function impair OFF or ON visually evoked responses and direction tuning in ON-OFF DSGCs, respectively. In the mouse OPL, interactions between the transmembrane glycoprotein Dystroglycan and the extracellular matrix-like protein Pikachurin (both expressed exclusively by photoreceptors) control the correct apposition of bipolar cell dendritic tips to photoreceptor ribbon synapses, as well as their mutual synaptic connectivity (Sato et al., 2008; Omori et al., 2012). In the rod pathway, the leucine-rich repeat-containing protein ELFN1 (selectively expressed in rods) interacts trans-synaptically with mGluR6 glutamate receptors (expressed on rod bipolar cell dendrites) (Cao et al., 2015). Notably, mice lacking ELFN1 lack synapses between rod photoreceptors and rod bipolar cells, but exhibit normal connectivity between cones and cone bipolar cells. Again specifically for the rod pathway, another leucine-rich repeat protein, Netrin-G ligand 2 (NGL-2), expressed only on the axon tips of horizontal cells, is required for horizontal cell axon lamination in the OPL as well as for their selective synaptic matching with rods, but not cones (Soto et al., 2013).

Lamination is not the only feature that gives rise to precise connectivity and function. Also dendritic structure and arborisation in the horizontal plane of the retina play key roles in generating the receptive fields and functional properties of retinal neurons (London and Hausser, 2005; Lefebvre et al., 2015). The most notable example of planar dendritic arbour development specified by cell-surface proteins is represented by the clustered protocadherins (Pcdhs), which control dendritic self-avoidance and self/non-self discrimination in mouse SACs (Lefebvre et al., 2012; Kostadinov and Sanes, 2015). Unlike in wild-type SACs (Fig. 1.14A), dendritic branches belonging to

individual SACs lacking all 22 *Pcdh-γ* genes overlap extensively and form bundles, therefore resulting in dramatic changes in arbour shape as well as incomplete dendritic field coverage and ectopic formation of autapses (i.e., synapses between same-cell neurites; Fig. 1.14B left). These phenotypes are caused by loss of homotypic Pcdh-γ interactions between same-cell dendrites that normally trigger repulsion and self-avoidance. Intriguingly, the genetic mechanism underlying this phenomenon is very similar to DSCAMs in *Drosophila* (Zipursky and Sanes, 2010). Like *Drosophila* DSCAMs, vertebrate Pcdhs show stochastic, combinatorial expression profiles generating single-cell identity (Esumi et al., 2005; Kaneko et al., 2006). Also, it has been shown that Pcdhs exhibit isoform-specific homophilic binding (Schreiner and Weiner, 2010; Thu et al., 2014). Hence, since each cell expresses a unique combination of Pcdh-γ isoforms, self/non-self discrimination is accomplished through repulsive isoneuronal interactions between sibling dendrites. On the contrary, heteroneuronal interactions with dendrites of other cells do not trigger repulsion. Consistent with this, expressing the same single Pcdh-γ isoform in all SACs leads to decreased dendritic co-fasciculation and synaptic connectivity between neighbouring SACs (Fig. 1.14C left) (Lefebvre et al., 2012; Kostadinov and Sanes, 2015). As it may be expected, the morphological and connectivity defects observed when deleting all 22 *Pcdh-γ* genes or artificially expressing a single Pcdh-γ isoform in all SACs both impair the direction tuning of DSGCs (Fig. 1.14A-C right) (Kostadinov and Sanes, 2015). A related example is the repulsive heterotypic signalling between Semaphorin-6A and Plexin-A2 in ON SACs (Sun et al., 2013). In mice lacking these proteins, ON SACs miss extensive portions of their dendritic fields, have asymmetric dendritic arbours, and exhibit self-avoidance defects (Fig. 1.14D left), unlike OFF SACs that instead show normal dendritic arborisation. Also, it appears that only the ON directional motion responses of ON-OFF DSGCs are affected in these mutant mice (Fig. 1.14D right).

Finally, individual retinal cell type populations are arranged in 'mosaics' across the retina, namely they are distributed as non-random arrays of regularly spaced cells that tile the retina (Cook and Chalupa, 2000). This regular coverage is thought to enable each retinal cell type population to process information uniformly across the whole visual field. How do retinal cell types form such mosaics? Molecular candidates playing a clear role in this process are the Multiple Epidermal Growth Factor-like domains protein 10 (MEGF10) and MEGF11 (Kay et al., 2012). By being selectively expressed in SACs and horizontal cells, MEGF10 and MEGF11 regulate the mosaic

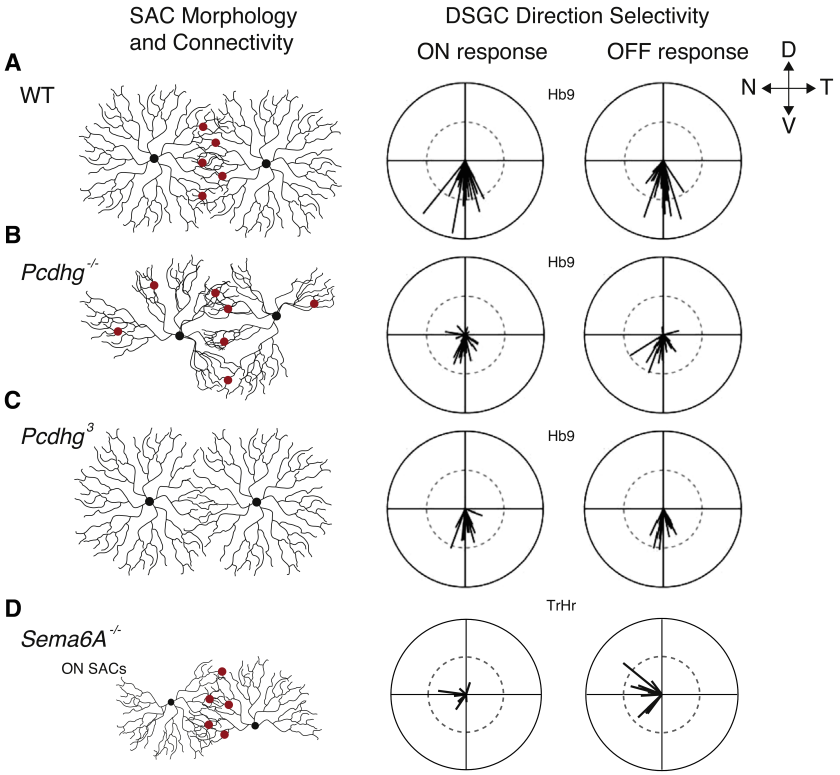

Figure 1.14. Cell-surface molecules regulating planar dendritic morphology in the IPL. A, Starburst amacrine cells (SACs) in wild type (WT) mice have radially symmetric neurites and form GABAergic synapses with other adjacent SACs (left). SAC connections with direction-selective ganglion cells (DSGCs) are not showed. Tuning of DSGCs is also reported (right) with amplitude representing degree of tuning and angle representing the preferred direction. D, dorsal; N, nasal; V, ventral; T, temporal. **B,** In mice lacking all 22 protocadherin-γ genes (*Pcdhg*$^{-/-}$), SAC neurites do not show self-avoidance, resulting in loss of radially symmetric morphology, co-fasciculation and ectopic formation of autapses (left). Both ON and OFF direction selectivity of Hb9-GFP^{+} DSGCs are weaker than in WT mice and are not consistently tuned toward the ventral direction (right). **C,** In mice artificially expressing a single Pcdh-γ isoform (*Pcdhg*^{3}), SACs have radially symmetric morphology but display little dendritic overlap and rarely form GABAergic synapses with other SACs (left). The tuning of Hb9-GFP^{+} DSGCs is also weaker than in WT (right). **D,** In mice lacking Sema6A, the neurites of ON SACs show impaired self-avoidance resulting in loss of radially symmetric morphology (left). ON direction tuning of Trhr-GFP^{+} DSGCs is weaker than in WT, whereas OFF direction tuning remain unaffected (right). Images in (**A-D**) are from (Morrie and Feller, 2016).

spacing and retinal coverage of these neurons in a cell-type-specific fashion through repulsive homotypic interactions. Notably, in mice lacking these transmembrane proteins, the cell bodies of SACs and horizontal cells are arranged in random disordered distributions, whereas their dendrites do not exhibit obvious stratification abnormalities. Similarly, DSCAM and DSCAML, which have more diffuse expression patterns in the mouse retina, were shown to direct mosaic spacing and self-avoidance of several different cell types (Fuerst et al., 2008; Fuerst et al., 2009). However, a recent study using both gain- and loss-of-function approaches suggests that the cell clumping and neurite co-fasciculation phenotypes observed in mice lacking DSCAM is not consistent with a self-avoidance function but, instead, it could be explained by the role this protein has in driving cell-death and balancing the overall adhesive attraction between cells of the same type (Li et al., 2015).

1.3.2 Roles of Neural Activity in Retinal Circuit Development

In addition to the molecularly specified wiring processes described above, activity-dependent mechanisms also play important roles in the maturation and refinement of retinal circuits [reviewed in (Wong and Ghosh, 2002; Firth et al., 2005; Tian, 2008; Okawa et al., 2014b)]. The main sources of synaptic activity in the developing retina are: (1) spontaneous neurotransmitter release, (2) spontaneous waves of correlated activity, and (3) visual experience. Early studies showed that synaptic neurotransmission, potentially driven by retinal waves, is required for the normal arborisation and stratification of RGC dendrites. Work in the cat retina reported that selective pharmacological activation of mGluR6 glutamate receptors (which hyperpolarise ON cone bipolar cells and rod bipolar cells) impairs the segregation between ON and OFF RGC dendritic arbours in the IPL during development, and results in an increased fraction of RGCs with multi-stratified dendrites and ON-OFF response polarity (Bodnarenko and Chalupa, 1993; Bodnarenko et al., 1995; Bisti et al., 1998). Both glutamatergic and cholinergic neurotransmission appear to influence the structural remodelling of chick RGC dendrites by facilitating the dynamic extension and retraction of filopodia (Wong et al., 2000; Wong and Wong, 2001) as well as their stabilisation (Lohmann et al., 2002). On the other hand, pharmacologically blocking action potential generation in the retina does not affect the dynamic remodelling of RGC dendrites (Wong et al., 1991; Wong et al., 2000).

More recent studies using genetically targeted disruption of transmitter release in specific cell subpopulations demonstrated additional, subtler roles played by neurotransmission in regulating retinal circuit connectivity [reviewed in (Okawa et al., 2014b)]. To give some notable examples, the selective blockade of glutamate release from all ON bipolar cells in mice through tetanus toxin light chain expression reduces synapse formation selectively between these bipolar cells and ON RGCs or the ON portion of ON-OFF RGC dendrites, but does not influence connectivity between OFF bipolar cells and RGCs (Fig. 1.15A) (Kerschensteiner et al., 2009; Okawa et al., 2014a). Interestingly, in sustained ON alpha RGCs this effect seems to be specific for type 6 ON bipolar cells (Fig. 1.15A bottom) (Morgan et al., 2011). Unlike in the cat retina (Bodnarenko and Chalupa, 1993; Bodnarenko et al., 1995), however, blocking glutamatergic neurotransmission from ON bipolar cells in mice does not affect RGC dendritic arborisation or stratification in the IPL, nor it changes ON bipolar cell axonal morphology (Tagawa et al., 1999; Kerschensteiner et al., 2009; Okawa et al., 2014a). Consistent with a role of neurotransmission in promoting synaptogenesis, genetically

increasing spontaneous glutamate release from mouse bipolar cells leads to higher rates of synapse formation between bipolar and ganglion cells, but no change in retinal circuit organisation or IPL stratification (Soto et al., 2012). On the other side, inhibitory neurotransmission is involved in the maturation and maintenance (but not formation) of inhibitory synapses onto bipolar cells, with specific roles depending on bipolar cell type, subcellular compartment (dendrite vs. axon), receptor class (GABA vs. glycine receptors), or receptor type ($GABA_A$ vs. $GABA_C$ receptors) (Schubert et al., 2013; Hoon et al., 2015).

Retinal waves and visual experience also have distinct roles in retinal circuit development. Retinal waves consist in spontaneous and periodic bursts of neural activity propagating in a wave-like fashion across the developing inner retina, thus driving neighbouring RGCs to fire correlated action potentials (Firth et al., 2005). These waves occur before rods and cones are fully mature, therefore before vision can occur. The circuit mechanisms underlying retinal waves vary during development. Specifically, there are 'stage I' waves mainly mediated by gap junctions (before birth), then 'stage II' waves mediated by acetylcholine (postnatal days 0-11 in mice) and, lastly, 'stage III' waves mediated by glutamate (postnatal days 11-21 in mice) (Huberman et al., 2008a). Arroyo et al. (2016) showed that, in the first mouse postnatal week, cholinergic retinal waves modulate the gap junction coupling between intrinsically photosensitive RGCs by driving phasic release of dopamine. Cholinergic retinal waves do not seem to be essential for the normal IPL stratification of retinal cell neurites in mouse (Bansal et al., 2000). However, in the turtle retina, chronic pharmacological block of cholinergic retinal waves from early development appears to inhibit the planar growth of RGC dendritic fields (Mehta and Sernagor, 2006), whereas artificially increasing the normal acetylcholine-dependent spontaneous firing rate through dark rearing results in larger RGC receptive field areas (Sernagor and Grzywacz, 1996). Depriving animals from visual experience through dark rearing revealed several other structural and functional effects in retinal cells, indicating important roles played by activity-dependent plasticity in late development (i.e., after eye opening at postnatal days 13-15 in mice). Visual deprivation in mice blocks the postnatal redistribution of RGC dendrites across the IPL depth (Xu and Tian, 2007), and results in a higher fraction of RGCs with ON-OFF response polarity (Tian and Copenhagen, 2003). Dark rearing also appears to inhibit the planar growth of RGC dendrites (Xu et al., 2014), therefore leading to RGCs with smaller receptive field centres (Akimov and Renteria, 2014). Furthermore, it reduces

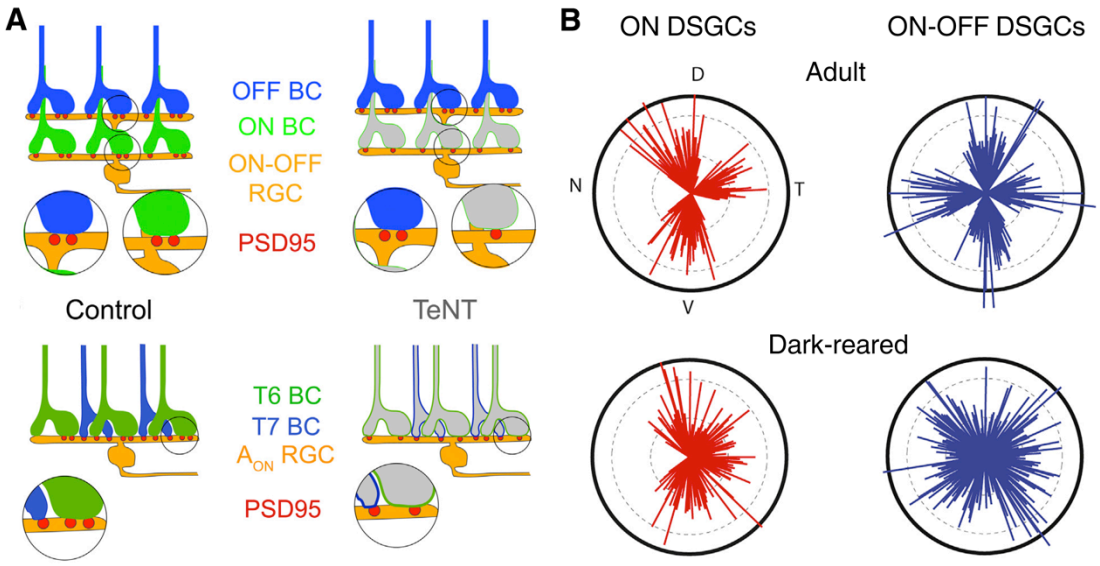

Figure 1.15. Roles of neural activity in retinal circuit development. A, Suppressing glutamatergic neurotransmission from all ON bipolar cells (BCs, green) through tetanus toxin light chain (TeNT) expression leads to reduced number of excitatory postsynaptic densities (marked by PSD95, red) between ON BCs and bistratified ON-OFF retinal ganglion cells (RGCs, orange). Synaptic connections between OFF BCs (blue) and ON-OFF RGCs are instead unaffected. In sustained ON alpha RGCs (bottom) this phenomenon is specific for type 6 ON BCs (T6 BCs, green). Image is from (Okawa et al., 2014b). **B,** Visual deprivation through dark rearing in mice blocks the refinement of direction-selective ganglion cell (DSGC) preferred directions, which do not cluster along cardinal directions as in control animals. Both ON (left, red) and ON-OFF (right, blue) DSGCs are affected by dark rearing. Image is from (Bos et al., 2016).

the amplitude of RGC light responses, likely due to long-lasting excitatory/inhibitory imbalance with a shift toward larger inhibitory inputs (Tian and Copenhagen, 2001; Di Marco et al., 2009). Strikingly, visual experience in mice is required for the normal connectivity between cone photoreceptors and cone bipolar cells, but not between rods and rod bipolar cells (Dunn et al., 2013).

Finally, the role of neural activity in the development of retinal direction-selective circuits has been investigated in great detail. Notably, neither visual experience nor normal cholinergic retinal waves appear to influence the emergence of directionally tuned responses in mouse (Elstrott et al., 2008) or rabbit (Chan and Chiao, 2008) ON-OFF DSGCs. In addition, pharmacologically blocking GABAergic or cholinergic neurotransmission, or preventing action potential generation during development do not affect ON-OFF DSGC tuning in rodents (Sun et al., 2011; Wei et al., 2011). However, recent studies in mouse and rabbit indicate that visual experience is crucial for the normal refinement in the distribution of ON and ON-OFF DSGC preferred directions, from initially diffuse at eye opening to defined subpopulations clustered along the cardinal axes at adult stages (Fig. 1.15B) (Chan and Chiao, 2013; Bos et al., 2016). By contrast, in zebrafish larvae, even though visual experience is the main source of neural activity in the developing retina [but see (Zhang et al., 2016)], dark rearing does

not change the normal distribution of preferred directions or the tuning of DSGCs (Lowe et al., 2013). Consistent with a more rapid and molecularly hardwired development of retinal circuits in zebrafish larvae compared to mammals, neither the pharmacological block of chemical neurotransmission nor visual deprivation over development alters the fine-scale neurite stratification pattern of retinal cells in the IPL (Nevin et al., 2008).

1.3.3 The Teneurins

The studies discussed in section 1.3.1 identified several cell-interaction molecules involved in the assembly of defined retinal circuits. However, a complete characterisation of the molecular wiring mechanisms leading to the mature retinal circuitry is still far from our reach. In this context, the teneurins represent an interesting family of large type II transmembrane proteins [reviewed in (Tucker and Chiquet-Ehrismann, 2006; Tucker et al., 2007; Young and Leamey, 2009; Mosca, 2015)]. Teneurins possess a single transmembrane domain and their basic structural organisation is phylogenetically conserved (Minet and Chiquet-Ehrismann, 2000; Tucker et al., 2012). In vertebrates, the teneurin family comprises four members – Tenm1-4 (also called Odz1-4) – whereas in invertebrates fewer members have been identified – one in *Caenorhabditis elegans* (Ten-1) and two in *Drosophila melanogaster* (Ten-a and Ten-m). In all vertebrate teneurins, the large extracellular domain contains eight epidermal growth factor (EGF)-like repeats, multiple tyrosine-aspartate (YD) repeats, and five NHL (NCL-1, HT2A, and Lin-41) repeats (Fig. 1.16). Interestingly, teneurins are highly expressed in interconnected regions of the central nervous system, both in vertebrates (Oohashi et al., 1999; Otaki and Firestein, 1999; Rubin et al., 1999; Ben-Zur et al., 2000; Tucker et al., 2000; Zhou et al., 2003; Kenzelmann et al., 2008) and invertebrates (Baumgartner et al., 1994; Levine et al., 1994; Fascetti and Baumgartner, 2002). This is particularly evident in the vertebrate visual system where they are expressed all along the visual pathway – namely in the retina and superior colliculus/optic tectum, as well as in the lateral geniculate nucleus and primary visual cortex in mammals (Minet et al., 1999; Rubin et al., 2002; Li et al., 2006; Leamey et al., 2007; Leamey et al., 2008; Kenzelmann-Broz et al., 2010; Dharmaratne et al., 2012; Young et al., 2013; Leamey and Sawatari, 2014). Ultrastructural and biochemical data indicate that teneurins can form both homo- and heterodimers in *cis* by establishing disulfide bonds between two of their EGF-like repeats (Oohashi et al., 1999; Feng et al., 2002). Furthermore, it has been shown that Teneurin-1 and -2 can be proteolytically

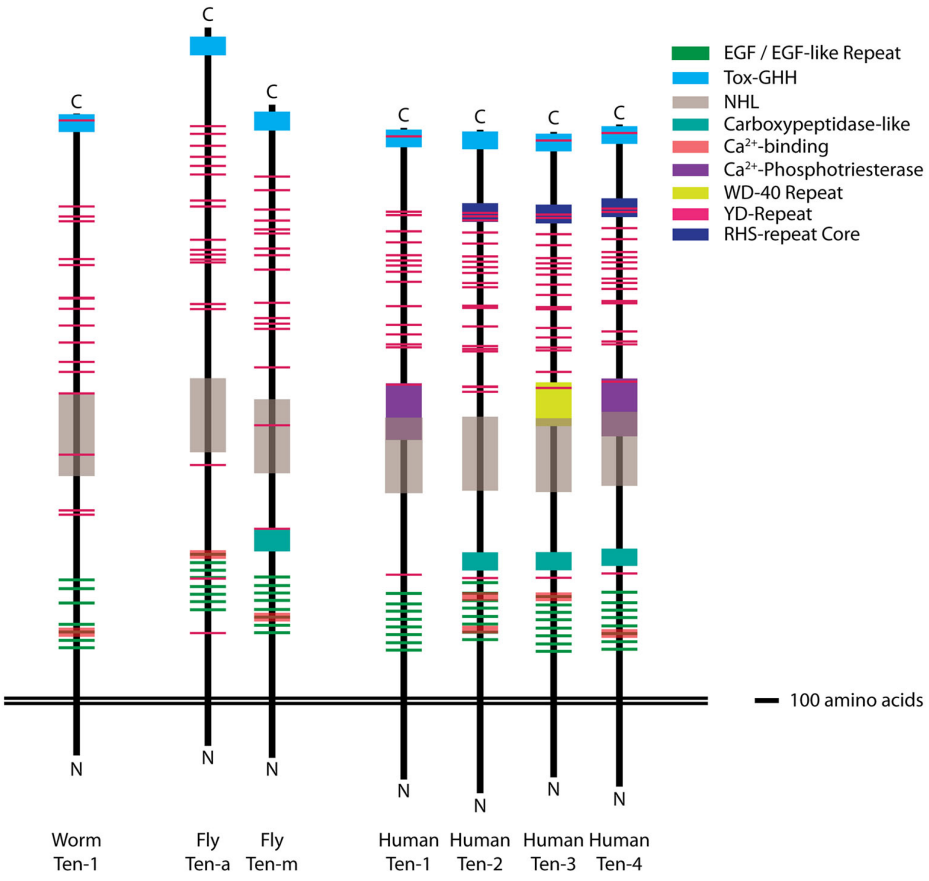

Figure 1.16. Molecular structure of teneurins in vertebrates and invertebrates. Schematic of the structural organisation of the *C. elegans* Ten-1, *Drosophila* Ten-m and Ten-a, and human Tenm1-4 proteins. Across different phyla, the structural organisation of teneurins is conserved and qualitatively similar. Each structural domain is colour-coded (legend) and scaled according to size (scale corresponds to 100 amino acids). The NHL (grey) and Ca^{2+}-binding (red) domains are represented at 65% transparency to allow the visualisation of other overlapping domains. Top (C-terminus) is extracellular, whereas bottom (N-terminus) is intracellular. Image is from (Mosca, 2015).

cleaved at multiple locations, with the different protein fragments potentially playing distinct signalling roles (Rubin et al., 1999; Bagutti et al., 2003; Nunes et al., 2005; Kenzelmann et al., 2008; Scholer et al., 2015; Vysokov et al., 2016). For example, the N-terminal intracellular domain of Teneurin-1 and -2 can be cleaved near the transmebrane domain and, subsequently, translocate into the nucleus where it interacts with transcriptional regulators (Bagutti et al., 2003; Nunes et al., 2005; Scholer et al., 2015). Also, the released extracellular domain of Teneurin-2 can elicit intracellular Ca^{2+} signalling by interacting with the cell-adhesion G-protein-coupled receptor Latrophilin-1 (Silva et al., 2011; Vysokov et al., 2016). Lastly, the C-terminal end of the Teneurin-1 extracellular domain, also termed Teneurin C-terminal-Associated peptide (TCAP)-1, can be either cleaved or independently transcribed and has neuromodulatory functions [reviewed in (Tan et al., 2012; Chen et al., 2013b)].

In both vertebrate and invertebrate species, *in vitro* and *in vivo* studies demonstrated that teneurins interact in *trans* both homophilically through their NHL domain (Rubin et al., 2002; Hong et al., 2012; Beckmann et al., 2013; Hattori et al., 2013), and heterophilically with the cell-adhesion G-protein-coupled receptors latrophilins in mammals (Silva et al., 2011; O'Sullivan et al., 2012; Boucard et al., 2014; O'Sullivan et al., 2014) or between Ten-a and Ten-m in *Drosophila* (Mosca et al., 2012; Mosca and Luo, 2014). Notably, these *trans*-interactions are crucial in mediating cell-cell recognition and adhesion. Elegant studies in *Drosophila* revealed that teneurins play an instructive role in the synaptic matching between specific pre- and postsynaptic cells in the olfactory system (Hong et al., 2012) and at the neuromuscular junction (Mosca et al., 2012). More specifically, Hong et al. (2012) carried out genetic screens to identify cell-surface proteins controlling synaptic specificity between defined subsets of presynaptic olfactory receptor neurons and postsynaptic projection neurons. By using loss- and gain-of-function genetic manipulations the authors proved that trans-synaptic homophilic interactions mediated by teneurins instruct the recognition between synaptic partners expressing high levels of the same teneurin. Similarly, Mosca et al. (2012) demonstrated that homophilic Ten-m signalling regulates the selection of target muscles by specific motor neurons. Notably, both studies showed that interfering with the normal expression pattern of teneurins leads to severe mismatch and targeting errors between defined synaptic partners. In addition, teneurins regulate other fine-scale neural wiring processes, such as neurite outgrowth (Minet et al., 1999; Suzuki et al., 2014), axon pathfinding (Drabikowski et al., 2005; Zheng et al., 2011), axon myelination (Suzuki et al., 2012), cell-type-specific dendrite morphogenesis (Hattori et al., 2013), synapse organisation (Mosca et al., 2012; Mosca and Luo, 2014), as well as axon projection topography and mapping (Leamey et al., 2007; Dharmaratne et al., 2012). The precise roles played by homo- versus heterophilic *trans*-interactions during these wiring events are still unclear. However, it appears that homophilic interactions are crucial for cell-cell recognition and matching between specific subsets of cells (Fig. 1.17A) (Hong et al., 2012; Beckmann et al., 2013), whereas heterophilic interactions are involved in synapse adhesion and organisation (Fig. 1.17B) (Silva et al., 2011; Boucard et al., 2014; Mosca and Luo, 2014; Mosca, 2015). Intriguingly, *Drosophila* teneurins have been shown to control synaptic partner matching through homophilic signalling and synapse organisation through heterophilic signalling between the same subsets of olfactory neurons (Hong et al., 2012; Mosca and Luo, 2014).

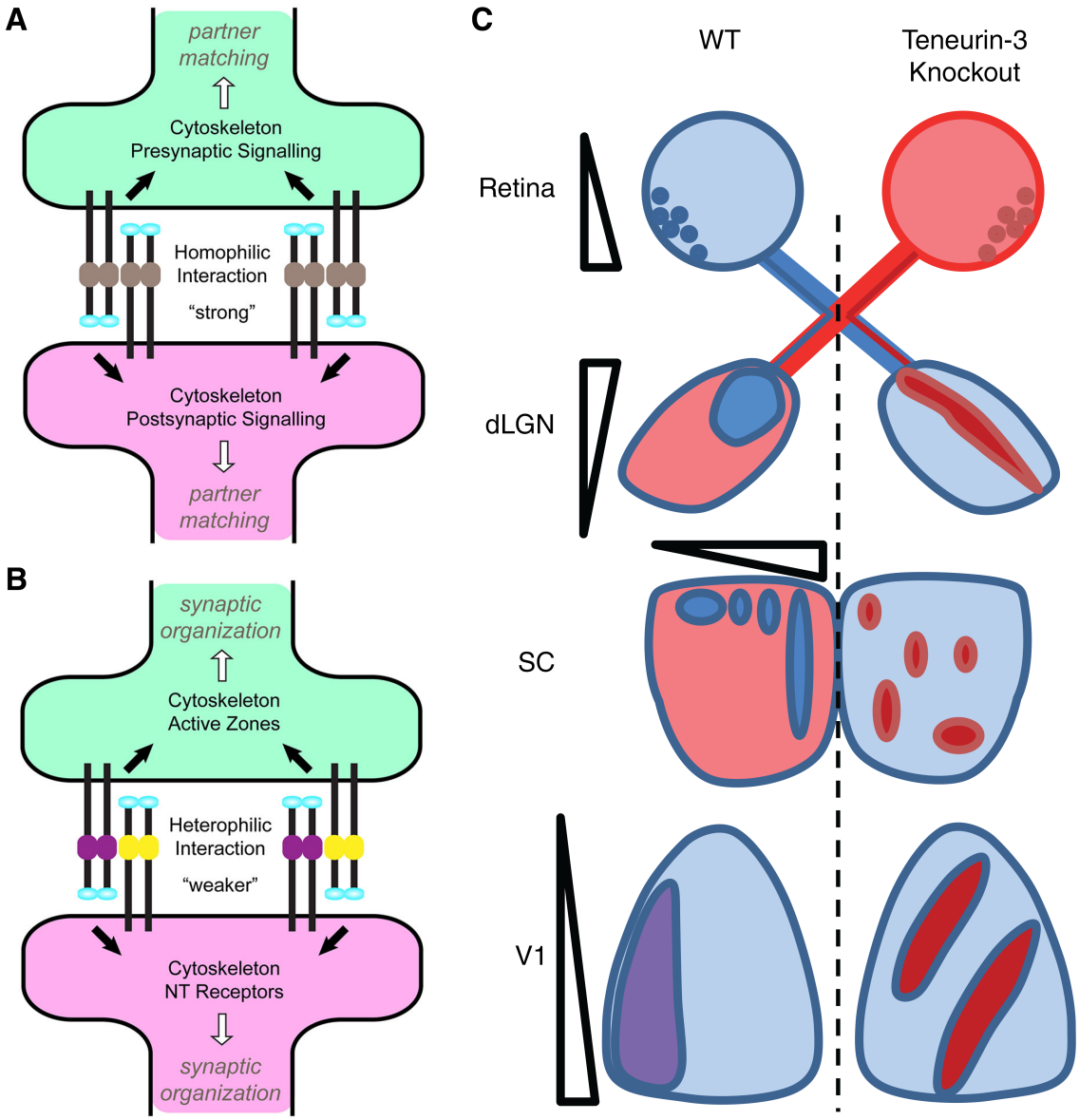

Figure 1.17. Teneurin *trans* interactions and role of Teneurin-3 in the mouse visual system. AlB, A model for how tension created by homophilic (**A**) vs. heterophilic (**B**) teneurin cell-cell interactions in *trans* could distinguish synaptic partner matching from synaptic organization. The higher strength of homophilic interactions alters cytoskeletal dynamics on the pre- (green) and postsynaptic (magenta) sides, activating signalling pathways that transition growth cones from exploring neurites to stable structures amenable to synapse formation. Weaker heterophilic interactions, instead, regulate cytoskeletal organization and active zone apposition, leading to synaptic organization via signalling mechanisms distinct from synaptic partner matching. Images in (**A**) and (**B**) are from (Mosca, 2015). **C,** Schematic diagram illustrating the role of Teneurin-3 in the development of the mouse ipsilateral visual pathway. Lighter colours illustrate contralateral projections, whereas darker colours represent ipsilateral projections. The gradient of Teneurin-3 expression in each visual area is also indicated (left). The dotted line shows the midline. In wild type (WT) mice (left), ipsilateral retinal ganglion cell projections are confined whithin the dorso-medial core of the dorsal lateral geniculate nucleus (dLGN) and rostro-medial portion of the superior colliculus (SC). These are represented in the lateral half of primary visual cortex (V1). In Teneurin-3 knockout mice (right), ipsilateral retinal ganglion cell projections project aberrantly to the ventro-lateral dLGN and caudo-lateral SC. Within V1, the ipsilateral projections from dLGN form ocular dominance-like bands aberrantly extending into the medial portion of V1. Image is from (Leamey and Sawatari, 2014).

In mammals, a considerable amount of work indicates that Teneurin-3 is required for the correct topographic mapping of ipsilaterally projecting RGC axons in the dorsal lateral geniculate nucleus (dLGN) (Leamey et al., 2007; Carr et al., 2014) and superior colliculus (SC) (Dharmaratne et al., 2012; Carr et al., 2013). Teneurin-3 shows a high-ventral-to-low-dorsal gradient of expression in the retina and topographically matching expression gradients in the dLGN, SC and primary visual cortex (V1; Fig. 1.17C left). Notably, mice lacking Teneurin-3 exhibit RGC axon mapping defects and abnormal projection patterns in both dLGN and SC (Fig. 1.17C right). Surprisingly, these abnormalities appear to be specific for the subpopulation of RGCs projecting ipsilaterally, even though Teneurin-3 is also expressed in contralaterally projecting RGCs. The mapping phenotypes observed in Teneurin-3 knockout mice result in an expansion and aberrant representation of dLGN ipsilateral inputs in V1 (Merlin et al., 2013), as well as in impairments in performing visually guided behaviours (Leamey et al., 2007). A different but related role seems to be played by the mouse Teneurin-2, which is expressed in the retina, SC, dLGN and V1, but does not show any obvious expression gradient in these brain areas (Young et al., 2013). Mice lacking Teneurin-2 have fewer RGCs projecting ipsilaterally to the dLGN and SC, which results in decreased neural activity driven by ipsilateral visual input in V1 as well as in visual deficits associated specifically with the dorsal visual field. Topographic mapping is not affected in Teneurin-2 knockout mice, nor are contralateral RGC projections despite Teneurin-2 being expressed uniformly across the whole retina. In zebrafish, Teneurin-3 is expressed early during embryonic development (Mieda et al., 1999) and has an expression pattern in the visual system similar to the mammalian Teneurin-3, namely high expression in the retina and optic tectum (Thisse et al., 2001). Interestingly, a large-scale mutagenesis screen identified a mutant zebrafish with decreased Teneurin-3 expression that is characterised by resistance to pharmacologically induced epileptic seizures (Baraban et al., 2007; Hortopan et al., 2010).

Mutations in teneurins have also been linked with various neurological disorders in humans. Most notably, large-scale genome-wide association studies found a strong link between an intronic variation in the Teneurin-4 gene locus and bipolar disorder (Sklar et al., 2011; Green et al., 2013). Recently, missense mutations in the Teneurin-4 gene have been suggested to cause essential tremor in some members of three Spanish families (Hor et al., 2015). However, it has also been reported that one of the identified mutations is present in a Chinese cohort of healthy individuals (Chao et al.,

2016). Another recent study applied whole-exome sequencing to a family multiply affected with congenital general anosmia and identified some affected members having a rare X-linked missense mutation in the Teneurin-1 gene (Alkelai et al., 2016). Interestingly, both mice lacking Teneurin-1 and mice carrying the human mutation showed defective olfactory-driven behaviour. In regards to Teneurin-3, a genome-wide association study of an Australian family linked a variation in a large (~5 mega base pairs) genomic region containing the Teneurin-3 gene to a dominantly inherited form of cerebellar ataxia (Storey et al., 2009). Moreover, in a recent study combining autozygome and exome analysis, a homozygous null mutation in the Teneurin-3 gene was identified in two siblings with bilateral colobomatous microphthalmia from a consanguineous family in Saudi Arabia (Aldahmesh et al., 2012). Subsequently, another study reported an unrelated patient with bilateral colobomatous microphthalmia and intellectual disability having a homozygous Teneurin-3 loss-of-function splicing mutation (Chassaing et al., 2016). Therefore, even though loss-of-function studies in mice and zebrafish did not report overall eye malformations (Leamey et al., 2007; Hortopan et al., 2010; Dharmaratne et al., 2012), these studies in humans indicate that Teneurin-3 is strongly linked to eye development.

To conclude, teneurins have multiple roles in neural circuit assembly, both in vertebrates and invertebrates. Their main function appears to be the cell-cell recognition and adhesion between specific subsets of cells. Given the high expression levels of Teneurin-3 in interconnected regions of the vertebrate visual system as well as the reported detrimental effects in visual system development and visually guided behaviours caused by Teneurin-3 loss of function, Teneurin-3 represents an intriguing candidate for retinal circuit wiring. In support of this idea, Teneurin-3 is expressed in subpopulations of amacrine and ganglion cells in the mouse retina (Hindges Lab, unpublished data).

1.4 Aims of the Project

During my PhD project, I investigated the role played by Teneurin-3 in the developing retina from multiple points of view and at different scales using the larval zebrafish as vertebrate model system. The main biological questions driving this study include: (1) what cell classes/types express Teneurin-3? (2) Does Teneurin-3 instruct connectivity between defined synaptic partners? (3) Are Teneurin-3 or Teneurin-3-expressing cells required for specific retinal computations? If so, what are the underlying circuit

mechanisms? To address these questions several innovative experimental strategies had to be developed and optimised, including the generation of a novel combinatorial mutant zebrafish lacking the vast majority of skin pigmentation, and therefore allowing unobstructed optical access of the eyes (see Chapter 3). Firstly, the expression pattern of *teneurin-3* (*tenm3*) in the larval zebrafish visual system was described and the morphological features of cells expressing *tenm3* were characterised (see Chapter 4). Secondly, loss-of-function approaches were used to assess whether *tenm3* is required for the correct structural and functional development of defined retinal cells and circuits (see Chapter 5). Lastly, the functional role played by identified *tenm3*-expressing amacrine cells was analysed at cellular and circuit levels (see Chapter 6).

Chapter 2

Materials and Methods

2.1 Animals

Zebrafish were maintained at 28.5°C on a 14 hr ON/10 hr OFF light cycle in Danieau solution [58 mM NaCl, 0.7 mM KCl, 0.4 mM $MgSO_4$, 0.6 mM $Ca(NO_3)_2$ 5.0 mM HEPES, pH 7.6]. Transgenic lines used in this study include *Tg(isl2b:Gal4)*^{zc60Tg} (Ben Fredj et al., 2010), *Tg(UAS:Kaede)*^{s1999tTg} (gift of Prof. Chi Bin-Chien), *Tg(UAS:SyGCaMP3)*^{kg1Tg} (Nikolaou et al., 2012), *Tg(UAS:tagRFP-CAAX)*^{zf456Tg} (Hunter et al., 2013), *Tg(UAS:KillerRed)*^{s1996tTg} (Del Bene et al., 2010), *Tg(elavl3:GCaMP5G)*^{a4598Tg} (Ahrens et al., 2013), *Tg(elavl3:GCaMP6f)*^{jf1Tg} (Dunn et al., 2016b), *Tg(UAS:GCaMP5)*^{zf662Tg} (gift from Dr. Elena Dreosti, Department of Cell and Developmental Biology, University College London, London, UK), and *Tg(-1.8ctbp2:SyGCaMP6)*^{uss1Tg} (Johnston et al., 2014). The *Tg(tenm3:Gal4)*^{kg302Tg} zebrafish line was generated through BAC transgenic insertion (*kg302Tg*) by the author (see *BAC Transgenesis*). The *tenm3*^{KO} mutant line was generated in this study through transcription activator-like effector nuclease (TALEN)-mediated genome editing (*tenm3*$^{kg69/kg69}$) from Ekkwill zebrafish (see *TALEN-mediated tenm3 Knockout*). The AB strain of zebrafish was used for *in situ* hybridization, RT-PCR, visual background adaptation and mosaic labeling of retinal ganglion cells (RGCs). WT retinae used in Fig. 4.3D and 5.9C-F were obtained from Ekkwill larvae.

Confocal functional imaging experiments were performed in the pigmentation mutant, *nacre*, which lacks all neural crest-derived melanophores (Lister et al., 1999). Two-photon functional imaging experiments in the retina were performed in a triple pigmentation mutant (*alb*$^{b4/b4}$;*nacre*$^{w2/w2}$;*roy*$^{a9/a9}$) which is characterised by a general decrease in melanin synthesis (*alb*$^{b4/b4}$) (Streisinger et al., 1986) and lacks all neural crest-derived melanophores (*nacre*$^{w2/w2}$) (Lister et al., 1999) and iridophores (*roy*$^{a9/a9}$) (White et al., 2008). The rationale behind this strategy was to have an unobstructed optical access of the retina without raising fish in 200 µM phenylthiourea (PTU) (Karlsson et al., 2001), which has been shown to impair both the normal development of zebrafish (Elsalini and Rohr, 2003; Li et al., 2012b) and the retinal responses to light stimuli (Page-McCaw et al., 2004). Importantly, *alb*$^{b4/b4}$;*nacre*$^{w2/w2}$;*roy*$^{a9/a9}$ larvae and adult zebrafish are viable and do not display evident morphological, functional or

behavioural abnormalities. Larvae used for *in vivo* and *ex vivo* imaging of morphological and molecular features (not involving functional experiments) were raised in 200 µM PTU (Sigma) in Danieau solution to avoid pigment formation. This work was approved by the local Animal Welfare and Ethical Review Body (King's College London), and was carried out in accordance with the Animals (Experimental Procedures) Act, 1986, under license from the United Kingdom Home Office.

2.2 *In Situ* Hybridization

To make the *tenm3* antisense riboprobe, a 981 bp cDNA fragment (ORF 7034-8014) was cloned into a StrataClone Blunt PCR Cloning Vector pSC-B-amp/kan (Agilent Technologies), and the orientation of the insertion was determined by DNA sequencing. The sequences of primers used to amplify the fragment through PCR are as follows: forward primer 5'-GGGACTATGACATTCAAGCAGGTC-3'; reverse primer 5'-CATTGT TGGCACTGTCGGCCAG-3'. The antisense RNA probe was generated from the linearised plasmid using T3 RNA polymerase (Life Technologies) and digoxigenin-labeled nucleotides (Roche). Whereas, the sense digoxigenin-labeled RNA probe was generated using T7 RNA polymerase (Life Technologies). After synthesis, riboprobes were treated with DNase I (Ambion) for 15 minutes at 37°C.

The same protocol described in Thisse and Thisse (2008) was used to perform whole-mount *in situ* hybridizations. Briefly, embryos were fixed in 4% paraformaldehyde (PFA) in PBS overnight at 4°C, dehydrated in methanol and stored at -20°C. Subsequently, embryos were rehydrated in 75% methanol in PBT (0.1% Tween-20 in PBS), 50% methanol in PBT, 25% methanol in PBT, and PBT for 5 minutes each. 2, 3 and 5 dpf embryos were digested with proteinase K (10 µg/ml; Sigma) at room temperature for 20, 30 and 60 minutes, respectively. Subsequently, they were fixed in 4% PFA in PBS for 20 minutes at room temperature and washed several times in PBT. They were then transferred to hybridization mix (HM; 50% formamide, 5x SSC, 0.1% Tween-20, 50 µg/ml heparin, 0.5 mg/ml yeast tRNA, and 9 mM citric acid to pH 6.0 in DEPC ddH_2O) and incubated for 4 hours at 65°C. The HM was replaced with a solution containing 1 µg/ml of digoxigenin-labeled RNA probe in HM and the embryos were incubated overnight at 65°C. Washes were performed at the hybridization temperature in 65% HM/35% 2x SSC, 35% HM/65% 2x SSC, 2x SSC, for 10 minutes each and, lastly, in 0.2x SSC + 0.1% Tween-20 for 20 minutes and 2 times 20 minutes each in 0.1x SSC + 0.1% Tween-20. A series of washes was performed at room temperature in 65% 0.2x SSC/35% PBT, 35% 0.2x SSC/65% PBT, and PBT for

10 minutes each. Embryos were then incubated in blocking solution (5% sheep serum in PBT) for 4 hours at room temperature. The blocking solution was replaced with alkaline phosphatase-conjugated anti-digoxigenin Fab fragments (Roche) diluted 1:2000 in blocking solution and embryos were incubated at 4°C overnight. After washing at least 8 times 1 hour each in PBT at room temperature followed by overnight wash in PBT at 4°C, embryos were rinsed 3 times 20 minutes each in NTMT staining buffer (0.1 M Tris-HCl pH 9.5, 50 mM $MgCl_2$, 0.1 M NaCl, 0.1% Tween-20). The staining buffer was then replaced with 2% NBT/BCIP stock solution (Roche) in NTMT and embryos were incubated in the dark at room temperature. To stop the reaction, embryos were washed in PBS and fixed in 4% PFA in PBS for 20 minutes at room temperature. After several washes in PBS, embryos were washed in 15% and 30% sucrose in PBS for 2 hours each at room temperature, then in 40% sucrose in PBS overnight at 4°C. Subsequently, embryos were embedded in OCT (VWR International) and frozen in dry ice. Lastly, 20 µm-thick sections were cut using a cryostat and stored in 70% glycerol in PBS.

2.3 Morpholino Microinjections

2-2.5 ng/1.8 nl (0.24-0.3 pmols) of morpholino oligonucleotides (MOs; Gene Tools) in Danieau solution were injected into one-cell stage zebrafish embryos. The sequences of MOs used are as follows: splice-blocking *tenm3* MO 5'-ACGGTTGCTctgtg gaaaaaaatca-3' (intronic sequence in lower case); standard control MO 5'-CCTCTT ACCTCAGTTACAA TTTATA-3'.

2.4 RT-PCR

Total RNA was isolated from multiple dechorionated embryos (~30) using TRIzol reagent (Life Technologies). cDNA was synthesised using SuperScript III reverse transcriptase (Life Technologies) and random primers (Promega, C1181). The obtained cDNA was then used as template for amplification through PCR. For the *tenm3* MO, the sequences of the primers are as follows: forward primer 5'-ATGCCATCC TCTCTCTCCAGTCCA-3'; reverse primer 5'-ACTTCTTGAACTTGAAGGCGCTGC-3'. They target exon 2 and exon 4 of the tenm3-001 splice variant, respectively. Full-length and shorter splice variants were extracted from agarose gel using QIAquick Gel Extraction Kits (Qiagen), cloned into StrataClone Blunt PCR Cloning Vectors pSC-B-amp/kan (Agilent Technologies) and sent for sequencing.

2.5 Behavioural Assessment

2.5.1 Visual Background Adaptation

Visual background adaptation of 4 dpf larvae was assessed by exposure to bright light for more than 3 hours, followed by visual inspection of pigmentation using a stereomicroscope.

2.5.2 Optomotor Response Assay

Individual 5 dpf larvae were positioned in a 35 mm petri dish containing Danieau solution. The LCD screen of an iPhone 5 (Apple) controlled by a MacBook Pro (Apple) through Duet Display (Kairos Technologies) was used to display black and white square-wave gratings (85% contrast, spatial frequency 0.33 cycles/mm, temporal frequency 3.5 cycles/s) moving in 4 directions (90° angular distance) at the bottom of the petri dish. Visual stimuli were generated in Keynote (Apple). Each larva was tested 5 times in total (each trial lasted 6 s followed by 10 s of static gratings) and scored according to the trials it responded to (i.e., fish turns and swims in the direction of the moving gratings). The behaviour of larvae was visually monitored using an M165 FC stereomicroscope (Leica).

2.6 Genome Editing

2.6.1 TALEN-mediated Tenm3 Knockout

Zebrafish *tenm*3 knockout mutants (*tenm3*^{KO}) were generated by TALEN-mediated genome editing. The exon encoding the transmembrane domain of the Tenm3 protein was targeted. The DNA sequences targeted by the TALEN constructs are the following (5'>3'): left, TCAAAGTACTGTTCATGG; right, GTGCCATGGCCGTCTCCA. TALEN constructs were designed using ZiFiT targeter version 4.2 (Sander et al., 2010), and assembled following the REAL assembly protocol (Reyon et al., 2012). The T7 transcription mMessage mMachine kit (Life Technologies) was used to produce the 5' capped TALEN mRNA, 200 pg of which was injected into Ekkwill zebrafish embryos at one-cell stage (Sander et al., 2011). Founders were identified using the Surveyor nuclease mismatch assay (Transgenomic) and outcrossed to generate heterozygous F1 offspring, which were subsequently fin-clipped and genotyped by PCR amplifying and sequencing a 400 bp amplicon using primers that flanked the target site. The primers used for genotyping are the following (5'>3'): tenm3_fw CAGGCACTT TCTCTTTAAGACAGG; tenm3_rev CTCACGTGATCCTCTCTCAGC. Zebrafish were selected when indels leading to frame shifts and consequent premature stop codons

causing truncations in the transmembrane domain of Tenm3 were detected. The *tenm3*^{KO} mutant zebrafish line (*tenm3*$^{kg69/kg69}$) used for all subsequent experiments is characterised by a 14-bp deletion (5'-ACAGCCCTCAGTGC-3') in the following genomic location of *tenm3*: chromosome 1, 38,921,612-38,921,625.

2.6.2 BAC Transgenesis

The *Tg(tenm3:Gal4)* transgenic zebrafish line was generated through bacterial artificial chromosome (BAC) transgenic insertion (*kg302Tg*) following a previously described protocol (Bussmann and Schulte-Merker, 2011). In summary, the recombineering procedure used to generate *tenm3:Gal4* BAC constructs consists of three main steps. Firstly, three different *Escherichia coli* BAC clones (CH211-58M24, 200 kb; CH211-130I22, 155 kb; CH211-169K10, 150 kb; BACPAC Resources, CHORI) containing partially overlapping regions of the *tenm3* genomic sequence were transformed with *pRed-Flp4*, a plasmid encoding the homology-directed repair machinery needed for DNA recombineering in an L-rhamnose inducible operon. Second, the *iTol2* cassette (*iTol2-amp*^{R}) containing two long terminal repeats (LTRs) of the Medaka fish *Tol2* transposon, as well as two 50-bp homologies on each end was inserted into *tenm3* BAC vector backbones. Importantly, the LTRs are needed for single-copy integration of the BAC into the zebrafish genome when co-injected with *Tol2* transposase mRNA into one-cell embryos. Lastly, the transcriptional activator *Gal4FF* gene together with a kanamycin resistance cassette possessing 50-bp homology arms (*Gal4FF-kan*^{R}) was inserted at the start ATG site of the *tenm3* gene (the exon containing the start ATG codon is in chromosome 1: 38,879,739-38,879,945). Each recombineering step was followed by resistance selection of positive colonies. Moreover, the temperature-sensitive origin of replication of the *pRed-Flp4* plasmid, which replicates at 30°C but not at 37°C, allowed purification of the BACs without plasmid contamination.

Here is a detailed, point-by-point description of the protocol used (Bussmann and Schulte-Merker, 2011). Identification of BAC clones containing the *tenm3* gene of interest was performed using Ensembl (www.ensembl.org). Primers of ~70 bp length were designed to allow the insertion of the cassettes into the BAC vector: 50 bp homology arms (HAs) homologous to the vector backbone and 20 bp to amplify the *iTol2-amp*^{R} cassette. In addition, gene-specific primers were designed so that they contained 50 bp HAs at both sides of the start ATG codon of the *tenm3* gene (positions –53 to –4 and +4 to +53) and ~20 bp to amplify the *Gal4FF:kan*^{R} cassette.

E. coli stocks containing the BAC vectors were streaked on lysogeny broth (LB) agar plates containing 11.3 µg/ml chloramphenicol (Cm) and incubated overnight at 37°C to obtain single colonies. Three single colonies per BAC were picked and resuspended in 30 µl of LB to perform colony PCRs using primers tenm3BAC_control_fw and tenm3BAC_control_rev. PCR product sizes were checked on a 1× Tris-acetate-EDTA (TAE) 1% agarose gel. Positive colonies were grown overnight at 37ºC in LB containing 11.3 µg/ml Cm, using 20 µl of the resuspended colony. Overnight cultures were used to generate glycerol stocks and stored at –80ºC. PCR conditions to confirm BAC clones and cassette insertions into the BAC backbone were: (1) initial denaturation 95ºC 5 min; (2) denaturation 94ºC 30 s; (3) annealing 58ºC 30 s; (4) elongation 72ºC 30 s; (2) to (4) repeated for 32× cycles; (5) final elongation 72ºC 6 min. The colony PCR master mix components for BAC clone confirmation and cassette insertion conformation were: PCR master mix total volume 20 µl; suspended bacterial colony 1 µl; 10× PCR buffer (Qiagen) 2 µl; 10 mM dNTPs 0.5 µl; 10 µM forward primer 0.5 µl; 10 µM reverse primer 0.5 µl; Taq polymerase (Qiagen) 0.2 µl; ddH_2O 15.3 µl. To generate the insertion DNA products, PCRs were carried out using the Phusion high-fidelity polymerase (New England Biolabs) and the following primers: *iTol2-amp*^{R} cassette (primers ptarBac_itol2_fw and ptarBac_itol2_rev); *Gal4FF:kan*^{R} cassette (primers tenm3BAC_Gal4FF_fw and tenm3BAC_KanR_rev). PCR reactions and conditions were as follows: PCR master mix total volume 100 µl; 5 ng/µl plasmid template 1 µl; 5× Phusion HF buffer (New England Biolabs) 20 µl; 10 mM dNTPs 2 µl; 10 µM forward primer 2.5 µl; 10 µM reverse primer 2.5 µl; Phusion DNA polymerase (New England Biolabs) 1 µl; ddH_2O 71 µl. The PCR conditions to generate cassettes were: (1) initial denaturation 98ºC 30 s; (2) denaturation 98ºC 10 s; (3) annealing 58ºC 20 s; (4) elongation 72ºC 60 s; (2) to (4) repeated for 32× cycles; (5) final elongation 72ºC 6 min. PCR product sizes were confirmed on a 1× TAE 1% agarose gel. Then 2 µl of DpnI restriction enzyme were added to the PCR reaction and incubated for 4 hours at 37°C to digest plasmid DNA. PCR products were precipitated by adding 5 µl of 5 M LiCl and 300 µl of 100% ethanol, incubated at –20°C for 30 min and subjected to centrifugation (13,000 rpm, 30 min at 4ºC). The pellets were washed with 70% ethanol, centrifuged (13,000 rpm, 5 min at 4 ºC) and re-suspended in ddH_2O.

To transform bacteria with the *pRed-Flp4* plasmid, 40 µl of the BAC clone glycerol stock were first grown in a 1.5 ml LB culture containing 11.3 µg/ml Cm (3 hours at 37ºC). The culture was then centrifuged (5,000 rpm, 5 min at 4ºC) and the pellet was re-suspended in 1 ml of ice-cold ddH_2O. This wash procedure was repeated

twice, and after the final centrifugation, ~50 µl of the supernatant were left on the tube. Subsequently, 1 µl of 10 ng/µl *pRed-Flp4* plasmid was added and transferred to a pre-chilled 1 mm electroporation cuvette. Bacteria were electroporated (1,800 V, 25 µF, 200 Ω, time constant between 4.8-5.2 ms) and 1 ml of LB without antibiotics was added. After growing bacteria for 1 hour at 37ºC, they were seeded on LB plates containing 11.3 µg/ml Cm and 60 µg/ml hygromycin (Hyg). Finally, three single colonies were picked, transferred to LB containing 11.3 µg/ml Cm and 60 µg/ml Hyg and grown overnight at 30ºC.

To insert the *iTol2-amp*^{R} cassette into the BAC vector, 40 µl of the previously transfected bacterial culture were used to grow a 1.5 ml LB culture containing 11.3 µg/ml Cm and 60 µg/ml Hyg (2.5 hours at 30ºC). Then, 67 µl of 25% w/v L-rhamnose (Alfa Aesar) were added to the culture to induce the expression of genes mediating homology-directed repair machinery, and culturing was continued for 1 hour at 37ºC. The electroporation procedure was carried out as described for the *pRed-Flp4* transformation. After electroporation, bacteria were grown for 1 hour at 30ºC, and then plated on LB plates containing 11.3 µg/ml Cm, 60 µg/ml Hyg and 16.7 µg/ml ampicillin (Amp). Correct *iTol2-amp*^{R} cassette insertion was confirmed by colony PCR, as described for BAC clone confirmation, using primers pTarBAC_HA1_control_fw + amp_HA1_control_rev (for HA1) and amp_HA2_control_fw + pTarBAC_HA2_ control_rev (for HA2) (see Table 1). PCR product sizes were checked on a 1x TAE 1% agarose gel. Positive colonies were grown overnight at 30ºC in LB containing 11.3 µg/ml Cm, 60 µg/ml Hyg and 16.7 µg/ml Amp.

Finally, the *Gal4FF:kan*^{R} cassette was inserted into the BAC vector as described for the *iTol2-amp*^{R} cassette insertion. 40 µl of the previously transfected bacterial culture were used to grow a 1.5 ml LB culture containing 11.3 µg/ml Cm, 60 µg/ml Hyg and 16.7 µg/ml Amp (2.5 hours at 30ºC). After electroporation, bacteria were grown for 1 hour at 30ºC, and then plated on LB plates containing 11.3 µg/ml Cm, 16.7 µg/ml Amp, and 16.7 µg/ml kanamycin (Kan). Correct cassette insertion was confirmed by colony PCR, as described for BAC clone confirmation, using primers tenm3BAC_control_fw + Gal4ff_HA1_control_rev (for HA1) and kanR_HA2_control_fw + tenm3BAC_control_rev (for HA2) (see Table 1). Positive colonies were grown overnight at 37ºC in LB containing 11.3 µg/ml Cm, 16.7 µg/ml Amp, and 16.7 µg/ml Kan. BAC DNA was extracted and purified using HiPure Midiprep kit (Invitrogen) and subsequently kept in ddH_2O at 4ºC for maximum 2 weeks.

Table 1

List of primers used for recombineering (5' > 3').

itol2 cassette amplification	
ptarBac_itol2_fw	GCGTAAGCGGGGCACATTTCATTACCTCTTTCT CCGCACCCGACATAGATCCCTGCTCGAGCCGG GCCCAAGTG
ptarBac_itol2_rev	CGCGGGGCATGACTATTGGCGCGCCGGATCGA TCCTTAATTAAGTCTACTAATTATGATCCTCTAG ATCAGATCT
Gal4FF-Kan cassette amplification	
tenm3BAC_Gal4FF_fw	ATTTTATTTTCTTCCTTTGGTTTAAAGTGATTTTT CTTTCTATAGGTTCTACCATGAAGCTACTGTCTT CTATCGAAC
tenm3BAC_KanR_rev	GGTTGAGAATGGGAATGCTCAGTGACTGATGG ACTGGAGAGAGAGGATGGTCAGAAGAACTCGT CAAGAAGGCG
itol2 cassette insertion control	
pTarBAC_HA1_control_fw	CTGTCAAACATGAGAATTGGTC
amp_HA1_control_rev	ACATTTCCCCGAAAAGTGG
amp_HA2_control_fw	CTGAGATAGGTGCCTCACTG
pTarBAC_HA2_control_rev	GAGAGCCTTCAACCCAGTC
Gal4FF-Kan cassette insertion control	
tenm3BAC_control_fw	GCTACTCACCATTGCTGTGGCC
Gal4FF_HA1_control_rev	AGTAGCGACACTCCCAGTTG
kanR_HA2_control_fw	TCCTCGTGCTTTACGGTATC
tenm3BAC_control_rev	CGCCTGTGTGGTGGCATTAC

To create first transient and subsequently stable transgenic zebrafish lines, isolated BAC DNA constructs (120 ng/µl) were co-injected with *Tol2* transposase mRNA (100 ng/µl) into *Tg(UAS:GCaMP5)* zebrafish embryos at the early one-cell stage. Transient expression, visible as GCaMP5 fluorescence, already gave a reliable indication of the final expression in the stable transgenic line. All three BAC constructs produced analogous transient expression patterns. The CH211-58M24 (200 kb) BAC construct was used to generate the *Tg(tenm3:Gal4)* zebrafish line because of its higher

level of Gal4FF expression compared to the other two BAC constructs. The CH211-58M24 BAC construct contains genomic regions 100 kb upstream and 100 kb downstream of the *tenm3* start codon site, but does not cover the entire *tenm3* genomic locus (~400 kb). The BAC DNA preparation was obtained using the HiPure Midiprep kit (Invitrogen), with modifications for BAC DNA isolation as described by the manufacturer. *Tol2* transposase mRNA was prepared by *in vitro* transcription from *Xba*I-linearised *pDB600* plasmid (Balciunas et al., 2006) using the T3 transcription mMessage mMachine kit (Life Technologies). RNA was purified using the RNeasy MinElute Cleanup kit (Qiagen). Germ line transmission was identified by mating sexually mature adult fish to wild-type fish and, subsequently, examining their progeny for GCaMP5 fluorescence. Positive embryos were raised to adulthood and outcrossed to generate the *Tg(tenm3:Gal4)* single transgenic line, which was then used as driver line.

2.7 Imaging

2.7.1 Whole-animal Image Acquisition

Whole-animal images of adult zebrafish were taken with a Nikon D7000 digital SLR camera equipped with a Sigma 150 mm macro lens. Adult zebrafish were anesthetised with 0.2% tricaine (MS222, Sigma) in fish facility water and placed in a 90 mm petri dish containing fish facility water. Imaging of larvae was performed using a ZEISS Axioskop microscope connected to EXi Blue CCD cameras (Retiga) and Volocity acquisition software (PerkinElmer). Larval zebrafish were anesthetised with 0.02% Tricaine in Danieau solution and immobilised in 1% low melting point agarose (Sigma) on glass slides.

2.7.2 Confocal Imaging

Imaging was performed using an LSM 710 confocal microscope equipped with a spectral detection scan head and a 20×/1.0 NA water-immersion objective (Carl Zeiss). Optical sections were typically obtained at 1 µm intervals through the Z axis and 1 AU pinhole aperture. Maximum intensity projections and 3D rotated images were generated using either ImageJ (Schneider et al., 2012) or ZEN (Carl Zeiss).

2.7.3 In Vivo Confocal Calcium Imaging

Functional time-series of visually evoked calcium responses in RGCs were acquired at a rate of 4.1 Hz and 0.415 × 0.415 µm lateral XY sampling (256 × 256 pixels) and 1 AU

pinhole aperture, using the confocal setup described above. Excitation was provided by 488 nm multi-line laser. The point spread functions (PSFs) of the confocal setup were not measured by the author. According to published measurements using the LSM 710 confocal microscope equipped with a 1.0 NA water-immersion objective (Carl Zeiss) (Cole et al., 2011), the maximum PSF lateral XY sampling size is 83 nm whereas the maximum PSF axial Z sampling size is 316 nm. The theoretical lateral and axial resolution limit for 488-nm excitation light is 249 nm and 948 nm, respectively. The average diameter of a presynaptic bouton in zebrafish RGCs is ~0.8 µm (Meyer and Smith, 2006). Thus, the physical XY dimensions of voxels are below that of a typical presynaptic bouton. Non-anaesthetised *Tg(isl2b:Gal4;UAS:SyGCaMP3)*, *Tg(tenm3:Gal4;UAS:KillerRed;elavl3:GCaMP5G)* and *UAS:GCaMP6f*-injected *Tg(isl2b:Gal4)* larvae were immobilised in 2% low melting point agarose (Sigma) prepared in Danieau solution and mounted dorsal side up on a raised glass platform that was placed in a custom-made Danieau-filled chamber. The agarose was sufficient to restrain the larvae so that anaesthesia was not required. Imaging was performed in the afternoon (1-8 pm).

2.7.4 In Vivo Two-photon Calcium Imaging

Two-photon functional imaging in the retina was performed using an A1R MP microscope equipped with a 4-channel GaAsP NDD and an Apochromat 25×/1.1 NA water-immersion objective (Nikon). Excitation was provided by a Chameleon Ultra II Mode-locked titanium-sapphire laser (Coherent) tuned to 930 nm. Time-series of visually evoked calcium responses in *tenm3*$^{+}$ ACs and BCs were acquired at a rate of 7.8 Hz and 0.397 × 0.397 µm lateral XY sampling (256 × 128 pixels). The point spread functions (PSFs) of the multiphoton setup were not measured by the author. Following activation of the laser scanning, we waited 60 seconds before starting the visual stimulation to ensure the retina adapted to the background light level caused by the multi-photon laser. 4 dpf *Tg(tenm3:Gal4;UAS:SyGCaMP3)*, *Tg(-1.8ctbp2:SyGCaMP6)* and *UAS:GCaMP6f*-injected *Tg(tenm3:Gal4)* larvae were first paralysed for 10-15 minutes in α-bungarotoxin (1 mg/ml; Biotium) prepared in Danieau solution. Subsequently, larvae were immobilised in 2% low melting point agarose (Sigma) and mounted on a raised custom-made glass platform with the dorsal side up (45° angle) and one eye facing an LCD screen (see Visual Stimulation) that was placed underneath a custom-made Danieau-filled chamber. Imaging was performed in the afternoon (1-8 pm).

2.7.5 Light-sheet Imaging

Whole-brain light-sheet imaging was performed using a ZEISS Lightsheet Z.1 microscope equipped with two 10x/0.2 NA illumination objectives and one 20x/1.0 NA water-immersion detection objective (Carl Zeiss). 488 nm laser excitation light was used to elicit GCaMP6f fluorescence and a 505-545 BP filter was used for emitted light detection. The pivot scanner (Carl Zeiss) was used to deliver homogeneous illumination and, therefore, avoid shadows along the illumination axis. The thickness of the light sheet was 5.39 µm at the centre and 10.8 µm at the edges of the field of view. Exposure time was 29.97 ms. The size of volumetric images was 623 × 798 × 283 μm^3 (1500 × 1920 × 490 pixels) with a XYZ sampling of 0.415 × 0.415 × 0.631 µm. 4 dpf *nacre*, *casper* and *crystal Tg(elavl3:GCaMP6f)* larvae were first paralysed for 10-15 minutes in α-bungarotoxin (1 mg/ml; Biotium) prepared in Danieau solution. Subsequently, larvae were immobilised in 2% low melting point agarose (Sigma) and placed inside a glass capillary (20 µl volume, 701904; Brand). Subsequently, the section of the agarose cylinder containing the head of the larva was extruded from the capillary and oriented so that the dorsal side of the head was facing the detection objective and the eyes were facing the two illumination objectives. Whole-brain light-sheet imaging of *casper* mutant larvae was performed using a custom-made light-sheet microscope built by Dr Martin Meyer (King's College London) and equipped with a 20x/1.0 NA water-immersion XLUMPlanFLN detection objective (Olympus). The point spread functions (PSFs) of the light-sheet setups were not measured by the author.

2.8 Visual Stimulation

2.8.1 Moving and Static Stimuli in Confocal Preparation

Moving bar stimuli were generated and controlled using custom-written Labview and MATLAB code (MathWorks), implemented on a ViSaGe stimulus presenter (Cambridge Research Systems) and delivered via a DLP Pico PK301 pocket LED projector (Optoma) as previously described (Lowe et al., 2013). A diffusion filter (3026, Rosco) was bonded to one side of the chamber to serve as a projection screen. The agarose in front of the eye facing the projection screen was removed, allowing an unobstructed view of the projected image on the side of the chamber. Larvae were positioned 3 cm away from the screen, and the projected image filled a visual field of ~97° × 63°. Visual stimuli consisted of light (56 cd/m^2) or dark bars (8 cd/m^2) (175% and 25% of mean luminance, respectively) on a mean grey background (32 cd/m^2). As no qualitative differences between light and dark bars were noted, data obtained using the two stimuli

were combined. Each bar was 10° in width moving at a speed of 20°/s and separated from the preceding bar by 30°, enabling more than one bar on the screen at any one time. The long axes of the bars were orthogonal to the direction of motion. For the moving vs. static gratings stimuli used to obtain data displayed in Fig. 6.9, either moving square-wave gratings (75% contrast, spatial frequency 0.05 cycles/degree equivalent to 10° bar width, temporal frequency 1 cycles/s) or static square-wave gratings with alternating contrast (75% contrast, spatial frequency 0.05 cycles/degree equivalent to 10° bar width) were used. Each of the 12 directions of motion was presented once (3 seconds) in a pseudo-random order unique to each slice in every animal imaged. Each inter-epoch interval was 10 seconds to enable SyGCaMP3 or GCaMP6f signals to return to baseline. A blank-screen null condition of 2 seconds was also interleaved.

2.8.2 Moving Gratings in Two-photon Preparation

Moving gratings stimuli in the two-photon preparation were generated and controlled using PsychoPy (Peirce, 2008), and delivered through an LCD screen (SKD5VA-3, GoodWell Technology) positioned underneath a custom-made Perspex chamber. A long-pass red glass filter (>610 nm, FGL610, Thorlabs) was positioned between the LCD screen and the chamber to allow for simultaneous imaging and visual stimulation. Therefore, the provided visual stimuli could only activate long wavelength-sensitive (L or red) cones, which are the most abundant cones in the larval zebrafish retina (~35% of all cones) (Suzuki et al., 2013). Larvae were positioned 2 cm away from the screen and the image on the LCD screen filled a visual field of ~140° × 100° (mean background luminance 30.4 cd/m^2). Visual stimuli consisted of square-wave gratings (100% contrast, spatial frequency 1.66 cycles/cm, temporal frequency 1 cycles/s). Each grating bar was 8.5° in width and the long axes of the bars were orthogonal to the direction of motion. Each of the 12 directions of motion was presented once (6 seconds) with and inter-epoch interval of 10 seconds to enable SyGCaMP3 or SyGCaMP6 signals to return to baseline. A blank-screen null condition of 6 seconds was also interleaved. TTL triggers (0-5-0 Volts) to record epoch time events where generated through a LabJack USB DAQ device (U3-LV, LabJack Corporation). Following activation of the laser scanning, we waited 60 seconds before starting the visual stimulation to ensure the retina adapted to the background light level caused by the multi-photon laser.

2.9 Single Cell Labelling

2.9.1 Labelling of Individual RGCs

To mosaically label RGCs for morphological analyses, an activator plasmid containing Gal4 driven by an upstream *ath5* promoter (*Ath5:Gal4*) (gift of Prof. Steve Wilson, UCL, UK) was co-injected with effector plasmids, where expression is driven by a UAS motif in frame with either GFP (*UAS:GFP*) or tdTomato (*UAS:tdTomato*) (Ben Fredj et al., 2010). The plasmids were injected at a concentration of 20 ng/µl each in Danieau solution. Plasmid DNA was prepared using miniprep kits (Qiagen).

To label individual RGCs for functional analyses, *UAS:GCaMP6f* DNA constructs (Chen et al., 2013a; Nikolaou and Meyer, 2015) were injected into 1-4 cell-stage *Tg(isl2b:Gal4)* embryos. The *pGP-CMV-GCaMP6f* plasmid used to clone the *UAS:GCaMP6f* DNA construct (Nikolaou and Meyer, 2015) was a gift from Douglas Kim (Addgene plasmid # 40755). Plasmid DNA was prepared using midiprep kits (Qiagen) and injected at a concentration of 30 ng/µl in Danieau solution. Only larvae showing single GCaMP6f-expressing RGC axons in the optic tectum were used for functional analyses. After functional identification of orientation-selective RGCs (OSGCs), larvae were fixed, cryosectioned and immunostained (see *Immunohistochemistry*) to visualise the morphology of GCaMP6f$^+$ dendritic arbours of OSGCs.

2.9.2 Mosaic Labelling of Tenm3$^+$ ACs

To mosaically label *tenm3*$^+$ ACs, *UAS:eGFP-CAAX* (gift from Dr. Andy Symonds, MRC Centre for Developmental Neurobiology, King's College London, London, UK), *UAS:eGFP* (Ben Fredj et al., 2010) or *UAS:GCaMP6f* (Nikolaou and Meyer, 2015) DNA constructs were injected into 1-4 cell-stage *Tg(tenm3:Gal4)* embryos. Plasmid DNA was prepared using midiprep kits (Qiagen) and injected at a concentration of 40-50 ng/µl in Danieau solution.

2.10 Optogenetic Ablation *of Tenm3$^+$* ACs

The optogenetic ablation of *tenm3*$^+$ ACs was performed using the genetically encoded photosensitizer KillerRed (Bulina et al., 2006b; Del Bene et al., 2010) following previously described guidelines (Bulina et al., 2006a; Teh et al., 2010). At 2 dpf, the eyes of KillerRed$^+$ *Tg(tenm3:Gal4;UAS:KillerRed;elavl3:GCaMP5G)* and *Tg(tenm3:Gal4;UAS:KillerRed)* larvae, and KillerRed$^-$ *Tg(tenm3:Gal4;elavl3:GCaMP5G)* and *Tg(tenm3:Gal4)* control larvae were illuminated with continuous intense green light

(540-552 nm; filter set 15, BP 546/12 nm) for 40 minutes using a wide-field fluorescence microscope (Zeiss Axioskop) equipped with a 40× objective and a 100 Watts mercury lamp employed at maximal light intensity and objective aperture. In KillerRed^{+} larvae, strong photobleaching (~90% decrease in relative fluorescence) was observed after green light illumination, indicating effective KillerRed phototoxicity. To detect cell death, 3-4 hours following illumination the larvae were fixed in 4% paraformaldehyde (PFA) at 4°C overnight. Subsequently, larvae were cryosectioned and fluorometric terminal deoxynucleotidyl transferase dUTP nick end labeling (TUNEL; DeadEnd, Promega) assays were performed on sections following standard protocols.

2.11 Pharmacology

2.11.1 Block of Glutamate Receptors in the Optic Tectum

To isolate RGC axonal calcium responses from tectal cell dendritic responses in 4 dpf *Tg(tenm3:Gal4;UAS:KillerRed;elavl3:GCaMP5G)* and *Tg(tenm3:Gal4;elavl3:GCaMP5G)* larvae, the NMDA and AMPA/kainate glutamate receptor antagonists D-2-amino-5-phosphonovaleric acid (APV; Sigma) and 2,3-dihydroxy-6-nitro-7-sulfamoyl-benzo[f]quinoxaline-2,3-dione (NBQX; Sigma), 100 µM and 20 µM in Danieau solution respectively, were pressure-injected into one tectal hemisphere as previously described (Hunter et al., 2013). Larvae were imaged immediately post-injection. Animals were only included in the analyses if visual responses were not detected in tectal cell bodies following pharmacological treatment.

2.11.2 $GABA_A$ Receptors Block

To block γ-aminobutyric acid (GABA)-mediated inhibition from amacrine cells, the $GABA_A$ receptor chloride channel blocker picrotoxin (Sigma) was used at a final concentration of 100 µM, as previously described (Nikolaev et al., 2013). Functional calcium imaging was first performed in 4 dpf *Tg(isl2b:Gal4;UAS:SyGCaMP3)* larvae in Danieau solution with no drug. Subsequently, larvae were mounted in 2% low melting point agarose (Sigma) in Danieau solution with freshly made 100 µM picrotoxin and then imaged again. Importantly, also the Danieau solution in the imaging chamber contained 100 µM picrotoxin.

2.11.3 Glycine Receptors Block

To block glycine-mediated inhibition from amacrine cells, the glycine receptor antagonist strychnine (Sigma) was used at a final concentration of 70 µM (Hirata et al.,

2013). Functional calcium imaging was first performed in 5 dpf *Tg(isl2b:Gal4; UAS:SyGCaMP3)* larvae in Danieau solution with no drug. Subsequently, larvae were mounted in 2% low melting point agarose (Sigma) in Danieau solution with freshly made 70 µM strychnine and then imaged again. Importantly, also the Danieau solution in the imaging chamber contained 70 µM strychnine.

2.12 Immunohistochemistry

The primary antibodies used in the study were diluted in blocking solution as follows: chicken anti-GFP (1:500; Abcam, AB13970), rabbit anti-GABA (1:100; Sigma, A2052), guinea pig anti-GABA (1:500; Abcam, AB17413), mouse anti-Parvalbumin (1:300; Millipore, MAB1572), rabbit anti-TH (1:500; Millipore, AB152), goat anti-ChAT (1:100; Millipore, AB144P), rabbit anti-glycine (1:50; Abcam, AB9442). The primary antibody used to detect the Tenm3 protein in Fig. 4.3D and 5.9C-F is a custom-made polyclonal rabbit anti-Tenm3 antibody (1:150 dilution in blocking solution; Eurogentec) designed to recognise the following protein sequence, 445-TIDTGEVDVGRRAVQ-459, which is located in the extracellular domain of the zebrafish Tenm3 protein. The secondary antibodies used in the study were goat or donkey anti-chicken, anti-mouse, anti-rabbit, anti-guinea pig and anti-goat conjugated to Alexa Fluor 488 or 568 fluorophores (1:1000 dilution in blocking solution; Life Technologies). Nuclei were counterstained with TO-PRO-3 Iodide (1:1000 dilution in blocking solution; Life Technologies, T3605).

Immunostainings of zebrafish larvae on cryosections were performed following standard procedures. Briefly, larvae were fixed in 4% PFA overnight, rehydrated with PBS for 3 × 10 minutes, cryoprotected in 15%, 30% sucrose at room temperature for 2 hours and, lastly, 40% sucrose at 4°C overnight. Larvae used to immunostain Tenm3 in the retina were subjected to the following antigen retrieval procedure (Inoue and Wittbrodt, 2011): the cryoprotected larvae were incubated in 150 mM Tris-HCl pH 9.0 at room temperature for 5 minutes, followed by heating at 70°C for 15 minutes and, finally, re-cryoprotected in 40% sucrose at 4°C overnight. The cryoprotected larvae were then embedded in molds using O.C.T. compound (VWR International) and cryosectioned (18 µm thickness). Cryosections were mounted on glass slides (Superfrost plus, Thermo Scientific) and dried overnight at room temperature. Subsequently, slides were equilibrated 3 × 5 minutes in PBT (0.1% Tween-20 in PBS) and then blocked with 3% goat or donkey serum + 1% BSA in PBT for 1 hour at room temperature. After blocking, the slides were incubated with the respective primary antibodies at 4°C overnight. Lastly, slides were washed 3 × 30 minutes in PBT,

incubated with the respective secondary antibodies at room temperature for 2-3 hours, and then washed 3 × 30 minutes in PBT. To preserve the immunostained cryosections, Fluoromount-G (eBioscience) was used. Slides were then covered with glass coverslips and stored at 4°C until use.

2.13 Analysis

2.13.1 Functional Analyses

In vivo calcium imaging data were analysed as previously described (Lowe et al., 2013). In summary, functional time-series were processed before analysis as follows: time-series images from each experiment were corrected for motion with a rigid-body algorithm (SPM12; http://www.fil.ion.ucl.ac.uk/spm/), median filtered with a kernel size of 1 voxel to remove dark and shot noise, and spatially smoothed with a 2D Gaussian kernel = 2 voxels to improve signal-to-noise. A baseline (B) that corrects for low-frequency drifts was determined using a cubic-spline algorithm extrapolating between knots averaged from 5 s of the inter-epoch interval data. Both relative signal intensity changes ($\Delta F = F - B$; where F = raw fluorescence) and normalised signal intensity changes [$\%\Delta F/F_0 = (F - B)/B$] were calculated at each voxel. ΔF was used for population functional data (voxel-wise analysis), whereas $\%\Delta F/F_0$ was used for single cell functional data (manually defined regions of interest, ROIs, of dendritic or axonal arbours of GCaMP6f-labelled cells). For each voxel or ROI the integral response over the epoch-interval was calculated to provide a single response metric of each presented direction of stimulus motion. The integral within each epoch window is a summary metric more resistant to saturation effects of the calcium probe than maximum signal change. A threshold for each voxel within an acquisition image sequence was determined from the variance of ΔF changes during the inter-epoch intervals and null condition, threshold = 5 × SDs. All voxels that were supra-threshold within at least two visual presentation epochs were regarded as visually responsive and subjected to further characterisation.

To analyse the direction and orientation selectivity of visually responsive voxels or ROIs, direction- and orientation-selective indices (DSI and OSI) (Niell and Stryker, 2008), based on fitted von-Mises or Gaussian profiles (Swindale, 1998), were calculated together with an estimate for their goodness of fit, R^2. The DSI was defined as $(R_{pref} - R_{null})/(R_{pref} + R_{null})$, where R_{pref}, the response to the preferred direction, was the integral response over the preferred direction epoch-interval. R_{null} was similarly calculated as the integral response evoked by the direction opposite to the preferred

direction (180° angular distance). The OSI was defined as $(R_{pref} - R_{orth})/(R_{pref} + R_{orth})$, where R_{pref}, the response to the preferred orientation, was the integral response over the preferred orientation epoch-interval. R_{orth} was similarly calculated as the integral response evoked by the orientation orthogonal to the preferred orientation (90° angular distance). To minimise cross talk and over-fitting associated with DSI and OSI metrics, a stringent approach was undertaken. For a voxel or ROI to be regarded as direction-selective (DS) or orientation-selective (OS), mutually exclusive criteria were used: DS if DSI > 0.5 and OSI < 0.5; and OS if OSI > 0.5 and DSI < 0.5. In both cases, the goodness of fit (R^2) for DSI and OSI, respectively, had to be > 0.8; thus, the fitted curves explained at least 80% of the integral responses. A single von Mises distribution was used to fit responses of DS voxels and estimate their preferred direction of motion angle from the centre of the fitted curve, respectively. The sum of two von Mises or Gaussian distributions (180° angular distance apart) was used to fit responses of OS voxels or OS ROIs, respectively, and estimate their preferred orientation of motion angles from the centres of the fitted curves. Grouped cumulative histograms of the preferred direction or orientation of motion angles were generated from the calculated preferred angles of identified DS or OS voxel. The distribution of preferred angles for each identified DS or OS subpopulation of voxels was fitted by a Gaussian distribution with peak centre (mean), height (amplitude) and standard deviation being free dimensions. Circular variance was also calculated for comparison as an alternative metric of orientation selectivity (Circular variance < 0.4) (Batschelet, 1981).

2.13.2 Morphological Analyses

To determine the IPL stratification profile of *tenm3*$^+$ AC neurites and OSGC dendrites, rectangular 10 µm-wide ROIs were drawn across the IPL. The Plot Profile function in ImageJ (Schneider et al., 2012) was applied to the ROIs to calculate fluorescence intensity traces across the IPL depth. The traces obtained from multiple larvae were then normalised and averaged using SigmaPlot (Systat Software). The dendritic field area and orientation angle of individual eGFP-CAAX- or GCaMP6f-labelled *tenm3*$^+$ ACs were measured using ImageJ (Schneider et al., 2012) in 3D rotated images generated through ZEN (Carl Zeiss). To quantify the dendritic field elongation of individual *tenm3*$^+$ ACs, the eccentricity of dendritic arbour profiles [$e = \sqrt{(1 - b^2/a^2)}$; a = length of the ellipse semi-major axis, b = length of the ellipse semi-minor axis] was calculated following ellipse fitting in ImageJ (Schneider et al., 2012). 3D morphological reconstructions of individual *tenm3*$^+$ ACs were obtained using the Simple Neurite

Tracer plugin in FIJI (Schindelin et al., 2012). To estimate the total number of type I-IV *tenm3*$^{+}$ ACs required to tile the retina with a coverage factor of 1, the mean IPL area (49,903 ± 3,707 µm^2, mean ± SD; n = 14 retinae from 14 larvae at 4 dpf) was divided by the observed mean dendritic field area of each *tenm3*$^{+}$ AC type and, subsequently, the obtained values were used to estimate the respective relative frequency.

To determine the brain volume imaged in 4 dpf *nacre*, *casper* and *crystal Tg(elavl3:GCaMP6f)* larvae, the number of GCaMP6f^{+} voxels in each volumetric image was calculated by applying the adjust>threshold function followed by the analyse>histogram>list command in ImageJ (Schneider et al., 2012). Subsequently, the obtained values were multiplied by the volume of a single voxel (0.415 × 0.415 × 0.631 µm^3 = 1.086 × 10^{-1} µm^3).

2.13.3 Statistical Analyses

Statistical analyses and tests were carried out using Prism 6 (GraphPad), SigmaPlot 11 (Systat Software) or MATLAB R2014b (MathWorks). Before performing statistical tests, descriptive statistics (e.g., normality tests to see whether values come from a Gaussian distribution or F-test to compare variances) were used to choose the appropriate statistical test. The criterion for statistical significance was set at $p < 0.05$. To quantitatively measure and assess the effects of treatments or genetic manipulations between animal groups, the effect size (Cohen's *d*) and its 95% confidence interval were also calculated (not shown). No statistical method was used to predetermine sample sizes, but sample sizes are similar to those generally employed in the field and in most cases provided a high statistical power (i.e., power > 0.8).

2.14 Simulation of OSGC Output

To simulate the tuning profile of orientation-selective ganglion cells (OSGCs) the following algorithm was used:

$$O_{hOSGC} = \sum_{i=m}^{n} (\beta_i + w\alpha_i)$$

The tuning profile of OSGCs tuned to horizontal bars moving along the vertical axis (0°; hence, O_{hOSGC}) was simulated by summating normalised bipolar cell (BC) excitatory input (β) and OS *tenm3*$^{+}$ amacrine cell (AC) inhibitory input (α) for each stimulus orientation (i) across the whole orientation space. The orientation space ranges from 'm' to 'n', which are negative (-90°) and positive (90°) angles orthogonal to the preferred orientation (0°), respectively. Values used for 'α' are the experimentally

observed average responses of orthogonal orientation-tuned *tenm3*$^{+}$ ACs (i.e., *tenm3*$^{+}$ ACs tuned to vertical bars moving along the horizontal axis; OSI > 0.5, DSI < 0.5, R^2 > 0.8; n = 20 larvae). Note that, since the OS *tenm3*$^{+}$ AC input is inhibitory, a negative synaptic weight factor (w) is used in the algorithm. As a consequence, the OS inhibitory input provided by *tenm3*$^{+}$ ACs has a subtractive effect on OSGC output. Values used for 'β' are the experimentally observed average responses of BC terminals (n = 20 larvae). Three different orientation-tuning levels of excitatory BC input were tested, namely: (1) untuned BC input (average responses of all visually responsive BC voxels), (2) weakly OS (OSI > 0, DSI < 0.5, R^2 > 0) preferred orientation-tuned BC input; (3) highly OS (OSI > 0.5, DSI < 0.5, R^2 > 0.8) preferred orientation-tuned BC input. The experimentally observed average response profile of OSGCs tuned to horizontal bars moving along the vertical axis (n = 23 larvae) was used as a comparison to evaluate the accuracy of the simulated OSGC response profile.

Chapter 3

Generation of a Zebrafish Pigmentation Mutant for *in vivo* Imaging

3.1 Introduction

To understand complex biological phenomena, structural and functional information has to be extracted from intact animal systems at different spatial scales. Optical transparency of animals is a highly desirable feature to study these biological processes *in vivo* using light microscopy. Pigment molecules, such as melanin, haemoglobin and myoglobin, are the main sources of visible light absorption in biological tissues (Pawley, 2005; Jacques, 2013). Lipids and collagen, on the other hand, constitute the primary molecules responsible for light scattering. Recently, several tissue-clearing techniques have been developed to reduce light scattering in fixed biological tissues by selectively removing lipids in a non-destructive way (Richardson and Lichtman, 2015). However, the only molecules that can be removed from living systems without dramatically impairing their viability are pigment molecules localised in defined tissues, such as melanin present in the skin. Here, a combinatorial genetic approach has been used to generate a viable, fully transparent zebrafish mutant, named *crystal*, lacking the vast majority of skin pigmentation. Compared to the previously described combinatorial pigmentation mutant *casper* that has pigmented eyes (White et al., 2008), the *crystal* mutant constitutes a significant improvement for *in vivo* imaging of tissues inside or between the eyes.

In zebrafish, multiple populations of cells produce pigments that ultimately restrict the optical accessibility of tissues (Kelsh et al., 1996; Singh and Nusslein-Volhard, 2015). The three main kinds of pigment cells (or chromatophores) are the melanophores (black appearance), iridophores (silvery or blue) and xanthophores (yellow; Fig. 3.1A). In addition to these three populations, which in zebrafish larvae derive from neural crest cells, there is another population of pigment cells forming the retinal pigment epithelium (RPE), which originates from optic lobe neuroepithelial cells (Fig. 3.1B) (Bharti et al., 2006). Common strategies to reduce zebrafish skin pigmentation can be grouped in two categories: (1) use of chemical compounds interfering with the synthesis of melanin, the most popular one being

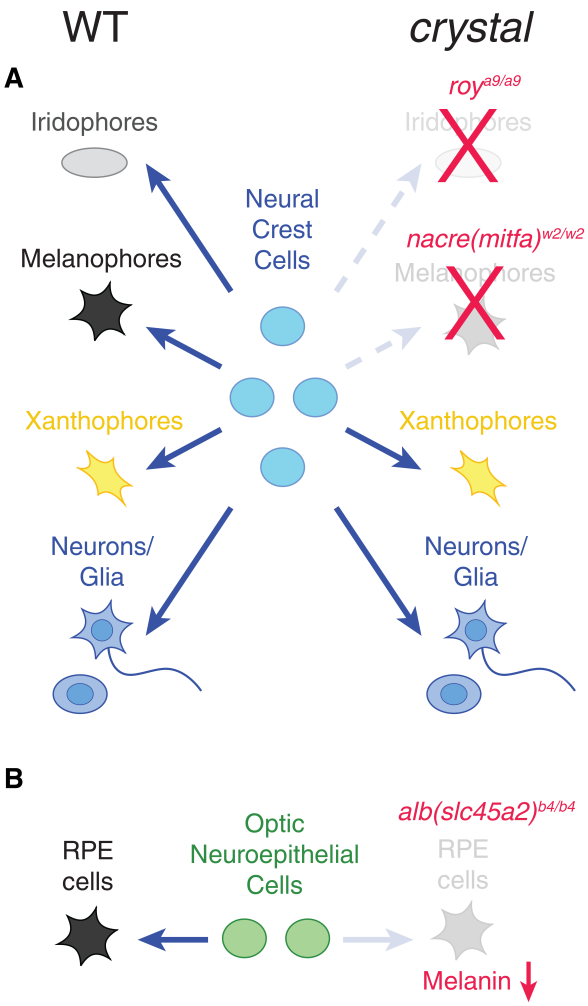

Figure 3.1. Pigment cell types and related mutations in larval zebrafish. A|B, Left: schematic diagram of the main populations of pigment cells in wild type (WT) zebrafish. Centre: cell lineages generating the different populations of pigment cells. Right: mutations affecting genes controlling either pigment cell formation (*nacre*$^{w2/w2}$ and *roy*$^{a9/a9}$) or melanin production (*alb*$^{b4/b4}$) used to generate the *crystal* mutant. Pigment cells in (**A**) derive from neural crest cells, whereas those forming the retinal pigment epithelium (RPE, **B**) derive from optic neuroepithelial cells.

1-phenyl-2-thiourea (PTU) (Karlsson et al., 2001); (2) use of pigmentation mutants in which genes controlling either pigment formation, chromatophore formation or interactions between chromatophores have been inactivated (Kelsh et al., 1996; Lister et al., 1999; White et al., 2008). The first strategy, despite being straightforward (i.e., embryos can be simply raised in medium containing 200 µM PTU), is associated with toxic side effects that impair morphogenesis, behaviour and survival. For example, PTU has been shown to interfere not only with tyrosinase (the enzyme that catalyses the production of melanin) (Whittaker, 1966; Ryazanova et al., 2012), but also with other enzymes, such as thyroid peroxidase (Li et al., 2012b) and dopamine beta-hydroxylase (Johnson et al., 1970). Therefore, the poor selectivity of this drug results in severe consequences including reduced thyroid hormone synthesis (Elsalini and Rohr,

2003), decreased eye size (Li et al., 2012b), abnormal cranial neural crest and extraocular muscle development (Bohnsack et al., 2011), impaired retinal light adaptation (Page-McCaw et al., 2004), as well as anxiety (Parker et al., 2013) and reduced mobility, hatching and survival (Karlsson et al., 2001). In contrast, the second strategy is considerably less disruptive since it takes advantage of viable mutations affecting the function of genes expressed in specific subsets of cells where they are involved in defined processes of pigment production (Singh and Nusslein-Volhard, 2015). Since the formation of each pigment type is controlled independently of the others, the combination of different mutations is required to produce fully transparent zebrafish. This approach has been previously implemented to generate the double mutant *casper*, which lacks all melanophores and iridophores (White et al., 2008). Here, this strategy is further developed to generate a fully optically clear combinatorial mutant (*crystal*) that not only lacks all melanophores and iridophores, but also has a non-pigmented RPE. This particular feature makes *crystal* larvae especially suited for imaging tissues inside or between the eyes while avoiding the use of chemical pigmentation blockers. Importantly, *crystal* mutants show no behavioural or viability deficits as compared to wild type animals. To further validate the *in vivo* application of this novel mutant, whole-brain light-sheet imaging and two-photon functional recordings of neural activity in the retinae of *crystal* larvae are also performed.

3.2 Results

3.2.1 Generation of 'Crystal': a Fully Transparent Zebrafish for in vivo Imaging

To generate optically clear zebrafish lacking the vast majority of skin pigmentation without using chemical compounds inhibiting pigment formation, a combinatorial genetic approach has been undertaken. Three previously described viable mutations affecting different populations of chromatophores (Fig. 3.1 right) were selected and combined through crossbreeding (Fig. 3.2): (1) the *nacre*$^{w2/w2}$ mutant lacks all melanophores due to a mutation in the *mitfa* gene (Lister et al., 1999). Since the *nacre* mutation does not affect the population of cells forming the RPE, this structure is still pigmented in this single mutant. (2) The *albino* (*alb*$^{b4/b4}$) mutant is characterised by a general deficiency in the production of melanin due to a mutation in the *slc45a2* gene (Streisinger et al., 1986). (3) The *roy orbison* (*roy*$^{a9/a9}$) mutant shows a complete lack of iridophores (White et al., 2008). The gene responsible for this mutant phenotype is currently unknown. The resulting combinatorial triple mutant (*nacre*$^{w2/w2}$;*alb*$^{b4/b4}$;*roy*$^{a9/a9}$;

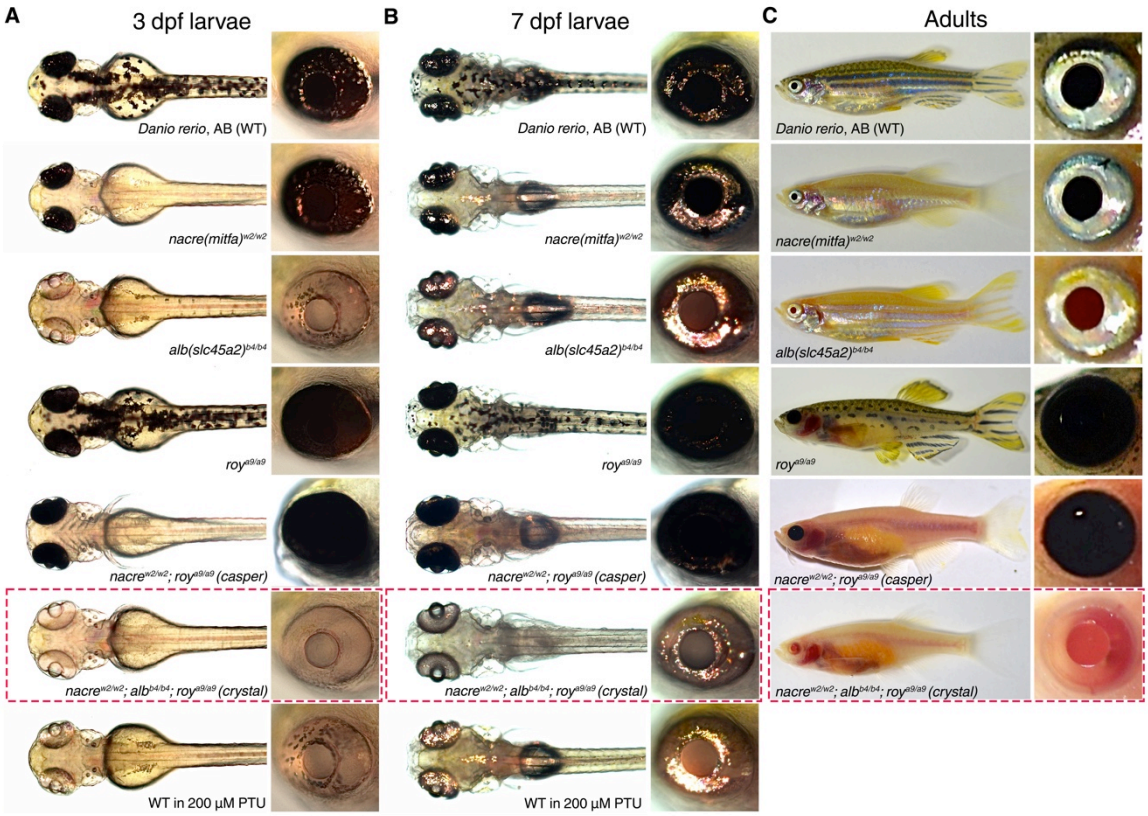

Figure 3.2. Generation of *crystal*, a fully transparent combinatorial pigmentation mutant. A-C, Pigmentation phenotypes of wild type, single mutant, *casper* and *crystal* zebrafish at embryonic (3 dpf, **A**), larval (7 dpf, **B**) and adult (> 3 month old, **C**) stages. Red dashed boxes indicate *crystal* mutants. Insets on the right display eye pigmentation phenotypes. 3 dpf and 7 dpf zebrafish treated with 200 µM PTU are shown at the bottom of (**A**) and (**B**). Note that the optical transparency of *crystal* fish is higher than that of wild type, single mutant, *casper* and PTU-treated fish.

red boxes in Fig. 3.2), which was named *crystal*, lacks the vast majority of dark and reflective pigments normally present at the cutaneous level and, as a consequence, appears optically clear. The internal organs are clearly visible in adult (> 3 months old) *crystal* mutants as opposed to wild type and single mutant fish (Fig. 3.2C). Compared to the previously described double mutant *casper* (*nacre*$^{w2/w2}$;*roy*$^{a9/a9}$) (White et al., 2008), where internal organs are also visible, the triple mutant *crystal* (*nacre*$^{w2/w2}$;*alb*$^{b4/b4}$;*roy*$^{a9/a9}$) lacks melanin in the RPE (Fig. 3.2C). Consequently, the eyes of *crystal* fish are considerably less pigmented than wild type, single mutant and *casper* fish, and therefore are easily accessible to optical investigation (see right insets in Fig. 3.2A-C). The pigmentation phenotype of *crystal* fish is already evident at embryonic (e.g., 3 dpf, Fig. 3.2A) and larval (e.g., 7 dpf, Fig. 3.2B) stages. Importantly, the optical clarity of *crystal* larvae is even superior to that of larvae treated with 200 µM PTU (Fig. 3.2A,B), since PTU inhibits melanin production but does not interfere with iridophore function (Karlsson et al., 2001). Moreover, unlike PTU-treated animals, adult *crystal* mutants are viable and produce normal numbers of offspring. Heterozygous fish

(*nacre*$^{w2/+}$;*alb*$^{b4/+}$;*roy*$^{a9/+}$) do not exhibit any visible pigmentation phenotype. Overall, the *crystal* mutant constitutes a significant improvement in the optical accessibility of both larval and adult zebrafish, even superior to the previously described combinatorial mutant *casper* (White et al., 2008), which is characterised black-pigmented eyes.

3.2.2 Crystal Zebrafish Larvae Exhibit Normal Visual Behaviour

An ideal system for *in vivo* imaging has to be characterised not only by optical clarity but also by normal functional and behavioural viability. The use of PTU to quickly obtain transparent zebrafish larvae is widespread across the research community. However, numerous studies reported severe morphological and behavioural side effects caused by the toxicity of PTU treatment (see 3.1). To compare the behavioural viability of *crystal* larvae to wild type larvae and to larvae raised in medium containing 200 µM PTU, the ability of 5 dpf larvae to perform the optomotor response was tested. During optomotor response assays, freely swimming zebrafish larvae respond to whole-field moving stimuli (e.g., dark and light bars) by swimming in the same direction of stimulus motion (Fig. 3.3A) (Orger et al., 2004). They do so to compensate for the optic flow-induced perception of apparent involuntary displacement, and therefore regain the desired course of locomotion. Individual larvae were tested five times in total and scored according to the number of trials they responded to (i.e., fish turns and swims in the direction of the moving stimulus).

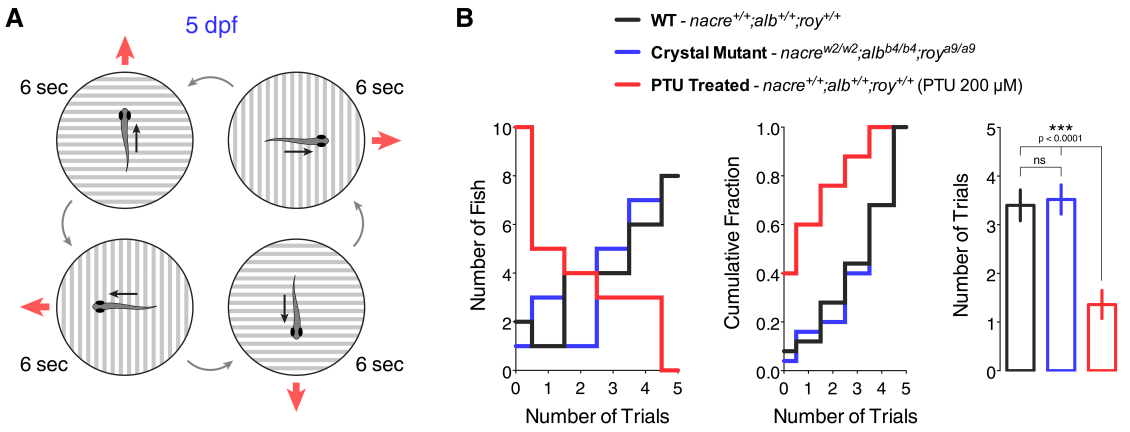

Figure 3.3. PTU impairs zebrafish visual behaviour. A, Schematic diagram illustrating the optomotor response behavioural assay. Individual 5 dpf larvae were positioned in a petri dish containing Danieau solution. An LCD screen controlled by a computer was used to display black and white square-wave gratings moving in 4 directions (red arrows) at the bottom of the petri dish. Each larva was tested 5 times in total (each trial lasted 6 seconds) and scored according to the trials it responded to (i.e., fish turns and swims in the direction of the moving gratings). **B,** Quantification of the optomotor response assays for 5 dpf wild type (WT, black), *crystal* (blue) and PTU-treated (red) larvae (n = 25 larvae in each group). The frequency distribution (left), cumulative frequency distribution (centre) and mean ± SEM (right) of number of responsive trials per larva are reported. Note that PTU-treated larvae show a significant decrease in the number of trials they respond to. ns, non-significant; ***p < 0.001; one-way ANOVA with post-hoc Tukey's HSD test.

Notably, *crystal* larvae exhibited a response rate equivalent to wild type larvae as opposed to PTU-treated larvae, which instead showed a dramatic behavioural impairment (Fig. 3.3B; mean number of responsive trials ± SEM, WT 3.40 ± 0.32 trials out of 5, n = 25 larvae; *crystal* 3.52 ± 0.30 trials, n = 25; PTU-treated 1.36 ± 0.29 trials, n = 25; $p < 0.0001$, $F_{2,72} = 16.17$, one-way ANOVA with post-hoc Tukey's HSD test).

3.2.3 Abnormal Visual Responses in PTU-treated Zebrafish Larvae

Given the observed behavioural consequences of PTU treatment, whether PTU has any effect on zebrafish visual system function was further investigated by recording visually induced neural responses in the optic tectum – the main retinorecipient brain area in zebrafish. The optic tectum receives inputs from all functional types of retinal ganglion cells (Robles et al., 2014), including some types that are tuned to stimulus direction of motion (direction-selective cells) or stimulus orientation (orientation-selective cells; see 1.1 and 1.2) (Nikolaou et al., 2012). Using a transgenic fish line where the genetically encoded calcium indicator GCaMP5G is expressed pan-neuronally (Ahrens et al., 2013), visual responses to moving dark and light bars in both the tectal neuropil and periventricular neurons were analysed through *in vivo* calcium imaging (Fig. 3.4A and Movie 3.1) (Nikolaou and Meyer, 2015). Compared to untreated *Tg(elavl3:GCaMP5G)* larvae, 4 dpf PTU-treated larvae (treatment from 1 dpf to 3 dpf) showed a large decrease in visual responses (Fig. 3.4B; mean number of visually responsive voxels ± SEM, control 19463 ± 1294 voxels, n = 12 larvae; PTU-treated 4110 ± 708 voxels, n = 12; $p < 0.0001$, $t_{22} = 10.41$, unpaired two-tailed t-test) with direction- and orientation-selective neural responses being absent or severely impaired, respectively (Fig. 3.4B; mean number of direction-selective voxels ± SEM, control 128 ± 22.75 voxels, n = 12 larvae; PTU-treated 0 ± 0 voxels, n = 12; $p = 0.0002$, $t_{11} = 5.62$, unpaired two-tailed t-test with Welch's correction; mean number of orientation-selective voxels ± SEM, control 1239.25 ± 229.99 voxels, n = 12; PTU-treated 12.66 ± 3.01 voxels, n = 12; $p = 0.0002$, $t_{11} = 5.33$, unpaired two-tailed t-test with Welch's correction). These data indicate that PTU has deleterious consequences in both zebrafish behaviour and neural function, and should be therefore avoided whenever these two biological processes are under investigation. Since PTU is a highly non-selective drug (see 3.1) and is generally applied at the whole-animal level, it is difficult to attribute any of the detrimental effects observed to a specific biochemical pathway.

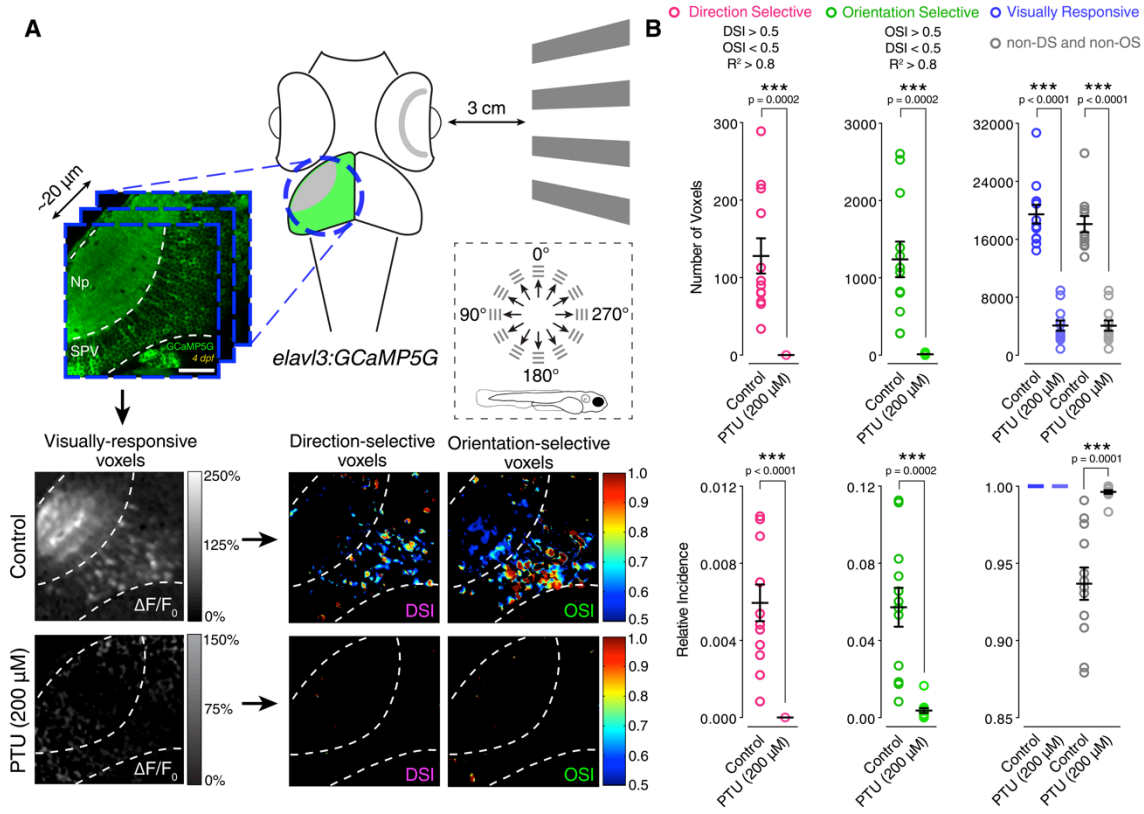

Figure 3.4. PTU impairs zebrafish visual system function. A, Functional calcium imaging of tectal cells and retinal ganglion cell axons expressing GCaMP5G (green) in 4 dpf *Tg(elavl3:GCaMP5G)* larvae. Distance of right eye from projection screen is 3 cm. Recordings are performed from 3 Z-planes (approximately 20 µm total volume thickness) in the contralateral optic tectum at 4 Hz image acquisition rate. Dashed box shows the angles of moving bars relative to zebrafish larva orientation. Mean $\Delta F/F_0$ images of calcium recordings in untreated (control) and PTU-treated larvae followed by mapping of direction-selective (DS) and orientation-selective (OS) voxels are displayed. Np, neuropil; SPV, stratum periventriculare; DSI, direction selectivity index; OSI, orientation selectivity index. Scale bar is 40 µm. **B,** Average number (top) and relative frequency (bottom) of DS, OS, visually responsive and non-DS/non-OS voxels per Z-plane in control and PTU-treated 4 dpf larvae (n = 12 larvae in each group). Criteria used to identify DS and OS voxels are reported at the top. Note the dramatic reduction in visually responsive, DS and OS voxels following 200 µM PTU treatment. Error bars are ± SEM. ***p < 0.001, unpaired two-tailed Student's t test.

3.2.4 Whole-brain Light-sheet Imaging of Crystal Larvae

The next aim was to validate the *in vivo* application of *crystal* larvae by performing whole-brain light-sheet imaging (Keller and Ahrens, 2015). Light-sheet microscopy has recently experienced a series of significant technological advancements and is generally used to study nervous system activity and development with cellular resolution at the whole-animal level (Ahrens et al., 2013; Chhetri et al., 2015; Tomer et al., 2015; Wolf et al., 2015). In typical zebrafish light-sheet preparations, the excitation light is provided laterally and fluorophore emission light is collected through an objective positioned orthogonally to the illumination plane. However, due to the strong pigmentation of the eyes, imaging of areas inside or between these structures is

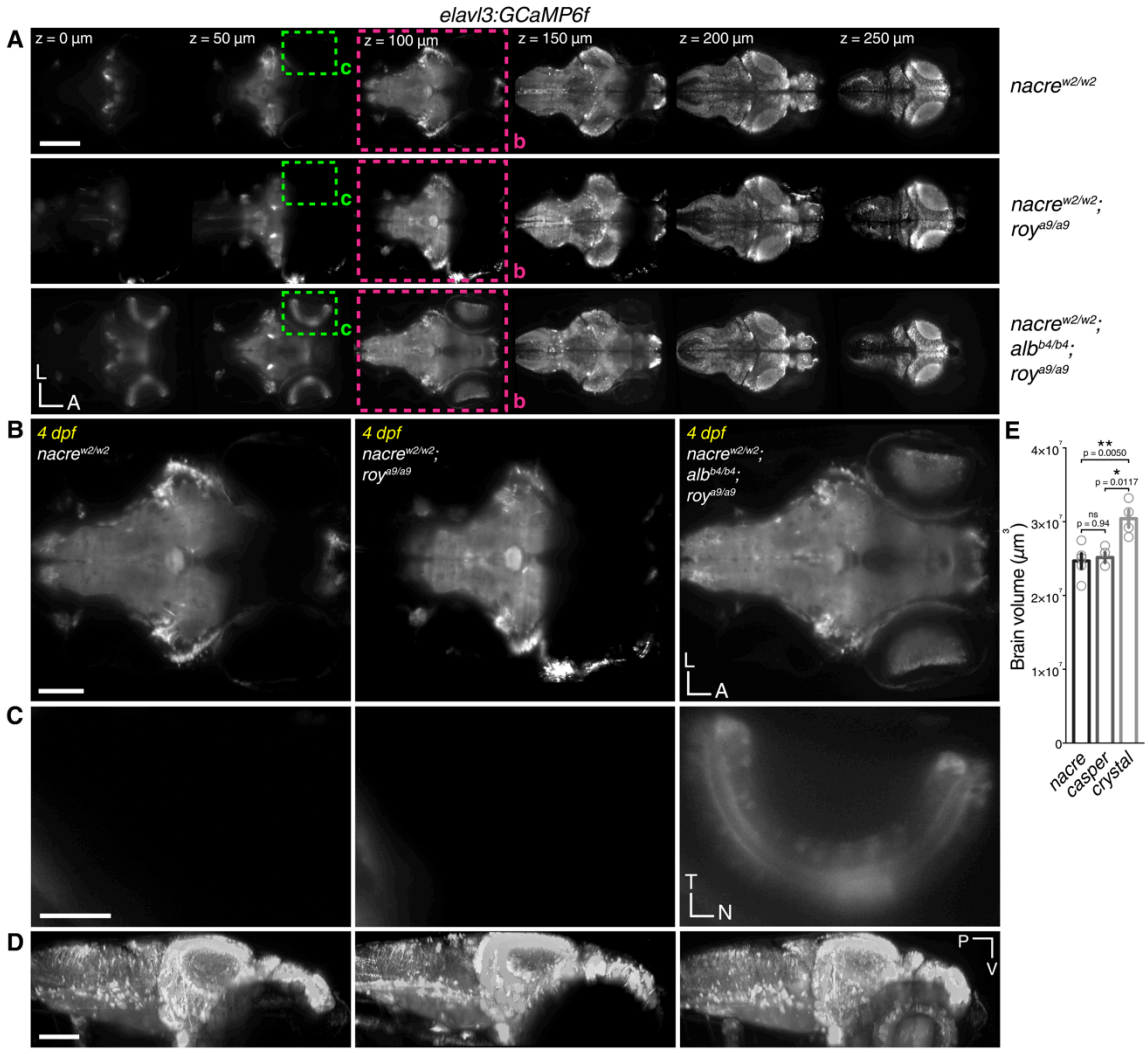

Figure 3.5. Improved optical accessibility of zebrafish larvae in whole-brain light-sheet imaging using *crystal*. A, Volumetric imaging of the larval zebrafish brain with light-sheet microscopy in 4 dpf *nacre* (top), *casper* (middle) and *crystal* (bottom) *Tg(elavl3:GCaMP6f)* larvae (n = 4-5 larvae in each group). Six different volume sections per larva out of 450 (total xyz volume of 798 × 623 × 283 µm^3) are displayed. L, left; A, anterior. Scale bar is 200 µm. **B,** Single volume sections of the brain (100 µm Z plane) in *nacre* (left), *casper* (middle) and *crystal* (right) larvae. Note the dark region between the eyes of the *nacre* and *casper* larvae due to the excitation light being absorbed or reflected by pigments present on the surface of the eyes. L, left; A, anterior. Scale bar is 100 µm. **C,** Insets showing the labelling of amacrine and ganglion cells in the left retina of the *crystal* larva (right) compared to *nacre* (left) and *casper* (middle) larvae, where no GCaMP6f fluorescence is detected in the eyes. T, temporal; N, nasal. Scale bar is 50 µm. **D,** 3D reconstructions of the brain (lateral view) of *nacre* (left), *casper* (middle) and *crystal* (right) *Tg(elavl3:GCaMP6f)* larvae shown in (**A**). Note the improved optical accessibility (~18% of brain volume) enabled by *crystal*. P, posterior; V, ventral. Scale bar is 100 µm. **E,** Average brain volume in *nacre*, *casper* and *crystal* 4 dpf *Tg(elavl3:GCaMP6f)* larvae. Error bars are ± SEM. ns, non-significant; *p < 0.05; **p < 0.01; one-way ANOVA with post-hoc Tukey's HSD test.

normally problematic. The optical accessibility of the nervous system in *crystal, nacre* and *casper* larvae was therefore assessed using the pan-neuronal *Tg(elavl3:GCaMP6f)* line (Dunn et al., 2016b) (Fig. 3.5A and Movie 3.2). In the imaging setup used, the sheet of laser light (488 nm) is generated by two objectives positioned on the lateral sides of the larva. In 4 dpf *crystal* larvae, the excitation light can easily reach deep (i.e., ventral) regions of the brain (Fig. 3.5B) as well as the retinae (Fig.

3.5C) without being absorbed or reflected by pigments normally present on the surface of the eyes, like in *nacre* or *casper* larvae (note the dark regions in the left and middle panels of Fig. 3.5B,C). Therefore, *crystal* allows a fully unobstructed optical access of the larval zebrafish brain in its entirety (i.e., including the eyes), as opposed to *nacre* and *casper* mutants where a substantial portion of the nervous system (~18%) is not accessible through standard light-sheet imaging (Fig. 3.5A,D,E; mean volume ± SEM, *crystal* $3.04 \pm 0.12 \times 10^7$ µm^3, n = 4 larvae; *casper* $2.51 \pm 0.07 \times 10^7$ µm^3, n = 4; *nacre* $2.47 \pm 0.10 \times 10^7$ µm^3, n = 5; p = 0.0040, $F_{2,10} = 10.09$, one-way ANOVA with post-hoc Tukey's HSD test). Even though the optical accessibility of crystal larvae through light-sheet imaging is significantly higher than *nacre* and *casper* mutants, it is noteworthy that the spatial definition of brain regions between the eyes appears lower than other regions of the brain, likely due to scattering of excitation light by the lenses. Despite this fact, the light-sheet signal detected from these regions in *crystal* mutants is still many-fold higher than in the other animal groups (Fig. 3.5A,B).

3.2.5 Two-photon Calcium Imaging in the Intact Retina Using Crystal

To further assess the *in vivo* application of *crystal* larvae, two-photon functional imaging of neural activity was performed in the retina, a brain region that is not optically accessible in wild type, single pigmentation mutant or *casper* larvae (Fig. 3.2) unless embryos are raised in medium containing PTU (Odermatt et al., 2012; Nikolaev et al., 2013). To record visual responses in the larval retina through calcium imaging, 4 dpf *Tg(elavl3:GCaMP6f) crystal* larvae were immobilised in 2% low melting point agarose with one eye facing an LCD screen where square-wave gratings moving in 12 different directions were displayed (Fig. 3.6A; n = 8 larvae). Visually evoked calcium transients were recorded from amacrine and ganglion cells at 4 Hz using near-infrared (930 nm) two-photon laser excitation (Movie 3.3). Voxel-wise analysis was then used to identify visually responsive voxels (Fig. 3.6B) and quantify direction and orientation selectivity of visual responses at subcellular resolution (0.248 × 0.248 μm voxel XY size, Fig. 3.6C) (Lowe et al., 2013). $\Delta F/F_0$ calcium traces from 6 selected regions of interest (ROIs) comprising several voxels (Fig. 3.6B) are displayed as examples (Fig. 3.6D). Interestingly, not only stimulus-locked responses could be recorded, but also the presence of direction-selective (DSI > 0.5, ROI# 4 and 5) and orientation-selective (OSI > 0.5, ROI# 1-3) responses was observed (Fig. 3.6C,D), indicating that the retina is functional in *crystal* larvae. A previous study has reported that adult zebrafish mutants

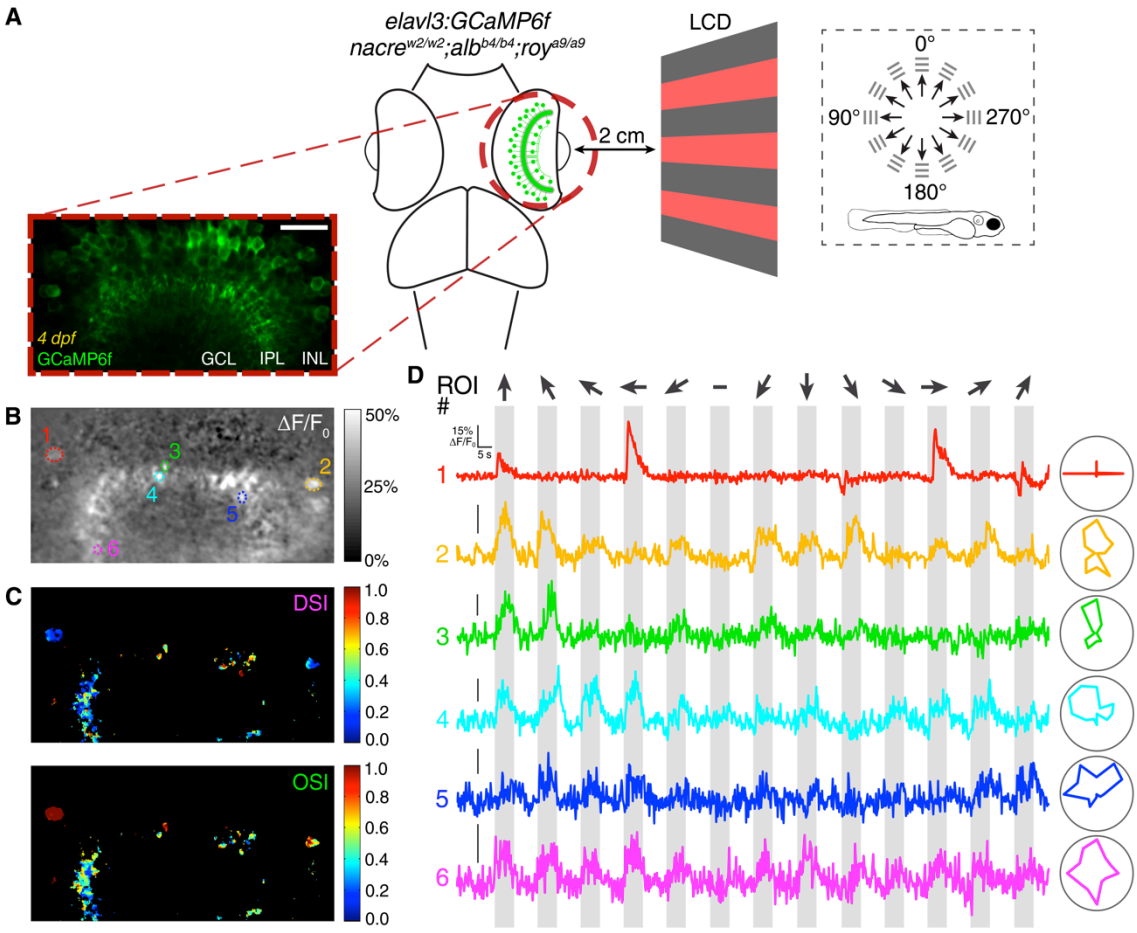

Figure 3.6. Calcium imaging of visually evoked neural activity in the retina using *crystal*. A, Two-photon functional calcium imaging of amacrine cells and ganglion cell dendrites expressing GCaMP6f (green) in 4 dpf *crystal Tg(elavl3:GCaMP6f)* larvae (n = 8 larvae). Distance of the eye from LCD screen is 2 cm. Recordings are performed from 2-4 Z-planes (approximately 20 µm total volume thickness) at 4 Hz image acquisition rate. Dashed box shows the angles of moving gratings relative to zebrafish larva orientation. INL, inner nuclear layer; GCL, ganglion cell layer; IPL, inner plexiform layer. Scale bar is 20 µm. **B**|**C,** Mean $\Delta F/F_0$ image of a representative calcium recording (**B**) followed by voxel-wise analysis of direction and orientation selectivity of visual responses (**C**). DSI, direction selectivity index; OSI, orientation selectivity index. **D,** $\Delta F/F_0$ calcium traces during a representative tuning experiment from the 6 selected regions of interest (ROIs) shown in (**b**). Polar plots showing the tuning profiles (i.e., integral $\Delta F/F_0$ responses to different stimuli) of individual ROIs are reported on the right. Stimulus epochs are shown in grey. Dark arrows indicate the different directions of gratings motion. The blank-screen null condition is indicated by a '–' sign.

with hypopigmented eyes show deficits in performing visual escape assays under defined luminance conditions (Ren et al., 2002). Thus, even though the visual behaviour assays above demonstrated that *crystal* larvae perform the optomotor response as well as wild type larvae (Fig. 3.3), it cannot be excluded that *crystal* mutants might show abnormal retinal responses under certain luminance conditions. However, given the deleterious effects caused by PTU treatment (Fig. 3.3 and 3.4; see 3.1), the *crystal* mutant represents, to date, the most viable strategy to perform *in vivo* functional imaging in the intact retina of larval zebrafish.

3.3 Discussion

Here, a viable and optically transparent combinatorial pigmentation mutant zebrafish, named *crystal*, has been generated. This novel mutant constitutes an ideal tool for completely unobstructed imaging of biological phenomena *in vivo* through light microscopy. More specifically, compared to *casper* mutants (White et al., 2008), *crystal* fish are superior in terms of optical transparency when imaging inside or between the eyes. The viability and *in vivo* application of *crystal* larvae have been validated through the optomotor response assay, whole-brain light-sheet imaging and two-photon functional imaging of neural activity in the intact retina. Importantly, *crystal* larvae show a higher viability than larvae treated with the chemical pigmentation blocker PTU. Thus, it is reasonable to envisage that *crystal* will be an invaluable tool for other *in vivo* applications, such as one-photon (Ahrens et al., 2013) or two-photon (Wolf et al., 2015) volumetric calcium imaging of neural activity across the entire brain in semi-restrained behaving (Bianco and Engert, 2015) or paralysed fictively swimming (Vladimirov et al., 2014) zebrafish larvae, as well as to study the wiring, function and plasticity of neural circuits in normally highly pigmented, optically inaccessible structures like the eyes (Nikolaev et al., 2013; Randlett et al., 2013).

Chapter 4

Characterisation of Teneurin-3-expressing Neurons

4.1 Introduction

As described in the introductory chapter, retinal ganglion cells (RGCs) develop stereotypic dendritic arborisation patterns and make specific synaptic connections with amacrine and bipolar cells in the inner plexiform layer (IPL) (Masland, 2012a). The formation of such precise connections is critical for the processing of visual information and the generation of feature selectivity in RGCs (Wassle, 2004; Gollisch and Meister, 2010). Recent developmental studies have shown that the assembly of neuropil strata and synaptic connectivity in the IPL are regulated by both adhesive (Yamagata and Sanes, 2008) and repulsive cues (Matsuoka et al., 2011a). In particular, cell-adhesion transmembrane proteins selectively expressed in specific retinal cell types play crucial roles in mediating the matching between defined pre- and postsynaptic partners (Yamagata and Sanes, 2008; Duan et al., 2014; Krishnaswamy et al., 2015). However, we are still far from a complete understanding of the molecular mechanisms specifying synaptic connectivity within the retina, and between the retina and retinorecipient nuclei in the brain.

In this context, teneurins represent intriguing candidates in the control of retinal circuit wiring (see 1.3.3) (Young and Leamey, 2009; Tucker et al., 2012). The essential role of teneurins in synaptic partner matching and target choice has been elegantly demonstrated in the *Drosophila* olfactory system (Hong et al., 2012) and neuromuscular synapses (Mosca et al., 2012). In mice, teneurins regulate the generation of binocular visual circuits by controlling the development of ipsilaterally projecting RGCs (Leamey et al., 2007; Dharmaratne et al., 2012; Young et al., 2013). However, a role for teneurins in mediating synapse-specific wiring in the vertebrate retina has yet to be demonstrated. During my PhD, the role played by *teneurin-3* (*tenm3)* in the assembly of retinal circuits during development has been investigated using zebrafish as animal model system. To start addressing this biological question, the endogenous expression pattern of *tenm3* in the zebrafish visual system was analysed. The data presented here show that *tenm3* is expressed in RGCs, amacrine cells and the optic tectum. Additionally, the morphological properties of a subset of amacrine cells expressing *tenm3* were also characterised.

4.2 Results

4.2.1 Tenm3 Is Expressed in Interconnected Regions of the Developing Visual System

Between 2 and 5 dpf, zebrafish retinal cells undergo a rapid phase of morphological and functional development associated with a wave of intense synapse formation (Schmitt and Dowling, 1999; Meyer and Smith, 2006; Mumm et al., 2006; Lowe et al., 2013). To reveal the expression pattern of *tenm3* in the zebrafish visual system during this developmental period, *in situ* hybridization analyses using a specific digoxigenin-labeled antisense riboprobe against *tenm3* were carried out. In the retina, *tenm3* mRNA expression was observed in the ganglion cell layer (GCL) and the inner third of the inner nuclear layer (INL), where amacrine cells are located (Fig. 4.1A). Since in zebrafish only a very small number of displaced amacrine cells is present in the GCL (Connaughton et al., 1999), the majority of signal detected in this layer can be

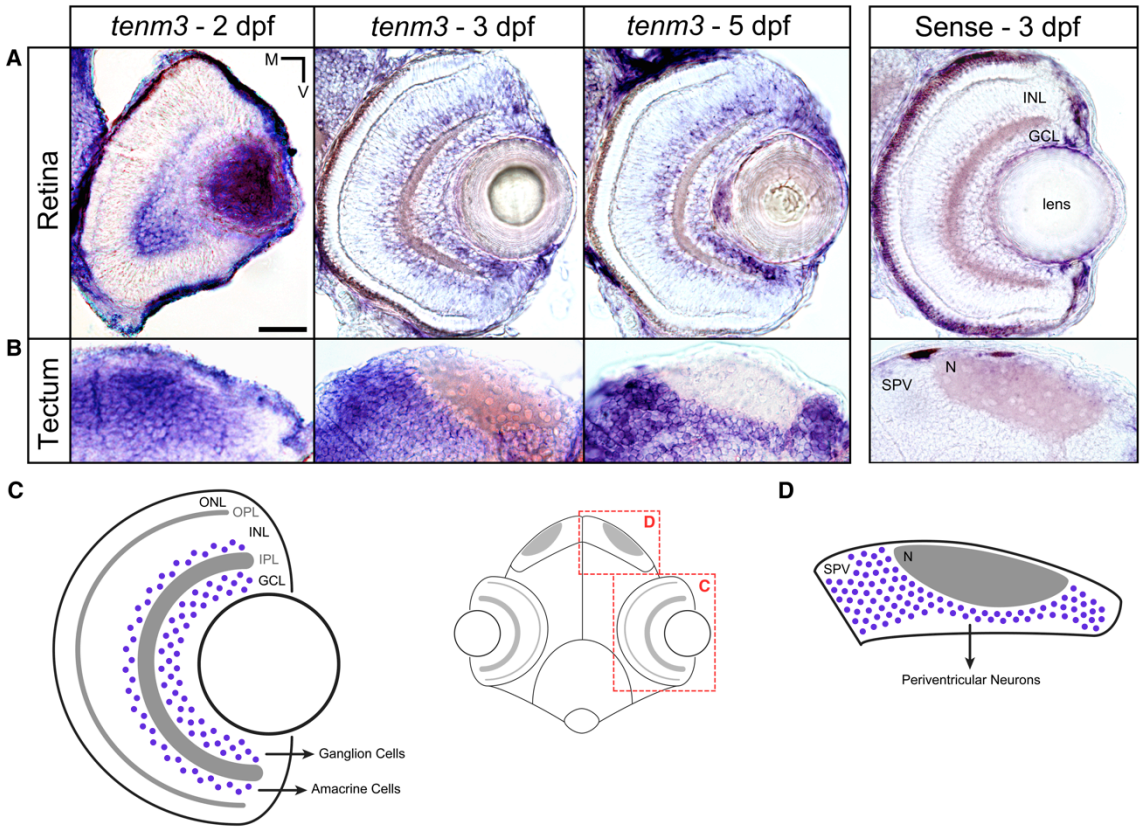

Figure 4.1. *Tenm3* is expressed in interconnected regions of the zebrafish visual system. A, Retinal cryosections showing *tenm3* mRNA expression in the lower third of the inner nuclear layer (INL) and ganglion cell layer (GCL) of right retina at 2, 3 and 5 dpf. Scale bar is 40 µm. **B,** Tectal cryosections showing *tenm3* mRNA expression in the stratum periventriculare (SPV) of right tectal hemisphere at 2, 3 and 5 dpf. N, neuropil; M, medial; V, ventral. In both (**A**) and (**B**), control *in situ* hybridizations using the sense *tenm3* riboprobe are shown on the right. All images are in transverse plane. **C,** Schematic showing the expression pattern of *tenm3* in the retina. *Tenm3*-positive cells are represented as blue circles. Neuropil layers are indicated in grey. Anatomical reference is reported on the right. IPL, inner plexiform layer; ONL, outer nuclear layer; OPL, outer plexiform layer. **D,** Schematic showing the expression pattern of *tenm3* in the optic tectum.

attributed to RGCs. At 2 dpf, *tenm3* is expressed more strongly in the ventral part of the retina, but this gradient disappears at subsequent stages (Fig. 4.1A). At 3 and 5 dpf, *tenm3* acquires a sparse expression pattern, suggesting that at these stages of development only a subset of cells are *tenm3*-positive. *Tenm3* is also expressed in the optic tectum, which is the main RGC target region (Fig. 4.1B). At 2 dpf, *tenm3* is highly expressed in the medial portion of the stratum periventriculare (SPV), where cell bodies of most tectal cells are located. Between 3 and 5 dpf, this medial-to-lateral gradient gradually decreases and, at 5 dpf, *tenm3* shows a salt-and-pepper expression pattern (Fig. 4.1B). No signal could be detected in the retina or the optic tectum when using a control *tenm3* sense riboprobe (Fig. 4.1A,B right). In summary, *tenm3* is expressed by RGCs, amacrine cells and tectal neurons, consistent with a possible role of *tenm3* in instructing connectivity along the visual pathway (Fig. 4.1C,D).

4.2.2 Neurite Stratification Pattern of Tenm3^{+} Amacrine Cells

To selectively visualise the morphology of *tenm3*-expressing retinal cells, a transgenic approach aimed to reproduce the endogenous expression pattern of *tenm3* was undertaken. Specifically, bacterial artificial chromosomes (BACs) containing different, partially overlapping regions of the zebrafish *tenm3* genomic locus (Fig. 4.2A) were used to generate BAC constructs in which Gal4FF is under transcriptional control of regulatory elements upstream and downstream of the *tenm3* start codon (Fig. 4.2B). All three *tenm3:Gal4* BAC constructs produced similar transient expression patterns. The BAC construct giving the highest intensity level of fluorescent labelling was selected to generate a *Tg(tenm3:Gal4)* transgenic line through the Tol2 system that was subsequently crossed with reporter/actuator transgenic lines (Fig. 4.3A,B). Importantly, the *Tg(tenm3:Gal4)* BAC line produces patterns of Gal4 expression in brain regions where *tenm3* is endogenously expressed, including the retina and optic tectum (Fig. 4.4). In the retina, the *Tg(tenm3:Gal4)* line labels a subset of ACs (hereafter referred to as *tenm3*$^{+}$ ACs), but fails to drive expression in RGCs (Fig. 4.3C,D), possibly due to a lack of RGC-specific regulatory elements in the BAC construct used for transgenesis. The *Tg(tenm3:Gal4;UAS:tagRFP-CAAX)* line was then used to selectively visualise the morphological development of *tenm3*$^{+}$ ACs from 2 to 5 dpf (Fig. 4.5A and Movie 4.1). During this developmental period, the IPL width occupied by *tenm3*$^{+}$ AC dendrites gradually increases up to 4 dpf, and then plateaus at 5 dpf (Fig. 4.5B; IPL thickness, mean ± SD, 2 dpf 7.10 ± 1.08 µm, 3 dpf 11.38 ± 0.60 µm,

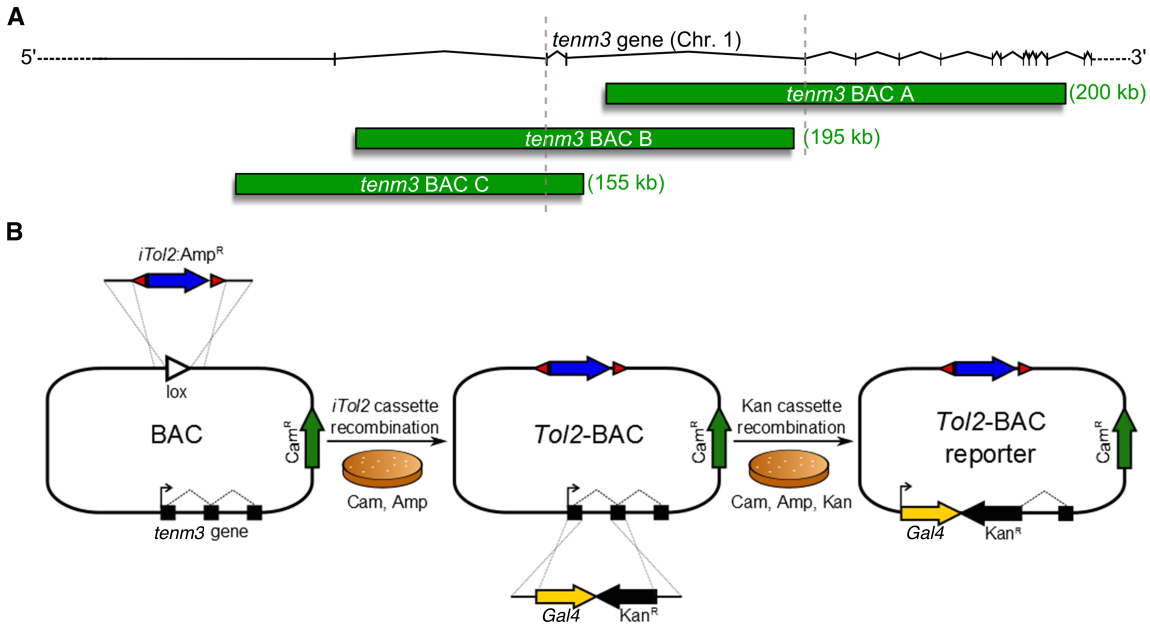

Figure 4.2. Generation of *tenm3:Gal4* BAC constructs through recombineering. A, Schematic representing the overlapping *tenm3* genomic locations covered by three different BAC clones (green) used to generate *tenm3:Gal4* constructs. Length in kilo-base pairs (kb) is reported in brackets. Exons are represented as black vertical lines, whereas introns are represented as segmented lines. The grey vertical dashed lines indicate start codons in the *tenm3* gene, which is contained in chromosome (Chr.) 1. **B,** Schematic illustrating the recombineering of the iTol2 cassette and *Gal4* driver gene into *tenm3* BAC clones. The iTol2-amp linear fragment with 50-bp overhangs matching sequences flanking a loxP site is introduced into a BAC clone containing a genomic fragment of the *tenm3* gene (left). After selection on chloramphenicol (Cam) + ampicillin (Amp) plates, bacteria containing the resulting Tol2-BAC plasmid are electroporated with a PCR product containing *Gal4* and *kanamycin* resistance (*Kan*^{R}) genes with 50-bp homologous sequences that match regions directly upstream and downstream of the *tenm3* start codon (black arrow, middle). After selection on chloramphenicol + ampicillin + kanamycin plates, colonies containing the *tenm3:Gal4* Tol2-BAC are obtained (right).

4 dpf 14.93 ± 1.09 µm, 5 dpf 15.25 ± 0.93 µm, n = 13 larvae). Interestingly, *tenm3*$^{+}$ ACs stratify their neurites in three precise IPL strata located at 5%, 61%, and 94% depth (0% corresponds to the INL/IPL border, 100% to the IPL/GCL border), which were named S5, S61 and S94, respectively (Fig. 4.5C). This tri-laminar IPL stratification pattern starts becoming visible at 3 dpf and progressively refines over the following two developmental days (Fig. 4.5D; strata relative IPL position at 5 dpf, mean ± SD, S5 4.78 ± 2.44%, S61 60.83 ± 3.14%, S94 93.85 ± 1.87%, n = 13 larvae). Overall, by selectively labelling ACs expressing *tenm3,* the *Tg(tenm3:Gal4)* BAC line provides a genetic tool to characterise in detail the morphological and functional features of *tenm3*$^{+}$ ACs.

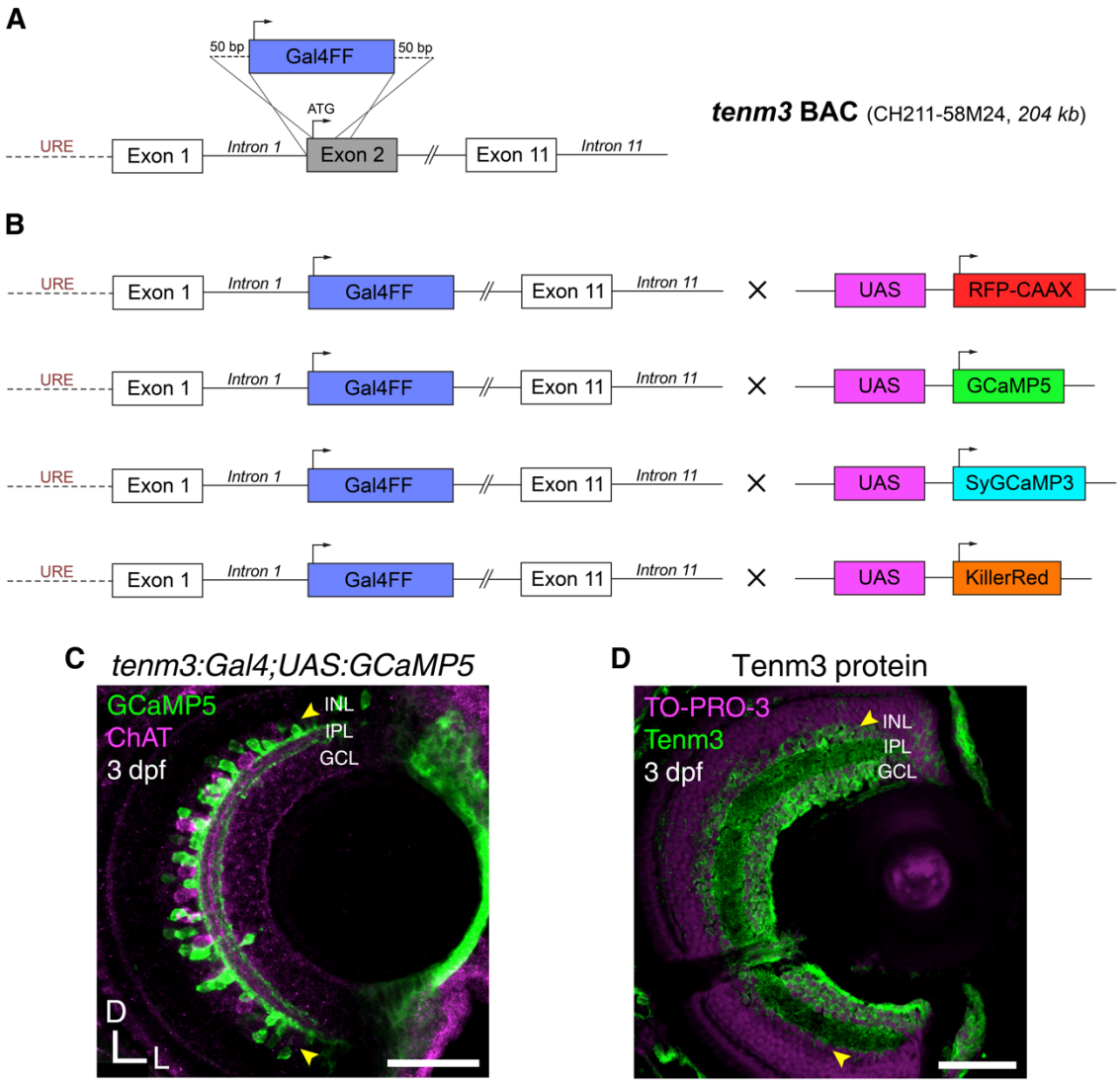

Figure 4.3. *Tg(tenm3:Gal4)* BAC transgenic lines and labelling in the retina. A, Schematic representing the *tenm3:Gal4FF* BAC construct (*tenm3* BAC A in Fig. 4.2A) used to generate a zebrafish transgenic line labelling *tenm3*-expressing cells. BAC clone code and length are reported in brackets. Start codons (ATG) are indicated by black arrows. Exons are represented as boxes, introns as lines. Note that the selected BAC clone contains the *tenm3* gene up to intron 11. URE, upstream regulatory elements. **B,** Crosses between the *Tg(tenm3:Gal4*) driver line and four different reporter lines: *Tg(UAS:tagRFP-CAAX)* in red, *Tg(UAS:GCaMP5)* in green, *Tg(SyGCaMP3)* in cyan, and *Tg(UAS:KillerRed)* in orange. **C,** Immunostaining showing *tenm3* BAC transgenic labelling of a subset of amacrine cells in a 3 dpf *Tg(tenm3:Gal4;UAS:GCaMP5G)* larva. GCaMP5 expression is showed in green, whereas choline acetyltransferase (ChAT) expression is showed in magenta as a reference. Yellow arrowheads indicate *tenm3*$^{+}$ amacrine cells in the inner portion of the inner nuclear layer (INL). GCL, ganglion cell layer; IPL, inner plexiform layer. D, dorsal; L, lateral. Scale bar is 40 µm. **D,** Immunostaining showing the expression of Tenm3 protein (green) in the retina of a 3 dpf WT larva. Cell bodies are labelled with the nuclear stain TO-PRO-3 (magenta). Yellow arrowheads indicate Tenm3^{+} amacrine cells in the inner portion of the INL. Scale bar is 40 µm.

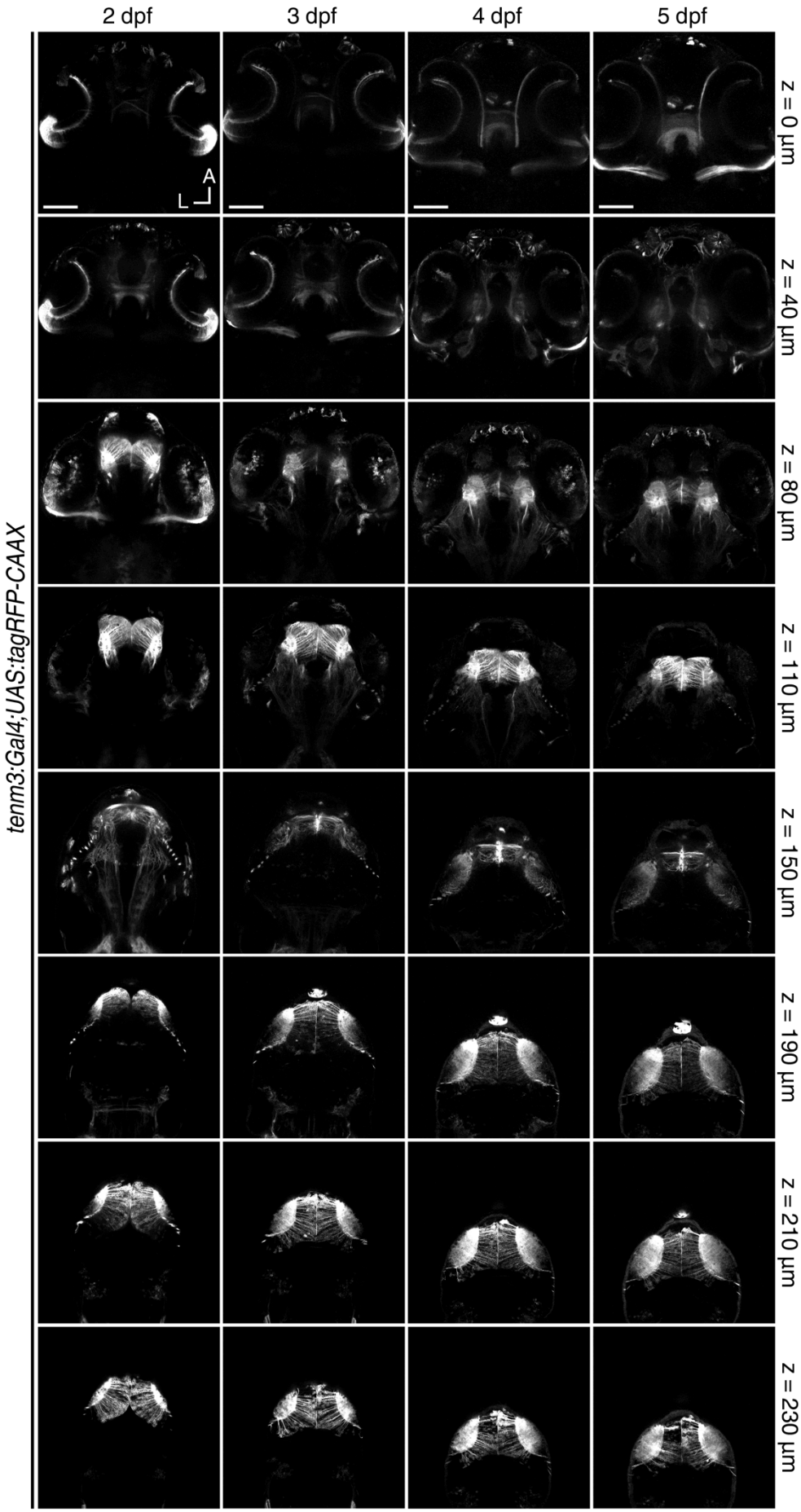
2 dpf
3 dpf
4 dpf
5 dpf
tenm3:Gal4;UAS:tagRFP-CAAX
z = 0 µm
z = 40 µm
z = 80 µm
z = 110 µm
z = 150 µm
z = 190 µm
z = 210 µm
z = 230 µm
A
L

Figure 4.4. *Tg(tenm3:Gal4;UAS:tagRFP-CAAX)* BAC transgenic labelling in the brain. Overview of the brain regions labelled by the *Tg(tenm3:Gal4;UAS:tagRFP-CAAX)* BAC transgenic zebrafish line from 2 to 5 dpf. Eight Z-planes are displayed per developmental stage (approximately 230 µm total volume thickness). The most ventral regions (z = 0 µm) are displayed at the top, whereas the most dorsal ones (z = 230 µm) are at the bottom. Note that tagRFP-CAAX is expressed in the retina (0-80 µm Z-axis depth), thalamus (80-150 µm Z-axis depth), and optic tectum (150-230 µm Z-axis depth), which are brain regions where *tenm3* is highly expressed. A, anterior; L, left. Scale bars are 100 µm.

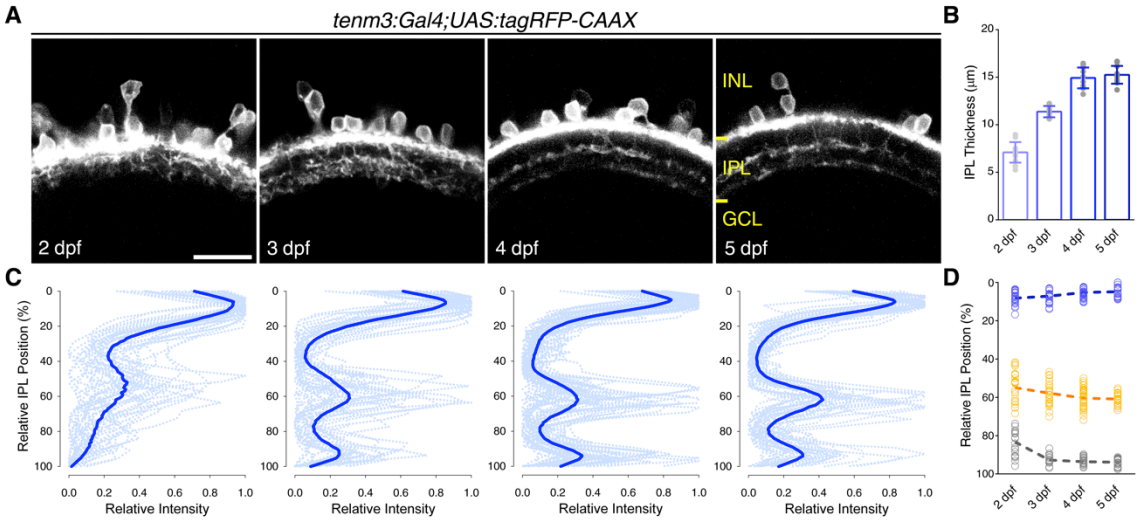

Figure 4.5. Neurite stratification of *tenm3*$^+$ amacrine cells in the IPL during development. A, Inner plexiform layer (IPL) stratification pattern of *tenm3*$^+$ AC neurites in *Tg(tenm3:Gal4;UAS:tagRFP-CAAX)* larvae from 2 to 5 dpf. INL, inner nuclear layer; GCL, ganglion cell layer. Scale bar is 20 µm. **B,** IPL thickness from 2 to 5 dpf (mean ± SD, n = 13 larvae). **C,** IPL fluorescence intensity profiles of *tenm3*$^+$ AC neurites from 2 to 5 dpf (n = 13 larvae). Thin traces represent individual IPL profiles, whereas thick traces indicate average IPL profiles. 0% corresponds to the INL/IPL boundary, whereas 100% corresponds to the IPL/GCL boundary. **D,** Fluorescence peak relative IPL positions of the strata formed by *tenm3*$^+$ AC neurites from 2 to 5 dpf.

4.2.3 Neurotransmitter Identity of Tenm3$^+$ *ACs*

To characterise the neurotransmitter identity of *tenm3*$^+$ ACs, immunohistochemical co-labelling of these ACs together with markers for the major AC classes was carried out. These analyses showed that most *tenm3*$^+$ ACs are γ-aminobutyric acid (GABA)-positive and express the calcium-binding protein Parvalbumin (Fig. 4.6A,B,F; frequency of GABA$^+$ cells in *tenm3*$^+$ ACs, 54.2 ± 4.2%, mean ± SD, n = 13 retinae; frequency of Parvalbumin$^+$ cells in *tenm3*$^+$ ACs, 52.7 ± 3.0%, mean ± SD, n = 10 retinae). *Tenm3*$^+$ ACs also comprise dopaminergic ACs, which constitute a very small fraction of the whole AC population in zebrafish (Fig. 4.6C; frequency of tyrosine hydroxylase$^+$ cells in *tenm3*$^+$ ACs, 3.5 ± 1.1%, mean ± SD, n = 9 retinae) (Xi et al., 2011). Negligible or no co-localisation was observed between *tenm3*$^+$ ACs and cholinergic or glycinergic ACs, respectively (Fig. 4.6D,E; frequency of choline acetyltransferase$^+$ cells in *tenm3*$^+$ ACs, 1.2 ± 1.6%, mean ± SD, n = 10 retinae; frequency of glycine$^+$ cells in *tenm3*$^+$ ACs,

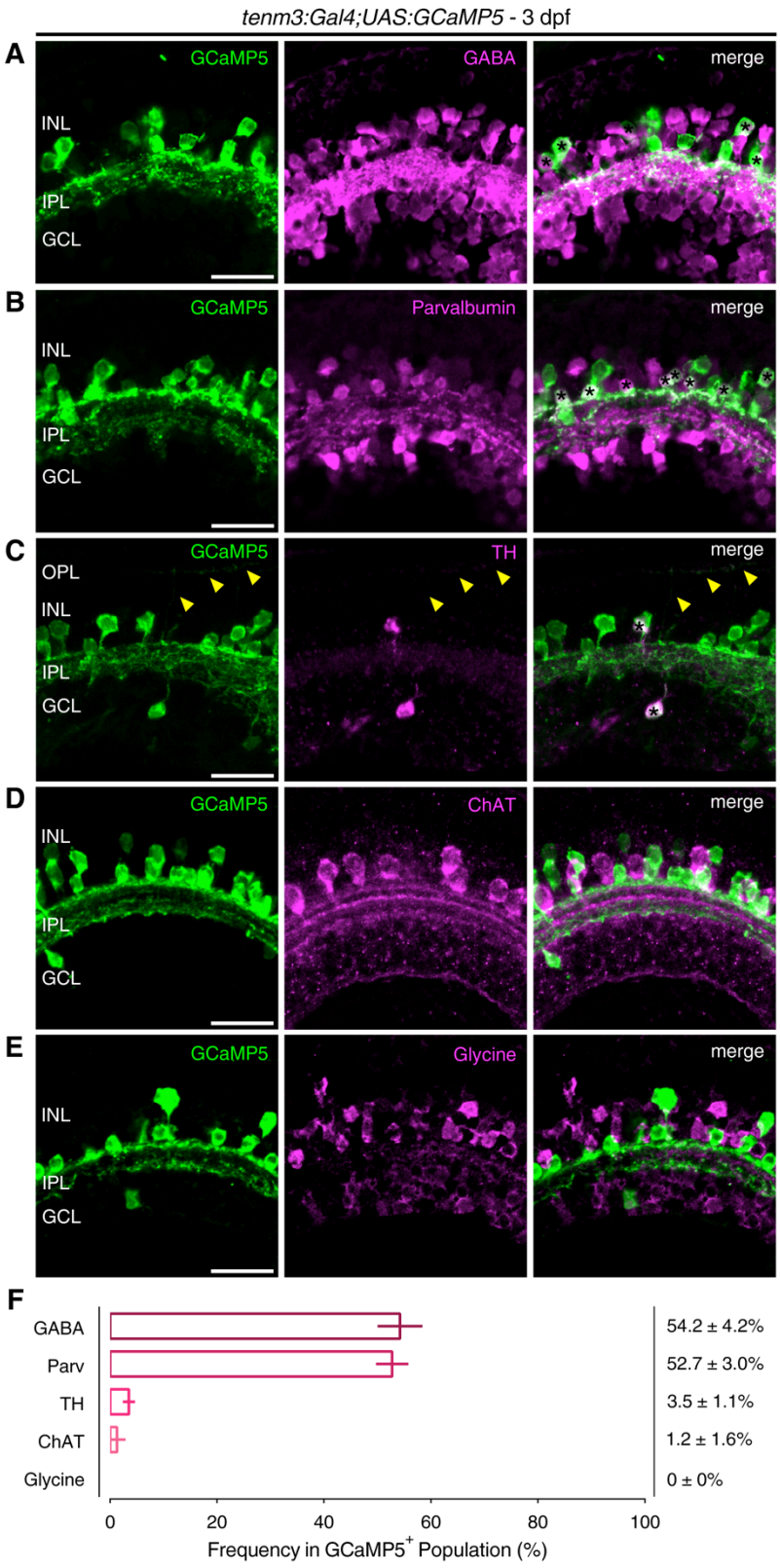

Figure 4.6. Most *tenm3*$^{+}$ amacrine cells express the neurotransmitter GABA. A-E, Immunostaining showing the expression of γ-aminobutyric acid (GABA; **A**), parvalbumin (**B**), tyrosine hydroxylase (TH; **C**), choline acetyltransferase (ChAT; **D**) and glycine (**E**) (all in magenta) in 3 dpf *Tg(tenm3:Gal4; UAS:GCaMP5)* larvae, where *tenm3*$^{+}$ ACs are labelled with GCaMP5 (green). Yellow arrowheads indicate neurites of TH^{+} interplexiform ACs (**C**). INL, inner nuclear layer; GCL, ganglion cell layer; OPL, outer plexiform layer; IPL, inner plexiform layer. Scale bars are 20 µm. **F,** Percentage of GCaMP5^{+} cells co-localising with antigen^{+} cells (mean ± SD). GABA, n = 13 retinae; Parvalbumin, n = 10 retinae; TH, n = 9 retinae; ChAT, n = 10 retinae; Glycine, n = 5 retinae.

0 ± 0%, mean ± SD, n = 5 retinae). In mammals, the only cholinergic ACs are the SACs, which generate RGC direction selectivity in most direction-selective circuits (see 1.2.1). Given the extremely low level of co-labelling between *tenm3*$^+$ ACs and cholinergic ACs, *tenm3*$^+$ ACs likely do not include SACs. However, whether zebrafish possess cholinergic ACs that are morphologically and functionally homologous to mammalian SACs has yet to be determined.

4.2.4 Single Cell Morphologies of Tenm3$^+$ *AC Types*

To analyse the morphology of *tenm3*$^+$ ACs at the single cell level, *tenm3*$^+$ ACs were sparsely labelled by injecting *UAS:eGFP-CAAX* DNA constructs into 1-4 cell-stage *Tg(tenm3:Gal4)* embryos. Using this strategy, seven types of *tenm3*$^+$ ACs characterised by distinct morphological properties were identified (Fig. 4.7A-F; n = 125 cells from 65 larvae). These types differ in terms of their observed frequency (Fig. 4.7I), IPL dendritic stratification, dendritic field area (Fig. 4.7J) and, interestingly, dendritic field elongation, quantified by calculating the eccentricity of their dendritic fields (Fig. 4.7G,H). The most frequent *tenm3*$^+$ AC type (type I, 43% of *tenm3*$^+$ ACs, n = 53 cells) is a narrow-field AC (type I dendritic field area, 463 ± 124 µm^2, mean ± SD) with a dendritic arbour mono-stratified in S5 (Fig. 4.7A). Type II and III *tenm3*$^+$ ACs (19% and 16% of *tenm3*$^+$ ACs, n = 24 and 20 cells, respectively) are medium-field ACs (dendritic field area, mean ± SD, type II 1494 ± 442 µm^2; type II 1559 ± 450 µm^2) characterised by highly elongated dendritic fields (Fig. 4.7B,C,H; dendritic field eccentricity, mean ± SD, type I 0.374 ± 0.100; type II 0.897 ± 0.042; type III 0.889 ± 0.053; type IV ON 0.3827 ± 0.104; type IV OFF 0.404 ± 0.118; $F_{4,91} = 209.5$, $p < 0.0001$, one-way ANOVA with post-hoc Tukey's HSD test). Their dendritic arbours stratify differently in the IPL with type II *tenm3*$^+$ ACs having mono-stratified neurites in S5, and type III *tenm3*$^+$ ACs showing a bi-stratified dendritic arbour in S5 and S61. Type IV-ON and IV-OFF *tenm3*$^+$ ACs (each 8% of *tenm3*$^+$ ACs, n = 10 cells for both types) are mono-stratified medium-field ACs (dendritic field area, mean ± SD, type IV ON 2767 ± 820 µm^2; type IV OFF 2441 ± 652 µm^2) characterised by circular dendritic fields of similar area but different IPL stratification pattern, with the ON type stratifying in the innermost stratum (S94) and the OFF type in the outermost stratum (S5; Fig. 4.7D,E). Lastly, type V and VI *tenm3*$^+$ ACs are the least frequent *tenm3*$^+$ AC types (each 3% of *tenm3*$^+$ ACs, n = 4 cells for both types) and possess wide-field dendritic arbours. Type V has extensive, radially arranged neurites covering most of the retina (Fig. 4.7F). Type VI corresponds

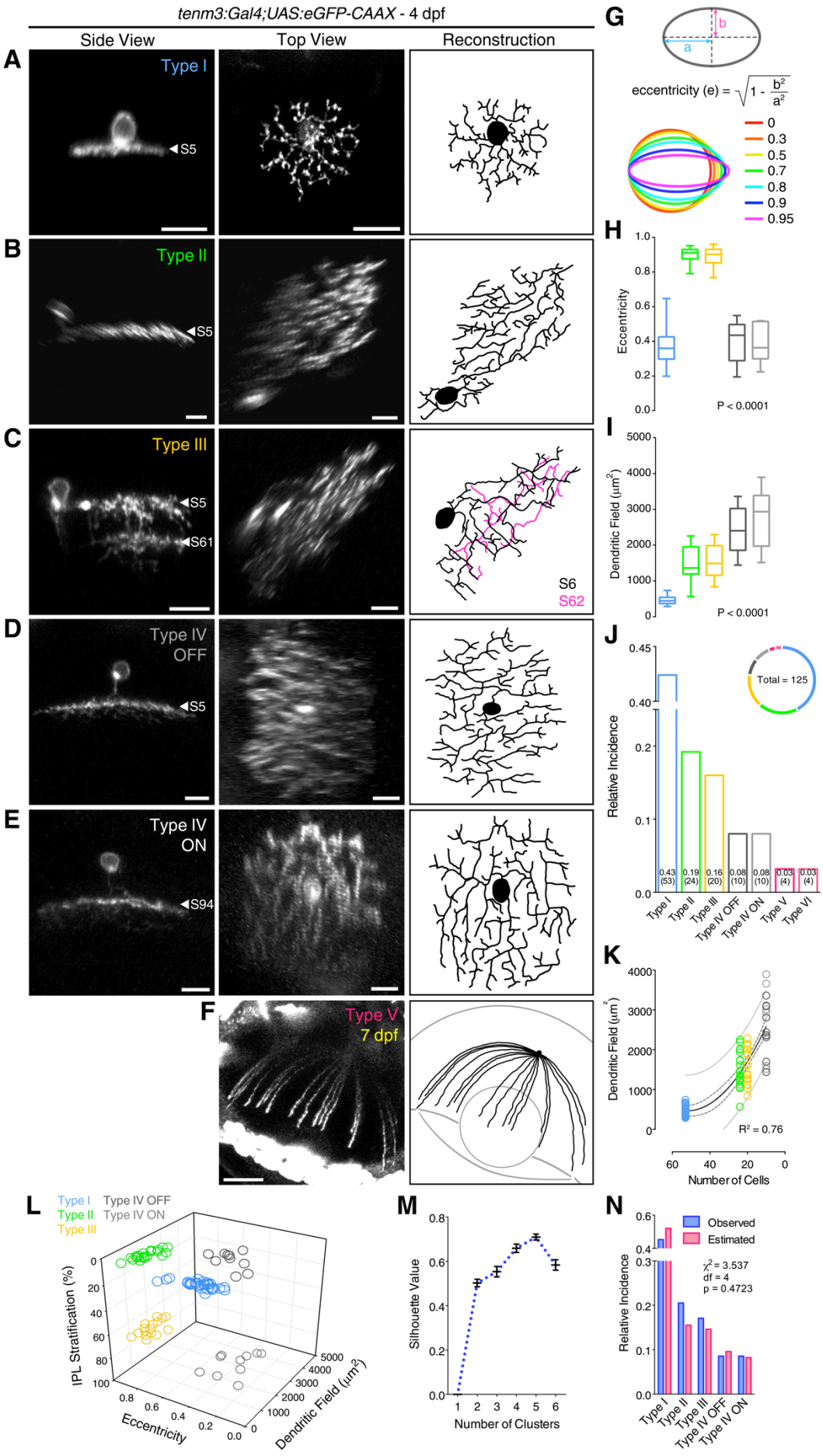
tenm3:Gal4;UAS:eGFP-CAAX - 4 dpf
Side View
Top View
Reconstruction
A
Type I
S5
B
Type II
S5
C
Type III
S5
S61
S6
S62
D
Type IV OFF
S5
E
Type IV ON
S94
F
Type V
7 dpf
G
a
b
eccentricity (e) = √(1 - b²/a²)
0
0.3
0.5
0.7
0.8
0.9
0.95
H
Eccentricity
P < 0.0001
I
Dendritic Field (µm²)
P < 0.0001
J
Relative Incidence
Total = 125
0.43 (53)
0.19 (24)
0.16 (20)
0.08 (10)
0.08 (10)
0.03 (4)
0.03 (4)
Type I
Type II
Type III
Type IV OFF
Type IV ON
Type V
Type VI
K
Dendritic Field (µm²)
R² = 0.76
Number of Cells
L
Type I
Type II
Type III
Type IV OFF
Type IV ON
IPL Stratification (%)
Eccentricity
Dendritic Field (µm²)
M
Silhouette Value
Number of Clusters
N
Observed
Estimated
χ² = 3.537
df = 4
p = 0.4723
Relative Incidence
Type I
Type II
Type III
Type IV OFF
Type IV ON

Figure 4.7. Morphological diversity of *tenm3*$^+$ amacrine cell types. A-F, Morphologies of single *tenm3*$^+$ ACs expressing eGFP-CAAX in 4 dpf *UAS:eGFP-CAAX*-injected *Tg(tenm3:Gal4)* larvae. The side views (left), top views (middle) and top view 3D reconstructions (right) are shown. IPL strata location of *tenm3*$^+$ AC neurites is indicated by the letter 'S' followed by the relative IPL position. The 3D reconstructed neurites of the bi-stratified type III *tenm3*$^+$ AC are color-coded according to the stratum they are located. Note that the type V *tenm3*$^+$ AC shown in (**F**) is from a 7 dpf larva. Scale bars are 10 µm in (**A-E**) and 40 µm in (**F**). **G,** Diagram illustrating the quantification of dendritic field elongation by calculating the eccentricity of dendritic arbour profiles following ellipse fitting. 'a' is the length of the semi-major axis and 'b' is the length of the semi-minor axis. **H-J,** Dendritic field elongation (i.e., eccentricity; **H**), dendritic field area (**I**), and relative frequency (**J**) of identified *tenm3*$^+$ AC types (n = 125 cells from 65 larvae). The number of observed cells for each *tenm3*$^+$ AC type is reported in brackets (**J**). Box plots indicate interquartile ranges (boxes), medians (lines in boxes) and ranges (min-max, whiskers). P values are the results of one-way ANOVA. **K,** Relationship between dendritic field area of type I-IV *tenm3*$^+$ ACs and their observed frequency (in number of cells). The continuous curve shows the nonlinear regression of the data with a second order polynomial function indicating a quadratic relationship between the two variables. Thick and thin dashed curves report the 95% confidence and prediction bands of the nonlinear fit, respectively. Goodness of fit value (R^2) is reported at the bottom right corner. **L**I**M,** k-means clustering of type I-IV *tenm3*$^+$ ACs based on their IPL stratification, dendritic field area and dendritic field elongation. Individual cell data points are colour-coded according to which *tenm3*$^+$ AC type they have been classified (**L**). Analysis of mean silhouette values for increasing number of clusters indicates that 5 clusters best describe the dataset (**M**). Importantly, the 5 cell clusters obtained by k-means are consistent with the classification of the most frequent *tenm3*$^+$ ACs into 5 different types. Error bars are ± SEM. **N,** Observed (blue) and estimated (red; assuming a retinal coverage factor of 1) relative frequencies of type I-IV *tenm3*$^+$ ACs. Results of the two-tailed chi-square test are reported.

to the dopaminergic interplexiform AC previously described in goldfish (Fig. 4.6C) (Dowling and Ehinger, 1978). Importantly, k-means clustering based on IPL stratification, dendritic field area and dendritic field elongation support the notion that the different *tenm3*$^+$ ACs identified here are indeed defined AC types (Fig. 4.7L,M; type V and VI ACs were not included in the clustering). Moreover, several lines of evidence suggest that type I-IV *tenm3*$^+$ ACs are arranged in mosaics tiling the retina with a coverage factor close to 1: (a) their frequency scales quadratically as a function of their dendritic field area (Fig. 4.7K; nonlinear regression of a second order polynomial – 'quadratic' function, $y = b_0 + b_1X + b_2X^2$, $b_2 = 1.191$, $R^2 = 0.76$). (b) Their observed frequency does not differ significantly from the frequency estimated assuming a retinal coverage factor of 1 (Fig. 4.7N; estimated frequency in number of cells, type I 60.90; type II 18.17; type III 17.09; type IV OFF 9.61; type IV ON 11.22; $\chi^2 = 3.537$, df = 4, p = 0.4723, two-tailed chi-square test). Taken together, these data indicate that *tenm3*$^+$ ACs are a heterogeneous cell population comprising defined AC types with specific morphological features and neurotransmitter identity.

4.3 Discussion

How retinal circuits wire up during development is still largely unknown. Among the cell-adhesion molecules known to be involved in the development of neural circuits, the teneurins represent intriguing candidates. Recent studies in *Drosophila* showed that teneurins control the synaptic matching between defined subsets of neurons (Hong et

al., 2012; Mosca et al., 2012). However, a similar role in the wiring of the vertebrate retina has not yet been demonstrated. As a first step in investigating a potential role of *tenm3* in retinal circuit assembly, the expression pattern of *tenm3* in the larval zebrafish visual system has been characterised. *In situ* hybridization analyses and BAC transgenic labelling show that *tenm3* is expressed early in the developing visual system. In particular, RGCs as well as their pre- and postsynaptic cellular targets (i.e., amacrine cells and tectal neurons, respectively) express *tenm3*, suggesting a potential role in synaptic matching through homophilic interactions between neuronal partners along the visual pathway. Interestingly, BAC labelling indicates that, at least in amacrine cells, *tenm3* is expressed by morphologically and physiologically defined cell types. Previous studies in mice showed that *teneurin-3* regulates the development of topography in the retinogeniculate (Leamey et al., 2007) and retinocollicular pathways (Dharmaratne et al., 2012), specifically for the ipsilaterally projecting RGC population. However, the fact that *tenm3* is not exclusively expressed in ipsilaterally projecting RGCs (Leamey et al., 2007) and is also found in the visual system of species where RGCs project contralaterally only, like chick (Kenzelmann-Broz et al., 2010) and zebrafish (this study) (Mieda et al., 1999), clearly suggests that *tenm3* may have alternative functions in vertebrate visual system development.

Chapter 5

Role of Teneurin-3 in Visual Circuit Assembly

5.1 Introduction

The wiring of visual circuits during development requires the coordinated action of different molecular cues selectively expressed in defined subsets of neurons. In the vertebrate retina (Fig. 5.1A), some of these molecules and their roles have been identified (see 1.3.1), but we are still far from a complete understanding of the players and mechanisms instructing cell-type-specific circuit assembly. In this regard, the recognition molecule Teneurin-3 (Tenm3) is expressed in subsets of zebrafish RGCs and ACs (Fig. 5.1B) as well as tectal neurons during a period of intense synaptic formation (see 4.2.1), and therefore constitutes a potential player in retinal circuit wiring. Here, loss-of-function approaches disrupting the transmembrane localisation and architecture of Tenm3 are used to assess its possible requirement for the normal development of retinal circuit structure and function (Fig. 5.1C). Notably, *tenm3* knockdown was found to induce stratification and targeting errors in both RGC dendrites and axons. Interestingly, these errors appear to be limited to a subset of RGCs. In addition, orientation- but not direction-selective RGC responses are severely

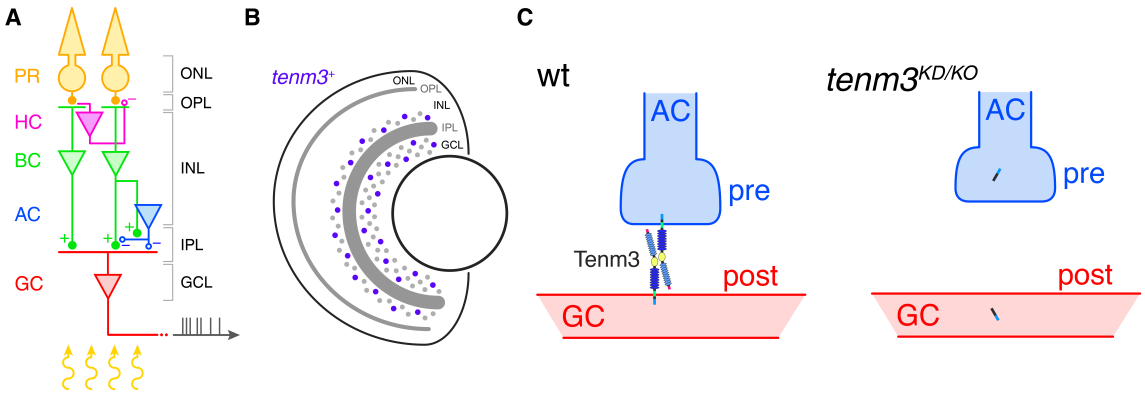

Figure 5.1. Tenm3 expression and potential role in retinal circuit wiring. A, Basic neural circuit structure of the vertebrate retina. Cell classes are represented in colours, whereas layers are shown in black. Excitatory synapses are indicated by '+' (filled circles), inhibitory synapses are labelled with '–' (empty circles). PR, photoreceptor; HC, horizontal cell; BC, bipolar cell; AC, amacrine cell; RGC, retinal ganglion cell; ONL, outer nuclear layer; INL, inner nuclear layer; GCL, ganglion cell layer; OPL, outer plexiform layer; IPL, inner plexiform layer. **B,** Schematic showing *tenm3* mRNA expression in the retina of zebrafish larvae. Blue circles indicate *tenm3*$^{+}$ ACs and RGCs. **C,** Schematic diagram of the potential role Tenm3 could play during development. Trans-synaptic homophilic interactions could mediate the synaptic matching between defined presynaptic (pre, blue) amacrine cell (AC) types and postsynaptic (post, red) ganglion cell (GC) types (left). Tenm3 loss-of-function (through gene knockdown, KD, or knockout, KO) would cause an incorrect wiring of these AC and GC types (right).

impaired in *tenm3* morphants and mutants, thus supporting the idea that *tenm3* is involved in the wiring of functionally defined visual circuits. Lastly, *tenm3* knockout also affects *tenm3*-expressing amacrine cells, which not only fail to correctly stratify their neurites in the IPL but also exhibit abnormal planar morphologies.

5.2 Results

5.2.1 Knockdown of Tenm3 through Morpholino Oligonucleotides

To start investigating the function of Tenm3 in retinal circuit development, antisense morpholino oligonucleotides (MOs) were used to knock down *tenm3* expression levels. A splice-blocking MO (Draper et al., 2001) was designed to target the boundary between intron 2 and exon 3 of *tenm3* pre-mRNA (hereafter referred to as *tenm3* MO; Fig. 5.2A top). Reverse transcription polymerase chain reaction (RT-PCR) followed by cDNA sequencing revealed that the injection of *tenm3* MO into one-cell stage zebrafish embryos leads to the deletion of exon 3 (which encodes part of the intracellular domain) from *tenm3* mRNA (Fig. 5.2A bottom). This causes a frameshift in exon 4 (normally encoding the transmembrane domain) and a subsequent early stop codon in exon 5, resulting in the deletion of the transmembrane and extracellular domains (Fig. 5.2B). *Tenm3* morphants are viable and do not show any obvious morphological defect. However, 4 dpf *tenm3* MO-injected larvae fail to show a normal visually mediated background adaptation (VBA) and therefore appear darker compared to wild type (WT) and control MO-injected larvae (Fig. 5.2C). Since the VBA is a

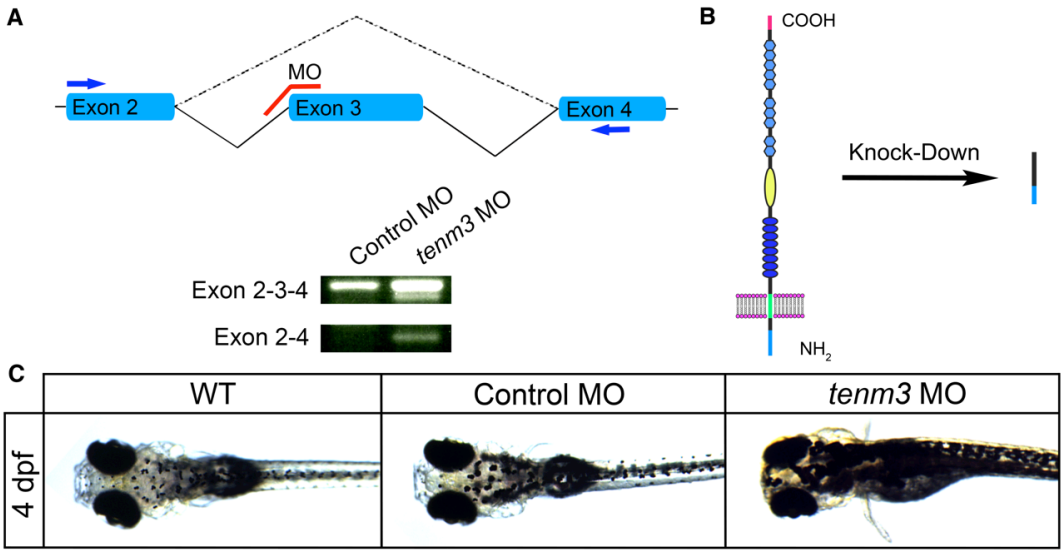

Figure 5.2. Knockdown of *tenm3* through splice-blocking morpholino oligonucleotides. A, Schematic detailing the targeting site of splice-blocking *tenm3* morpholino (MO), which is shown in red (top). Exons are represented in cyan. Solid lines indicate introns. The dashed line indicates exon 3 deletion caused by *tenm3* MO injections. Primers used for RT-PCR are reported as blue arrows. RT-PCR analysis of *tenm3* mRNA structure in control MO- and *tenm3* MO-injected embryos (bottom). Two shorter splice

variants are distinguished in *tenm3* morphants. cDNA sequence comparison revealed that the shortest splice variant lacks exon 3. **B,** Schematic detailing the effect resulting from exon 3 deletion caused by the splice-blocking *tenm3* MO. The full-length protein is represented on the left. The N-terminus is located intracellularly, whereas the C-terminus is in the extracellular space. **C,** At 4 dpf, *tenm3* morphant larvae fail to visually adapt their skin pigmentation to the level of background illumination.

neuroendocrine response dependent on RGC function (Neuhauss et al., 1999; Kay et al., 2001), this observation suggests that the knockdown of *tenm3* negatively impacts the normal development of the retina.

5.2.2 Tenm3 Regulates RGC Dendritic Stratification in the IPL

To examine RGC dendritic stratification in the IPL *in vivo*, the *Tg(Isl2b:Gal4;UAS:Kaede)* double transgenic zebrafish line, where the fluorescent protein Kaede is expressed in the vast majority of RGCs, was used. At 5 dpf, when RGC dendrites exhibit obvious stratification, four Kaede-positive strata are visible in the IPL of WT and control MO-injected larvae (Fig. 5.3A,B left). Fluorescence intensity measurements across the IPL of multiple larvae show that these strata are positioned at 5%, 33%, 66% and 95% depth of the IPL (with 0% corresponding to the INL/IPL border, and 100% to the IPL/GCL border), and thus were named S5, S33, S66 and S95, respectively (Fig. 5.3E; WT n = 7 larvae, control MO n = 7). The presence of four RGC dendritic strata in the IPL of 5 dpf zebrafish larvae is consistent with previous work using the *Tg(Brn3c:MGFP)* transgenic line, where approximately 50% of RGCs are labelled (Mumm et al., 2006). In 5 dpf *tenm3* morphants, by contrast, strata within the IPL are poorly defined (Fig. 5.3A,B right). The average fluorescence intensity profile reveals that only three Kaede-positive strata are present in the IPL of *tenm3* morphants at this stage (Fig. 5.3E; red line, n = 10 larvae). Particularly, only one irregularly laminated stratum is visible in the central portion of the IPL, instead of the two middle strata (S33 and S66) found in WT and control MO retinae. Also, the outermost stratum (S5) is not tightly stratified and appears thicker compared to S5 in control groups. No significant difference in IPL width was observed between the three groups (IPL width, mean ± SEM, WT 15.2 ± 0.2 µm, n = 7 larvae; control MO 15.0 ± 0.1 µm, n = 7; *tenm3* MO 15.1 ± 0.2 µm, n = 10; $F_{2,21}$ = 0.08, p = 0.92, one-way ANOVA with post-hoc Tukey's HSD test). In addition to these stratification abnormalities in the IPL, ectopic RGC processes in the INL of *tenm3* morphants were detected (Fig. 5.3B right; n = 19 out of 20 larvae), a phenomenon never observed in WT and control MO larvae where all RGC dendrites are confined within the IPL (Fig. 5.3B left; n = 10 larvae per group). Strikingly, in some cases these processes reach the outer plexiform layer (OPL;

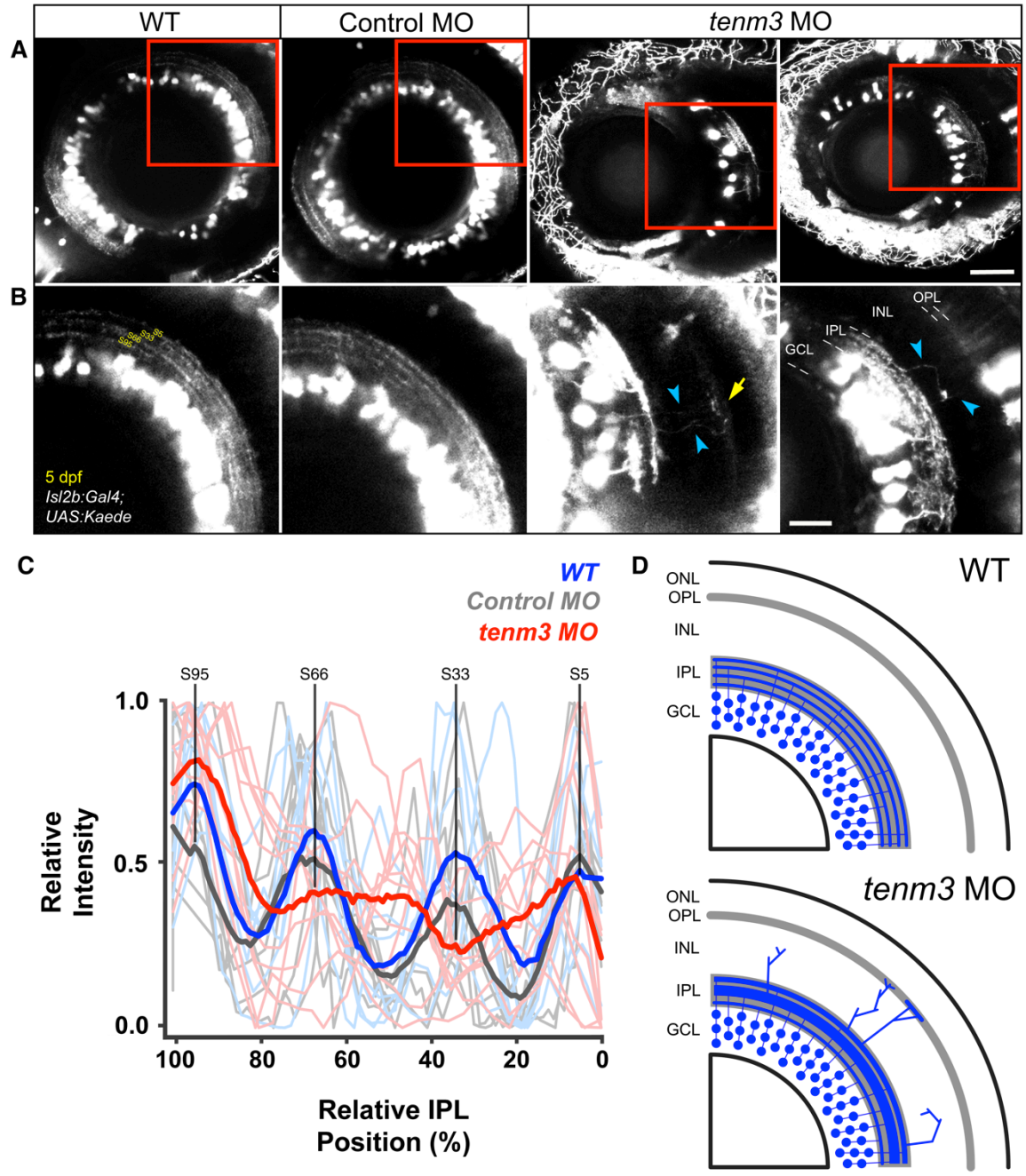

Figure 5.3. *Tenm3* is required for correct stratification of RGC dendrites. **A,** Kaede-expressing RGCs in the retinae of 5 dpf WT, control MO- and *tenm3* MO-injected Tg(*Isl2b:Gal4;UAS:Kaede*) larvae. Scale bar is 40 µm. **B,** Insets in (**A**) showing the dendritic stratification pattern of Kaede-positive RGCs. Aberrant projections are detected in *tenm3* MO-injected larvae (right; cyan arrowheads and yellow arrow) but not in control fish (left). All images represent maximum intensity projections of ~20 µm confocal Z stacks. Scale bar is 20 µm. GCL, ganglion cell layer; INL, inner nuclear layer; IPL, inner plexiform layer; OPL, outer plexiform layer. **C,** Fluorescence intensity profiles of dendritic IPL stratification in 5 dpf WT (blue), control MO- (grey) and *tenm3* MO-injected (red) larvae. Thin traces represent intensity profiles of IPLs of single larvae. Thick traces indicate average profiles (WT, n = 7 larvae; control MO, n = 7; *tenm3* MO, n = 10). 0% corresponds to the boundary between INL and IPL; 100% corresponds to the boundary between IPL and GCL. Four peaks positioned at 5%, 33%, 66% and 95% depth of the IPL are present in control groups. They correspond to S5, S33, S66, S95 Kaede-positive strata in (**B**), respectively. An aberrant stratification pattern is present in *tenm3* morphants (red line). **D,** Schematic summarizing the defects observed in the retinae of *tenm3* morphant larvae. RGCs are indicated in blue. Neuropil layers are in grey. ONL, outer nuclear layer.

Fig. 5.3B right, yellow arrow). Ectopic RGC processes extending into the INL were also seen in *tenm3* morphant retinae at 3 dpf, when RGCs start to stratify their dendritic arbours within the IPL (data not shown).

To resolve the changes in RGC dendritic morphology in greater detail, individual RGCs were mosaically labelled by co-injecting *Ath5:Gal4*, *UAS:GFP* and *UAS:tdTomato* DNA constructs into one-cell stage embryos. Using this approach it was possible to determine that the neurites mistargeting into outer layers of the retina observed in *tenm3* morphants originate from RGC dendrites (Fig. 5.4A) and that this phenotype is restricted to a subset of cells (n = 5 cells out of 98 in 49 larvae). This mistargeting phenotype resembles the morphology of the biplexiform RGC type observed by Robles et al. (2014) in the larval zebrafish retina at 6-7 dpf. However, in this study no RGC with biplexiform morphology was observed in WT or control MO-injected larvae at 5 dpf, and the frequency of the observed phenotype (5.1%) was higher than the very low frequency reported for biplexiform RGCs (0.6%) (Robles et al., 2014).

The mosaic labelling strategy also allowed to visualise the precise IPL dendritic stratification patterns of single RGCs (Fig. 5.4B). Interestingly, 5 dpf *tenm3* morphants show a significantly higher proportion of RGCs possessing diffuse dendritic arbours (*tenm3* MO 25 diffuse vs. 73 stratified cells in 49 larvae; WT 12 diffuse vs. 77 stratified cells in 34 larvae; control MO 12 diffuse vs. 80 stratified cells in 39 larvae; χ^2 = 6.596, df = 2, p = 0.037, two-tailed chi-square test). Looking at the relative proportions between monostratified, bistratified, multistratified and diffuse RGCs, it appears that the increase in number of RGCs with diffuse dendritic arbours is exclusively at the expense of monostratified RGCs (Fig. 5.4C; WT 55.1% monostratified, 24.7% bistratified, 6.7% multistratified, 13.5% diffuse; control MO 55.5% monostratified, 22.8% bistratified, 8.7% multistratified, 13% diffuse; *tenm3* MO 40.8% monostratified, 25.5% bistratified, 8.2% multistratified, 25.5% diffuse). Further identification and classification of the 11 morphological RGC types previously reported in the adult zebrafish retina (Mangrum et al., 2002) revealed that the monostratified RGC types are not indiscriminately affected by *tenm3* knockdown. In fact, some RGC monostratified types decrease in frequency in *tenm3* morphants whereas others show frequencies comparable to those found in control animals (Fig. 5.4D). Overall, these data show that *tenm3* knockdown causes structural abnormalities in the developing retina (Fig. 5.3D), and that changes in RGC dendritic stratification appear to be limited to subsets of RGC types.

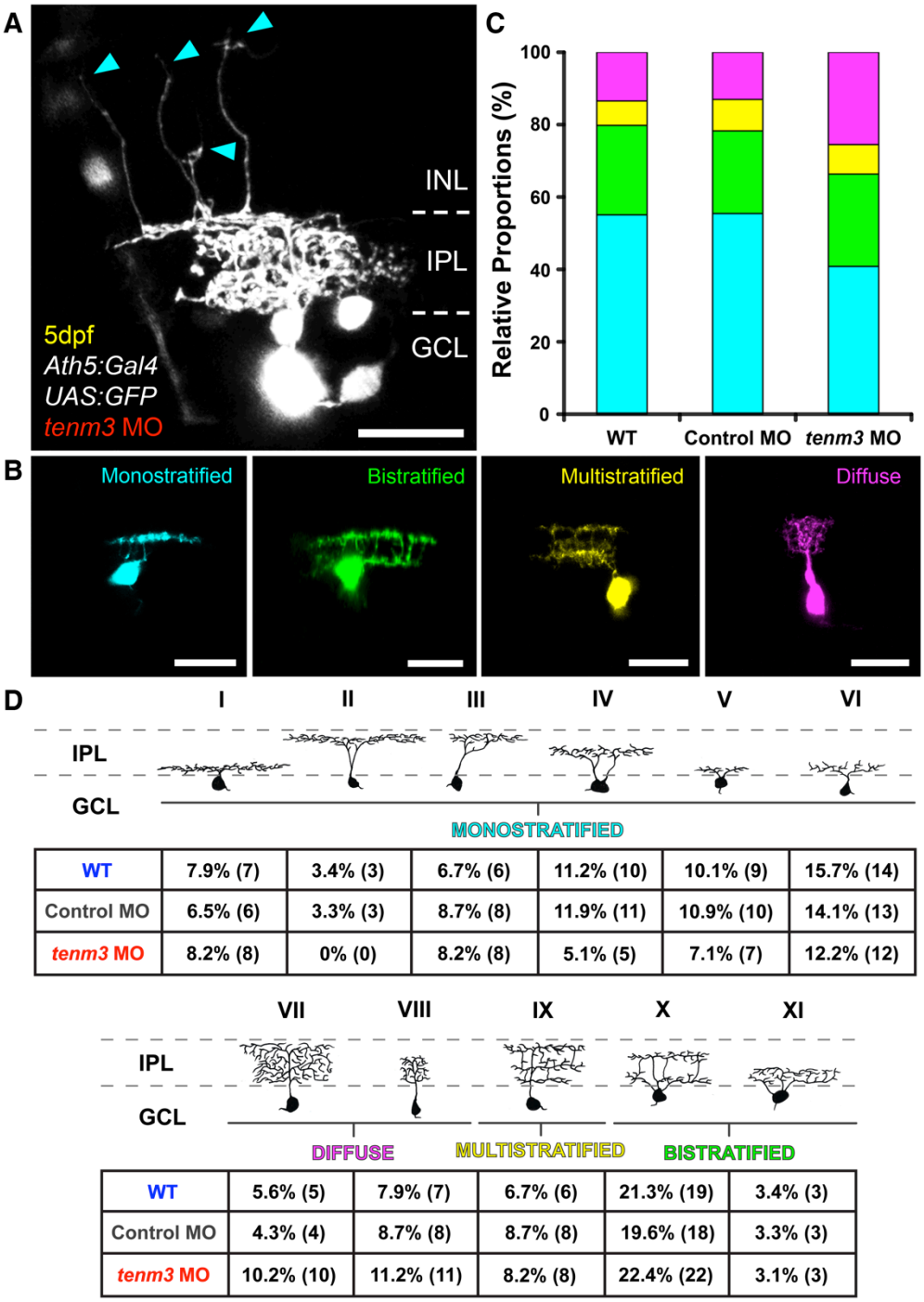

WT	7.9% (7)	3.4% (3)	6.7% (6)	11.2% (10)	10.1% (9)	15.7% (14)
Control MO	6.5% (6)	3.3% (3)	8.7% (8)	11.9% (11)	10.9% (10)	14.1% (13)
tenm3 MO	8.2% (8)	0% (0)	8.2% (8)	5.1% (5)	7.1% (7)	12.2% (12)

WT	5.6% (5)	7.9% (7)	6.7% (6)	21.3% (19)	3.4% (3)
Control MO	4.3% (4)	8.7% (8)	8.7% (8)	19.6% (18)	3.3% (3)
tenm3 MO	10.2% (10)	11.2% (11)	8.2% (8)	22.4% (22)	3.1% (3)

Figure 5.4. Higher proportion of RGCs with diffuse dendritic arbours in *tenm3* morphants. A, Lateral view of mosaically labeled RGCs in the retinae of a 5 dpf *tenm3* MO-injected larva. Ectopic RGC dendritic processes extending in outer layers of the retina are indicated by cyan arrowheads. GCL, ganglion cell layer; INL, inner nuclear layer; IPL, inner plexiform layer. Scale bar is 20 µm. **B,** Representative RGCs with monostratified (cyan), bistratified (green), multistratified (yellow) and diffuse (magenta) dendritic arbours. All images represent maximum intensity projections of ~30 µm confocal Z stacks that have been rotated to best show dendritic arborisations. Scale bars are 20 µm. **C,** Bar graph showing the proportions of 5 dpf RGCs possessing monostratified, bistratified, multistratified and diffuse dendritic arbours relative to the total number mosaically labeled RGCs within each animal group (WT n = 89 cells in 34 larvae; control MO n = 92 cells in 39 larvae; *tenm3* MO n = 98 cells in 49 larvae). Note the increase in the proportion of RGCs with diffuse dendritic arbours at the expense of monostratified RGCs in *tenm3* morphant larvae. **D,** Summary table showing the morphological classification and frequency of the 11 RGC types within each group (number of cells found per each type are reported in brackets). In *tenm3* morphants, 4 diffuse RGCs (4.1% of cells) showed dendritic arborisation patterns that could not be classified in any of the 11 types and, therefore, were not included in the table.

5.2.3 Laminar Targeting Errors in a Subset of RGC Axons Upon Tenm3 Knockdown

Next, RGC axonal arborisation in the tectal neuropil was examined. Similar to the IPL in the retina, this structure is characterised by a stereotypic lamination pattern (Xiao et al., 2011; Robles et al., 2013). Using the *Tg(Isl2b:Gal4;UAS:Kaede)* zebrafish line, it was possible to visualise the four main retinorecipient laminae of the optic tectum that, from the most superficial to the deepest, are named stratum opticum (SO), stratum fibrosum et griseum superficiale (SFGS), stratum griseum centrale (SGC) and lamina at the interface between the stratum album centrale and the stratum periventriculare (SAC/SPV; Fig. 5.5A) (Nevin et al., 2010). In 3 dpf WT and control MO larvae, all RGC axons are restricted to these four laminae and no RGC axon is found outside the neuropil region (Fig. 5.5A,B left; n = 15 larvae per group). In *tenm3* morphants, however, neurites projecting into the SPV were observed (Fig. 5.5A,B right, cyan arrowheads; n = 18 out of 23 larvae). 3D reconstructions and neurite tracing revealed that these processes arise principally from the deepest lamina (SAC/SPV) and, in some cases, are up to 30-40 µm long and possess several branches (Fig. 5.5B right, cyan arrowheads). In addition, tectal laminae of *tenm3* morphants are less precisely delimited and axons aberrantly cross lamina borders (Fig. 5.5A right, yellow arrow).

To examine in more detail how the lamination defects seen at the population level arise, individual RGCs were labelled through mosaic expression of either GFP or tdTomato driven by the *ath5* promoter (Fig. 5.5C). As a rule, individual RGC axons arborise in a planar fashion within a single tectal lamina or sublamina (the SO and SFGS are further subdivided into 2 and 6 sublaminae, respectively) (Robles et al., 2013). This behaviour was confirmed in 4 dpf control groups, where 100% of labelled axons (WT n = 102 axons in 50 larvae; control MO n = 94 axons in 45 larvae) showed planar arborisation patterns (Fig. 5.5C-E; RGC arbour thickness, mean ± SEM, WT 5.1 ± 0.1 µm; control MO 5.3 ± 0.1 µm; n = 20 axons per group). In contrast, RGCs with abnormally laminated axons were found in *tenm3* morphants (Fig. 5.5C right). Intriguingly, these axons represent only a fraction of the total number of labelled RGCs (Fig. 5.5D; 12.7%, n = 20 axons out of 157 in 80 larvae). They are characterised by axonal processes projecting towards adjacent laminae (Fig. 5.5C right, cyan arrowhead) and significantly broader cross-sectional profiles (RGC axonal arbour thickness, mean ± SEM, *tenm3* MO 16.9 ± 1.4 µm; n = 20 axons, $F_{2,57} = 57.97$, $p < 0.0001$, one-way ANOVA with post-hoc Tukey's HSD test) than those observed in

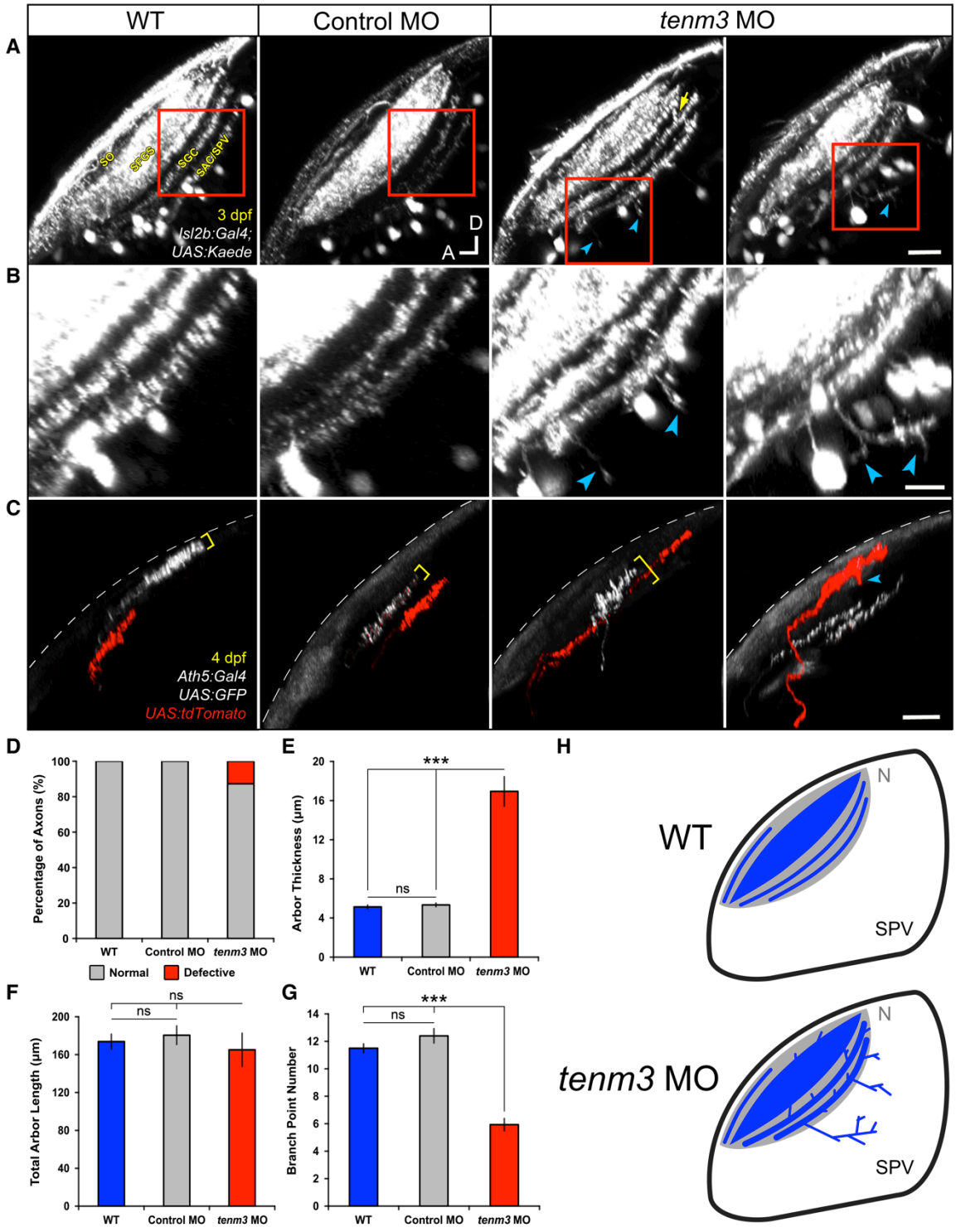

Figure 5.5. Laminar targeting errors in a subset of RGC axons in *tenm3* morphants. A, The four main retinorecipient laminae of the tectum are visible in 3 dpf Tg(*Isl2b:Gal4;UAS:Kaede*) larvae. A few tectal cells are also labeled in this line. SO, stratum opticum; SFGS, stratum fibrosum et griseum superficiale; SGC, stratum griseum centrale; SAC, stratum album centrale; SPV, stratum periventriculare. Scale bar is 20 µm. A, anterior; D, dorsal. **B,** Insets in (**A**) showing RGC axon lamination in deep laminae of the tectal neuropil. Aberrant projections are detected in *tenm3* MO-injected larvae (right; cyan arrowheads and yellow arrow) but not in control fish (left). Scale bar is 10 µm. **C,** Lateral view of mosaically labeled RGC axons at 4 dpf. GFP-positive axons are shown in white, whereas tdTomato-positive axons are shown in red. Dashed lines indicate the skin overlaying the tectum. All images represent maximum intensity projections of ~50 µm confocal Z stacks that have been rotated around the longitudinal axis to best show axonal lamination. Scale bar is 20 µm. **D,** Quantification of axon laminar targeting errors in mosaically labeled RGCs (WT n = 102 axons in 50 larvae; control MO n = 94 axons in 45 larvae; *tenm3* MO n = 157

axons in 80 larvae). **E-G,** Graphs showing average arbor thickness (**E**), total arbor length (**F**) and branching point number (**G**) of single RGC axons (n = 20 axons per group). All graphs show mean values ± SEM. ***p < 0.001; ns, not significant by one-way ANOVA followed by Tukey's HSD test. **H,** Schematic summarizing the defects observed in the optic tecta of *tenm3* morphant larvae. RGC axons are indicated in blue. Neuropil layers are in grey. N, neuropil.

control animals (Fig. 5.5E). The total arbour length of aberrant RGC axons is comparable to that of control groups (Fig. 5.5F; RGC axonal arbour length, mean ± SEM, *tenm3* MO 165.1 ± 17.4 µm; WT 173.8 ± 7.7 µm; control MO 180.5 ± 9.7 µm; n = 20 axons per group, $F_{2,57}$ = 0.33, p = 0.72, one-way ANOVA with post-hoc Tukey's HSD test) but their number of branch points is significantly lower (Fig. 5.5G; RGC axon branch points, mean ± SEM, *tenm3* MO 5.9 ± 0.4; WT 11.5 ± 0.3; control MO 12.4 ± 0.5; n = 20 axons per group, $F_{2,57}$ = 48.86, p < 0.0001, one-way ANOVA with post-hoc Tukey's HSD test), suggesting that knockdown of *tenm3* impairs their capacity to either make or stabilise new branches, without affecting overall arbour length. Taken together, these results indicate that *tenm3* is required for the correct laminar targeting and arborisation of a subset of RGC axons (Fig. 5.5H).

5.2.4 Tenm3 is Required for the Development of RGC Orientation Selectivity

To investigate the functional consequences in the retinal output following *tenm3* knockdown, direction- and orientation-selective responses of RGC axon terminals innervating the tectal neuropil were analysed. Light or dark drifting bars moving in 12 different directions were presented to one eye of 5 dpf *Tg(Isl2b:Gal4;UAS:SyGCaMP3)* double transgenic larvae while performing calcium imaging in the contralateral optic tectum (Fig. 5.6A) (Nikolaou et al., 2012). Since SyGCaMP3 is based on the fusion between the synaptic vesicle protein synaptophysin and the genetically encoded calcium indicator GCaMP3, this transgenic line enables the targeting of the probe specifically to RGC presynaptic terminals and hence the functional analysis of RGCs within the tectal target. RGCs of all three animal groups respond to drifting bars and exhibit complex patterns of stimulus responses (Fig. 5.6D and Movies 5.1-3). To characterise and map visual response properties (i.e., direction and orientation selectivity) present in the retinal output, an unbiased voxel-wise analysis strategy independent of cellular and neuropil morphology was used (Nikolaou et al., 2012; Lowe et al., 2013). Only visually responsive voxels were subjected to further characterisation. Direction and orientation selectivity indices (DSI and OSI) (Niell and Stryker, 2008) based on fitted von-Mises profiles (Swindale, 1998) were calculated together with an estimate for their goodness of fit – R^2. For a voxel to be regarded as direction-selective

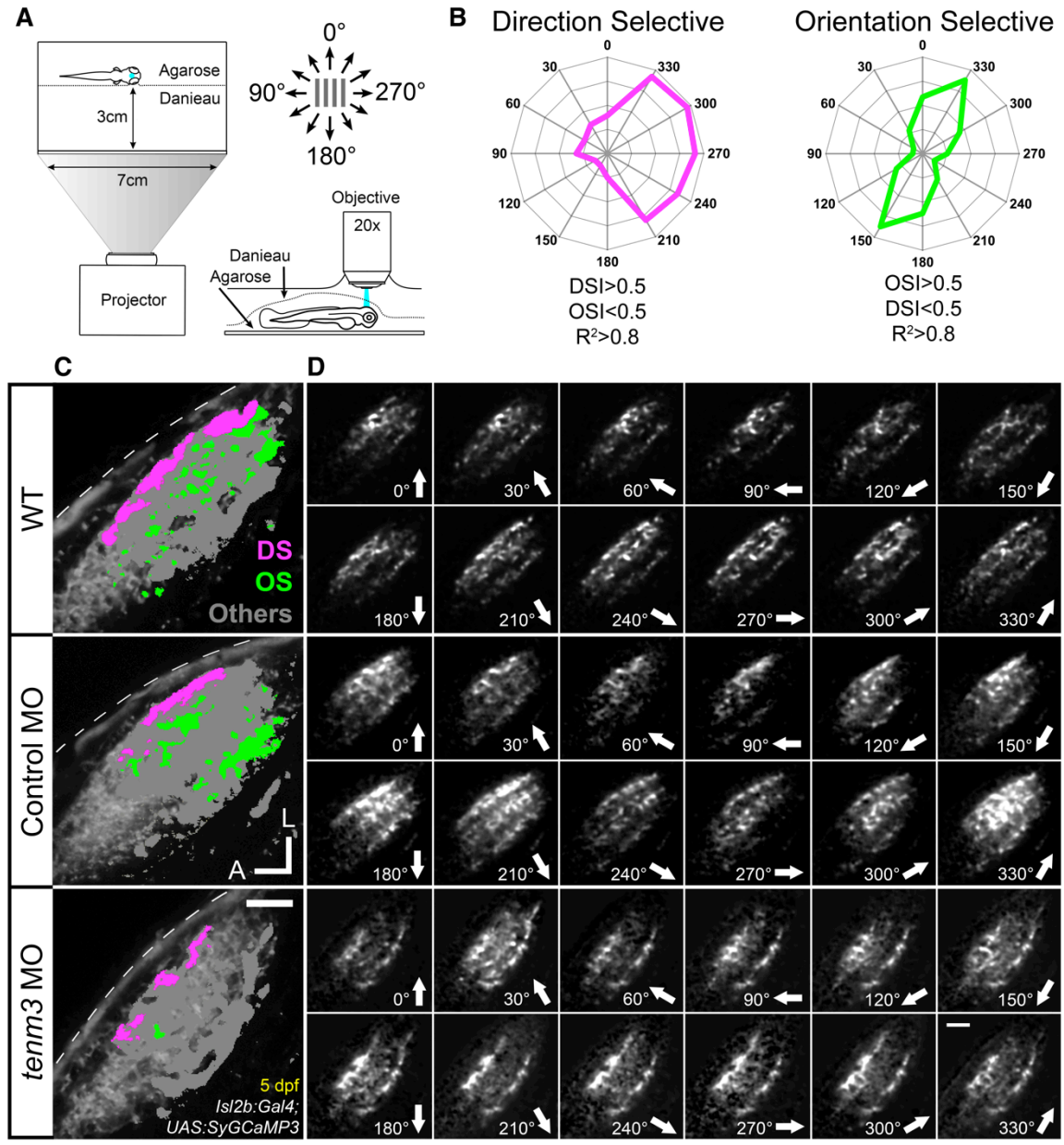

Figure 5.6. Analysis of RGC direction and orientation selectivity in control and *tenm3* morphant larvae. A, Schematic describing the experimental setup. Larvae are immobilized in agarose and placed with one eye facing a screen, where drifting bars moving in 12 directions are projected. Visually evoked SyGCaMP3 responses are recorded in the contralateral tectal neuropil. **B,** Polar plots of representative direction-selective (DS, magenta) and orientation-selective (OS, green) voxels showing relative integral responses to moving bars. Criteria employed to characterize the two classes of voxels are reported at the bottom. **C,** Parametric maps of single 5 dpf Tg(*Isl2b:Gal4;UAS:SyGCaMP3*) larvae (one larva per animal group) representing the spatial distribution of direction-selective (DS, magenta), orientation-selective (OS, green) and non-DS/non-OS visually responsive voxels (others, yellow) superimposed onto the mean fluorescence images of SyGCaMP3-expressing axons (greyscale). Note that the *tenm3* morphant larva (bottom) shows substantially fewer OS voxels than WT and control MO-injected larvae (top). Dashed lines indicate the skin overlaying the tectum. A, anterior; L, lateral. **D,** Montages showing visual responses (integral responses during individual epochs) in the tectal neuropil of larvae shown in (**C**). Note that all three larvae exhibit complex response patterns to moving bars. Direction of motion is shown at the bottom right in each panel. Scale bars in (**C,D**) are 20 µm.

(DS) or orientation-selective (OS), mutually exclusive criteria were employed: DS if $R^2 > 0.8$, DSI > 0.5 and OSI < 0.5; and OS if $R^2 > 0.8$, OSI > 0.5 and DSI < 0.5 (Fig. 5.6B).

Functional maps obtained from individual larvae (Fig. 5.6C) were spatially co-registered and used to generate parametric composite maps across multiple larvae (Fig. 5.7A; WT n = 8 larvae; control MO n = 11; *tenm3* MO n = 20). DS RGC (or DSGC) responses were observed in all three experimental groups (Fig. 5.7B). Moreover, the normal laminar organisation of DSGC axons within the superficial region of the SFGS (Nikolaou et al., 2012) is preserved in *tenm3* morphants. Further analysis of DSGC functional subtypes, identified by fitting von Mises distributions to the grouped population data of preferred angles (Nikolaou et al., 2012; Lowe et al., 2013), revealed that all three DSGC subpopulations – tuned to anterior (~260°), dorsoposterior (~40°)

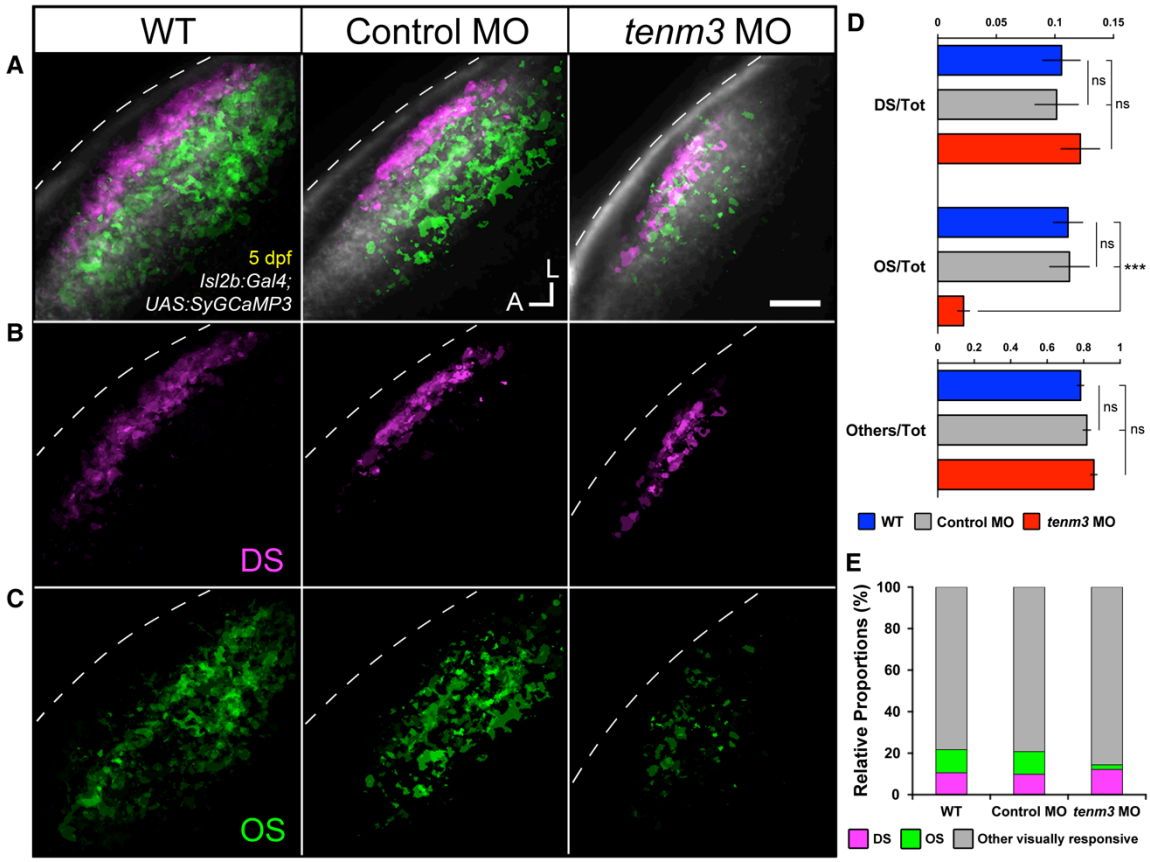

Figure 5.7. Impaired development of RGC orientation selectivity following *tenm3* knockdown. A, Composite parametric maps across multiple 5 dpf Tg(*Isl2b:Gal4;UAS:SyGCaMP3*) larvae representing the spatial distribution of direction-selective (DS; magenta) and orientation-selective (OS; green) voxels within each animal group (WT n = 8 larvae; control MO n = 11; *tenm3* MO n = 20). Within individual parametric maps, voxel brightness is proportional to the summed incidence of each functional response across all larvae imaged. The standard space template image derived for each group (greyscale) provides an anatomical reference. Dashed lines indicate the skin overlaying the tectum. Scale bar is 20 µm. A, anterior; L, lateral. **B,** Parametric maps of DS voxels only. **C,** Parametric maps of OS voxels only. **D,** Ratios between the different voxel classes and total visually responsive voxels within each group (WT n = 8 larvae; control MO n = 11; *tenm3* MO n = 20). Non-DS/non-OS voxels are classified as 'others'. All graphs show mean values ± SEM. ***p < 0.001; ns, not significant by one-way ANOVA followed by Tukey's HSD test. **E,** Bar graph showing the frequency of DS and OS voxel classes relative to visually responsive voxels within each group.

and ventroposterior (~150°) motion – found in control groups are also present in *tenm3* morphants (Fig. 5.8A,B). Overall, no difference between *tenm3* morphants and control groups was observed in the DSGC output.

In contrast, the OS RGC (or OSGC) output is severely impaired upon *tenm3* knockdown. Specifically, the overall number of OSGC voxels is decreased in *tenm3* morphants (Fig. 5.7C). Additionally, OSGC voxels, which are typically found in deeper sublaminae of the SFGS with little or no overlap with DSGCs in control animals (Nikolaou et al., 2012), show a substantial degree of overlap with DS voxels in *tenm3* morphants (Fig. 5.7A). To further confirm the OSGC impairment, the relative proportions of functional response classes within each experimental group were analysed. In *tenm3* morphants, a significant change in the ratio between OSGC voxels and the total population of visually responsive voxels was found (Fig. 5.7D; OS/tot, mean ± SEM, *tenm3* MO 0.022 ± 0.004, n = 20 larvae; WT 0.111 ± 0.012, n = 8; control MO 0.112 ± 0.016, n = 11; $F_{2,36} = 24.61$, $p < 0.0001$, one-way ANOVA with post-hoc Tukey's HSD test), so the OSGC output becomes the smallest population of RGCs responding to drifting bars in this group (Fig. 5.7E). The relative proportions of DSGC and non-DS/non-OS (classified as 'others') voxel populations, on the contrary, were similar between the three animal groups (Fig. 5.7D,E; DS/tot, mean ± SEM, WT 0.105 ± 0.015, control MO 0.101 ± 0.018, *tenm3* MO 0.121 ± 0.016, n = 39 larvae, $F_{2,36} = 0.42$, $p = 0.66$, one-way ANOVA with post-hoc Tukey's HSD test; others/tot, mean ± SEM, WT 0.783 ± 0.016, control MO 0.817 ± 0.019, *tenm3* MO 0.856 ± 0.016, n = 39 larvae, $F_{2,36} = 3.06$, $p = 0.059$, one-way ANOVA with post-hoc Tukey's HSD test), suggesting that they were not impaired by *tenm3* knockdown. Further analysis of OSGC functional subtypes revealed that all four OSGC subpopulations – tuned to bars oriented along the cardinal (~0°, ~90°) and diagonal axes (~40°, ~145°) – found in control groups are also present in *tenm3* morphants (Fig. 5.8C), yet with much smaller population sizes (Fig. 5.8D). Strikingly, the OSGC subpopulation tuned to horizontal bars moving along the vertical axis (~0°, yellow) appears to be the most severely affected by *tenm3* knockdown. These functional results indicate that visual responses of OSGCs are impaired by *tenm3* loss of function whereas DSGCs develop normally, therefore reinforcing the possible role of *tenm3* in the assembly of specific retinal circuits.

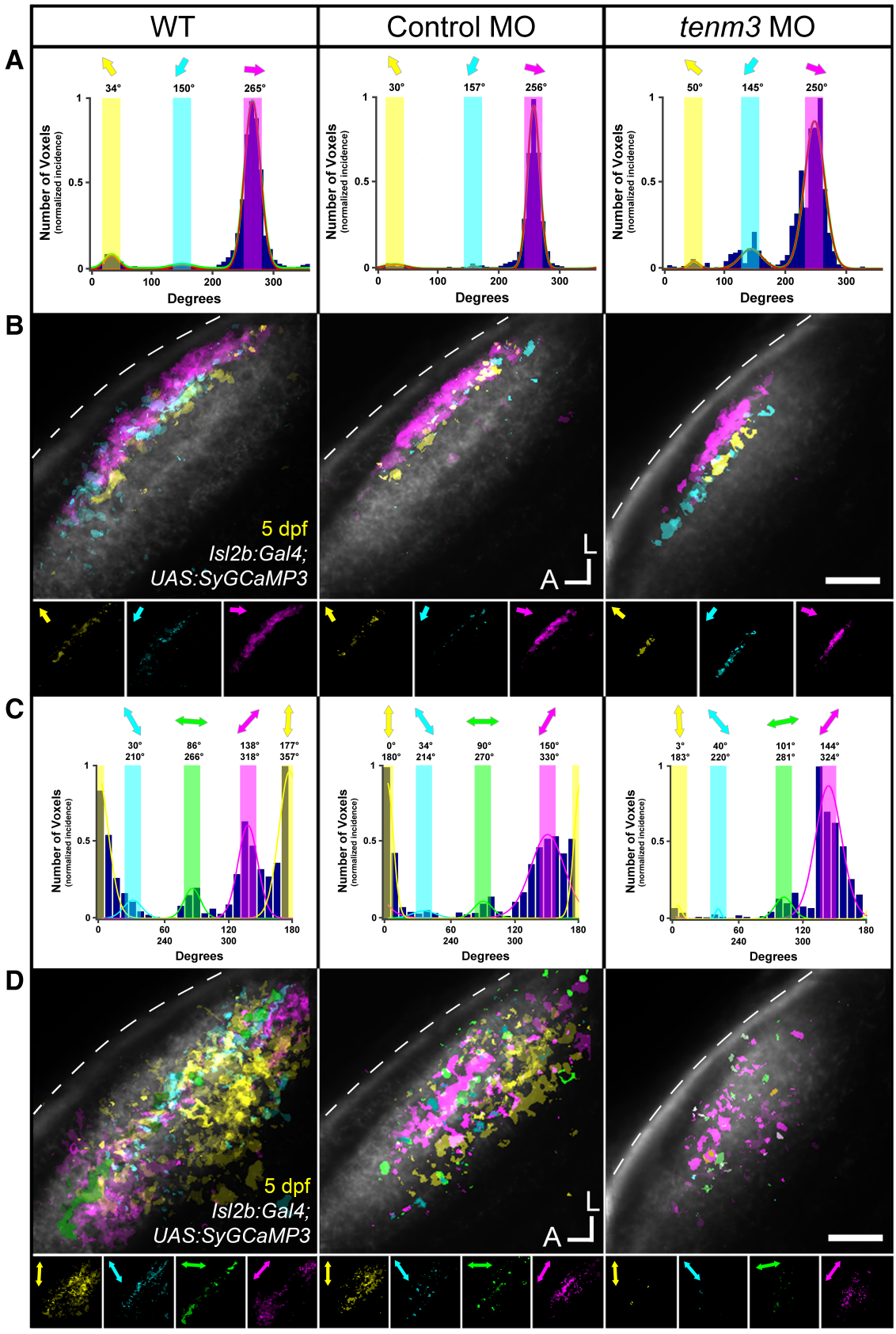

Figure 5.8. Subpopulations of direction- and orientation-selective RGC responses in control and *tenm3* morphant larvae. A, Cumulative histograms summarizing the incidence of direction-selective (DS) voxels within each animal group (WT n = 8 larvae; control MO n = 11; *tenm3* MO n = 20). Fitted von-Mises distributions reveal three subpopulations of DS responses tuned to three different directions of motion. Individual peak preferred angles are reported above. Note that all three animal groups develop three DS

RGC subtypes. Moreover, the sizes of individual DS response subpopulations are comparable across groups, with the dominant input corresponding to anterior motion selectivity. **B,** Composite parametric maps across multiple 5 dpf larvae representing the spatial distribution of the three DS voxel subtypes within each group (WT n = 8 larvae; control MO n = 11; *tenm3* MO n = 20). Note that the laminar organization of the three DS response subtypes in the tectal neuropil is analogous in all three groups, namely they are confined to superficial layers of the SFGS. Individual parametric maps for each voxel subtype are shown at the bottom. Colour-coding as in (**A**). The standard space template image derived for each group (greyscale) provides an anatomical reference. Dashed lines indicate the skin overlaying the tectum. Scale bar is 20 µm. A, anterior; L, lateral. **C,** Cumulative histograms summarizing the incidence of orientation-selective (OS) voxels within each animal group (WT n = 8 larvae; control MO n = 11; *tenm3* MO n = 20). Fitted von-Mises distributions reveal four subpopulations of OS responses tuned to four different stimulus orientations. Individual peak preferred angles are reported above. **D,** Composite parametric maps across multiple 5 dpf larvae representing the spatial distribution of the four OS response subtypes within each group (WT n = 8 larvae; control MO n = 11; *tenm3* MO n = 20). Individual parametric maps for each response subtype are shown at the bottom. Note that, even though *tenm3* morphants (right) show fewer OS responses than control larvae (left), all four OS response subtypes can be identified in their RGC output. Colour-coding as in (**C**). The standard space template image derived for each group (greyscale) provides an anatomical reference. Dashed lines indicate the skin overlaying the tectum. Scale bar is 20 µm. A, anterior; L, lateral.

5.2.5 RGC Orientation Selectivity is Impaired also in Tenm3^{KO} Mutants

To confirm the requirement of *tenm3* in the development of RGC orientation selectivity and further investigate its role in retinal circuit wiring, a zebrafish *tenm3* knockout mutant (*tenm3^{KO}*) was generated using Transcription Activator-Like Effector Nuclease (TALEN)-based genome editing. In *tenm3^{KO}* mutants, a 14-base pair deletion in the exon encoding the transmembrane domain of Tenm3 (Fig. 5.9A) leads to a reading frame shift and, subsequently, to a premature stop codon causing the loss of the entire extracellular domain (Fig. 5.9B-F). The RGC functional output of *tenm3^{KO}* mutants was then examined as described above (Nikolaou et al., 2012). Briefly, drifting bars moving in 12 different directions were presented to awake immobilised zebrafish larvae through a projection screen (Fig. 5.10A). Using the RGC-specific transgenic line *Tg(isl2b:Gal4;UAS:SyGCaMP3)*, population visual responses were simultaneously recorded through calcium imaging of RGC axon terminals in the contralateral optic tectum (Movie 5.4). Voxel-wise analysis was then used to isolate visually responsive voxels and identify DS and OS responses (Fig. 5.10B,C) (Lowe et al., 2013).

Consistent with *tenm3* knockdown results, 4 dpf *tenm3^{KO}* mutants have a large decrease in both the number of OS voxels (Fig. 5.11A; number of OS voxels per Z-plane, mean ± SEM, control 1308.6 ± 132.2, n = 23 larvae; *tenm3^{KO}* 533.0 ± 72.9, n = 22; two-tailed unpaired t-test with Welch's correction, $t_{34.1} = 5.13$, $p < 0.0001$) and the proportion of OSGC output relative to the whole population of responsive voxels (Fig. 5.11B; relative frequency of OS voxels per Z-plane, mean ± SEM, control 0.103 ± 0.008, n = 23 larvae; *tenm3^{KO}* 0.060 ± 0.008, n = 22; two-tailed unpaired t-test, $t_{43} = 3.63$, $p = 0.0007$). As a consequence, the relative proportion of 'non-tuned'

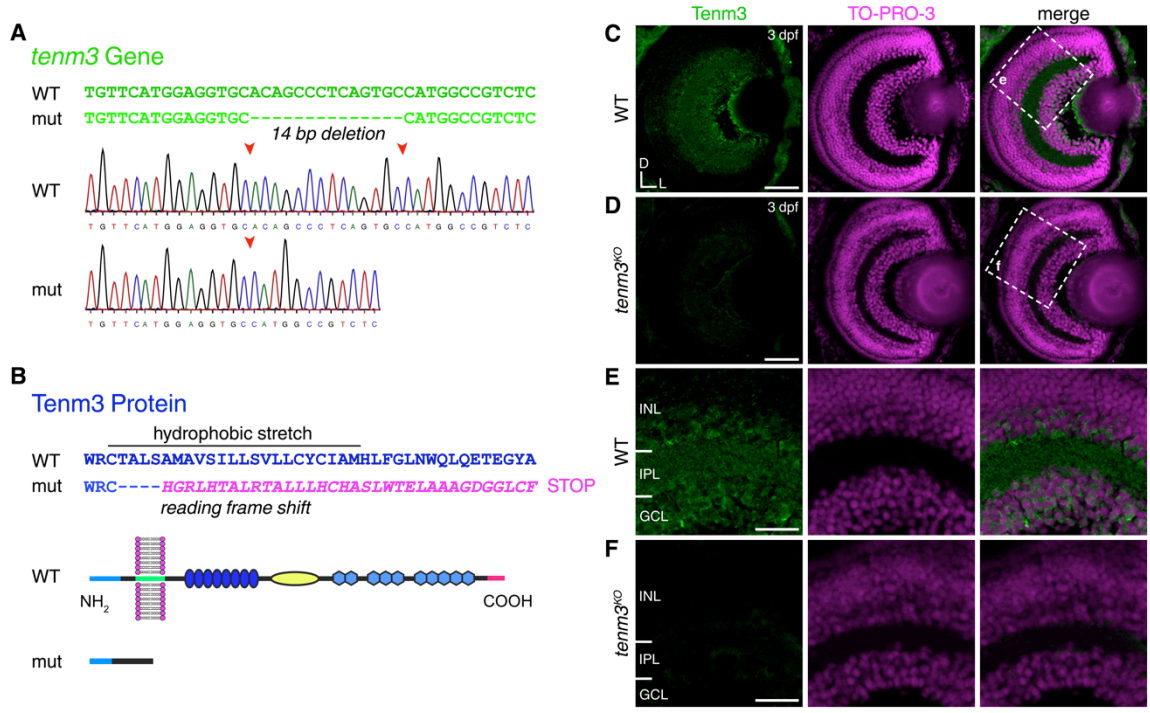

Figure 5.9. Generation of a *tenm3* knockout mutant through TALEN-mediated genome editing. A|B, TALEN-mediated *tenm3* gene knockout (**A**) and consequent structural changes in the Tenm3 protein (**B**). DNA sequencing chromatograms show the 14-base pair (bp) deletion present in *tenm3*^{KO} mutant (mut) larvae. This deletion in the gene region encoding the transmembrane domain of Tenm3 generates a reading frame shift and subsequent premature stop codon, therefore leading to the production of a non-functional Tenm3 protein missing its entire extracellular domain. **C|D,** Immunostaining showing the expression of Tenm3 (green) in retinae of 3 dpf WT (**C**) and *tenm3*^{KO} larvae (**D**). Cell bodies are labelled with the nuclear stain TO-PRO-3 (magenta). D, dorsal; L, lateral. Scale bars are 40 µm. **E|F,** Insets in (**C**) and (**D**) showing that, in the WT retina (**E**), Tenm3 is expressed in the inner nuclear layer (INL) and ganglion cell layer (GCL), whereas no Tenm3 expression is present in the *tenm3*^{KO} retina (**F**). IPL, inner plexiform layer. Scale bars are 20 µm. Importantly, all images in (**C-F**) were obtained using the same acquisition settings.

(non-DS and non-OS) RGC output is increased in *tenm3*^{KO} mutants (Fig. 5.11B; relative frequency of non-DS/non-OS voxels per Z-plane, mean ± SEM, control 0.847 ± 0.010, n = 23 larvae; *tenm3*^{KO} 0.888 ± 0.011, n = 22; two-tailed unpaired t-test, $t_{43} = 2.69$, p = 0.01). This impairment in the OSGC population is consistent with the lower degree of orientation selectivity, quantified by the orientation selectivity index (OSI), across visually responsive voxels in *tenm3*^{KO} mutants (Fig. 5.11D; two-sample Kolmogorov-Smirnov test, D = 0.096, p < 0.0001). By contrast, the DSGC population of responses did not show any impairment in *tenm3*^{KO} mutants (Fig. 5.11A-C; number of DS voxels per Z-plane, mean ± SEM, control 672.3 ± 105.2, n = 23 larvae; *tenm3*^{KO} 545.9 ± 119.0, n = 22; two-tailed unpaired t-test, $t_{43} = 0.79$, p = 0.42; relative frequency of DS voxels per Z-plane, mean ± SEM, control 0.049 ± 0.007; *tenm3*^{KO} 0.050 ± 0.009; two-tailed unpaired t-test, $t_{43} = 0.07$, p = 0.94), confirming that *tenm3* is not involved in the assembly of DS circuits. Equivalent results were obtained in 7 dpf *tenm3*^{KO} mutants

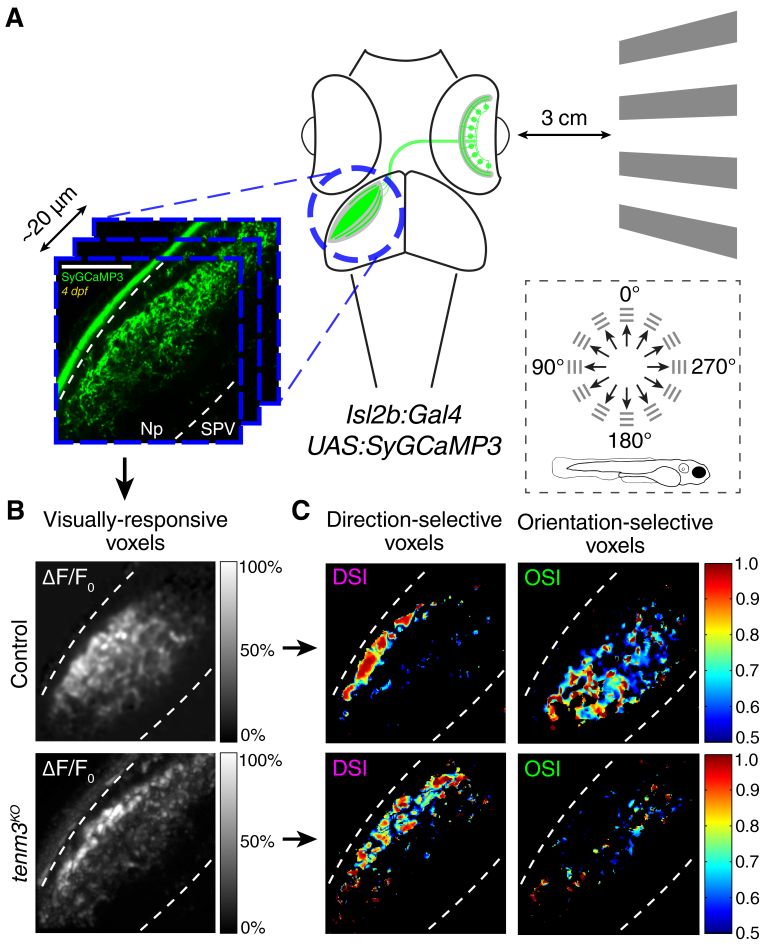

Figure 5.10. Analysis of RGC direction and orientation selectivity in control and *tenm3*^{KO} larvae. A, Functional calcium imaging of RGC axon terminals expressing SyGCaMP3 (green) in 4 dpf *Tg(isl2b:Gal4;UAS:SyGCaMP3)* larvae. Distance of right eye from projection screen is 3 cm. Recordings are performed from 2-4 Z-planes (approximately 20 µm total volume thickness) in the contralateral optic tectum. Dashed box shows the angles of moving bars relative to zebrafish larva orientation. Np, neuropil; SPV, stratum periventriculare. Scale bar is 40 µm. **B,** Mean $\Delta F/F_0$ images of calcium recordings in control (top) and *tenm3*^{KO} (bottom) larvae. **C,** Voxel-wise mapping of DS and OS responses. DSI, direction selectivity index; OSI, orientation selectivity index.

(Fig. 5.12A-D; number of DS voxels per Z-plane, mean ± SEM, control 660.0 ± 154.6, n = 12 larvae; *tenm3*^{KO} 532.6 ± 113.5, n = 13; two-tailed unpaired t-test, $t_{23} = 0.67$, p = 0.50; number of OS voxels per Z-plane, mean ± SEM, control 1250.0 ± 174.2; *tenm3*^{KO} 568.1 ± 58.9; two-tailed unpaired t-test with Welch's correction, $t_{13.5} = 3.70$, p = 0.0025), indicating that the development of RGC orientation selectivity is not simply delayed as a consequence of *tenm3* loss of function. A modest but significant decrease in the number of visually responsive voxels was observed in *tenm3*^{KO} mutants at 4 dpf (Fig. 5.11A; number of visually responsive voxels per Z-plane, mean ± SEM, control 12557 ± 741, n = 23 larvae; *tenm3*^{KO} 9101 ± 815, n = 22; two-tailed unpaired t-test, $t_{43} = 3.14$, p = 0.003), but not at 7 dpf (Fig. 5.12A; number of visually responsive voxels per Z-plane, mean ± SEM, control 11698 ± 1478, n = 12 larvae; *tenm3*^{KO} 9648 ± 930, n = 13; two-tailed unpaired t-test, $t_{23} = 1.19$, p = 0.24).

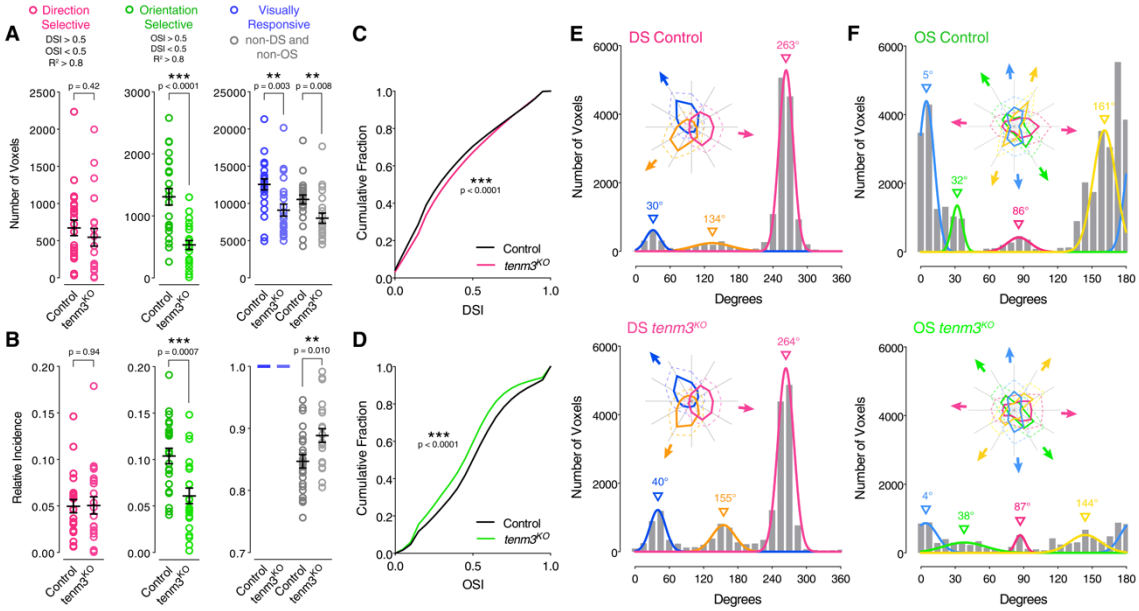

Figure 5.11. Tenm3 is required for RGC orientation selectivity. A|**B,** Average number (**A**) and relative frequency (**B**) of DS, OS, visually responsive and non-DS/non-OS voxels per Z-plane in control (n = 23 larvae) and *tenm3*^{KO} (n = 22 larvae) 4 dpf larvae. Criteria used to identify DS and OS voxels are reported at the top. Error bars are ± SEM. **p < 0.01, ***p < 0.001, unpaired two-tailed Student's t test. **C**|**D,** Cumulative distributions of DSI values ($R^2 > 0$) across voxels with OSI < 0.5 (**C**) and OSI values ($R^2 > 0$) across voxels with DSI < 0.5 (**D**) in control and *tenm3*^{KO} larvae. ***p < 0.001, two-sample Kolmogorov-Smirnov test. **E**|**F,** Cumulative histograms summarising the incidence of preferred angles for identified DS (**E**) and OS voxels (**F**) in control (n = 23; top) and *tenm3*^{KO} (n = 22; bottom) 4 dpf larvae. Overlaid curves are the fitted Gaussian distributions for each DS or OS subtype. Polar plots illustrate the mean (+ 1 SD) normalised response profiles for each DS or OS subtype.

Next, the extent to which the subtypes of DSGCs and OSGCs were affected by *tenm3* knockout was explored. The different subpopulations of DSGC and OSGC responses were identified by fitting Gaussian distributions to the grouped population data of preferred angles (Nikolaou et al., 2012; Lowe et al., 2013). As expected, population sizes and relative proportions of the three subtypes of DSGCs were not altered in *tenm3*^{KO} mutants (Fig. 5.11E and 5.12E), reinforcing the view that RGC direction selectivity develops through *tenm3*-independent mechanisms. Interestingly, the decrease in OS responses in *tenm3*^{KO} mutants was not equally represented among the four OSGC subtypes, with the small OSGC subpopulation tuned to vertical bars moving along the horizontal axis (~90°) being the least affected (magenta, Fig. 5.11F and 5.12F). Overall, these data confirm and further elucidate the crucial role played by *tenm3* in generating RGC orientation selectivity during development.

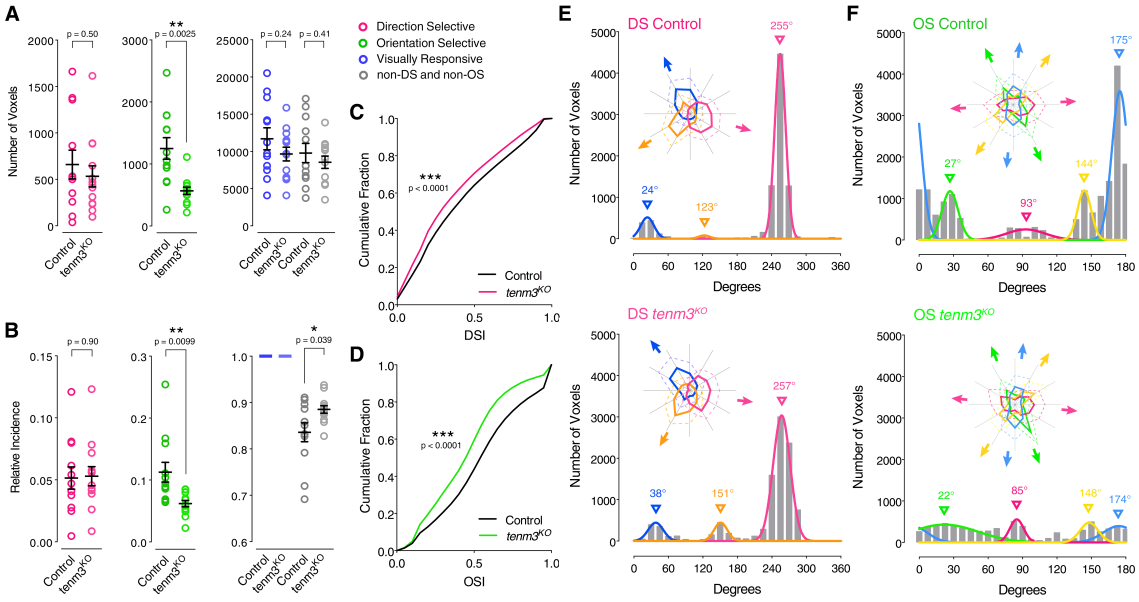

Figure 5.12. Tenm3 is required for RGC orientation selectivity in late development. A|**B,** Average number (**A**) and relative frequency (**B**) of DS, OS, visually responsive and non-DS/non-OS voxels per Z-plane in control (n = 12 larvae) and *tenm3*^{KO} (n = 13 larvae) 7 dpf *Tg(isl2b:Gal4;UAS:SyGCaMP3)* larvae. Error bars are ± SEM. *p < 0.05, **p < 0.01, unpaired two-tailed Student's t test. **C**|**D,** Cumulative distributions of DSI values ($R^2 > 0$) across voxels with OSI < 0.5 (**C**) and OSI values ($R^2 > 0$) across voxels with DSI < 0.5 (**D**) in control and *tenm3*^{KO} larvae. ***p < 0.001, two-sample Kolmogorov-Smirnov test. **E**|**F,** Cumulative histograms summarising the incidence of preferred angles for identified DS (**E**) and OS voxels (**F**) in control (n = 12; top) and *tenm3*^{KO} (n = 13; bottom) 7 dpf larvae. Overlaid curves are the fitted Gaussian distributions for each DS or OS subtype. Polar plots illustrate the mean (+ 1 SD) normalised response profiles for each DS or OS subtype.

5.2.6 IPL Stratification Defects of Tenm3^{+} *AC Neurites in Tenm3*^{KO} *Mutants*

Since *tenm3* is not only expressed in RGCs but also in ACs (see 4.2), potential structural defects in the IPL stratification of *tenm3*$^{+}$ AC neurites were investigated using the *Tg(tenm3:Gal4;UAS:tagRFP-CAAX)* line in *tenm3*^{KO} background. As described in section 4.2.2, *tenm3*$^{+}$ ACs normally stratify their neurites in three precise strata located at 5%, 61%, and 94% IPL depth (Fig. 5.13A). This tri-laminar IPL stratification pattern is already visible at 3 dpf and becomes more refined at 5 dpf. In *tenm3*^{KO} mutants, by contrast, *tenm3*$^{+}$ AC neurites do not stratify correctly in the IPL (Fig. 5.13B). This is particularly striking at 3 dpf when they fail to target the two innermost IPL strata and instead stratify diffusely across the IPL, as shown by fluorescence intensity measurements across the IPL of multiple larvae (Fig. 5.13C; control n = 13 larvae, *tenm3*^{KO} n = 13 larvae).

Do these stratification defects observed at the population level result from all *tenm3*$^{+}$ AC types stratifying abnormally in the IPL? Or, alternatively, are only a few types affected by *tenm3* knockout? Also, is there any change in the planar morphological features of *tenm3*$^{+}$ ACs (e.g., dendritic field area or elongation) in

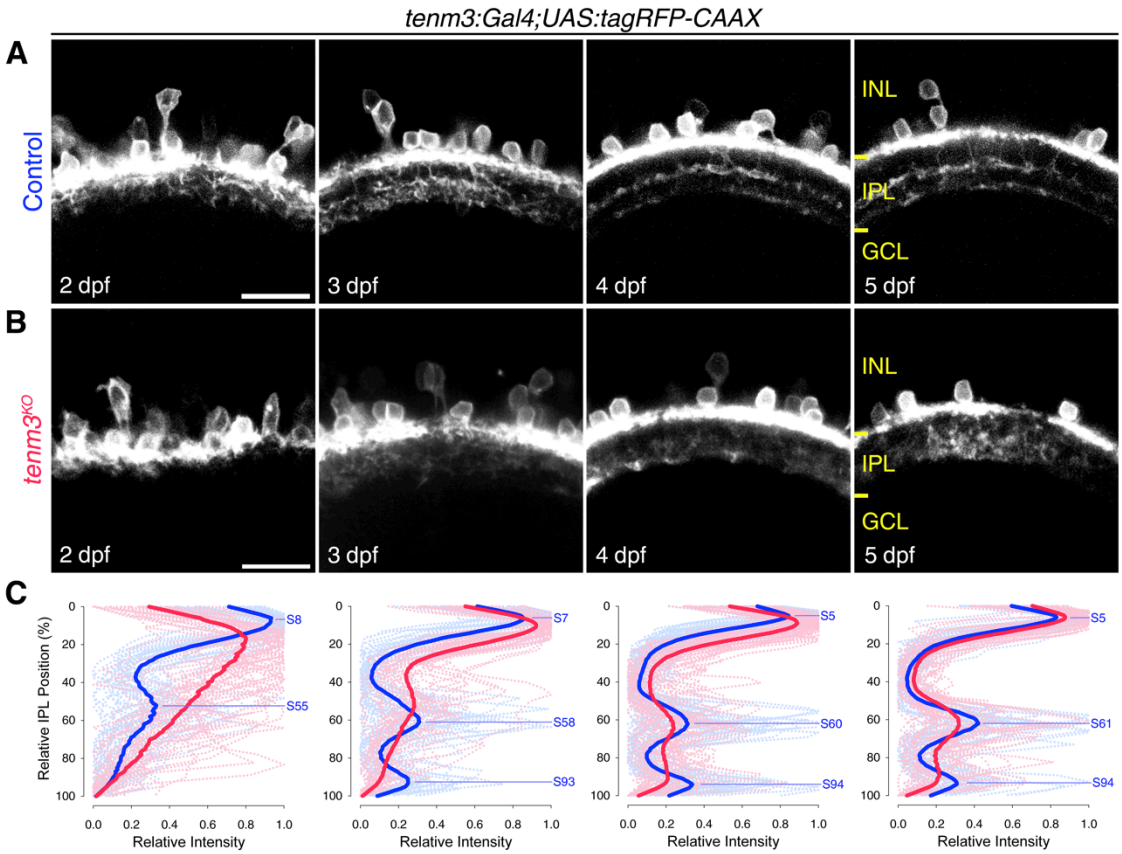

Figure 5.13. Tenm3 is required for normal neurite IPL stratification of *tenm3*$^{+}$ amacrine cells. A|**B,** Inner plexiform layer (IPL) stratification pattern of *tenm3*$^{+}$ AC neurites in control (**A**) and *tenm3*^{KO} (**B**) *Tg(tenm3:Gal4;UAS:tagRFP-CAAX)* larvae from 2 to 5 dpf. INL, inner nuclear layer; GCL, ganglion cell layer. Scale bars are 20 µm. **C,** IPL fluorescence intensity profiles of *tenm3*$^{+}$ AC neurites in control (blue; n = 13 larvae) and *tenm3*^{KO} larvae (red; n = 13 larvae) from 2 to 5 dpf. Thin traces represent individual IPL profiles, whereas thick traces indicate average IPL profiles. 0% corresponds to the INL/IPL boundary, whereas 100% corresponds to the IPL/GCL boundary. Fluorescence peaks indicating IPL strata in control larvae are labelled with the letter 'S' followed by their relative IPL position.

tenm3^{KO} mutants? To address these questions, individual *tenm3*$^{+}$ ACs where mosaically labelled with the cyan fluorescent protein mTFP1 in *Tg(tenm3:Gal4;UAS:tagRFP-CAAX);tenm3*^{KO} larvae. To classify *tenm3*^{KO} mutant *tenm3*$^{+}$ ACs into the different AC types identified in wild type control larvae (Fig. 4.7), k-means clustering based on IPL stratification, dendritic field area and dendritic field elongation was performed using fixed cluster centroids obtained from the initial clustering of control *tenm3*$^{+}$ ACs (Fig. 5.14; wide-field AC types were non included in the clustering analysis given their low labelling frequency, n = 2 cells out of 52). This allowed to assign *tenm3*^{KO} mutant *tenm3*$^{+}$ ACs having abnormal morphological properties to the pre-identified AC types in an automated way that depends on their similarity to the stereotypical morphological characteristics of control *tenm3*$^{+}$ ACs (Fig. 5.15A). No significant difference in the relative frequency of *tenm3*$^{+}$ AC types was observed

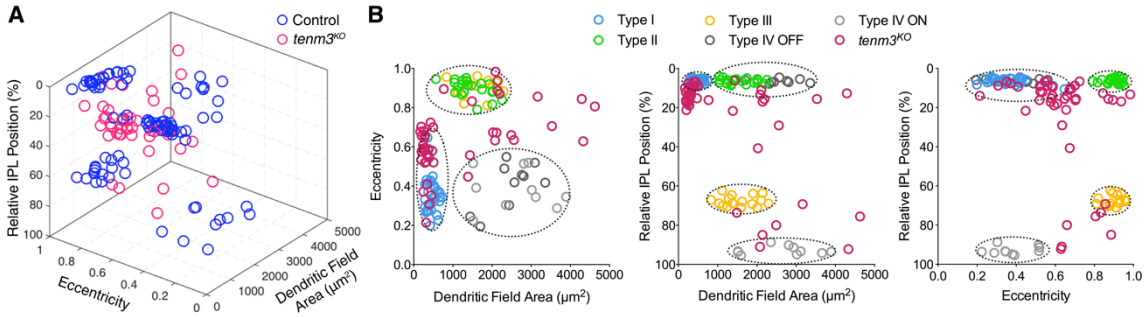

Figure 5.14. Abnormal morphological properties of single *tenm3*$^{+}$ amacrine cells in *tenm3*^{KO} mutants. A, 3D scatter plot summarising the morphological properties (i.e., IPL stratification, dendrite eccentricity and area) of single, mosaically labelled *tenm3*$^{+}$ ACs in 4 dpf control *UAS:eGFP-CAAX*-injected *Tg(tenm3:Gal4)* larvae (blue circles, n = 117 cells) and in 4-5 dpf *UAS:mTFP1*-injected *Tg(tenm3:Gal4;UAS:tagRFP-CAAX) tenm3*^{KO} larvae (magenta circles, n = 50 cells). **B,** 2D scatter plots representing pairwise comparison of morphological features in control *tenm3*$^{+}$ ACs clustered and classified into distinct types (coloured circles and dashed ellipses) and *tenm3*^{KO} mutant *tenm3*$^{+}$ ACs (magenta circles). Note the considerable number of *tenm3*^{KO} mutant *tenm3*$^{+}$ ACs having morphological features outside of the normal range observed in control cells (magenta circles outside dashed ellipses).

between control and *tenm3*^{KO} mutant larvae (relative frequency of control vs. *tenm3*^{KO}, type I 0.43 vs. 0.59, type II 0.19 vs. 0.13, type III 0.16 vs. 0.10, type IV ON 0.08 vs. 0.06, type IV OFF 0.08 vs. 0.08, type V 0.03 vs. 0.02, type VI 0.03 vs. 0.02; $\chi^2 = 6.235$, df = 6, p = 0.397, n = 125 cells control, n = 52 cells *tenm3*^{KO}, two-tailed chi-square test). Interestingly, the only morphological feature that is consistently different across type I-IV *tenm3*$^{+}$ ACs in *tenm3*^{KO} mutants is the width of neurite stratification in the IPL (Fig. 5.15B). In particular, the neurites of *tenm3*^{KO} mutant *tenm3*$^{+}$ ACs fail to form precise strata and, therefore, occupy a larger portion of the IPL (Fig. 5.16D). This also results in a shift of the relative IPL location with highest neurite density towards the centre of the IPL (Fig. 5.15B and 5.16C). Planar morphological features, on the other hand, appear to be affected in a cell-type-specific manner by *tenm3* knockout. Specifically, the dendritic field area is decreased in type I *tenm3*$^{+}$ ACs, increased in type III *tenm3*$^{+}$ ACs, and unchanged in the other AC types (Fig. 5.16A). Likewise, dendritic field elongation is higher in type I, IV ON and IV OFF *tenm3*$^{+}$ ACs, but lower in type II and III *tenm3*$^{+}$ ACs, which are the AC types characterised by a high dendritic field elongation in control larvae (Fig. 5.16B). Overall, these results reveal that *tenm3* is required not only for RGC dendritic arborisation, but also for the correct stratification of *tenm3*$^{+}$ AC neurites in the IPL. Interestingly, even though neurite IPL stratification is equally affected in all *tenm3*$^{+}$ AC types, planar morphological features show cell-type-specific changes.

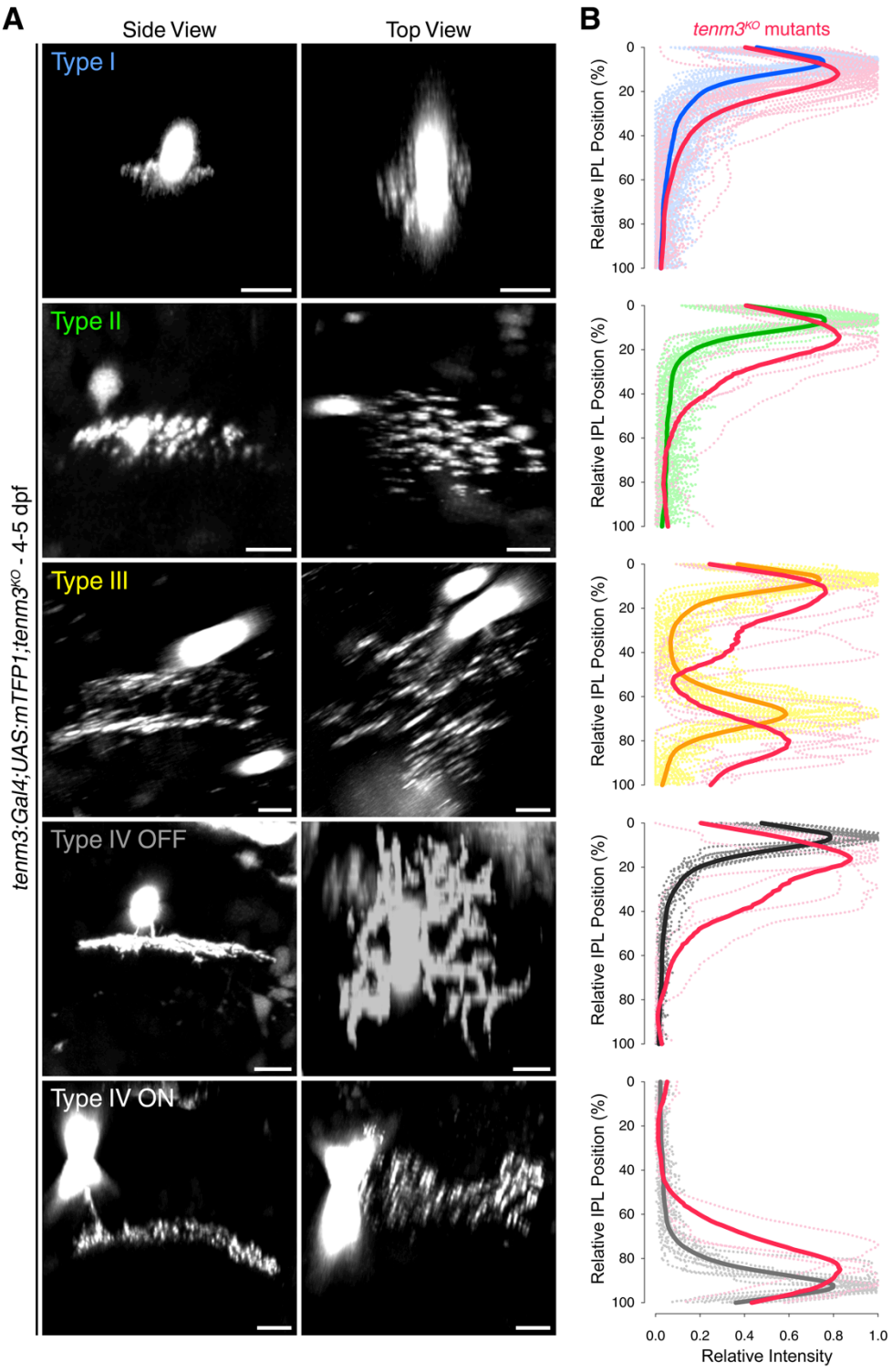

Figure 5.15. Neurite IPL stratification is consistently broader in all *tenm3*$^{+}$ amacrine cell types upon *tenm3* knockout. A, Morphologies of single *tenm3*$^{+}$ ACs expressing mTFP1 in 4-5 dpf *UAS:mTFP1*-injected *Tg(tenm3:Gal4;UAS:tagRFP-CAAX) tenm3*^{KO} larvae. Cells have been classified into the different *tenm3*$^{+}$ AC types identified in control larvae through k-means clustering. Side views (left) and top views (right) are shown. Scale bars are 10 µm. **B,** Neurite IPL fluorescence intensity profiles for each *tenm3*$^{+}$ AC type in control (colours; n = 117 cells) and *tenm3*^{KO} larvae (magenta; n = 50 cells). Note the broader IPL stratification pattern of all *tenm3*$^{+}$ AC types in *tenm3*^{KO} mutants. Thin traces represent individual IPL profiles, whereas thick traces indicate average IPL profiles. 0% corresponds to the INL/IPL boundary, whereas 100% corresponds to the IPL/GCL boundary.

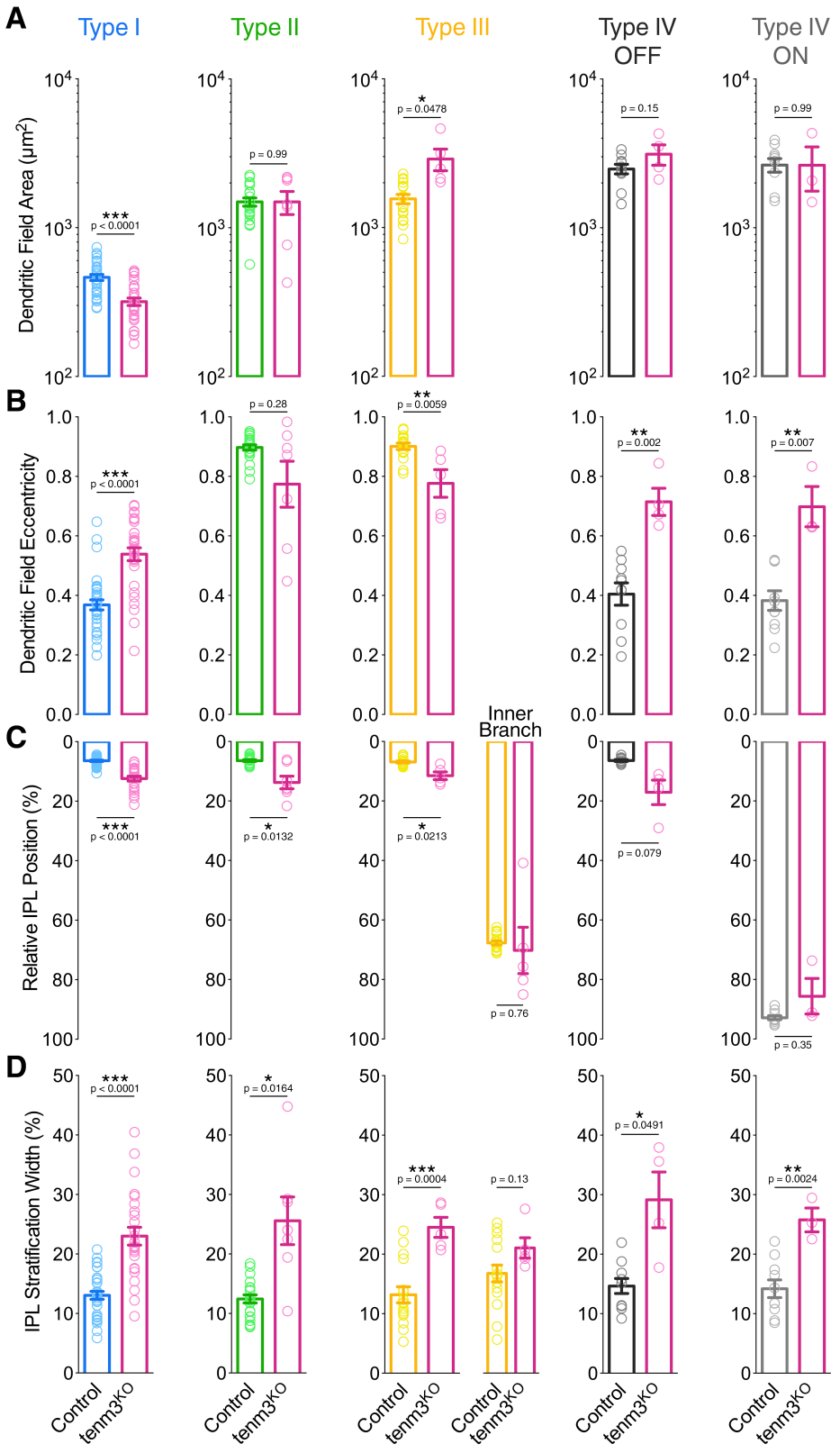

Figure 5.16. Planar morphological features of *tenm3*$^{+}$ amacrine cell dendrites are also affected in *tenm3*^{KO} mutants. A-D, Average dendritic field area (**A**), dendritic field elongation (**B**), relative IPL position of peak neurite stratification (**C**), and neurite IPL stratification width (**D**) for each *tenm3*$^{+}$ AC type in control (colours; n = 117 cells) and *tenm3*^{KO} larvae (magenta; n = 50 cells). In (**C**) and (**D**) results for the inner and outer dendritic branches of type III *tenm3*$^{+}$ ACs are reported separately. Error bars are ± SEM. *p < 0.05, **p < 0.01, ***p < 0.001, all unpaired two-tailed Student's t tests except for dendritic field eccentricity in (**B**) where Mann-Whitney tests were instead performed.

5.3 Discussion

The loss-of-function experiments described above demonstrate that *tenm3* is required for the correct structural and functional development of retinal circuits in the larval zebrafish. In particular, *tenm3* knockdown produces laminar targeting errors of RGC dendrites and axons, indicating that *tenm3* acts both in the retina and the optic tectum. Intriguingly, these errors appear to be restricted to a subset of RGCs, hinting that cells not expressing *tenm3* are unaffected. Similar results were obtained by examining the functional development of RGC visual response properties, inasmuch as the orientation-selective RGC output is strongly impaired by *tenm3* loss of function, whereas direction selectivity is unaffected. In addition, the IPL stratification of *tenm3*$^{+}$ ACs as well as their planar morphology is disrupted upon *tenm3* knockout, suggesting that the functional deficits found in OSGCs could potentially result from a synaptic mismatch between these two subpopulations of cells (Fig. 5.1C).

5.3.1 Role of Teneurins in Neural Circuit Wiring

Taken together, these findings support a role for *tenm3* in the establishment of cell-type-specific circuit wiring in the vertebrate visual system. But what specific wiring process does *tenm3* regulate? It is generally accepted that molecules mediating homophilic cell-cell adhesion can instruct the recognition between specific pre- and postsynaptic elements by triggering synapse formation/stabilisation (Sanes and Yamagata, 2009; Williams et al., 2010). Homophilic cell adhesion has been extensively studied in the IPL of the chick and mouse retina, where different immunoglobulin superfamily adhesion molecules are expressed by specific cell subsets and control the precise laminar/synaptic matching of their neurites (Yamagata et al., 2002; Yamagata and Sanes, 2008, 2012; Krishnaswamy et al., 2015). Interestingly, this homophilic matching mechanism appears to operate also in higher visual targets. For example, evidence in mouse showed that Cadherin-6 mediates the axon-target recognition between a specific subset of RGCs and their target nuclei in the brain (Osterhout et al., 2011). Consistent with these findings, elegant studies in *Drosophila* demonstrated that teneurins play an instructive role in the synaptic matching between specific pre- and postsynaptic cells in the olfactory system and at the neuromuscular junction (Hong et al., 2012; Mosca et al., 2012). In addition, teneurins have been shown to regulate other fine-scale neural wiring processes *in vivo*, such as cell-type-specific dendrite morphogenesis (Hattori et al., 2013), synapse organisation (Mosca et al., 2012; Mosca and Luo, 2014), and axon projection topography (Dharmaratne et al., 2012). In light of

these results and considering that teneurin-mediated homophilic cell recognition and adhesion inhibit neurite outgrowth *in vitro* (Beckmann et al., 2013), the simplest hypothesis would be that *tenm3* (by being expressed in RGCs, amacrine cells and tectal neurons) controls the stratification/matching of RGC neurites with their pre- and postsynaptic partners through selective stabilisation of branches/synapses contacting *tenm3*-expressing cells. In particular, the data presented here suggest that *tenm3* specifies the correct matching of functionally and morphologically defined subsets of ACs and RGCs forming a circuit underlying retinal orientation selectivity. Even though the results are suggestive of direct synaptic matching between *tenm3*$^{+}$ ACs and OSGCs (see also 6.2), the technical limitations of this study did not allow to unequivocally demonstrate the physical synaptic connections between these two neural populations and, therefore, future experiments will be required to further elucidate this point.

5.3.2 Homo- vs. Heterophilic Teneurin Trans-interactions

Given that *tenm3* is expressed in both RGCs and ACs, and that *tenm3* loss of function leads to specific morphological and functional impairments in RGCs as well as defects in *tenm3*$^{+}$ AC neurite IPL stratification, one possible explanation of *tenm3* mechanism of action could be through trans-synaptic homophilic interactions (Fig. 5.1C), as highlighted above. However, loss of selective *trans*-interactions with other cell-adhesion molecules known to bind heterophilically with teneurins, such as latrophilins (Silva et al., 2011; Boucard et al., 2014), may as well explain the phenotypes caused by *tenm3* loss of function. The precise roles played by teneurin homo- versus heterophilic *trans*-interactions during neural circuit wiring are still unclear. Yet, recent reports appear to indicate that homophilic interactions are crucial for the initial recognition and matching between specific subsets of neurons (Hong et al., 2012; Beckmann et al., 2013), whereas heterophilic interactions are involved in subsequent steps of synapse adhesion and organisation (Silva et al., 2011; Boucard et al., 2014; Mosca and Luo, 2014). Since teneurins can control these distinct processes even between the same sets of neurons (Hong et al., 2012; Mosca and Luo, 2014), sophisticated genetic manipulations will be required to disentangle the contribution of homo- versus heterophilic *trans*-interactions in neurons where a given teneurin and its heterophilic binding partners are simultaneously expressed. Interestingly, some latrophilin members are expressed in the zebrafish eye at larval and adult stages, although it is not clear whether they exhibit a cell-type-specific expression pattern

(Lange et al., 2012; Harty et al., 2015). Thus, the retinal orientation-selective circuit affected by *tenm3* loss of function represents a tractable *in vivo* vertebrate system to test the specific roles played by teneurin homo- and heterophilic *trans*-interactions during neural circuit wiring.

Chapter 6

Circuit Mechanisms Underlying Orientation Selectivity in the Retina

6.1 Introduction

The detection of oriented visual stimuli is a key neural computation performed by visual systems of many animals. Neurons performing this task are known as orientation-selective (OS) since they respond preferentially to elongated stimuli oriented along a specific axis in the visual field, but respond weakly to stimuli oriented orthogonally to their preferred axis. Orientation selectivity was first discovered in cat primary visual cortex by Hubel and Wiesel over 50 years ago (Hubel and Wiesel, 1962). Since then, numerous studies described OS neurons in visual systems of vertebrates and invertebrates, including primates (Hubel and Wiesel, 1968), rodents (Niell and Stryker, 2008), fish (Nikolaou et al., 2012) and insects (Fisher et al., 2015). Work in several vertebrate species identified OS cells in regions upstream of primary visual cortex, like the lateral geniculate nucleus (Marshel et al., 2012; Cheong et al., 2013; Piscopo et al., 2013) and the retina (Levick, 1967; Venkataramani and Taylor, 2010; Zhao et al., 2013; Baden et al., 2016), suggesting that the first steps in the processing of oriented stimuli take place early along the vertebrate visual pathway. In the retina, orientation selectivity is present among retinal ganglion cells (RGCs) (Levick, 1967; Bloomfield, 1994), the sole retinal output neurons, and amacrine cells (ACs) (Bloomfield, 1994; Murphy-Baum and Taylor, 2015), a class of inhibitory neurons that modulate and shape responses of RGCs, bipolar cells and other ACs. However, presently it is not fully understood how orientation selectivity emerges in these cells and whether they form a distinct retinal circuit, partially due to the lack of specific molecular markers allowing targeted labelling and manipulations.

The vertebrate retina consists of more than 70 neuron types (Masland, 2012a). Its primary function is to detect light stimuli, convert them into electrochemical signals and, subsequently, send the processed information to higher visual nuclei through parallel feature-specific neural pathways. Most of the information processing takes place in a layered neuropil structure called the inner plexiform layer (IPL) (Roska and Werblin, 2001). Essential neural substrates underlying the computations performed in the IPL are the specific and stereotypic synaptic connections between three classes of

neurons, namely bipolar cells (BCs), ACs and RGCs (Fig. 6.1A). How defined cell types belonging to these three retinal cell classes form a circuit computing orientation selectivity has yet to be described in its entirety (Fig. 6.1A,B). Here, using *tenm3* as a marker, crucial cellular players and mechanisms generating orientation selectivity are identified in the larval zebrafish retina. First, orientation tuning is found in *tenm3*-expressing (*tenm3*$^{+}$) AC types characterised by elongated dendritic arbours. Second, evidence suggesting that *tenm3*$^{+}$ ACs generate RGC orientation selectivity by being a source of γ-aminobutyric acid (GABA) feedforward inhibition is provided. Third, optogenetic ablation of *tenm3*$^{+}$ ACs further confirms that *tenm3*$^{+}$ ACs are required for normal orientation-selective RGC (OSGC) tuning. Fourth, anatomical data shows that *tenm3*$^{+}$ ACs co-stratify their neurites with OSGC dendrites. Fifth, orientation tuning is found also in a fraction of BC presynaptic terminals. Lastly, a circuit model describing how OSGCs acquire their orientation selectivity by integrating tuned *tenm3*$^{+}$ ACs and BC inputs is presented.

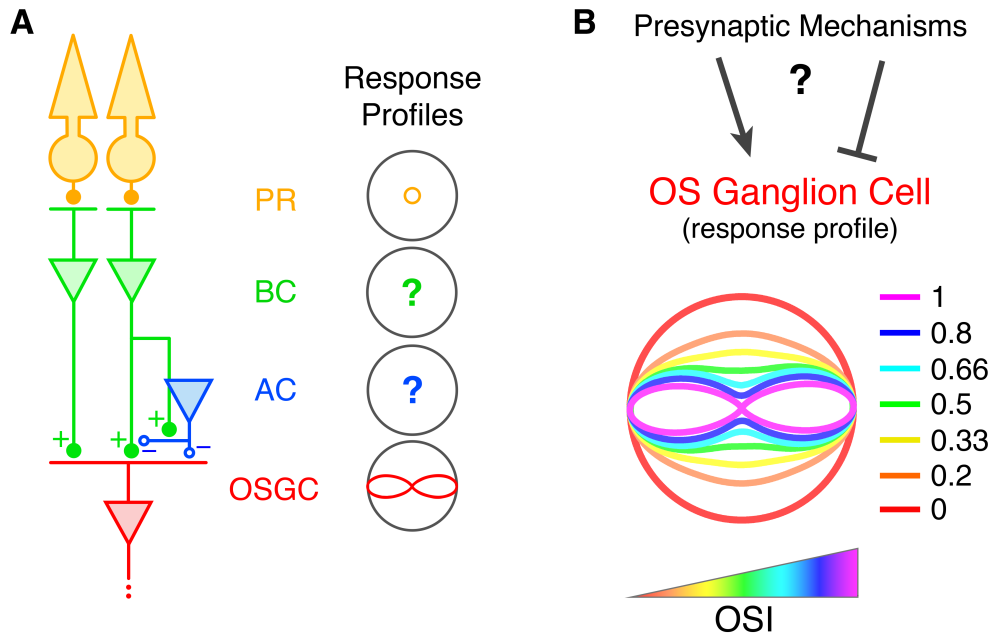

Figure 6.1. What are the presynaptic mechanisms generating orientation selectivity in RGCs? A, Schematic of the basic retinal circuit structure. Horizontal cells are not represented. Excitatory inputs are indicated by '+' (full circles), whereas inhibitory inputs are indicated by '–' (empty circles). Tuning profiles of example photoreceptor (PR, yellow) and orientation-selective ganglion cell (OSGC, red) are reported. Putative synapses between amacrine cell (AC, blue) and bipolar cell (BC, green) terminals are also represented. Unknown presence of orientation tuning among zebrafish BCs or ACs is indicated by green or blue question marks, respectively. **B,** The presynaptic cellular elements and mechanisms generating OSGC tuning are currently unknown. Both excitatory (black arrow) and inhibitory (black orthogonal lines) inputs could potentially contribute to the emergence of orientation selectivity in RGCs (i.e., orientation selectivity index, or OSI, > 0.5). The colour code describes the different levels of RGC orientation selectivity.

6.2 Results

6.2.1 Tenm3$^+$ ACs Show Orientation Tuning

The functional requirement of *tenm3* for the normal development of RGC orientation selectivity (see 5.2.4 and 5.2.5), together with the high dendritic field elongation of type II and III *tenm3*$^+$ ACs (see 4.2.4) – a feature previously described in rabbit orientation-sensitive ACs (Bloomfield, 1991, 1994; Murphy-Baum and Taylor, 2015) – led to the following hypothesis: type II and III *tenm3*$^+$ ACs could produce orientation-tuned responses when stimulating the retina with elongated stimuli oriented along particular axes in the visual field and, consequently, constitute cellular elements underlying the emergence of orientation selectivity in RGCs. To start testing this hypothesis, orientation tuning in the *tenm3*$^+$ AC population was analysed by performing *in vivo* two-photon calcium imaging in the retinae of *Tg(tenm3:Gal4;UAS:SyGCaMP3) crystal* larvae (Fig. 6.2A). Similarly to the setup described in 3.2.5, 4 dpf larvae were immobilised in 2% low melting point agarose with one eye facing an LCD screen where square-wave gratings moving in 12 different directions were displayed (Fig. 6.2A right). Visually evoked calcium transients were recorded from *tenm3*$^+$ ACs at 7.8 Hz using near-infrared (930 nm) two-photon laser excitation. Voxel-wise analysis was then used to identify visually responsive voxels and quantify orientation selectivity of visual responses at subcellular resolution (0.397 × 0.397 μm voxel XY size, 256 × 128 pixels). Importantly, *tenm3*$^+$ ACs show stimulus-locked responses to moving square-wave gratings (Movie 6.1). Notably, analyses using different metrics of orientation selectivity (i.e., OSI and circular variance) and progressively higher tuning stringency levels revealed that a large fraction of *tenm3*$^+$ ACs is tuned to elongated stimuli (Fig. 6.2B-D; n = 20 larvae). The distribution of preferred stimulus orientations across *tenm3*$^+$ ACs indicated the presence of four subpopulations of OS responses tuned to gratings oriented along the cardinal (13°, 90°) and diagonal axes (40°, 145°; Fig. 6.2E), similar to what was found in OSGCs (see 5.2.5) (Lowe et al., 2013). Compared to OSGCs, however, *tenm3*$^+$ ACs exhibited a higher degree of orientation selectivity (Fig. 6.2B,C).

Given the presence of different cell types in the *tenm3*$^+$ AC population (see 4.2.4), the tuning of single *tenm3*$^+$ ACs has to be investigated to know which one/s displays high orientation selectivity. Functional imaging of individually GCaMP6f-labelled *tenm3*$^+$ ACs followed by analyses of their tuning and dendritic field morphology was thus performed (Fig. 6.3A-D). Strikingly, the only *tenm3*$^+$ ACs that showed stimulus-locked visual responses characterised by high orientation tuning were those

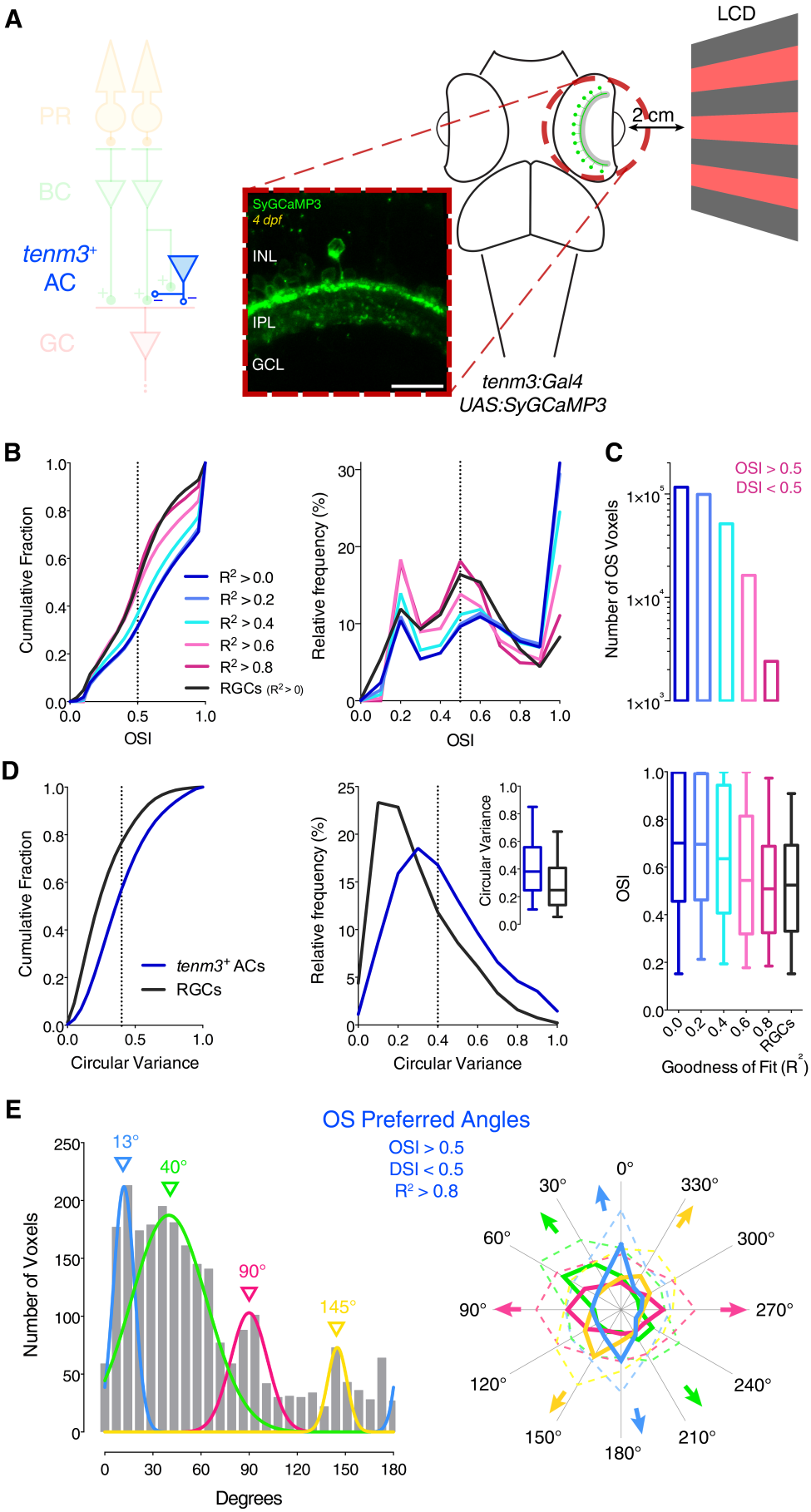
A
LCD
2 cm
PR
BC
tenm3+
AC
GC
SyGCaMP3
4 dpf
INL
IPL
GCL
tenm3:Gal4
UAS:SyGCaMP3
B
Cumulative Fraction
OSI
R2 > 0.0
R2 > 0.2
R2 > 0.4
R2 > 0.6
R2 > 0.8
RGCs (R2 > 0)
Relative frequency (%)
OSI
C
OSI > 0.5
DSI < 0.5
Number of OS Voxels
D
Cumulative Fraction
tenm3+ ACs
RGCs
Circular Variance
Relative frequency (%)
Circular Variance
OSI
Goodness of Fit (R2)
E
OS Preferred Angles
OSI > 0.5
DSI < 0.5
R2 > 0.8
13°
40°
90°
145°
Number of Voxels
Degrees

Figure 6.2. *Tenm3*$^{+}$ amacrine cells show orientation-selective responses. A, Two-photon functional calcium imaging of *tenm3*$^{+}$ AC synaptic terminals expressing SyGCaMP3 (green) in 4 dpf *Tg(tenm3:Gal4; UAS:SyGCaMP3)* larvae. Distance of the eye from LCD screen is 2 cm. Recordings are performed from 2-4 Z-planes (approximately 20 µm total volume thickness). INL, inner nuclear layer; GCL, ganglion cell layer; IPL, inner plexiform layer. Scale bar is 20 µm. **B,** Cumulative distribution (left) and relative frequency (right) of orientation selectivity index (OSI) values across voxels with DSI < 0.5 in *tenm3*$^{+}$ ACs (n = 20 larvae) and RGCs (black, n = 23 larvae). The colour code indicates the progressively higher goodness of fit (R^2 of the fitted von-Mises profiles) criteria applied to the data to identify voxels characterised by high orientation selectivity. The black dotted lines indicate the OSI threshold used to identify OS responses (OSI > 0.5). Depending on the R^2 value chosen as threshold, the number of voxels that satisfy the criteria, and therefore are represented in the distributions, varies. **C,** Total number of OS voxels (top) and distribution of OSI values (bottom) using progressively higher R^2 values in *tenm3*$^{+}$ ACs and RGCs (black, R^2 > 0). Boxplots indicate interquartile ranges (boxes), medians (lines in boxes) and 10-90 percentiles (whiskers). **D,** Cumulative distribution (left) and relative frequency (right) of circular variance values across all voxels in *tenm3*$^{+}$ ACs (blue, n = 20 larvae) and RGCs (black, n = 23 larvae). The black dotted lines indicate the circular variance threshold used to identify OS responses (circular variance < 0.4). Boxplots in the right inset indicate interquartile ranges (boxes), medians (lines in boxes) and 5-95 percentiles (whiskers). **E,** Cumulative histogram (left) summarising the incidence of preferred angles for identified *tenm3*$^{+}$ AC OS voxels in 4 dpf larvae (n = 20 larvae). Overlaid curves are the fitted Gaussian distributions for each OS subtype. Polar plots (right) illustrate the mean (+ 1 SD) normalised response profiles for each OS subtype.

that could be classified as type II or III ACs (Fig. 6.3E; frequency of OS cells among *tenm3*$^{+}$ ACs, type II 100%, 5/5 cells; type III 100%, 3/3 cell; n = 8 cells from 8 larvae). The other *tenm3*$^{+}$ AC types, instead, did not respond to grating stimuli, namely they did not exhibit visual responses that were time-locked to stimulus epochs (type I 0%, 0/11 cells; type IV ON 0%, 0/4 cells; type IV OFF 0%, 0/5 cells; type V no cell found; type VI 0%, 0/1 cell; n = 21 cells from 19 larvae). Interestingly, the degree of orientation selectivity of type II and III *tenm3*$^{+}$ ACs was correlated with the elongation of their dendritic fields (Fig. 6.3F; Spearman's correlation coefficient, r = 0.8024, p = 0.0222, n = 8 cells from 8 larvae), and the angular difference between their preferred stimulus orientation and dendritic field orientation was close to zero (Fig. 6.3G; 1.18 ± 19.70°, mean ± SD; Spearman's correlation coefficient, r = 0.9341, p = 0.0017), indicating that these *tenm3*$^{+}$ ACs respond maximally when the stimulus orientation coincides with the orientation of their dendritic fields. Additionally, the distribution of dendritic field orientations across sparsely eGFP-labelled type II and III *tenm3*$^{+}$ ACs revealed that they fully cover the orientation space (Fig. 6.4). Together, these data show that type II and III *tenm3*$^{+}$ ACs are orientation-selective and that their tuning likely results from their highly elongated dendritic fields.

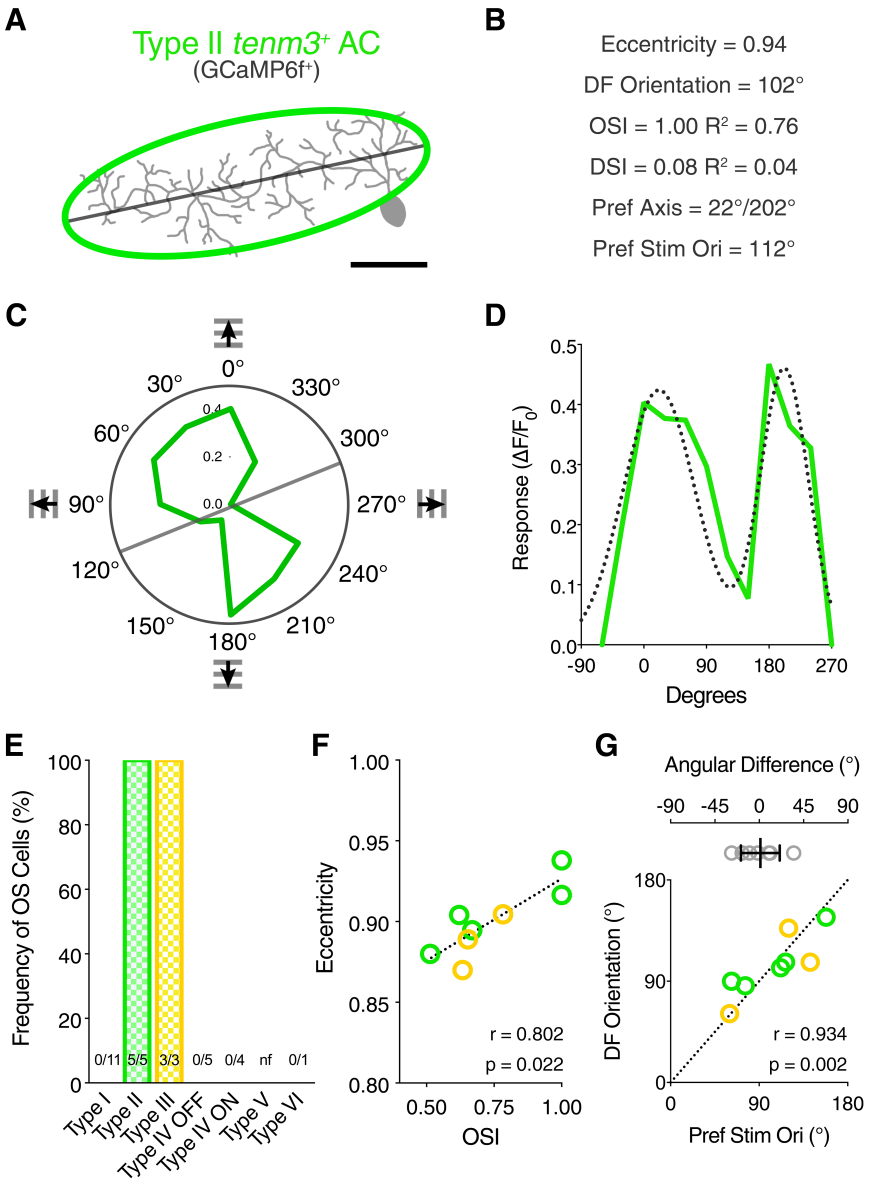

Figure 6.3. Type II and III *tenm3*$^+$ amacrine cells are orientation-selective. A-D, Summary of morphological and functional analyses of single GCaMP6f-labelled *tenm3*$^+$ ACs in 4 dpf *UAS:GCaMP6f*-injected *Tg(tenm3:Gal4)* larvae. An example of a type II *tenm3*$^+$ AC that showed stimulus-locked responses and high orientation selectivity is displayed. **A,** Morphological reconstruction of the example cell (grey, top view) with corresponding fitted ellipse profile (green) and dendritic field (DF) orientation (black line). Scale bar is 20 µm. **B,** Measurements of morphological and functional characteristics of the cell. OSI, orientation selectivity index; DSI, direction selectivity index; R^2, sum of two Gaussians distribution goodness of fit; Pref Stim Ori, preferred stimulus orientations. **C,** Polar plot representing the tuning profile of the cell (green, obtained by calculating the integral response to each stimulus) in response to gratings moving in different directions. Grey line indicates preferred stimulus orientation. Radial axis scale shows $\Delta F/F_0$ of integral calcium responses. **D,** Tuning profile (green) with fitted sum of two Gaussians (dotted black line). **E,** Bar histogram summarising the frequency of OS cells among *tenm3*$^+$ ACs in 4 dpf *Tg(tenm3:Gal4)* larvae injected with *UAS:GCaMP6f* DNA constructs (n = 29 cells from 27 larvae). The number of observed OS cells for each *tenm3*$^+$ AC type is reported at the bottom. nf, not found. **F,** Scatter plot representing the relationship between OSI and dendritic field eccentricity of OS type II and III *tenm3*$^+$ ACs (II, n = 5 cells; III, n = 3 cell). Spearman's correlation coefficient (r) with the corresponding p value is reported. Dotted line represents the linear regression fit to the data. **G,** Scatter plot representing the relationship between preferred stimulus orientation and dendritic field orientation of OS type II and III *tenm3*$^+$ ACs (II, n = 5 cells; III, n = 3 cell). Spearman's correlation coefficient (r) with the corresponding p value is reported. Dotted reference line indicates x = y. Top graph shows the angular difference between preferred stimulus orientation and dendritic field orientation (mean ± SD).

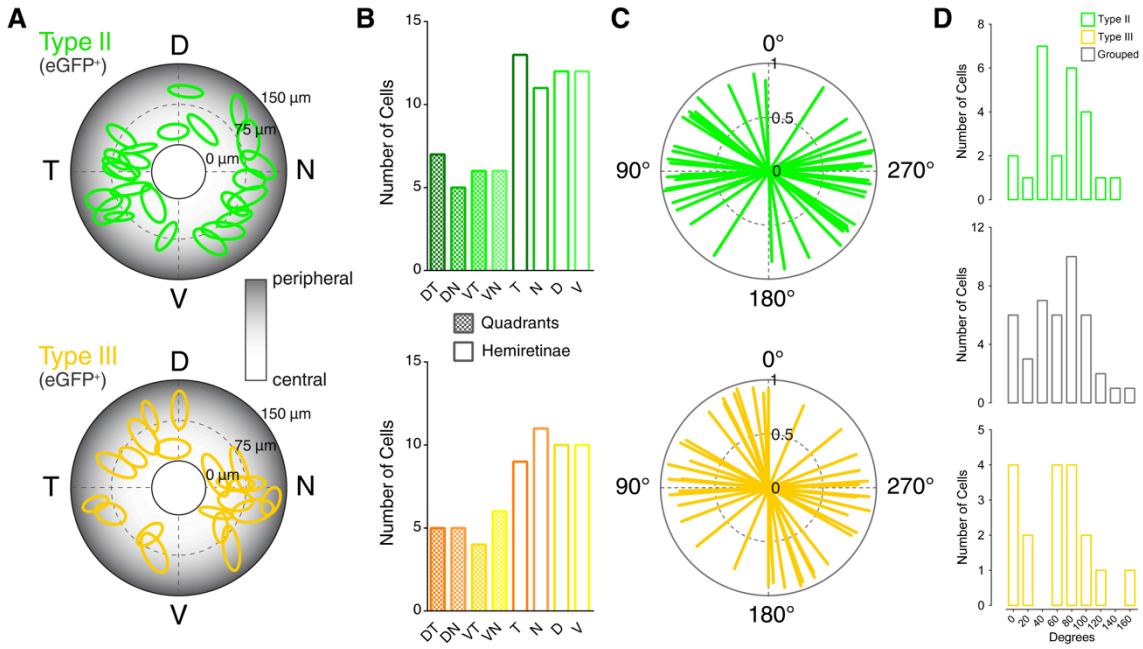

Figure 6.4. Type II and III *tenm3*$^{+}$ amacrine cells cover the orientation space and do not show retinal location bias. A, Retinal location mapping of individual eGFP-CAAX-labelled type II (green, top) and type III (yellow, bottom) *tenm3*$^{+}$ ACs in 4 dpf *UAS:eGFP-CAAX*-injected *Tg(tenm3:Gal4)* larvae (n = 24 and 20 cells in 39 larvae, respectively). D, dorsal; V, ventral; N, nasal; T, temporal. **B,** Frequencies of type II and III *tenm3*$^{+}$ ACs in number of cells per retinal quadrant or hemiretina. **C,** Grouped data summarising dendritic field orientation and elongation (quantified by the eccentricity of dendritic fields; radial axis) of individual eGFP-CAAX-labelled type II (green, top) and type III (yellow, bottom) *tenm3*$^{+}$ ACs (n = 24 and 20 cells in 39 larvae, respectively). Radial axis scale of the polar plots shows the eccentricity of dendritic fields. **D,** Frequencies of type II and III *tenm3*$^{+}$ ACs in number of cells per orientation (20° bin width; 0°-180° orientation space).

6.2.2 GABAergic Inhibition Generates RGC Orientation Selectivity

To further investigate the above hypothesis, the role played by *tenm3*$^{+}$ AC neurotransmission in generating OSGC tuning was assessed. Since immunohistochemical analyses revealed that the vast majority of *tenm3*$^{+}$ ACs are GABAergic (Fig. 6.5A,B and see 4.2.3), GABA-mediated inhibition was blocked using the $GABA_A$ receptor antagonist picrotoxin (100 µM). RGC visual responses were recorded through calcium imaging from the same *Tg(isl2b:Gal4;UAS:SyGCaMP3)* larvae before and after drug application. Notably, OSGCs were severely affected by GABA inhibition block, with a decrease in both OS responses and overall degree of RGC orientation selectivity comparable to the effects seen in *tenm3*^{KO} mutants (Fig. 6.5C-F; number of OS voxels per Z-plane, mean ± SEM, control 1441.0 ± 228.9, picrotoxin 669.3 ± 153.8, n = 15 larvae; two-tailed paired t-test, $t_{14} = 3.39$, $p = 0.0043$; relative frequency of OS voxels per Z-plane, mean ± SEM, control 0.110 ± 0.013; picrotoxin 0.050 ± 0.010; two-tailed paired t-test, $t_{14} = 3.77$, $p = 0.0020$). Similarly to the *tenm3* knockout experiments, the small OSGC subpopulation tuned to vertical bars was

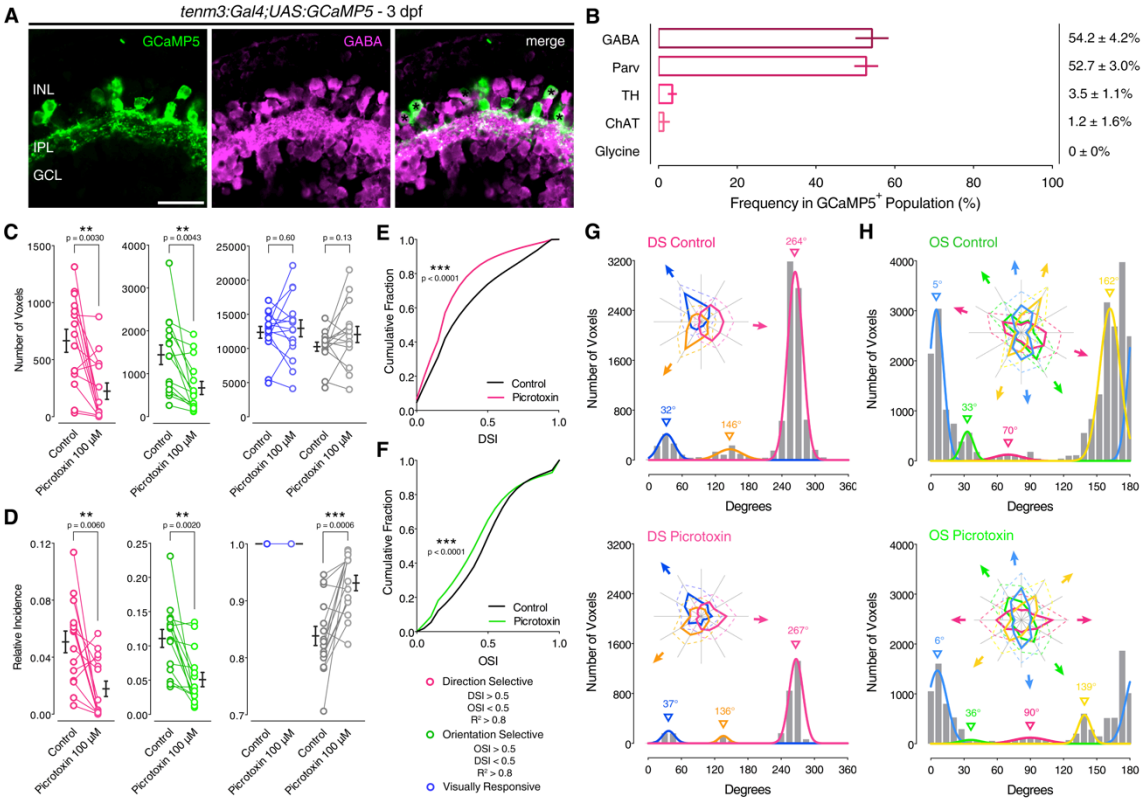

Figure 6.5. GABAergic inhibition generates RGC orientation selectivity. A, Immunostaining showing the expression of γ-aminobutyric acid (GABA, magenta) in 3 dpf *Tg(tenm3:Gal4;UAS:GCaMP5)* larvae, where *tenm3*$^{+}$ ACs are labelled with GCaMP5 (green). INL, inner nuclear layer; GCL, ganglion cell layer; IPL, inner plexiform layer. Scale bar is 20 µm. **B,** Percentage of GCaMP5^{+} cells co-localising with antigen^{+} cells (mean ± SD). GABA, n = 13 retinae; Parvalbumin, n = 10 retinae; TH, n = 9 retinae; ChAT, n = 10 retinae; Glycine, n = 5 retinae. Note that most *tenm3*$^{+}$ ACs are GABAergic (54.2 ± 4.2%). **C**|**D,** Average number (**C**) and relative frequency (**D**) of DS, OS, visually responsive and non-DS/non-OS voxels per Z-plane in 4 dpf *Tg(isl2b:Gal4;UAS:SyGCaMP3)* larvae (n = 15 larvae) before (control) and after (picrotoxin) the application of picrotoxin (100 µM). Error bars are ± SEM. **p < 0.01, ***p < 0.001, paired two-tailed Student's t test. **E**|**F,** Cumulative distributions of DSI values (R^2 > 0) across voxels with OSI < 0.5 (**E**) and OSI values (R^2 > 0) across voxels with DSI < 0.5 (**F**) before (control) and after (picrotoxin) the application of picrotoxin (100 µM). ***p < 0.001, two-sample Kolmogorov-Smirnov test. **G**|**H,** Cumulative histograms summarising the incidence of preferred angles for identified DS (**G**) and OS voxels (**H**) in 4 dpf larvae (n = 15 larvae) before (control) and after (picrotoxin) the application of picrotoxin (100 µM). Overlaid curves are the fitted Gaussian distributions for each DS or OS subtype. Polar plots illustrate the mean (+ 1 SD) normalised response profiles for each DS or OS subtype.

the least affected by the pharmacological block (magenta, Fig. 6.5H). RGC direction selectivity was also negatively impacted (Fig. 6.5C-G; number of DS voxels per Z-plane, mean ± SEM, control 665.9 ± 101.3; picrotoxin 223.6 ± 72.13, n = 15 larvae; two-tailed paired t-test, t_{14} = 3.57, p = 0.0030). Since directionally tuned GABAergic inputs from SACs play a key role in most mammalian DSGCs (Vaney et al., 2012), this observation suggests that a similar inhibitory mechanism may also be present in zebrafish. Compared to the impairments in RGC direction and orientation selectivity caused by blocking $GABA_A$ receptors, the effects produced by blocking glycine receptors using strychnine (70 µM) were minimal (Fig. 6.6; number of DS voxels per Z-plane, mean ± SEM, control 1355.0 ± 166.1; strychnine 1032.0 ± 161.8, n = 11 larvae;

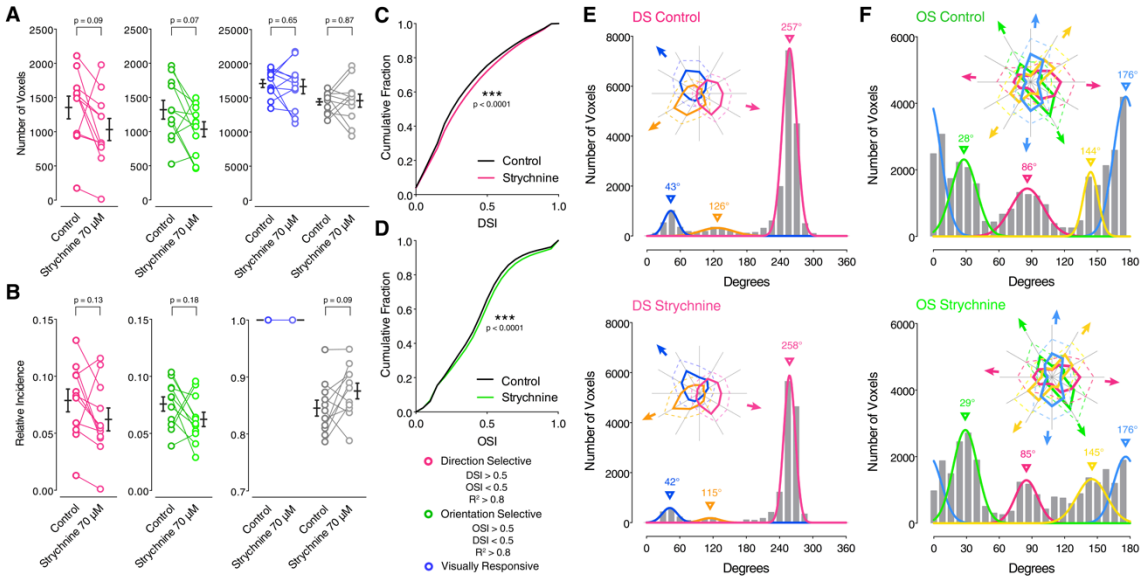

Figure 6.6. Glycinergic inhibition is not essential for RGC orientation selectivity. A|**B,** Average number (**A**) and relative frequency (**B**) of DS, OS, visually responsive and non-DS/non-OS voxels per Z-plane in 5 dpf *Tg(isl2b:Gal4;UAS:SyGCaMP3)* larvae (n = 11 larvae) before (control) and after (strychnine) the application of strychnine (70 µM). Error bars are ± SEM. Paired two-tailed Student's t test. **C**|**D,** Cumulative distributions of DSI values ($R^2 > 0$) across voxels with OSI < 0.5 (**C**) and OSI values ($R^2 > 0$) across voxels with DSI < 0.5 (**D**) before (control) and after (strychnine) the application of strychnine (70 µM). ***p < 0.001, two-sample Kolmogorov-Smirnov test. **E**|**F,** Cumulative histograms summarising the incidence of preferred angles for identified DS (**E**) and OS voxels (**F**) in 5 dpf larvae (n = 11 larvae) before (control) and after (strychnine) the application of strychnine (70 µM). Overlaid curves are the fitted Gaussian distributions for each DS or OS subtype. Polar plots illustrate the mean (+ 1 SD) normalised response profiles for each DS or OS subtype.

two-tailed paired t-test, $t_{10} = 1.87$, p = 0.0909; number of OS voxels per Z-plane, mean ± SEM, control 1321.0 ± 137.3; strychnine 1035.0 ± 109.7; two-tailed paired t-test, $t_{10} = 2.02$, p = 0.0699). Given that only type II and III *tenm3*$^+$ ACs are orientation-tuned, anti-GABA immunostaining of sparsely eGFP-labelled *tenm3*$^+$ ACs was performed to see whether these two AC types are GABAergic. Consistent with the above results, both type II and III *tenm3*$^+$ ACs do indeed express the neurotransmitter GABA (Fig. 6.7). Overall, these data suggest that OSGCs require GABAergic inhibitory input, likely provided by type II and III *tenm3*$^+$ ACs, to acquire their orientation tuning.

6.2.3 Tenm3$^+$ *ACs are Required for OSGC Tuning*

To directly test whether *tenm3*$^+$ ACs play a central role in the emergence of RGC orientation selectivity, the *Tg(tenm3:Gal4)* line was used to selectively ablate these cells and assess the functional consequences in RGCs. In the *Tg(tenm3:Gal4;UAS:KillerRed;elavl3:GCaMP5G)* line, the genetically encoded photosensitiser KillerRed (Bulina et al., 2006b) is expressed in *tenm3*$^+$ ACs, whereas GCaMP5G is expressed pan-neuronally (Fig. 6.8) (Ahrens et al., 2013). At 2 dpf, *tenm3*$^+$ ACs were

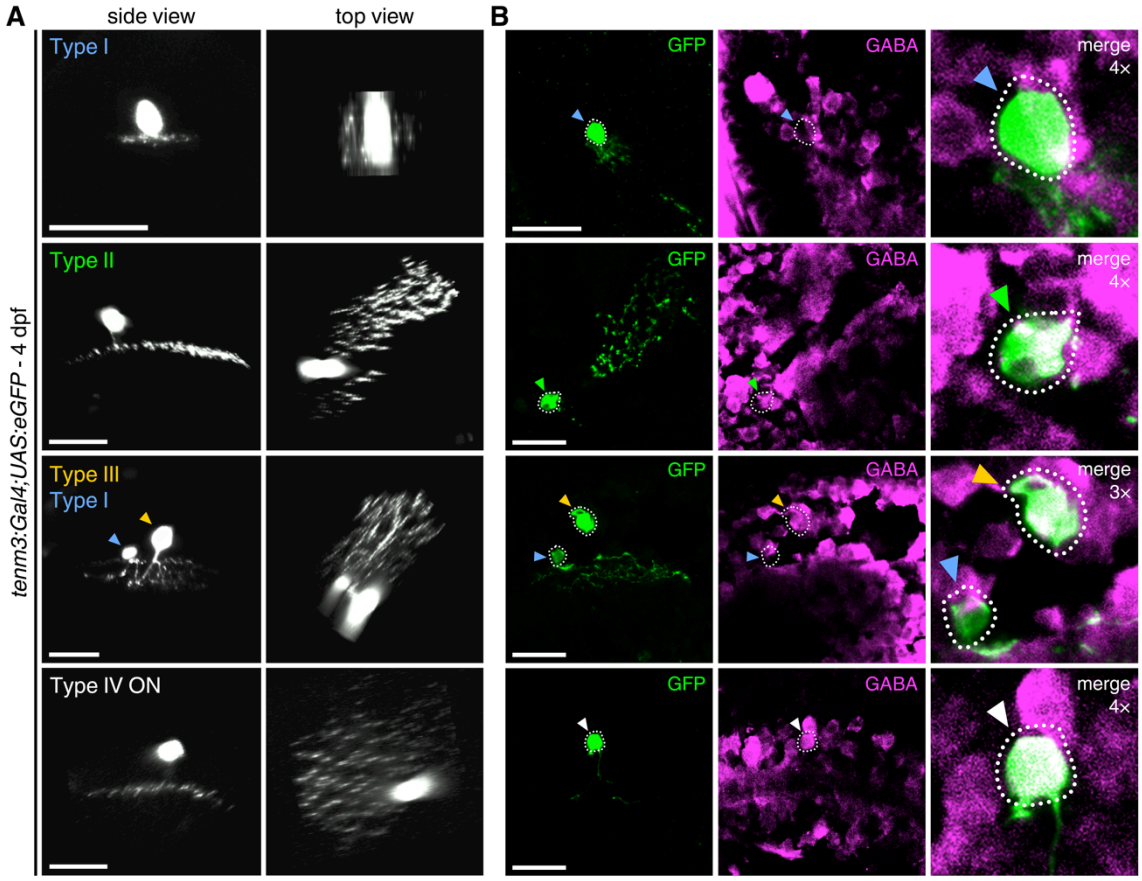

Figure 6.7. Type II-IV, but not type I, *tenm3*$^{+}$ amacrine cells are GABAergic. A, Mosaically labelled *tenm3*$^{+}$ ACs expressing eGFP in 4 dpf *UAS:eGFP*-injected *Tg(tenm3:Gal4)* larvae. Both side views (left) and top views (right) are shown. Scale bars are 20 µm. **B,** Immunostaining showing the expression of γ-aminobutyric acid (GABA; magenta) in the identified eGFP-expressing *tenm3*$^{+}$ ACs (green) reported in (**A**). Arrowheads are colour-coded according to the *tenm3*$^{+}$ AC type each cell is classified into. Note that both type II (green arrowheads) and type III (yellow arrowheads) *tenm3*$^{+}$ ACs express the neurotransmitter GABA. Interestingly, type I *tenm3*$^{+}$ ACs (cyan arrowheads) do not appear to express GABA. Note that the merged images (right) have been enlarged by the reported magnification factors to help visualisation. Scale bars are 20 µm.

optogenetically ablated by illuminating the retina with intense green light (540-552 nm) for 40 minutes (Fig. 6.9 and 6.10). Subsequently, at 4 dpf, RGC visual responses to moving bars were recorded in the optic tectum through calcium imaging (Movie 6.2). To isolate RGC axonal calcium responses from tectal cell dendritic responses the glutamate receptor antagonists APV and NBQX (100 µM and 20 µM, respectively) were locally applied in the tectum (Fig. 6.8) (Hunter et al., 2013). Unlike KillerRed-positive larvae, control larvae subjected to the same procedures did not exhibit retinal cell death (Fig. 6.10B; n = 3 larvae for each group). Notably, larvae subjected to *tenm3*$^{+}$ AC ablation, showed a dramatic impairment in RGC orientation selectivity, but no detrimental change in DSGC responses (Fig. 6.11A-D; number of OS voxels per Z-plane, mean ± SEM, control 328.00 ± 82.64, n = 16 larvae; ablated 78.63 ± 20.91,

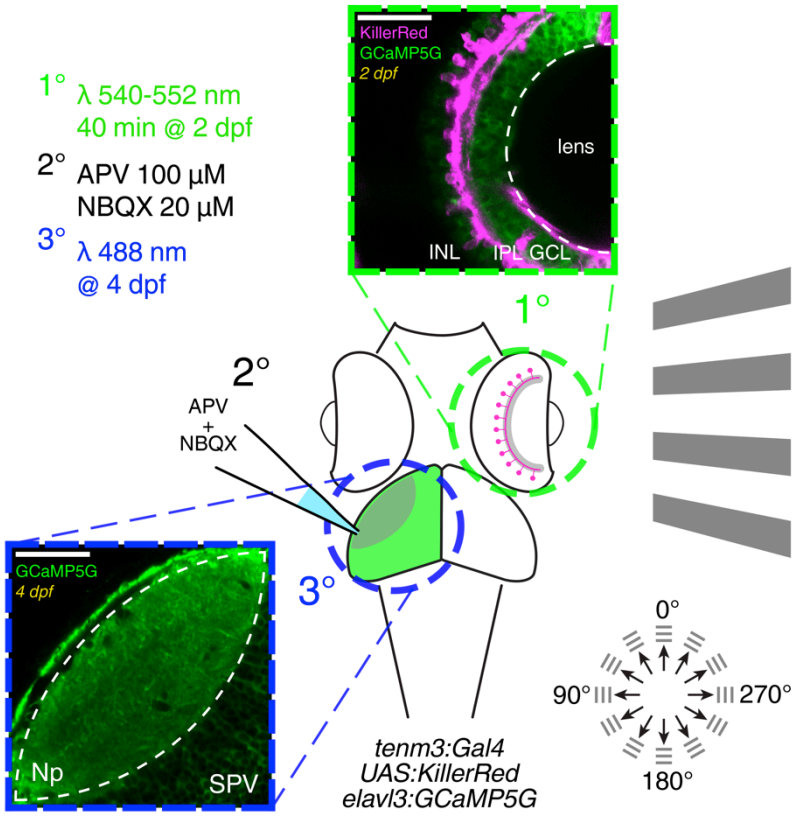

Figure 6.8. Functional analysis of RGC output following *tenm3*$^{+}$ amacrine cell ablation. Summary of the experimental procedures used to record visual responses from larvae where *tenm3*$^{+}$ ACs were optogenetically ablated. At 2 dpf, the eyes of *Tg(tenm3:Gal4;UAS:KillerRed;elavl3:GCaMP5G)* larvae, where KillerRed is selectively expressed in *tenm3*$^{+}$ ACs only (magenta), are illuminated with green light (540-552 nm) for 40 minutes. Then, at 4 dpf, visual responses to moving bars are recorded through calcium imaging of RGC axon terminals (expressing GCaMP5G; green) in the optic tectum contralateral to the illuminated eye. Local application of the glutamate receptor antagonists APV and NBQX (100 µM and 20 µM, respectively) is used to isolate RGC axonal calcium responses from tectal cell dendritic responses. INL, inner nuclear layer; GCL, ganglion cell layer; IPL, inner plexiform layer; Np, neuropil; SPV, stratum periventriculare. Scale bars are 40 µm.

n = 16 larvae; two-tailed unpaired t-test with Welch's correction, $t_{16.91}$ = 2.92, p = 0.0095; relative frequency of OS voxels per Z-plane, mean ± SEM, control = 0.0631 ± 0.0124; ablated: 0.0211 ± 0.0048; two-tailed unpaired t-test with Welch's correction, $t_{19.45}$ = 3.14, p = 0.0052; number of DS voxels per Z-plane, mean ± SEM, control 14.44 ± 3.57; ablated 11.88 ± 3.66; two-tailed unpaired t-test, t_{30} = 0.50, p = 0.62; relative frequency of DS voxels per Z-plane, mean ± SEM, control 0.0039 ± 0.0011; ablated 0.0026 ± 0.0007; two-tailed unpaired t-test, t_{30} = 0.94, p = 0.35). The extent of the decrease in number of OS voxels, relative proportion of OSGC output and overall degree of RGC orientation selectivity was analogous to what was observed in *tenm3*^{KO} mutants and following pharmacological block of GABAergic inhibition. Moreover, the OSGC subpopulation tuned to vertical stimuli was the least affected by *tenm3*$^{+}$ AC ablation (magenta, Fig. 6.11F), matching the *tenm3* knockout and GABA block results.

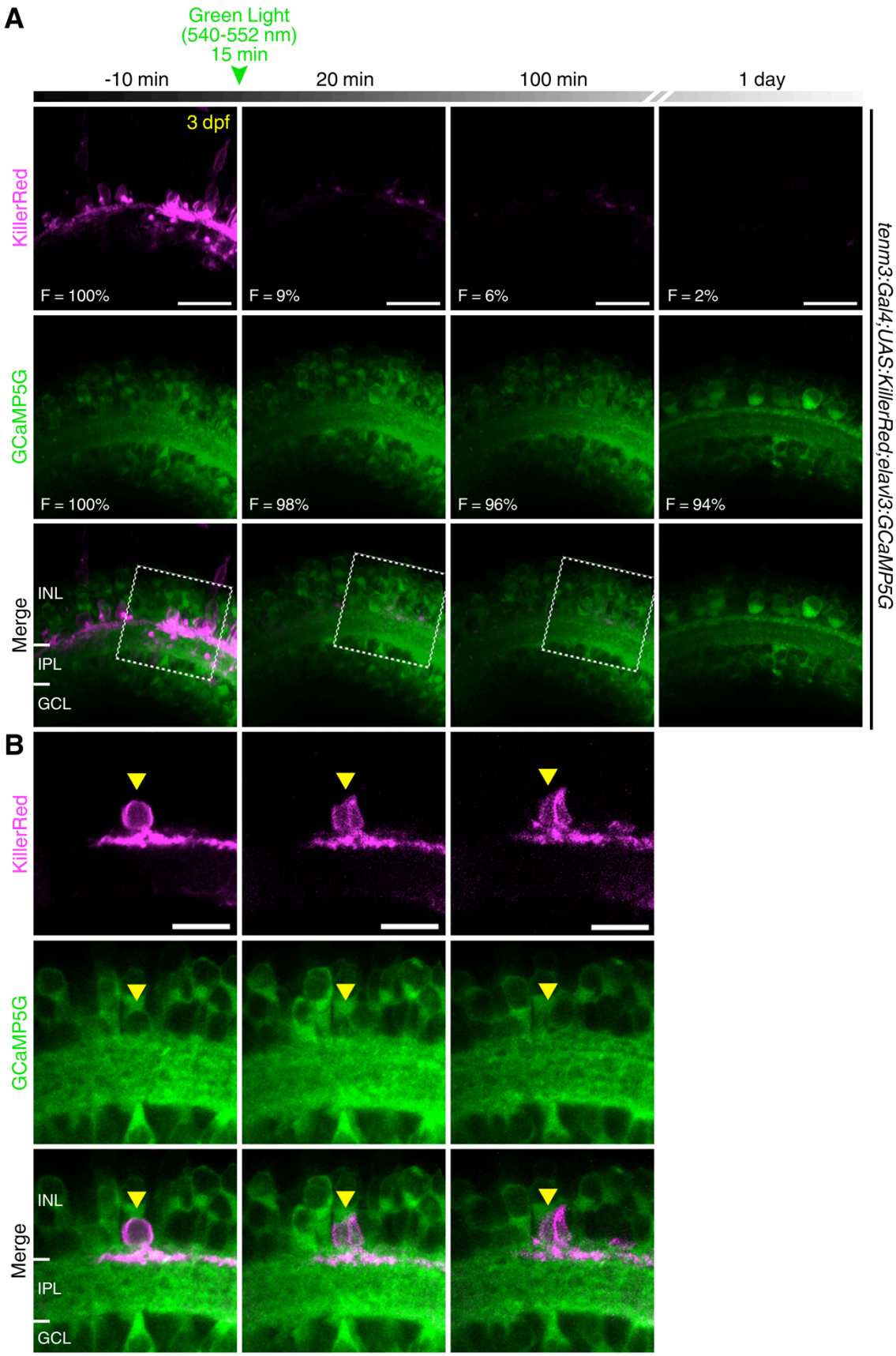
A
Green Light
(540-552 nm)
15 min
-10 min
20 min
100 min
1 day
3 dpf
KillerRed
GCaMP5G
Merge
F = 100%
F = 9%
F = 6%
F = 2%
F = 100%
F = 98%
F = 96%
F = 94%
INL
IPL
GCL
tenm3:Gal4;UAS:KillerRed;elavl3:GCaMP5G
B
KillerRed
GCaMP5G
Merge
INL
IPL
GCL

Figure 6.9. KillerRed photobleaching and light-induced cellular toxicity. A, Proof-of-principle experiment showing the effects of 15 minutes illumination with green light on the KillerRed (magenta) fluorescence level (F) in the retina of a 3 dpf *Tg(tenm3:Gal4; UAS:KillerRed;elavl3:GCaMP5G)* larva. Strikingly, strong photobleaching (~90% decrease in fluorescence) is observed after green light illumination, indicating effective KillerRed phototoxicity. This large decrease in KillerRed fluorescence is visible even one day after illumination. No significant decrease in the overall GCaMP5G fluorescence (green) is detected after illumination. Importantly, all images were obtained using the same acquisition settings. Scale bars are 20 µm. **B,** Inset of (**A**) showing the dramatic morphological changes of a single KillerRed-expressing *tenm3*$^{+}$ AC (yellow arrowhead) following green light illumination. Notably, also the GCaMP5G fluorescence appears to decrease in this cell, probably due to the production of phototoxic reactive oxygen species in the cytoplasm. The magenta channel signal has been increased post-acquisition to compensate for the ~90% decrease in fluorescence resulting from the illumination procedure. Inner nuclear layer, INL; GCL, ganglion cell layer; IPL, inner plexiform layer. Scale bars are 10 µm.

Compared to data acquired using the *Tg(isl2b:Gal4;UAS:SyGCaMP3)* line (Fig. 6.7E,F), differences in the relative proportions of DSGC and OSGC subtypes as well as in their preferred directions or orientations were observed both in control and *tenm3*$^{+}$ AC ablated groups (Fig. 6.11E,F), likely resulting from the use of a different transgenic line or the pharmacological treatment used to isolate RGC responses. The results obtained by ablating *tenm3*$^{+}$ ACs strongly support the hypothesis that the output of *tenm3*$^{+}$ ACs is crucial in generating RGC orientation selectivity.

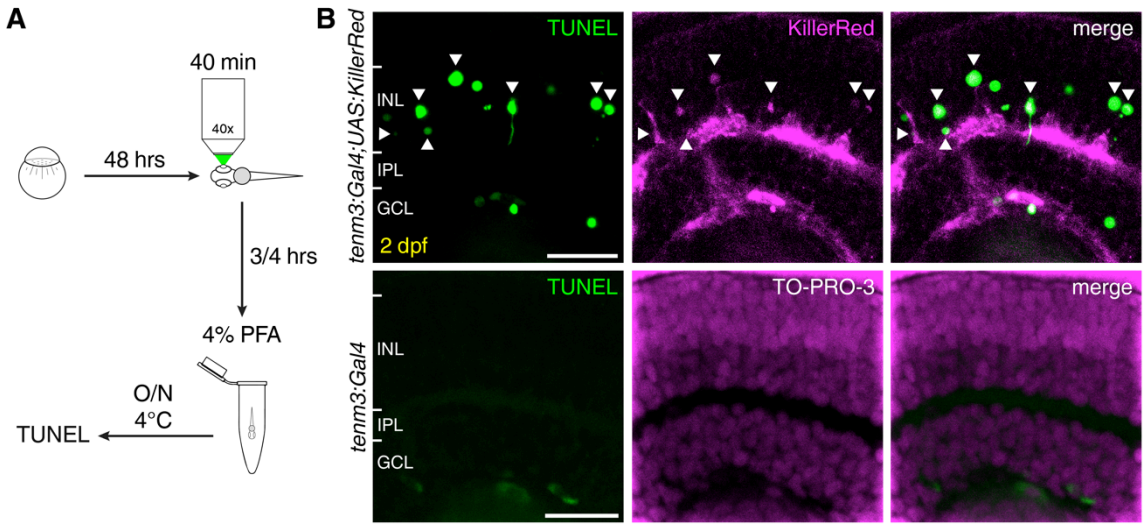

Figure 6.10. Optogenetic ablation of *tenm3*$^{+}$ amacrine cells using KillerRed. A, Schematic summarising the experimental procedure used to validate the optogenetic ablation of *tenm3*$^{+}$ ACs. At 2 dpf, the eyes of *Tg(tenm3:Gal4;UAS:KillerRed)* and *Tg(tenm3:Gal4)* control larvae were illuminated with intense green light (540-552 nm) for 40 minutes using a wide-field fluorescence microscope equipped with a 40× objective. After 3-4 hours, the larvae were fixed in 4% paraformaldehyde (PFA) at 4°C overnight (O/N). Subsequently, larvae were cryosectioned and fluorometric terminal deoxynucleotidyl transferase dUTP nick end labeling (TUNEL) assays were performed on sections following standard protocols. **B,** TUNEL staining (green) shows the presence of apoptotic nuclei characteristic of dying cells in the retinae of 2 dpf *Tg(tenm3:Gal4;UAS:KillerRed)* larvae following 40 minutes of green light illumination (top, n = 3 larvae). In these larvae KillerRed (magenta) is selectively expressed in *tenm3*$^{+}$ ACs. White arrowheads indicate the sites of co-localisation between KillerRed^{+} cell bodies and TUNEL^{+} apoptotic nuclei in the inner nuclear layer (INL). Importantly, no cell death is detected in the retinae of 2 dpf *Tg(tenm3:Gal4)* control larvae that were subjected the same illumination procedure (bottom, n = 3 larvae). In the bottom panel, cell bodies are labelled with the nuclear stain TO-PRO-3 (magenta). GCL, ganglion cell layer; IPL, inner plexiform layer. Scale bars are 20 µm.

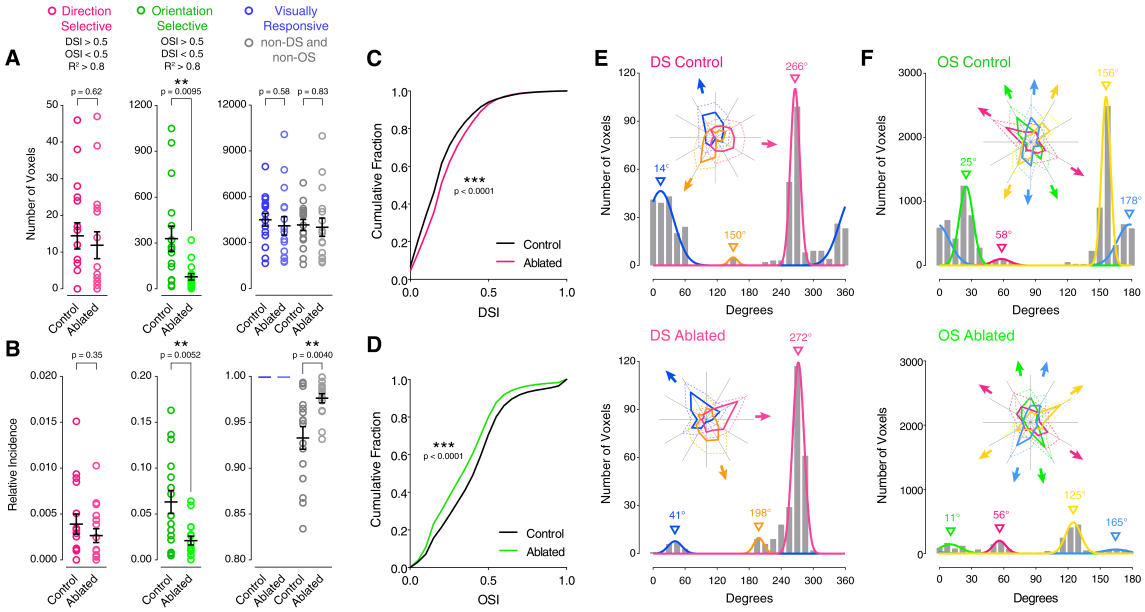

Figure 6.11. *Tenm3*$^+$ amacrine cells are required for RGC orientation selectivity. A|**B,** Average number (**A**) and relative frequency (**B**) of DS, OS, visually responsive and non-DS/non-OS voxels per Z-plane in control (n = 16 larvae) and *tenm3*$^+$ AC ablated (n = 16 larvae) 4 dpf larvae. Error bars are ± SEM. **p < 0.01, unpaired two-tailed Student's t test. **C**|**D,** Cumulative distributions of DSI values ($R^2 > 0$) across voxels with OSI < 0.5 (**C**) and OSI values ($R^2 > 0$) across voxels with DSI < 0.5 (**D**) in control and *tenm3*$^+$ AC ablated larvae. ***p < 0.001, two-sample Kolmogorov-Smirnov test. **E**|**F,** Cumulative histograms summarising the incidence of preferred angles for identified DS (**E**) and OS voxels (**F**) in control (n = 16; top) and *tenm3*$^+$ AC ablated (n = 16; bottom) 4 dpf larvae. Overlaid curves are the fitted Gaussian distributions for each DS or OS subtype. Polar plots illustrate the mean (+ 1 SD) normalised response profiles for each DS or OS subtype.

6.2.4 Neurite Co-stratification between OSGCs and Tenm3$^+$ *ACs*

An indication of potential synaptic connections between *tenm3*$^+$ ACs and OSGCs would be their neurite co-stratification in the IPL. Currently, no molecular marker or transgenic line exists to selectively label OSGCs and directly detect neurite co-stratification with *tenm3*$^+$ ACs. Therefore, individual RGCs were sparsely labelled with GCaMP6f (Chen et al., 2013a) and, after having functionally identified OSGCs, post-hoc immunostaining using antibodies against GCaMP6f was performed to analyse their IPL stratification pattern (Fig. 6.12A-D). Then, fluorescence intensity profiles of dendritic stratification from multiple OSGCs (5 out of 39 cells in 39 larvae) were averaged, and the resulting mean profile was overlaid to the IPL stratification profile of *tenm3*$^+$ ACs (Fig. 6.12E,F). Strikingly, as a population OSGCs stratify their dendrites in 3 strata located at 9%, 61% and 90% IPL depth, and show a high degree of overlap with the stratification profile of *tenm3*$^+$ AC neurites (Fig. 6.12F). These anatomical results, together with the functional data described above, strongly support the idea that *tenm3*$^+$ ACs and OSGCs are part of a retinal circuit computing orientation selectivity.

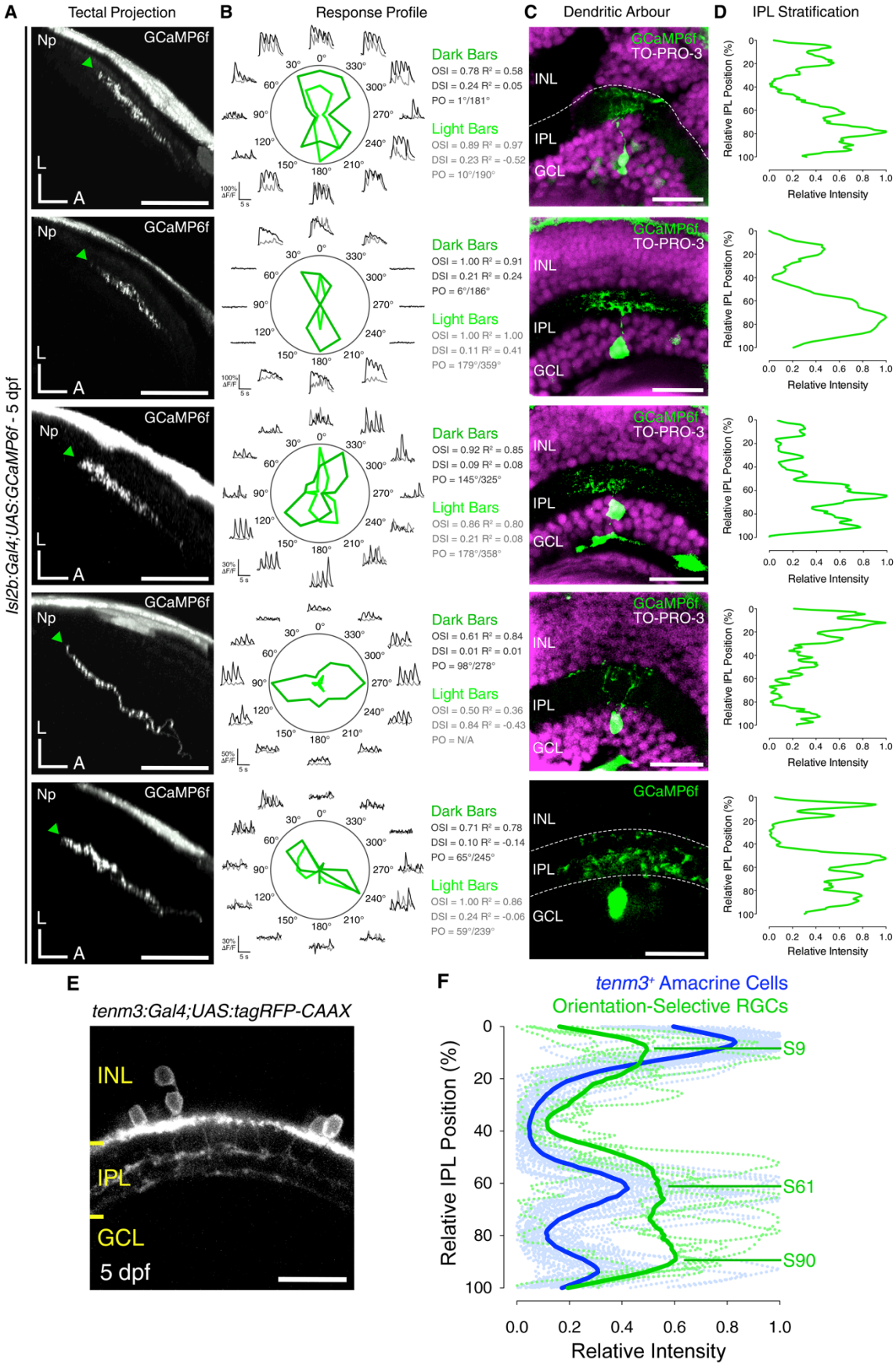
A
Tectal Projection
B
Response Profile
C
Dendritic Arbour
D
IPL Stratification
Isl2b:Gal4;UAS:GCaMP6f - 5 dpf
Np
GCaMP6f
L
A
Dark Bars
OSI = 0.78 R² = 0.58
DSI = 0.24 R² = 0.05
PO = 1°/181°
Light Bars
OSI = 0.89 R² = 0.97
DSI = 0.23 R² = -0.52
PO = 10°/190°
GCaMP6f
TO-PRO-3
INL
IPL
GCL
Relative IPL Position (%)
Relative Intensity
Dark Bars
OSI = 1.00 R² = 0.91
DSI = 0.21 R² = 0.24
PO = 6°/186°
Light Bars
OSI = 1.00 R² = 1.00
DSI = 0.11 R² = 0.41
PO = 179°/359°
Dark Bars
OSI = 0.92 R² = 0.85
DSI = 0.09 R² = 0.08
PO = 145°/325°
Light Bars
OSI = 0.86 R² = 0.80
DSI = 0.21 R² = 0.08
PO = 178°/358°
Dark Bars
OSI = 0.61 R² = 0.84
DSI = 0.01 R² = 0.01
PO = 98°/278°
Light Bars
OSI = 0.50 R² = 0.36
DSI = 0.84 R² = -0.43
PO = N/A
Dark Bars
OSI = 0.71 R² = 0.78
DSI = 0.10 R² = -0.14
PO = 65°/245°
Light Bars
OSI = 1.00 R² = 0.86
DSI = 0.24 R² = -0.06
PO = 59°/239°
E
tenm3:Gal4;UAS:tagRFP-CAAX
INL
IPL
GCL
5 dpf
F
tenm3⁺ Amacrine Cells
Orientation-Selective RGCs
S9
S61
S90
Relative IPL Position (%)
Relative Intensity

Figure 6.12. IPL dendritic co-stratification between OSGCs and *tenm3*$^+$ amacrine cells. A, Side views of axon projections (green arrowheads) of individual OSGCs expressing GCaMP6f in the optic tectum of 5 dpf *UAS:GCaMP6f*-injected *Tg(isl2b:Gal4)* larvae. Np, neuropil; A, anterior; L, lateral. Scale bars are 40 µm. **B,** Functional identification of individual OSGCs through analyses of their visual responses to moving bars. Polar plots represent the tuning profiles (obtained by calculating the integral response to each stimulus) of OSGCs for dark and light moving bars (dark and light green, respectively). Black and grey traces represent the $\Delta F/F_0$ calcium responses to moving dark and light bars, respectively. OSI, orientation selectivity index; DSI, direction selectivity index; R^2, Gaussian goodness of fit; PO, preferred orientation. **C**|**D,** Immunostaining for GCaMP6f (green) showing the dendritic morphology of functionally identified OSGCs (**C**) and corresponding normalised IPL fluorescence intensity profiles (**D**). 0% corresponds to the INL/IPL boundary, whereas 100% corresponds to the IPL/GCL boundary. Cell bodies are labelled with the nuclear stain TO-PRO-3 (magenta). INL, inner nuclear layer; GCL, ganglion cell layer; IPL, inner plexiform layer. Scale bars are 20 µm. **E,** IPL stratification of *tenm3*$^+$ AC neurites in 5 dpf *Tg(tenm3:Gal4;UAS:tagRFP-CAAX)* larvae. Scale bar is 20 µm. **F,** IPL fluorescence intensity profiles of OSGCs (green; n = 5 cells) and *tenm3*$^+$ AC neurites (blue; n = 13 larvae) at 5 dpf. 12.8% of functionally imaged RGCs were OS (5 out of 39 cells in 39 larvae). Thin traces represent individual IPL profiles, whereas thick traces indicate average IPL profiles. Fluorescence peaks indicating IPL strata formed by OSGC dendrites are labelled with the letter 'S' followed by their relative IPL position.

6.2.5 Orientation-selective Responses in Bipolar Cell Presynaptic Terminals

Since ACs have been shown to modulate BC output at the level of individual presynaptic terminals (Tachibana and Kaneko, 1988; Asari and Meister, 2012, 2014), tuned inhibitory input from type II and III *tenm3*$^+$ ACs could potentially generate orientation tuning in BC presynaptic terminals. To start investigating this idea calcium imaging was performed in the retinae of *Tg(-1.8ctbp2:SyGCaMP6)* larvae, where BC ribbon synapses are selectively labelled with SyGCaMP6 (Fig. 6.13A and Movie 6.3) (Johnston et al., 2014). Interestingly, some bipolar cell presynaptic terminals showed orientation-tuned responses across multiple trials (Fig. 6.13B-D, ROI #1). Voxel-wise analyses using different metrics of orientation selectivity (i.e., OSI and circular variance) and progressively higher tuning stringency levels further confirmed that a fraction of BC responses (~5% of visually responsive voxels) is indeed highly orientation-selective (OSI > 0.5, DSI < 0.5, R^2 > 0.8; Fig. 6.14A-C; n = 20 larvae). The degree of orientation selectivity across the whole population of BC terminals appeared to be lower than the *tenm3*$^+$ AC population, and more similar to RGCs (Fig. 6.15A,C). Similarly to OSGCs and *tenm3*$^+$ ACs, the preferred stimulus orientations of OS responses fall into four subpopulations tuned to gratings oriented along the cardinal (18°, 99°) and diagonal axes (44°, 149°; Fig. 6.14D). These results indicate that orientation selectivity is present in the synaptic output of some bipolar cell terminals.

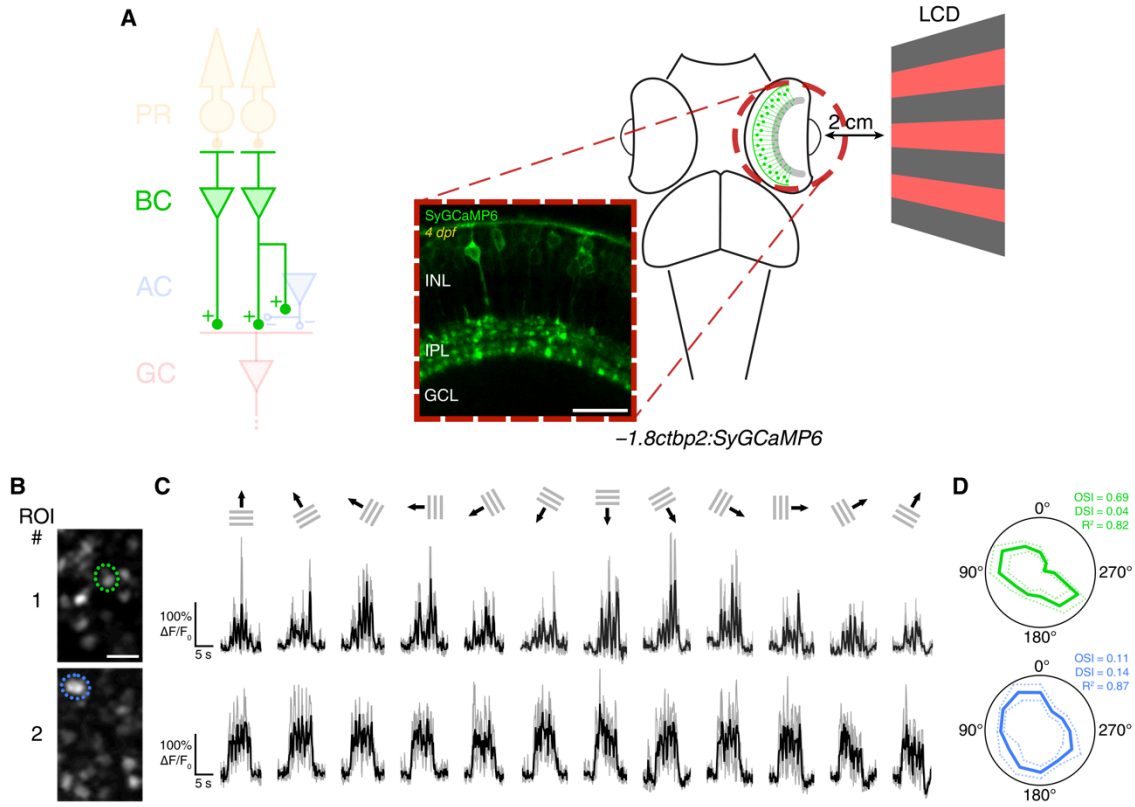

Figure 6.13. Analysis of orientation selectivity in bipolar cell terminals. A, Two-photon functional calcium imaging of BC ribbon synapses expressing SyGCaMP6 (green) in 4 dpf *Tg(-1.8ctbp2:SyGCaMP6)* larvae. Distance of the eye from LCD screen is 2 cm. Recordings are performed from 2-4 Z-planes (approximately 20 µm total volume thickness). Scale bar is 20 µm. **B-D,** Examples of visual responses to moving gratings in two BC terminals. **B,** Images showing the mean fluorescence across tuning experiments with identified regions of interest (ROIs). Scale bar is 5 µm. **C,** calcium responses of the two ROIs in (**B**) with black traces representing the average responses across three trials (grey traces) for each stimulus epoch. **D,** Polar plots illustrating the mean response profile (± SD, dotted lines) of each ROI with corresponding orientation selectivity index (OSI), direction selectivity index (DSI) and sum of two Gaussians distribution goodness of fit (R^2) values. Note that ROI #1 shows orientation selective responses.

6.2.6 Correlation between OS Subpopulations in Tenm3⁺ ACs, BCs and RGCs

Can *tenm3*⁺ ACs generate orientation selectivity in both RGCs and BCs? If activation of type II or III *tenm3*⁺ ACs along a particular axis in the visual field leads to inhibition of responses along that axis, one would expect that the distribution of OS subpopulations in *tenm3*⁺ ACs is inversely correlated to the distributions observed in BCs and RGCs. To test this idea, the frequency distributions of the four OS subpopulations in *tenm3*⁺ ACs, BCs and RGCs were analysed (Fig. 6.15D,E; relative proportion of OS subpopulations, *tenm3*⁺ ACs pop-1 18.58%, pop-2 56.50%, pop-3 18.78%, pop-4 6.14%, n = 20 larvae; BCs pop-1 58.22%, pop-2 14.53%, pop-3 5.95%, pop-4 21.30%, n = 20; RGCs pop-1 34.25%, pop-2 9.09%, pop-3 6.34%, pop-4 50.32%, n = 23). As expected, the *tenm3*⁺ AC distribution was found to be anti-correlated to BC and RGC

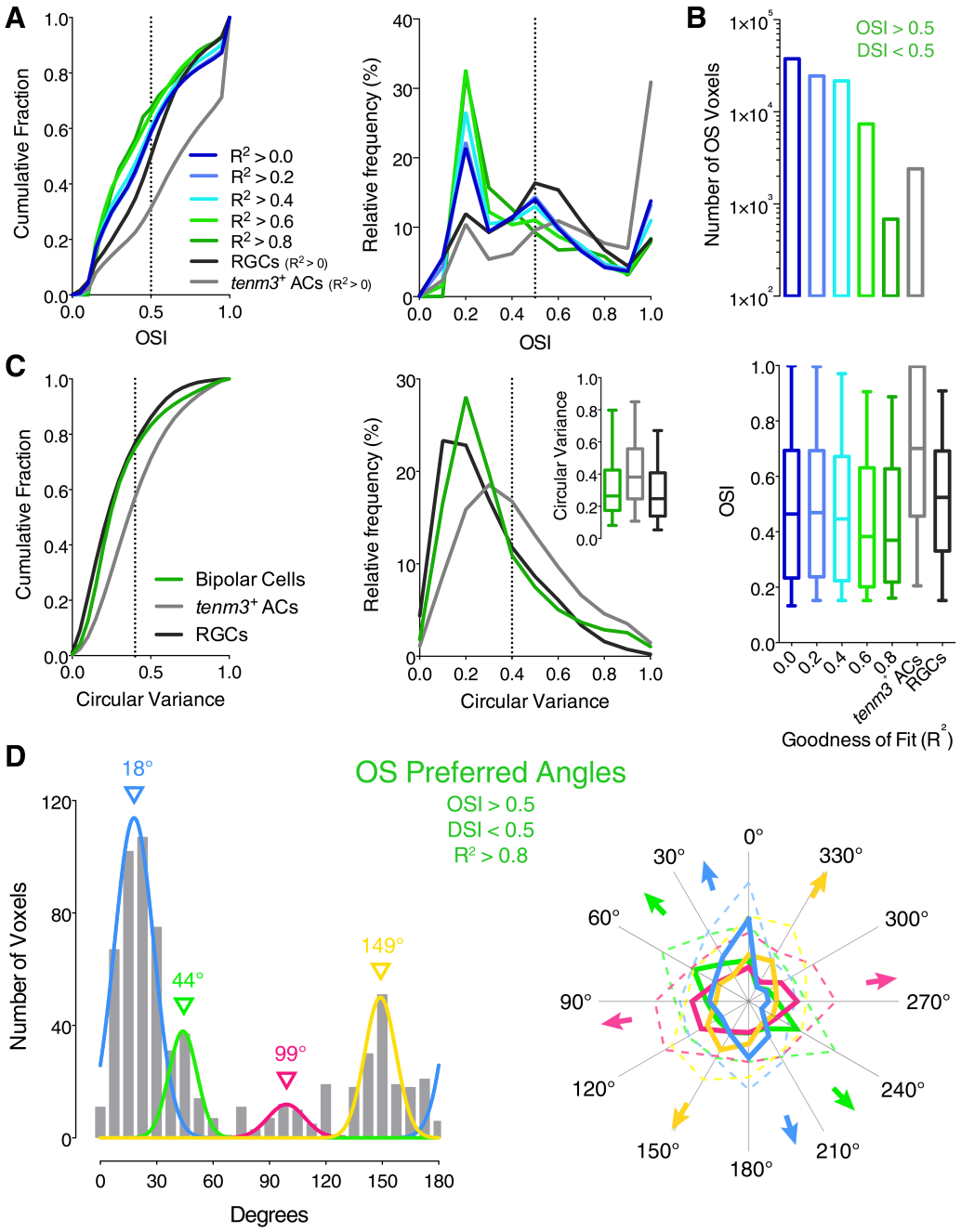

Figure 6.14. A fraction of bipolar cell terminals is orientation-tuned. A, Cumulative distribution (left) and relative frequency (right) of orientation selectivity index (OSI) values across voxels with DSI < 0.5 in BCs (n = 20 larvae), *tenm3*$^{+}$ ACs (grey, n = 20 larvae) and RGCs (black, n = 23 larvae). The colour code indicates the progressively higher goodness of fit (R^2 of the fitted von-Mises profiles) criteria applied to the data to identify voxels characterised by high orientation selectivity. The black dotted lines indicate the OSI threshold used to identify OS responses (OSI > 0.5). Depending on the R^2 value chosen as threshold, the number of voxels that satisfy the criteria, and therefore are represented in the distributions, varies. **B,** Total number of OS voxels (top) and distribution of OSI values (bottom) using progressively higher R^2 values in BCs, *tenm3*$^{+}$ ACs (grey, $R^2 > 0$) and RGCs (black, $R^2 > 0$). Boxplots indicate interquartile ranges (boxes), medians (lines in boxes) and 10-90 percentiles (whiskers). **C,** Cumulative distribution (left) and relative frequency (right) of circular variance values across all voxels in BCs (green, n = 20 larvae), *tenm3*$^{+}$ ACs (grey, n = 20 larvae) and RGCs (black, n = 23 larvae). The black dotted lines indicate the circular variance threshold used to identify OS responses (circular variance < 0.4). Boxplots in the right inset indicate interquartile ranges (boxes), medians (lines in boxes) and 5-95 percentiles (whiskers). **D,** Cumulative histogram summarising the incidence of preferred angles for identified OS BC voxels in 4 dpf larvae (n = 20 larvae). Overlaid curves are the fitted Gaussian distributions for each OS subtype. Polar plots illustrate the mean (+ 1 SD) normalised response profiles for each OS subtype.

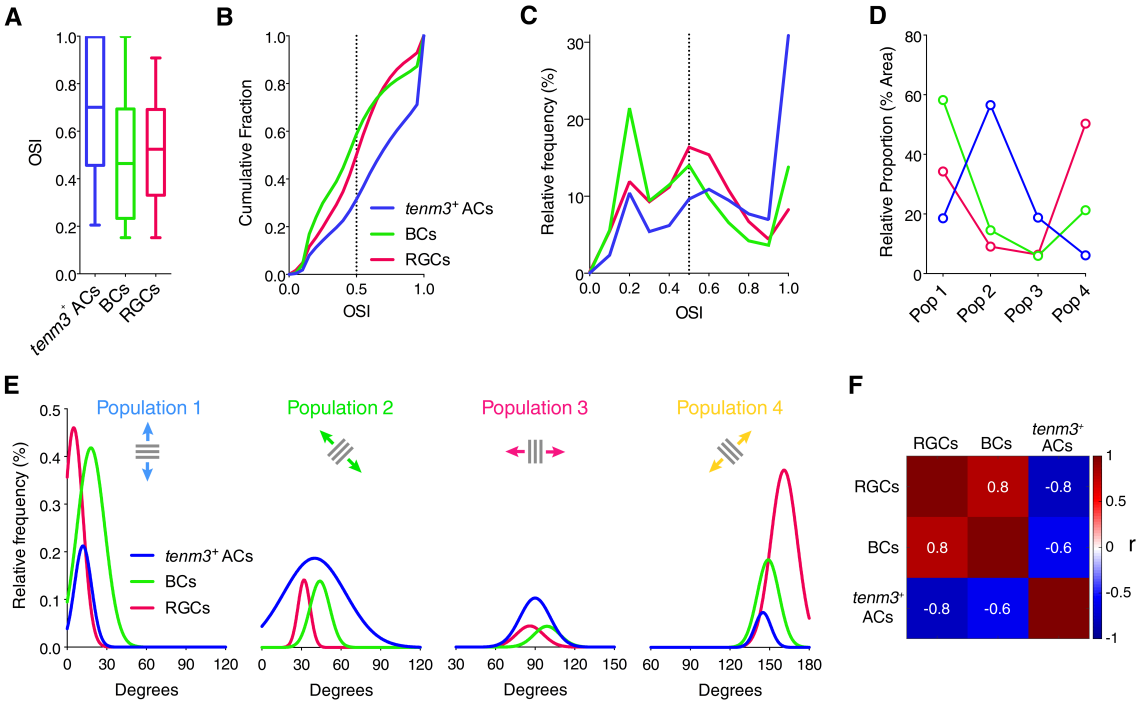

Figure 6.15. *Tenm3*$^+$ amacrine cells likely provide orthogonal orientation-tuned inhibitory input to RGCs and bipolar cell terminals. A-C, Degree of orientation selectivity (quantified by the OSI) across voxels with DSI < 0.5 and R^2 > 0 in *tenm3*$^+$ ACs (blue, n = 20 larvae), BCs (green, n = 20 larvae) and RGCs (red, n = 23 larvae). Box plots in (**A**) indicate interquartile ranges (boxes), medians (lines in boxes) and 10-90 percentiles (whiskers). The black dotted lines in (**B**) and (**C**) indicate the OSI threshold used to identify OS responses (OSI > 0.5). **D,** Relative proportions of the four different OS subpopulations (Pop 1-4) in *tenm3*$^+$ ACs (blue), BCs (green) and RGCs (red). Values are obtained by calculating the relative proportion (%) of the area under the normalised Gaussian curves in (**E**). **E,** Normalised frequency distributions of preferred stimulus orientations in OS *tenm3*$^+$ ACs (blue, n = 20 larvae), BCs (green, n = 20 larvae) and RGCs (red, n = 23 larvae). The Gaussian distributions of the four different OS subpopulations are reported in separate graphs. **F,** Correlation matrix showing Spearman's correlation coefficients (r) between the frequency distribution of the four OS subpopulations in *tenm3*$^+$ ACs, BCs and RGCs. Note the negative correlation between *tenm3*$^+$ ACs and BCs or RGCs.

distributions (Fig. 6.15F; Spearman's correlation coefficients, *tenm3*$^+$ ACs vs. RGCs r = – 0.8; *tenm3*$^+$ ACs vs. BCs r = – 0.6; RGCs vs. BCs r = 0.8). This not only indicates that the OS inhibition provided by type II and III *tenm3*$^+$ ACs to OSGCs is orthogonally tuned (i.e., tuned to the orientation orthogonal to the OSGC-preferred orientation), but also suggests that, similarly to OSGCs, orientation selectivity in BC terminals could be generated by orthogonal orientation-tuned inhibitory inputs from these *tenm3*$^+$ ACs.

6.3 Discussion

The vertebrate retina extracts information from visual scenes and sends it to higher brain areas through feature-specific neural pathways. Crucial neural substrates underlying this information processing in the retina are the stereotypic synaptic connections between defined neural cell types. How specific elements of the retinal circuitry perform computations is not yet completely understood. The data presented

here define cellular building blocks of a circuit in the larval zebrafish retina capable of detecting the orientation of elongated visual stimuli. In particular, the functional link between RGC orientation selectivity and the cell-adhesion molecule Tenm3 led to the identification of a class of genetically defined orientation-tuned ACs with elongated dendritic arbours. Pharmacological and cellular ablation experiments show that these *tenm3*$^{+}$ ACs and their GABAergic inhibitory output are crucial for the tuning of orientation-selective RGCs. In addition, orientation selectivity is also found among a fraction of bipolar cell presynaptic terminals. This study represents one of the most extensive characterisations of the retinal orientation-selective circuit in a single tractable system. By collecting functional and structural data from amacrine, bipolar and ganglion cells at cellular and population levels, a mechanistic explanation of how defined neural cell types in the retina generate a fundamental property of visual perception – i.e., orientation selectivity – is presented. Furthermore, these results elucidate the functional role of two novel AC types, therefore shedding some light on the most diverse and least understood retinal cell class (MacNeil et al., 1999).

6.3.1 A Circuit Model of Orientation Selectivity in the Retina

To integrate the obtained data into a general framework describing the computation of orientation selectivity in RGCs, a model of the retinal OS circuit was outlined. The model is based on the following principles: (a) the highly elongated dendritic fields of type II and III *tenm3*$^{+}$ ACs underlie their orientation tuning (Fig. 6.2 and 6.3). Specifically, these morphologically defined AC types respond maximally when the orientation of elongated visual stimuli coincides with the orientation of their dendritic fields. Interestingly, ACs characterised by elongated dendritic fields and orientation selectivity have been found also in the rabbit retina, although their genetic identity is still unknown (Bloomfield, 1994; Murphy-Baum and Taylor, 2015). (b) Type II and III *tenm3*$^{+}$ ACs provide orthogonal orientation-tuned inhibitory input to OSGCs and, potentially, BC presynaptic terminals (Fig. 6.15). This feedforward inhibition is mediated by GABA and generates orientation selectivity in OSGCs (Fig. 6.5, 6.11 and 6.12). Interestingly, pharmacological block of synaptic inhibition onto zebrafish BC terminals indicates that orientation selectivity in BC ribbon synapses is generated through AC inhibitory input (J. Johnston and L. Lagnado, personal communication), therefore supporting the idea that the OS inhibitory output of type II and III *tenm3*$^{+}$ ACs could be at the basis of orientation selectivity in both BCs and OSGCs. Studies in the rabbit and mouse retina showed that OSGCs receive preferred orientation-tuned excitatory inputs

and orthogonal orientation-tuned inhibitory inputs and, in rabbit, presynaptic GABAergic inhibition plays a pivotal role in the emergence of these OS inputs (Venkataramani and Taylor, 2010; Nath and Schwartz, 2016; Venkataramani and Taylor, 2016). Recent findings in *Drosophila* showed an analogous requirement of GABA signalling for orientation selectivity (Fisher et al., 2015), revealing strikingly similar mechanisms between vertebrates and invertebrates. (c) Stimulus orientation, not the axis of stimulus movement, is the visual feature OSGCs are selective to. This is supported by the observation that static gratings, even though less effective in eliciting RGC responses, produce results analogous to those obtained using moving gratings (Fig. 6.16). Again, such property has been observed in rabbit and mouse OSGCs as well (Levick, 1967; Nath and Schwartz, 2016). Additional mechanisms to those described here may contribute to the emergence of RGC orientation selectivity.

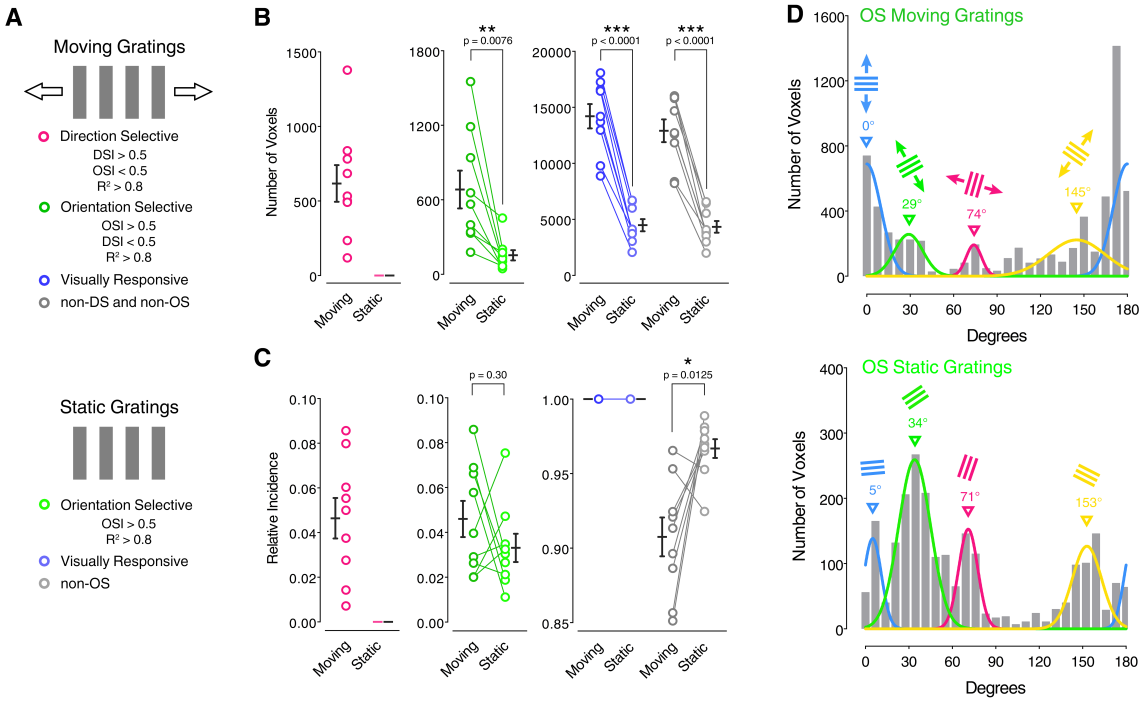

Figure 6.16. RGC orientation-selective responses using moving or static gratings. A, Diagram showing the criteria used to identify DS and OS voxels when using moving (top) or static gratings (bottom). The DSI cannot be calculated when using static stimuli, therefore only OS, visually responsive and non-OS voxels can be identified when larvae are stimulated with static gratings. **BIC,** Average number (**B**) and relative frequency (**C**) of DS, OS, visually responsive and non-DS/non-OS RGC voxels per Z-plane in 5 dpf *Tg(isl2b:Gal4;UAS:SyGCaMP3)* larvae (n = 9 larvae) using either moving or static gratings. Individual larvae are tested using both stimuli. Error bars are ± SEM. *p < 0.05, **p < 0.01, ***p < 0.001, paired two-tailed Student's t test. **D,** Cumulative histograms summarising the incidence of preferred angles for identified OS voxels in 5 dpf larvae (n = 9 larvae) using either moving (left) or static gratings (right). Overlaid curves are the fitted Gaussian distributions for each OS subtype, with the colour-coded bars indicating the preferred orientation of gratings. Note that, in both stimulus groups, OS populations with similar preferred angles are present, indicating that OSGCs are tuned to the stimulus orientation not its axis of movement.

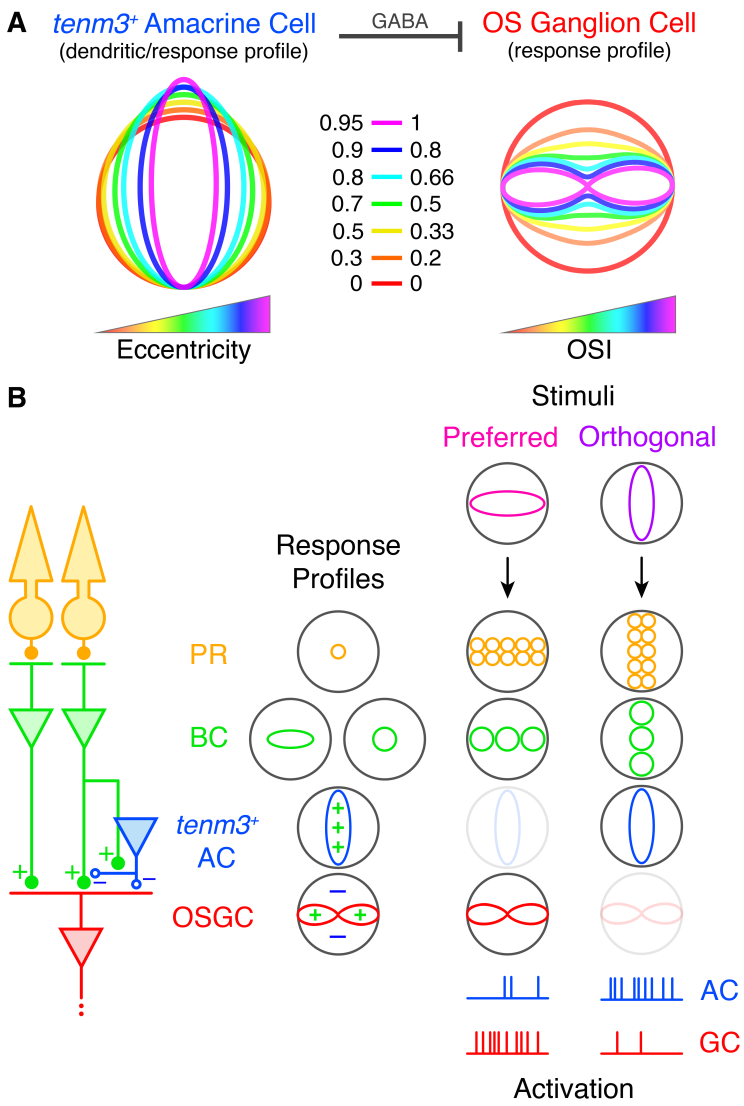

Figure 6.17. Circuit model of orientation selectivity in the retina. A, Hypothesised principles underlying the emergence of orientation selectivity in the retina. The high dendritic field elongation (quantified by the eccentricity of fitted elliptic profiles) of defined *tenm3*$^{+}$ AC types is at the basis of their high orientation tuning (left). Maximal activation of tuned AC types is obtained when the orientation of elongated visual stimuli coincides with the orientation of their dendritic fields. As a result, these tuned *tenm3*$^{+}$ AC types generate orientation selectivity in RGCs (quantified by the OSI, right) by providing orthogonal orientation-tuned GABAergic inhibitory input. The colour code describes the different levels of dendritic field elongation (left) and orientation selectivity (right). **B,** Examples of retinal OS circuit activation patterns for horizontal orientation-tuned OSGC preferred (magenta) and orthogonal (purple) stimuli. Excitatory input is indicated by '+' (full circles), whereas inhibitory input is indicated by '–' (empty circles). Putative synapses between OS *tenm3*$^{+}$ ACs and BC terminals are also represented. Tuning profiles of example photoreceptor (PR), bipolar cells (BCs), OS *tenm3*$^{+}$ amacrine cell (AC) and orientation-selective ganglion cell (OSGC) are also reported.

In a schematic example of this model (Fig. 6.17A,B), when the retina is stimulated with the OSGC-preferred stimulus orientation, the orthogonally tuned *tenm3*$^{+}$ AC is weakly activated, therefore allowing the OSGC to fire action potentials. When the orthogonal stimulus orientation is presented, instead, the orthogonally tuned *tenm3*$^{+}$ AC is strongly activated and, consequently, OSGC firing is inhibited.

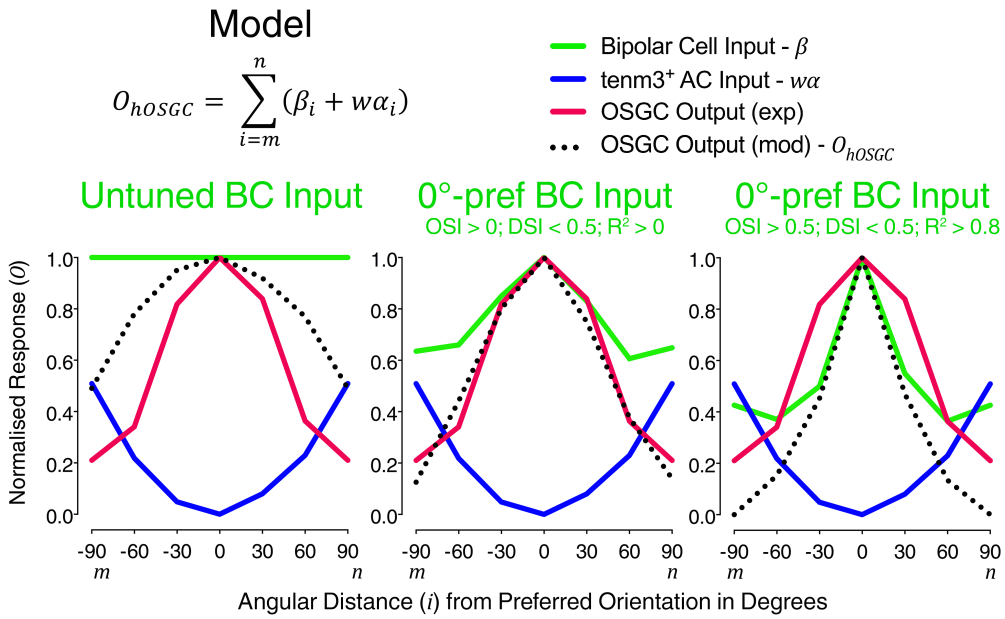

Figure 6.18. Simulation of OSGC tuning. Simulation of the tuning profile of orientation-selective ganglion cells (OSGCs; O_{hOSGC}, black dotted line) using experimentally observed average response profiles of orthogonally tuned OS *tenm3*$^+$ amacrine cells (ACs; α, blue line; n = 20 larvae), and bipolar cell (BC) terminals (β, green line; n = 20 larvae). Three different orientation-tuning levels of excitatory BC input were used: untuned (left), weakly tuned to preferred orientation (middle) and highly tuned to preferred orientation (right). The experimentally observed average response profile of OSGCs (n = 23 larvae) is shown in red. The algorithm used for the simulation is reported at the top with the related legend. Note that, since the OS *tenm3*$^+$ AC input (α) is inhibitory, a negative synaptic weight factor (w) is used in the algorithm. The orientation space ranges from '*m*' to '*n*', which are negative (-90°) and positive (90°) angles orthogonal to the preferred orientation (0°), respectively. Exp, experimental; mod, model; pref, preferred.

To further evaluate this model, the basic principles described above were implemented into a simple simulation of OSGC output (Fig. 6.18). To simulate the OSGC tuning profile (black dotted line), the experimentally observed average response profiles of OS *tenm3*$^+$ ACs (blue line) and BC presynaptic terminals (green line) were used. The OS inhibitory input provided by *tenm3*$^+$ ACs was assumed to have a subtractive effect on OSGC output, and three different orientation-tuning levels of excitatory BC input were tested. Interestingly, the average OSGC response profile observed experimentally (red line) was best reproduced when linearly integrating highly OS (OSI > 0.5, DSI < 0.5, R^2 > 0.8) orthogonal orientation-tuned inhibitory input from *tenm3*$^+$ ACs and weakly OS (OSI > 0, DSI < 0.5, R^2 > 0) preferred orientation-tuned excitatory input from BCs (Fig. 6.18 middle), indicating that OSGCs may receive BC input characterised by a substantial degree of heterogeneity in orientation tuning. This simulation also implies that OSGCs potentially integrate tuned input from both ACs and BCs to obtain the orientation selectivity observed *in vivo*. The results described above show that the tuned GABAergic inhibitory output of *tenm3*$^+$ ACs is necessary to generate normal RGC orientation selectivity. However, further experiments are needed to precisely determine

the relative contribution played by inhibitory AC versus excitatory BC tuned inputs in generating OSGC output. The strong similarities found between the OS circuit characterised here in the zebrafish retina and previous descriptions of orientation selectivity in mammalian retinae (Bloomfield, 1994; Venkataramani and Taylor, 2010; Nath and Schwartz, 2016; Venkataramani and Taylor, 2016) suggest that this model can be generalised to other vertebrate species.

6.3.2 Functional Significance of Orientation Selectivity

The widespread presence of orientation-selective cells in visual systems of many animals highlights the prominent functional role of orientation selectivity in vision. Studies on the statistical properties of natural scenes indicate that natural images can be described by local, oriented filters similar to the receptive fields of OS cells found in visual systems (Olshausen and Field, 1996). One striking example in humans is the key role played by horizontal visual information in the identification of faces (Dakin and Watt, 2009). However, a central question is, where does orientation selectivity emerge in visual circuits? Interestingly, both in vertebrates and invertebrates the detection of elongated visual stimuli takes place early in visual processing (Levick, 1967; Fisher et al., 2015). Even in mammalian species, including mice and monkeys, where for long time it was thought that orientation selectivity is an emergent property first generated in primary visual cortex (Hubel and Wiesel, 1962; Niell, 2013), OS cells have been found in non-cortical areas such as the lateral geniculate nucleus (Marshel et al., 2012; Cheong et al., 2013; Piscopo et al., 2013) and superior colliculus (Wang et al., 2010), as well as in the retina (Passaglia et al., 2002; Zhao et al., 2013; Baden et al., 2016; Nath and Schwartz, 2016). In this study, orientation selectivity was found in presynaptic terminals of BCs and ACs (Fig. 6.2, 6.3, 6.13 and 6.14), which are neurons only one and two synapses away from photoreceptors, respectively. Additionally, OS responses in these cells were observed as early as 4 dpf, when zebrafish larvae start performing visually guided behaviours, such as the optokinetic reflex. Even though, to date, there is no zebrafish behaviour that has been shown to specifically rely on OSGC output, the selective functional impairments caused by *tenm3* knockout and *tenm3*$^{+}$ AC ablation could be used to investigate whether retinal orientation selectivity is required for performing visual behaviours. Importantly, data presented in this study show that the cells and mechanisms underlying RGC orientation selectivity are different from those generating direction selectivity, in line with the notion that parallel retinal circuits process these two distinct visual features. This idea is further supported by the fact that

zebrafish OSGC and DSGC axonal projections terminate in different, non-overlapping neuropil laminae of the optic tectum (Nikolaou et al., 2012; Lowe et al., 2013).

To conclude, the findings reported here constitute a significant advancement in the understanding of how orientation selectivity emerges in the vertebrate retina, bringing together molecular markers, cell morphologies, pharmacology and function. Moreover, the *in vivo* system and relative genetic tools established in this study will allow to investigate the precise functional role played by retinal orientation selectivity in higher visual areas of the brain, as well as its role in performing visually guided behaviours.

Chapter 7

Conclusions and Perspectives

7.1 Summary

In this study, the function and assembly of retinal circuits expressing the cell-adhesion protein Teneurin-3 have been investigated in the larval zebrafish. The main findings of the study are the following: (1) *tenm3* is expressed in the developing visual system during a period of intense synapse formation. Specifically, it is expressed in amacrine, ganglion and tectal cells. (2) *Tenm3* is required for the precise stratification of RGC dendrites and axons, as well as *tenm3*$^{+}$ AC neurites. (3) *Tenm3* is also necessary for the development of RGC orientation selectivity, but it is dispensable for direction selectivity. (4) A class of orientation-tuned *tenm3*$^{+}$ ACs with elongated dendritic arbours generates orientation selectivity in RGCs, likely by providing orthogonal orientation-tuned GABAergic inhibition. (5) Orientation selectivity is present in visual responses of a subset of BC presynaptic terminals.

7.2 Putative Role for Teneurin-3 in Synaptic Specificity

The assembly of neural circuits during development is orchestrated by a multitude of molecular cues controlling different wiring processes. Past studies identified several molecules involved in the assembly of retinal circuits (see 1.3.1). Generally, these molecules are expressed in defined subsets of retinal cells and have specific developmental roles, such as neurite attraction, repulsion, self-avoidance, adhesion, as well as cell-type-specific synaptic partner matching. Together, these processes contribute to the formation of functionally defined retinal circuits computing essential visual properties (see 1.2). Likely, each circuit is assembled (to a certain degree) in parallel through the coordinated action of molecular cues expressed in a combinatorial fashion. Therefore, each of the above processes is often controlled by multiple cues with relative contributions that vary depending on cell types and circuits.

In this context, the work presented here shows that Tenm3 plays a role in the wiring of defined retinal circuits. Specifically, it appears that Tenm3 controls the matching between pre- and postsynaptic partners in the inner retina, possibly through selective recognition and adhesion. The structural and functional defects observed in morphologically and physiologically defined subsets of RGCs and ACs – i.e., OSGCs

and *tenm3*$^{+}$ ACs – seem to indicate a circuit-specific matching role similar to the one played by Sidekick-2 in the mouse retina (Krishnaswamy et al., 2015), and homologous to the role *Drosophila ten-m* and *ten-a* have in instructing synaptic specificity (Hong et al., 2012; Mosca et al., 2012). However, more advanced experimental techniques than the ones used here will be needed to fully dissect the connectivity between the populations of cells identified in this study, as well as to assess whether Tenm3 is required pre- and/or postsynaptically. In particular, electron microscope reconstructions of connectivity patterns (Briggman et al., 2011), genetically targeted trans-synaptic viral tracing (Yonehara et al., 2013), and cell-class-specific *tenm3* conditional knockout lines would greatly help to understand the complete circuit diagram formed by *tenm3*$^{+}$ cells and further explore the role Tenm3 plays in the assembly of the orientation-selective retinal circuit described here. Additionally, more detailed molecular and ultrastructural data will be essential to fully explain the *trans* interaction mechanisms underlying Tenm3 function, as well as the signalling pathways they regulate. Currently unanswered questions on the Tenm3 mechanism of action include: is Tenm3 expressed exclusively at synapses or it has a diffuse cellular distribution? Does Tenm3 interact with surface molecules other than Tenm3? If so, do these interactions occur in *cis* or *trans*, and what process do they regulate? What structural domains drive these interactions and what is their 3D configuration? Is Tenm3 required exclusively at the pre- or postsynaptic side? What are the intracellular interaction partners of Tenm3? Future studies addressing these questions will undoubtedly provide a more solid basis on how Tenm3 (and potentially teneurins in general) contributes to neural circuit wiring. The main take-home message about teneurins from this study is that, at least in the zebrafish retina, Tenm3 instructs cell-type specific connectivity and function, likely acting as a synaptic/neurite matchmaker.

Interestingly, *in situ* hybridization analyses revealing the expression patterns of other teneurin members in the larval zebrafish show that they are present in the visual system during development (Katherine Trevers and Robert Hindges, unpublished data). In particular, *tenm4* shows an expression pattern similar to *tenm3* (i.e., expression in amacrine, ganglion and tectal cells), therefore suggesting that it could play a similar role in visual circuit wiring. Loss-of-function experiments combined with assessment of the retinal functional output using multiple visual stimulation paradigms will be instrumental to explore the potential requirement of *tenm4* in the assembly of defined visual circuits. In addition, teneurins are not only expressed in the visual system, but are also expressed in other brain areas. For example, in mouse, *tenm3* is

highly expressed in the CA1 region of the hippocampus, where it shows a gradient of expression that matches *tenm3* expression in the subiculum and entorhinal cortex (Hindges lab, unpublished data; and Allen Brain Atlas), two brain regions that are highly connected with CA1 (van Strien et al., 2009). This system thus represents a defined brain circuit where *tenm3* wiring role can be tested in a mammalian organism.

7.3 *Tenm3*$^{+}$ Amacrine Cells as Key Cellular Elements in the Computation of RGC Orientation Selectivity

The response properties of RGCs result from the concerted activation of retinal microcircuit motifs with defined visual processing roles (see 1.2). Among the five classes of retinal neurons forming these microcircuits (see 1.1), amacrine cells constitute key inhibitory elements that greatly expand the computational power of the retina (see 1.1.2). For example, they are crucial for the emergence of direction selectivity, object motion sensitivity and approach sensitivity in RGCs (see 1.2.1 and 1.2.3). The data presented here further confirm their central role in performing retinal computations. In particular, the identification of orientation-tuned AC types possessing elongated dendritic arbours among *tenm3*$^{+}$ ACs, together with the finding that their ablation severely disrupts RGC orientation selectivity place these AC types at the centre of the retinal orientation-selective circuit. The data presented here indicate that orientation selectivity first arises in these AC types before being generated in OSGCs. Since these orientation-tuned AC types are inhibitory, the preferred orientation of any given OSGC would be orthogonal (i.e., 90° angular distance) to the dominant orientation resulting from weighting multiple tuned AC inputs. Even though *tenm3* knockout, GABA block, and ablation of *tenm3*$^{+}$ ACs all resulted in a severe functional impairment of most OSGC subtypes, the small subpopulation of OSGCs tuned to vertical bars moving along the horizontal axis appeared to be relatively unaffected by these experimental manipulations (see 5.2.5, 6.2.2 and 6.2.3). Importantly, this indicates that there are other mechanisms, in addition to those described here, capable of generating RGC orientation selectivity, and it highlights the heterogeneity present among OSGC subtypes (see also 1.2.2).

Observations made in this study suggest that orientation-tuned *tenm3*$^{+}$ AC types not only contribute to OSGC tuning, but also potentially generate the OS responses recorded in some BC presynaptic terminals. This idea was supported by the inverse correlation found between the frequency distributions of the four OS *tenm3*$^{+}$ AC subpopulations and those of OS BC presynaptic terminals (see 6.2.6). To test this

possibility in more detail, optogenetic ablation of *tenm3*$^{+}$ ACs using KillerRed followed by functional assessment of BC terminal orientation tuning in the *Tg(-1.8ctbp2: SyGCaMP6)* transgenic line could be performed. Additionally, more advanced experimental techniques (e.g., electron microscopy or viral tracing) would greatly help to thoroughly test this hypothesis and fully reconstruct the connectivity pattern of the various orientation-selective circuit elements. Being molecularly defined, orientation-tuned *tenm3*$^{+}$ ACs could well serve as genetic access points to dissect the micro-circuitry underlying retinal orientation selectivity. For example, by genetically targeting the delivery of peroxidase derivatives that catalyse the production of an electron-dense tracer to individually labelled type II and III *tenm3*$^{+}$ ACs, the cellular elements pre- and postsynaptic to these cell types could be identified and reconstructed using serial block-face scanning electron microscopy (Joesch et al., 2016).

Another interesting aspect to discuss is how the high dendritic field elongation of orientation-tuned AC types arise during development. Among the various plausible mechanisms, the following two (which are not mutually exclusive) could likely be implemented during development: (1) the presence of multiple molecular gradients in the retina (or perhaps a single radially arranged gradient – i.e., from central to peripheral retina) guiding the directional growth of neurites along defined retinal axes; (2) the selective extension of a single primary neurite with an initial directional bias that would then influence and drive the growth of an elliptically shaped dendritic field. Since *tenm3* knockout did not dramatically affect the dendritic field elongation of type II and III *tenm3*$^{+}$ ACs (see Fig. 5.16B), molecular cues other than Tenm3 regulate the emergence of this morphological property. In addition, activity-mediated mechanisms, such as retinal waves (see 1.3.2), could also contribute to the development of this property.

7.4 A Common Orientation-selective Retinal Circuit in Vertebrates?

Are the mechanisms and circuit elements underlying retinal orientation selectivity outlined in this study conserved across vertebrate species? Orientation-tuned amacrine cell types with elongated dendritic arbours have been previously described in the rabbit retina (see Fig. 1.9E,F) (Bloomfield, 1991, 1994; Murphy-Baum and Taylor, 2015). Even though their contribution to RGC orientation selectivity is still unclear, and no genetic marker has been found to selectively label these cells, they are intriguing homologue candidates of the orientation-tuned *tenm3*$^{+}$ AC types identified here in zebrafish. Interestingly, AC types with morphological features analogous to those

observed in zebrafish and rabbit orientation-tuned ACs (i.e., high dendritic field elongation) are present in the mouse retina [see AC type 28, 31, 32, and 37 in (Helmstaedter et al., 2013) supplemental information], but their functional properties are still unknown. Moreover, orientation-tuned responses have been reported in groups of mouse displaced amacrine cells [see AC group 33, 36 and 39 in (Baden et al., 2016) supplemental information], but no morphological data on these cells are currently available. Considering that some physiological and morphological similarities between rabbit and mouse OSGCs (see 1.2.2) point toward common circuit mechanisms, it is reasonable to hypothesise that homologous orientation-tuned ACs, likely with species-specific differences (Ding et al., 2016; Euler and Baden, 2016), exist across vertebrates. Given the powerful genetic technologies available in the mouse system, combined with the possibility of performing paired electrophysiological recordings in *ex vivo* preparations of the mouse retina, identifying orientation-tuned ACs in this animal system would be a significant step forward in the dissection of the retinal orientation-selective circuit in vertebrates.

7.5 The *Crystal* Mutant and its Potential Applications

As a final note, it is worth discussing the experimental advantages and disadvantages of the *crystal* mutant, which has been developed in this study to optically access the retina while avoiding the use of PTU. For the purposes of my PhD project, this novel pigmentation mutant constituted a tremendous improvement for recording neural activity in the retina through calcium imaging as compared to larvae treated with PTU. At least as revealed by scoring larvae performing optomotor response assays, *crystal* mutants do not appear to have visual behaviour impairments, as opposed to PTU-treated larvae that instead exhibit severely disrupted visual behaviour and function. However, the optomotor response assay performed here is a relatively qualitative test of visual behaviour. Thus, more quantitative behavioural assessments, such as automated optokinetic reflex assays measuring visual acuity (Mueller et al., 2011), will be required before using *crystal* mutants for more complex behavioural paradigms, like prey hunting (Bianco and Engert, 2015) or predator escape (Dunn et al., 2016a). It is possible that the lack of pigmentation in the retinal pigment epithelium of *crystal* mutants negatively affects visual acuity in certain luminance conditions (Ren et al., 2002; Dooley et al., 2013), or could increase the susceptibility to light-induced retinal degeneration at adult stages (Vihtelic and Hyde, 2000).

As demonstrated in this study, the experimental approaches that might benefit from the use of *crystal* zebrafish range from subcellular recordings of calcium dynamics in retinal neurons to large-scale, whole-brain imaging. For example, attempts to perform long-term volumetric calcium imaging of neural activity across the entire larval brain through two-photon microscopy (Wolf et al., 2015) could take advantage of the improved transparency offered by *crystal* larvae to avoid the photodamage resulting from high-power laser excitation light. Finally, the applications of *crystal* zebrafish are not limited to neuroscience, but may well be extended to other fields of life sciences. Indeed, since the characterisation of the *crystal* line was published in July 2016 (Antinucci and Hindges, 2016), there has already been high interest in this line. In particular, 12 laboratories from 5 countries across the world, with research interests ranging from skin pigmentation to organ regeneration, have requested the *crystal* line to carry out innovative, previously unfeasible experiments.

To conclude, this study constitutes a significant advancement in bridging neuronal morphology and genetic identity to circuit function. Specifically, the molecular link found between the cell-cell recognition protein Tenm3 and retinal orientation selectivity allowed to genetically access the circuit elements and mechanisms underlying this fundamental visual computation. The cellular heterogeneity present in the vertebrate retina makes this tissue ideal to investigate how morphological and molecular features of defined cell types are associated with specific information processing roles in neural circuits. Additionally, the larval zebrafish enables to study these biological processes at subcellular, cellular and systems levels. Here, these advantages have been exploited to reveal the presence of amacrine cell types with elongated dendritic fields that generate orientation selectivity in retinal ganglion cells by being a source of GABAergic inhibition. The data presented here also outline the potential circuit architecture underlying orientation selectivity as well as the molecular requirements for its correct assembly over development, and therefore represent a starting point to further investigate this intriguing neural circuit.

Bibliography

Ahrens MB, Orger MB, Robson DN, Li JM, Keller PJ (2013) Whole-brain functional imaging at cellular resolution using light-sheet microscopy. Nat Methods 10:413-420.

Akimov NP, Renteria RC (2014) Dark rearing alters the normal development of spatiotemporal response properties but not of contrast detection threshold in mouse retinal ganglion cells. Dev Neurobiol 74:692-706.

Aldahmesh MA, Mohammed JY, Al-Hazzaa S, Alkuraya FS (2012) Homozygous null mutation in ODZ3 causes microphthalmia in humans. Genet Med 14:900-904.

Alkelai A, Olender T, Haffner-Krausz R, Tsoory MM, Boyko V, Tatarskyy P, Gross-Isseroff R, Milgrom R, Shushan S, Blau I, Cohn E, Beeri R, Ephrat LL, Pras E, Lancet D (2016) A role for TENM1 mutations in Congenital General Anosmia. Clin Genet 10.1111/cge.12782.

Amthor FR, Takahashi ES, Oyster CW (1989) Morphologies of rabbit retinal ganglion cells with complex receptive fields. J Comp Neurol 280:97-121.

Antinucci P, Hindges R (2016) A crystal-clear zebrafish for in vivo imaging. Sci Rep 6:29490.

Antinucci P, Abbas F, Hunter PR (2016a) Orientation Selectivity in the Retina: ON Cell Types and Mechanisms. J Neurosci 36:8064-8066.

Antinucci P, Nikolaou N, Meyer MP, Hindges R (2013) Teneurin-3 specifies morphological and functional connectivity of retinal ganglion cells in the vertebrate visual system. Cell Rep 5:582-592.

Antinucci P, Suleyman O, Monfries C, Hindges R (2016b) Neural Mechanisms Generating Orientation Selectivity in the Retina. Curr Biol 26:1802-1815.

Arroyo DA, Kirkby LA, Feller MB (2016) Retinal Waves Modulate an Intraretinal Circuit of Intrinsically Photosensitive Retinal Ganglion Cells. J Neurosci 36:6892-6905.

Asari H, Meister M (2012) Divergence of visual channels in the inner retina. Nat Neurosci 15:1581-1589.

Asari H, Meister M (2014) The projective field of retinal bipolar cells and its modulation by visual context. Neuron 81:641-652.

Baccus SA, Olveczky BP, Manu M, Meister M (2008) A Retinal Circuit That Computes Object Motion. J Neurosci 28:6807-6817.

Baden T, Berens P, Bethge M, Euler T (2013) Spikes in mammalian bipolar cells support temporal layering of the inner retina. Curr Biol 23:48-52.

Baden T, Nikolaev A, Esposti F, Dreosti E, Odermatt B, Lagnado L (2014) A synaptic mechanism for temporal filtering of visual signals. PLoS Biol 12:e1001972.

Baden T, Berens P, Franke K, Roman Roson M, Bethge M, Euler T (2016) The functional diversity of retinal ganglion cells in the mouse. Nature 529:345-350.

Bagutti C, Forro G, Ferralli J, Rubin B, Chiquet-Ehrismann R (2003) The intracellular domain of teneurin-2 has a nuclear function and represses zic-1-mediated transcription. J Cell Sci 116:2957-2966.

Baier H (2013) Synaptic laminae in the visual system: molecular mechanisms forming layers of perception. Annu Rev Cell Dev Biol 29:385-416.

Balciunas D, Wangensteen KJ, Wilber A, Bell J, Geurts A, Sivasubbu S, Wang X, Hackett PB, Largaespada DA, McIvor RS, Ekker SC (2006) Harnessing a high cargo-capacity transposon for genetic applications in vertebrates. PLoS Genet 2:e169.

Bansal A, Singer JH, Hwang BJ, Xu W, Beaudet A, Feller MB (2000) Mice lacking specific nicotinic acetylcholine receptor subunits exhibit dramatically altered spontaneous activity patterns and reveal a limited role for retinal waves in forming ON and OFF circuits in the inner retina. J Neurosci 20:7672-7681.

Baraban SC, Dinday MT, Castro PA, Chege S, Guyenet S, Taylor MR (2007) A large-scale mutagenesis screen to identify seizure-resistant zebrafish. Epilepsia 48:1151-1157.

Barlow HB, Hill RM (1963) Selective sensitivity to direction of movement in ganglion cells of the rabbit retina. Science 139:412-414.

Batschelet E (1981) Circular statistics in biology. London: Academic Press.

Baumgartner S, Martin D, Hagios C, Chiquet-Ehrismann R (1994) Tenm, a Drosophila gene related to tenascin, is a new pair-rule gene. Embo j 13:3728-3740.

Beckmann J, Schubert R, Chiquet-Ehrismann R, Muller DJ (2013) Deciphering teneurin domains that facilitate cellular recognition, cell-cell adhesion, and neurite outgrowth using atomic force microscopy-based single-cell force spectroscopy. Nano Lett 13:2937-2946.

Ben Fredj N, Hammond S, Otsuna H, Chien CB, Burrone J, Meyer MP (2010) Synaptic activity and activity-dependent competition regulates axon arbor maturation, growth arrest, and territory in the retinotectal projection. J Neurosci 30:10939-10951.

Ben-Zur T, Feige E, Motro B, Wides R (2000) The mammalian Odz gene family: homologs of a Drosophila pair-rule gene with expression implying distinct yet overlapping developmental roles. Dev Biol 217:107-120.

Bharti K, Nguyen MT, Skuntz S, Bertuzzi S, Arnheiter H (2006) The other pigment cell: specification and development of the pigmented epithelium of the vertebrate eye. Pigment Cell Res 19:380-394.

Bianco IH, Engert F (2015) Visuomotor transformations underlying hunting behavior in zebrafish. Curr Biol 25:831-846.

Bisti S, Gargini C, Chalupa LM (1998) Blockade of glutamate-mediated activity in the developing retina perturbs the functional segregation of ON and OFF pathways. J Neurosci 18:5019-5025.

Bleckert A, Schwartz GW, Turner MH, Rieke F, Wong RO (2014) Visual space is represented by nonmatching topographies of distinct mouse retinal ganglion cell types. Curr Biol 24:310-315.

Bloomfield SA (1991) Two types of orientation-sensitive responses of amacrine cells in the mammalian retina. Nature 350:347-350.

Bloomfield SA (1994) Orientation-sensitive amacrine and ganglion cells in the rabbit retina. J Neurophysiol 71:1672-1691.

Bloomfield SA, Volgyi B (2009) The diverse functional roles and regulation of neuronal gap junctions in the retina. Nat Rev Neurosci 10:495-506.

Bodnarenko SR, Chalupa LM (1993) Stratification of ON and OFF ganglion cell dendrites depends on glutamate-mediated afferent activity in the developing retina. Nature 364:144-146.

Bodnarenko SR, Jeyarasasingam G, Chalupa LM (1995) Development and regulation of dendritic stratification in retinal ganglion cells by glutamate-mediated afferent activity. J Neurosci 15:7037-7045.

Bohnsack BL, Gallina D, Kahana A (2011) Phenothiourea sensitizes zebrafish cranial neural crest and extraocular muscle development to changes in retinoic acid and IGF signaling. PLoS One 6:e22991.

Borst A, Euler T (2011) Seeing things in motion: models, circuits, and mechanisms. Neuron 71:974-994.

Borst A, Helmstaedter M (2015) Common circuit design in fly and mammalian motion vision. Nat Neurosci 18:1067-1076.

Bos R, Gainer C, Feller MB (2016) Role for Visual Experience in the Development of Direction-Selective Circuits. Curr Biol 26:1367-1375.

Boucard AA, Maxeiner S, Sudhof TC (2014) Latrophilins function as heterophilic cell-adhesion molecules by binding to teneurins: regulation by alternative splicing. J Biol Chem 289:387-402.

Briggman KL, Helmstaedter M, Denk W (2011) Wiring specificity in the direction-selectivity circuit of the retina. Nature 471:183-188.

Bulina ME, Lukyanov KA, Britanova OV, Onichtchouk D, Lukyanov S, Chudakov DM (2006a) Chromophore-assisted light inactivation (CALI) using the phototoxic fluorescent protein KillerRed. Nat Protoc 1:947-953.

Bulina ME, Chudakov DM, Britanova OV, Yanushevich YG, Staroverov DB, Chepurnykh TV, Merzlyak EM, Shkrob MA, Lukyanov S, Lukyanov KA (2006b) A genetically encoded photosensitizer. Nat Biotechnol 24:95-99.

Burrill JD, Easter SS, Jr. (1994) Development of the retinofugal projections in the embryonic and larval zebrafish (Brachydanio rerio). J Comp Neurol 346:583-600.

Bussmann J, Schulte-Merker S (2011) Rapid BAC selection for tol2-mediated transgenesis in zebrafish. Development 138:4327-4332.

Caldwell JH, Daw NW, Wyatt HJ (1978) Effects of picrotoxin and strychnine on rabbit retinal ganglion cells: lateral interactions for cells with more complex receptive fields. J Physiol 276:277-298.

Cang J, Feldheim DA (2013) Developmental mechanisms of topographic map formation and alignment. Annu Rev Neurosci 36:51-77.

Cao Y, Sarria I, Fehlhaber KE, Kamasawa N, Orlandi C, James KN, Hazen JL, Gardner MR, Farzan M, Lee A, Baker S, Baldwin K, Sampath AP, Martemyanov KA (2015)

Mechanism for Selective Synaptic Wiring of Rod Photoreceptors into the Retinal Circuitry and Its Role in Vision. Neuron 87:1248-1260.

Carr OP, Glendining KA, Leamey CA, Marotte LR (2013) Overexpression of Ten-m3 in the retina alters ipsilateral retinocollicular projections in the wallaby (Macropus eugenii). Int J Dev Neurosci 31:496-504.

Carr OP, Glendining KA, Leamey CA, Marotte LR (2014) Retinal overexpression of Ten-m3 alters ipsilateral retinogeniculate projections in the wallaby (Macropus eugenii). Neurosci Lett 566:167-171.

Cepko C (2014) Intrinsically different retinal progenitor cells produce specific types of progeny. Nat Rev Neurosci 15:615-627.

Chan YC, Chiao CC (2008) Effect of visual experience on the maturation of ON-OFF direction selective ganglion cells in the rabbit retina. Vision Res 48:2466-2475.

Chan YC, Chiao CC (2013) The distribution of the preferred directions of the ON-OFF direction selective ganglion cells in the rabbit retina requires refinement after eye opening. Physiol Rep 1:e00013.

Chao XY, Lin NEY, Tio M, Kumar P, Tan L, Au WL, Yih Y, Tan EK (2016) Essential tremor linked TENM4 mutation found in healthy Chinese individuals. Parkinsonism & Related Disorders 10.1016/j.parkreldis.2016.05.003.

Chassaing N, Ragge N, Plaisancie J, Patat O, Genevieve D, Rivier F, Malrieu-Eliaou C, Hamel C, Kaplan J, Calvas P (2016) Confirmation of TENM3 involvement in autosomal recessive colobomatous microphthalmia. Am J Med Genet A 170:1895-1898.

Chen H, Liu X, Tian N (2014) Subtype-dependent postnatal development of direction- and orientation-selective retinal ganglion cells in mice. J Neurophysiol 112:2092-2101.

Chen TW, Wardill TJ, Sun Y, Pulver SR, Renninger SL, Baohan A, Schreiter ER, Kerr RA, Orger MB, Jayaraman V, Looger LL, Svoboda K, Kim DS (2013a) Ultrasensitive fluorescent proteins for imaging neuronal activity. Nature 499:295-300.

Chen Y, Xu M, De Almeida R, Lovejoy DA (2013b) Teneurin C-terminal associated peptides (TCAP): modulators of corticotropin-releasing factor (CRF) physiology and behavior. Front Neurosci 7:166.

Cheong SK, Tailby C, Solomon SG, Martin PR (2013) Cortical-like receptive fields in the lateral geniculate nucleus of marmoset monkeys. J Neurosci 33:6864-6876.

Chhetri RK, Amat F, Wan Y, Hockendorf B, Lemon WC (2015) Whole-animal functional and developmental imaging with isotropic spatial resolution. Nat Methods 12:1171-1178.

Chow RW, Almeida AD, Randlett O, Norden C, Harris WA (2015) Inhibitory neuron migration and IPL formation in the developing zebrafish retina. Development 142:2665-2677.

Cleland BG, Levick WR (1974) Properties of rarely encountered types of ganglion cells in the cat's retina and an overall classification. J Physiol 240:457-492.

Cole RW, Jinadasa T, Brown CM (2011) Measuring and interpreting point spread functions to determine confocal microscope resolution and ensure quality control. Nat Protoc 6:1929-1941.

Connaughton VP (2011) Bipolar cells in the zebrafish retina. Vis Neurosci 28:77-93.

Connaughton VP, Behar TN, Liu WL, Massey SC (1999) Immunocytochemical localization of excitatory and inhibitory neurotransmitters in the zebrafish retina. Vis Neurosci 16:483-490.

Cook JE, Chalupa LM (2000) Retinal mosaics: new insights into an old concept. Trends Neurosci 23:26-34.

Dakin SC, Watt RJ (2009) Biological "bar codes" in human faces. J Vis 9:2.1-10.

Dalva MB, McClelland AC, Kayser MS (2007) Cell adhesion molecules: signalling functions at the synapse. Nat Rev Neurosci 8:206-220.

Damjanovic I, Maximova E, Maximov V (2009) On the organization of receptive fields of orientation-selective units recorded in the fish tectum. J Integr Neurosci 8:323-344.

De Franceschi G, Vivattanasarn T, Saleem Aman B, Solomon Samuel G Vision Guides Selection of Freeze or Flight Defense Strategies in Mice. Current Biology 10.1016/j.cub.2016.06.006.

de Wit J, Ghosh A (2016) Specification of synaptic connectivity by cell surface interactions. Nat Rev Neurosci 17:22-35.

Deans MR, Krol A, Abraira VE, Copley CO, Tucker AF, Goodrich LV (2011) Control of neuronal morphology by the atypical cadherin Fat3. Neuron 71:820-832.

Del Bene F, Wyart C, Robles E, Tran A, Looger L, Scott EK, Isacoff EY, Baier H (2010) Filtering of visual information in the tectum by an identified neural circuit. Science 330:669-673.

Della Santina L, Kuo SP, Yoshimatsu T, Okawa H, Suzuki SC, Hoon M, Tsuboyama K, Rieke F, Wong RO (2016) Glutamatergic Monopolar Interneurons Provide a Novel Pathway of Excitation in the Mouse Retina. Curr Biol 26:2070-2077.

Demb JB, Singer JH (2012) Intrinsic properties and functional circuitry of the AII amacrine cell. Vis Neurosci 29:51-60.

Demb JB, Singer JH (2015) Functional circuitry of the retina. Annual Review of Vision Science 1:263-289.

Dhande OS, Huberman AD (2014) Retinal ganglion cell maps in the brain: implications for visual processing. Curr Opin Neurobiol 24:133-142.

Dhande OS, Stafford BK, Lim J-HA, Huberman AD (2015) Contributions of Retinal Ganglion Cells to Subcortical Visual Processing and Behaviors. Annual Review of Vision Science 1:291-328.

Dhande OS, Estevez ME, Quattrochi LE, El-Danaf RN, Nguyen PL, Berson DM, Huberman AD (2013) Genetic dissection of retinal inputs to brainstem nuclei controlling image stabilization. J Neurosci 33:17797-17813.

Dharmaratne N, Glendining KA, Young TR, Tran H, Sawatari A, Leamey CA (2012) Ten-m3 is required for the development of topography in the ipsilateral retinocollicular pathway. PLoS One 7:e43083.

Di Marco S, Nguyen VA, Bisti S, Protti DA (2009) Permanent functional reorganization of retinal circuits induced by early long-term visual deprivation. J Neurosci 29:13691-13701.

Ding H, Smith RG, Poleg-Polsky A, Diamond JS, Briggman KL (2016) Species-specific wiring for direction selectivity in the mammalian retina. Nature 535:105-110.

Dooley CM, Schwarz H, Mueller KP, Mongera A, Konantz M, Neuhauss SC, Nusslein-Volhard C, Geisler R (2013) Slc45a2 and V-ATPase are regulators of melanosomal pH homeostasis in zebrafish, providing a mechanism for human pigment evolution and disease. Pigment Cell Melanoma Res 26:205-217.

Dowling JE, Ehinger B (1978) The interplexiform cell system. I. Synapses of the dopaminergic neurons of the goldfish retina. Proc R Soc Lond B Biol Sci 201:7-26.

Drabikowski K, Trzebiatowska A, Chiquet-Ehrismann R (2005) ten-1, an essential gene for germ cell development, epidermal morphogenesis, gonad migration, and neuronal pathfinding in Caenorhabditis elegans. Dev Biol 282:27-38.

Draper BW, Morcos PA, Kimmel CB (2001) Inhibition of zebrafish fgf8 pre-mRNA splicing with morpholino oligos: a quantifiable method for gene knockdown. Genesis 30:154-156.

Duan X, Krishnaswamy A, De la Huerta I, Sanes JR (2014) Type II cadherins guide assembly of a direction-selective retinal circuit. Cell 158:793-807.

Dunn FA, Wong RO (2014) Wiring patterns in the mouse retina: collecting evidence across the connectome, physiology and light microscopy. J Physiol 592:4809-4823.

Dunn FA, Della Santina L, Parker ED, Wong RO (2013) Sensory experience shapes the development of the visual system's first synapse. Neuron 80:1159-1166.

Dunn TW, Gebhardt C, Naumann EA, Riegler C, Ahrens MB, Engert F, Del Bene F (2016a) Neural Circuits Underlying Visually Evoked Escapes in Larval Zebrafish. Neuron 89:613-628.

Dunn TW, Mu Y, Narayan S, Randlett O, Naumann EA, Yang CT, Schier AF, Freeman J, Engert F, Ahrens MB (2016b) Brain-wide mapping of neural activity controlling zebrafish exploratory locomotion. Elife 5.

Ellis EM, Gauvain G, Sivyer B, Murphy GJ (2016) Shared and distinct retinal input to the mouse superior colliculus and dorsal lateral geniculate nucleus. J Neurophysiol 116:602-610.

Elsalini OA, Rohr KB (2003) Phenylthiourea disrupts thyroid function in developing zebrafish. Dev Genes Evol 212:593-598.

Elstrott J, Anishchenko A, Greschner M, Sher A, Litke AM, Chichilnisky EJ, Feller MB (2008) Direction selectivity in the retina is established independent of visual experience and cholinergic retinal waves. Neuron 58:499-506.

Esumi S, Kakazu N, Taguchi Y, Hirayama T, Sasaki A, Hirabayashi T, Koide T, Kitsukawa T, Hamada S, Yagi T (2005) Monoallelic yet combinatorial expression of variable exons of the protocadherin-alpha gene cluster in single neurons. Nat Genet 37:171-176.

Euler T, Baden T (2016) Computational neuroscience: Species-specific motion detectors. Nature 535:45-46.

Euler T, Detwiler PB, Denk W (2002) Directionally selective calcium signals in dendrites of starburst amacrine cells. Nature 418:845-852.

Euler T, Haverkamp S, Schubert T, Baden T (2014) Retinal bipolar cells: elementary building blocks of vision. Nat Rev Neurosci 15:507-519.

Famiglietti EV (1991) Synaptic organization of starburst amacrine cells in rabbit retina: analysis of serial thin sections by electron microscopy and graphic reconstruction. J Comp Neurol 309:40-70.

Famiglietti EV (1992) Dendritic co-stratification of ON and ON-OFF directionally selective ganglion cells with starburst amacrine cells in rabbit retina. J Comp Neurol 324:322-335.

Fascetti N, Baumgartner S (2002) Expression of Drosophila Ten-a, a dimeric receptor during embryonic development. Mech Dev 114:197-200.

Feldheim DA, O'Leary DD (2010) Visual map development: bidirectional signaling, bifunctional guidance molecules, and competition. Cold Spring Harb Perspect Biol 2:a001768.

Feng K, Zhou XH, Oohashi T, Morgelin M, Lustig A, Hirakawa S, Ninomiya Y, Engel J, Rauch U, Fassler R (2002) All four members of the Ten-m/Odz family of transmembrane proteins form dimers. J Biol Chem 277:26128-26135.

Firth SI, Wang CT, Feller MB (2005) Retinal waves: mechanisms and function in visual system development. Cell Calcium 37:425-432.

Fisher YE, Silies M, Clandinin TR (2015) Orientation Selectivity Sharpens Motion Detection in Drosophila. Neuron 88:390-402.

Franke K, Berens P, Schubert T, Bethge M, Euler T, Baden T (2016) Balanced excitation and inhibition decorrelates visual feature representation in the mammalian inner retina. bioRxiv 10.1101/040642.

Fried SI, Munch TA, Werblin FS (2002) Mechanisms and circuitry underlying directional selectivity in the retina. Nature 420:411-414.

Fuerst PG, Koizumi A, Masland RH, Burgess RW (2008) Neurite arborization and mosaic spacing in the mouse retina require DSCAM. Nature 451:470-474.

Fuerst PG, Bruce F, Tian M, Wei W, Elstrott J, Feller MB, Erskine L, Singer JH, Burgess RW (2009) DSCAM and DSCAML1 function in self-avoidance in multiple cell types in the developing mouse retina. Neuron 64:484-497.

Gauvain G, Murphy GJ (2015) Projection-specific characteristics of retinal input to the brain. J Neurosci 35:6575-6583.

Godinho L, Mumm JS, Williams PR, Schroeter EH, Koerber A, Park SW, Leach SD, Wong RO (2005) Targeting of amacrine cell neurites to appropriate synaptic laminae in the developing zebrafish retina. Development 132:5069-5079.

Gollisch T, Meister M (2010) Eye smarter than scientists believed: neural computations in circuits of the retina. Neuron 65:150-164.

Green EK, Hamshere M, Forty L, Gordon-Smith K, Fraser C, Russell E, Grozeva D, Kirov G, Holmans P, Moran JL, Purcell S, Sklar P, Owen MJ, O'Donovan MC, Jones L, Jones IR, Craddock N (2013) Replication of bipolar disorder susceptibility alleles and identification of two novel genome-wide significant associations in a new bipolar disorder case-control sample. Mol Psychiatry 18:1302-1307.

Greene MJ, Kim JS, Seung HS (2016) Analogous Convergence of Sustained and Transient Inputs in Parallel On and Off Pathways for Retinal Motion Computation. Cell Rep 14:1892-1900.

Guler AD, Ecker JL, Lall GS, Haq S, Altimus CM, Liao HW, Barnard AR, Cahill H, Badea TC, Zhao H, Hankins MW, Berson DM, Lucas RJ, Yau KW, Hattar S (2008) Melanopsin cells are the principal conduits for rod-cone input to non-image-forming vision. Nature 453:102-105.

Harty BL, Krishnan A, Sanchez NE, Schioth HB, Monk KR (2015) Defining the gene repertoire and spatiotemporal expression profiles of adhesion G protein-coupled receptors in zebrafish. BMC Genomics 16:62.

Hattar S, Liao HW, Takao M, Berson DM, Yau KW (2002) Melanopsin-containing retinal ganglion cells: architecture, projections, and intrinsic photosensitivity. Science 295:1065-1070.

Hattori Y, Usui T, Satoh D, Moriyama S, Shimono K, Itoh T, Shirahige K, Uemura T (2013) Sensory-neuron subtype-specific transcriptional programs controlling dendrite morphogenesis: genome-wide analysis of Abrupt and Knot/Collier. Dev Cell 27:530-544.

Hausselt SE, Euler T, Detwiler PB, Denk W (2007) A dendrite-autonomous mechanism for direction selectivity in retinal starburst amacrine cells. PLoS Biol 5:e185.

He S, Masland RH (1997) Retinal direction selectivity after targeted laser ablation of starburst amacrine cells. Nature 389:378-382.

He S, Levick WR, Vaney DI (1998) Distinguishing direction selectivity from orientation selectivity in the rabbit retina. Vis Neurosci 15:439-447.

Helmstaedter M, Briggman KL, Turaga SC, Jain V, Seung HS, Denk W (2013) Connectomic reconstruction of the inner plexiform layer in the mouse retina. Nature 500:168-174.

Hirata H, Ogino K, Yamada K, Leacock S, Harvey RJ (2013) Defective escape behavior in DEAH-box RNA helicase mutants improved by restoring glycine receptor expression. J Neurosci 33:14638-14644.

Hong W, Mosca TJ, Luo L (2012) Teneurins instruct synaptic partner matching in an olfactory map. Nature 484:201-207.

Hoon M, Okawa H, Della Santina L, Wong RO (2014) Functional architecture of the retina: development and disease. Prog Retin Eye Res 42:44-84.

Hoon M, Sinha R, Okawa H, Suzuki SC, Hirano AA, Brecha N, Rieke F, Wong RO (2015) Neurotransmission plays contrasting roles in the maturation of inhibitory synapses on axons and dendrites of retinal bipolar cells. Proc Natl Acad Sci U S A 112:12840-12845.

Hor H et al. (2015) Missense mutations in TENM4, a regulator of axon guidance and central myelination, cause essential tremor. Hum Mol Genet 24:5677-5686.

Hortopan GA, Dinday MT, Baraban SC (2010) Zebrafish as a model for studying genetic aspects of epilepsy. Dis Model Mech 3:144-148.

Hubel DH, Wiesel TN (1962) Receptive fields, binocular interaction and functional architecture in the cat's visual cortex. J Physiol 160:106-154.

Hubel DH, Wiesel TN (1968) Receptive fields and functional architecture of monkey striate cortex. J Physiol 195:215-243.

Huberman AD, Feller MB, Chapman B (2008a) Mechanisms underlying development of visual maps and receptive fields. Annu Rev Neurosci 31:479-509.

Huberman AD, Wei W, Elstrott J, Stafford BK, Feller MB, Barres BA (2009) Genetic identification of an On-Off direction-selective retinal ganglion cell subtype reveals a layer-specific subcortical map of posterior motion. Neuron 62:327-334.

Huberman AD, Manu M, Koch SM, Susman MW, Lutz AB, Ullian EM, Baccus SA, Barres BA (2008b) Architecture and activity-mediated refinement of axonal projections from a mosaic of genetically identified retinal ganglion cells. Neuron 59:425-438.

Hunter PR, Lowe AS, Thompson ID, Meyer MP (2013) Emergent properties of the optic tectum revealed by population analysis of direction and orientation selectivity. J Neurosci 33:13940-13945.

Inoue D, Wittbrodt J (2011) One for all--a highly efficient and versatile method for fluorescent immunostaining in fish embryos. PLoS One 6:e19713.

Ishikane H, Gangi M, Honda S, Tachibana M (2005) Synchronized retinal oscillations encode essential information for escape behavior in frogs. Nat Neurosci 8:1087-1095.

Jacques SL (2013) Optical properties of biological tissues: a review. Phys Med Biol 58:R37-61.

Jadzinsky PD, Baccus SA (2013) Transformation of visual signals by inhibitory interneurons in retinal circuits. Annu Rev Neurosci 36:403-428.

Joesch M, Mankus D, Yamagata M, Shahbazi A, Schalek R, Suissa-Peleg A, Meister M, Lichtman JW, Scheirer WJ, Sanes JR (2016) Reconstruction of genetically identified neurons imaged by serial-section electron microscopy. Elife 5.

Johnson GA, Boukma SJ, Kim EG (1970) In vivo inhibition of dopamine beta-hydroxylase by 1-phenyl-3-(2-thiazolyl)-2-thiourea (U-14,624). J Pharmacol Exp Ther 171:80-87.

Johnston J, Ding H, Seibel SH, Esposti F, Lagnado L (2014) Rapid mapping of visual receptive fields by filtered back projection: application to multi-neuronal electrophysiology and imaging. J Physiol 592:4839-4854.

Jusuf PR, Harris WA (2009) Ptf1a is expressed transiently in all types of amacrine cells in the embryonic zebrafish retina. Neural Dev 4:34.

Jusuf PR, Almeida AD, Randlett O, Joubin K, Poggi L, Harris WA (2011) Origin and determination of inhibitory cell lineages in the vertebrate retina. J Neurosci 31:2549-2562.

Kaneko R, Kato H, Kawamura Y, Esumi S, Hirayama T, Hirabayashi T, Yagi T (2006) Allelic gene regulation of Pcdh-alpha and Pcdh-gamma clusters involving both monoallelic and biallelic expression in single Purkinje cells. J Biol Chem 281:30551-30560.

Karlsson J, von Hofsten J, Olsson PE (2001) Generating transparent zebrafish: a refined method to improve detection of gene expression during embryonic development. Mar Biotechnol (NY) 3:522-527.

Katz LC, Shatz CJ (1996) Synaptic activity and the construction of cortical circuits. Science 274:1133-1138.

Kay JN, Chu MW, Sanes JR (2012) MEGF10 and MEGF11 mediate homotypic interactions required for mosaic spacing of retinal neurons. Nature 483:465-469.

Kay JN, Finger-Baier KC, Roeser T, Staub W, Baier H (2001) Retinal ganglion cell genesis requires lakritz, a Zebrafish atonal Homolog. Neuron 30:725-736.

Kay JN, Roeser T, Mumm JS, Godinho L, Mrejeru A, Wong RO, Baier H (2004) Transient requirement for ganglion cells during assembly of retinal synaptic layers. Development 131:1331-1342.

Kay JN, De la Huerta I, Kim IJ, Zhang Y, Yamagata M, Chu MW, Meister M, Sanes JR (2011) Retinal ganglion cells with distinct directional preferences differ in molecular identity, structure, and central projections. J Neurosci 31:7753-7762.

Keeley PW, Luna G, Fariss RN, Skyles KA, Madsen NR, Raven MA, Poche RA, Swindell EC, Jamrich M, Oh EC, Swaroop A, Fisher SK, Reese BE (2013) Development and plasticity of outer retinal circuitry following genetic removal of horizontal cells. J Neurosci 33:17847-17862.

Keller PJ, Ahrens MB (2015) Visualizing whole-brain activity and development at the single-cell level using light-sheet microscopy. Neuron 85:462-483.

Kelsh RN, Brand M, Jiang YJ, Heisenberg CP, Lin S, Haffter P, Odenthal J, Mullins MC, van Eeden FJ, Furutani-Seiki M, Granato M, Hammerschmidt M, Kane DA, Warga RM, Beuchle D, Vogelsang L, Nusslein-Volhard C (1996) Zebrafish pigmentation mutations and the processes of neural crest development. Development 123:369-389.

Kenzelmann D, Chiquet-Ehrismann R, Leachman NT, Tucker RP (2008) Teneurin-1 is expressed in interconnected regions of the developing brain and is processed in vivo. BMC Dev Biol 8:30.

Kenzelmann-Broz D, Tucker RP, Leachman NT, Chiquet-Ehrismann R (2010) The expression of teneurin-4 in the avian embryo: potential roles in patterning of the limb and nervous system. Int J Dev Biol 54:1509-1516.

Kerschensteiner D, Morgan JL, Parker ED, Lewis RM, Wong RO (2009) Neurotransmission selectively regulates synapse formation in parallel circuits in vivo. Nature 460:1016-1020.

Kim IJ, Zhang Y, Meister M, Sanes JR (2010) Laminar restriction of retinal ganglion cell dendrites and axons: subtype-specific developmental patterns revealed with transgenic markers. J Neurosci 30:1452-1462.

Kim IJ, Zhang Y, Yamagata M, Meister M, Sanes JR (2008) Molecular identification of a retinal cell type that responds to upward motion. Nature 452:478-482.

Kim JS, Greene MJ, Zlateski A, Lee K, Richardson M, Turaga SC, Purcaro M, Balkam M, Robinson A, Behabadi BF, Campos M, Denk W, Seung HS (2014) Space-time wiring specificity supports direction selectivity in the retina. Nature 509:331-336.

Kim T, Soto F, Kerschensteiner D (2015) An excitatory amacrine cell detects object motion and provides feature-selective input to ganglion cells in the mouse retina. Elife 4.

Kirkby LA, Sack GS, Firl A, Feller MB (2013) A role for correlated spontaneous activity in the assembly of neural circuits. Neuron 80:1129-1144.

Kolodkin AL, Tessier-Lavigne M (2011) Mechanisms and molecules of neuronal wiring: a primer. Cold Spring Harb Perspect Biol 3.

Kostadinov D, Sanes JR (2015) Protocadherin-dependent dendritic self-avoidance regulates neural connectivity and circuit function. Elife 4.

Krishnaswamy A, Yamagata M, Duan X, Hong YK, Sanes JR (2015) Sidekick 2 directs formation of a retinal circuit that detects differential motion. Nature 524:466-470.

Krol A, Henle SJ, Goodrich LV (2016) Fat3 and Ena/VASP proteins influence the emergence of asymmetric cell morphology in the developing retina. Development 143:2172-2182.

Lange M, Norton W, Coolen M, Chaminade M, Merker S, Proft F, Schmitt A, Vernier P, Lesch KP, Bally-Cuif L (2012) The ADHD-susceptibility gene lphn3.1 modulates dopaminergic neuron formation and locomotor activity during zebrafish development. Mol Psychiatry 17:946-954.

Leamey CA, Sawatari A (2014) The teneurins: new players in the generation of visual topography. Semin Cell Dev Biol 35:173-179.

Leamey CA, Glendining KA, Kreiman G, Kang ND, Wang KH, Fassler R, Sawatari A, Tonegawa S, Sur M (2008) Differential gene expression between sensory neocortical areas: potential roles for Ten_m3 and Bcl6 in patterning visual and somatosensory pathways. Cereb Cortex 18:53-66.

Leamey CA, Merlin S, Lattouf P, Sawatari A, Zhou X, Demel N, Glendining KA, Oohashi T, Sur M, Fassler R (2007) Ten_m3 regulates eye-specific patterning in the mammalian visual pathway and is required for binocular vision. PLoS Biol 5:e241.

Lee S, Zhang Y, Chen M, Zhou ZJ (2016) Segregated Glycine-Glutamate Co-transmission from vGluT3 Amacrine Cells to Contrast-Suppressed and Contrast-Enhanced Retinal Circuits. Neuron 90:27-34.

Lee S, Chen L, Chen M, Ye M, Seal RP, Zhou ZJ (2014) An unconventional glutamatergic circuit in the retina formed by vGluT3 amacrine cells. Neuron 84:708-715.

Lefebvre JL, Sanes JR, Kay JN (2015) Development of dendritic form and function. Annu Rev Cell Dev Biol 31:741-777.

Lefebvre JL, Kostadinov D, Chen WV, Maniatis T, Sanes JR (2012) Protocadherins mediate dendritic self-avoidance in the mammalian nervous system. Nature 488:517-521.

LeGates TA, Fernandez DC, Hattar S (2014) Light as a central modulator of circadian rhythms, sleep and affect. Nat Rev Neurosci 15:443-454.

Lettvin JY, Maturana HR, McCulloch WS, Pitts WH (1959) What the frog's eye tells the frog's brain. Proceedings of the IRE 47:1940-1951.

Levick WR (1967) Receptive fields and trigger features of ganglion cells in the visual streak of the rabbits retina. J Physiol 188:285-307.

Levick WR, Thibos LN (1980) Orientation bias of cat retinal ganglion cells. Nature 286:389-390.

Levick WR, Thibos LN (1982) Analysis of orientation bias in cat retina. J Physiol 329:243-261.

Levine A, Bashan-Ahrend A, Budai-Hadrian O, Gartenberg D, Menasherow S, Wides R (1994) Odd Oz: a novel Drosophila pair rule gene. Cell 77:587-598.

Li H, Bishop KM, O'Leary DD (2006) Potential target genes of EMX2 include Odz/Ten-M and other gene families with implications for cortical patterning. Mol Cell Neurosci 33:136-149.

Li S, Sukeena JM, Simmons AB, Hansen EJ, Nuhn RE, Samuels IS, Fuerst PG (2015) DSCAM promotes refinement in the mouse retina through cell death and restriction of exploring dendrites. J Neurosci 35:5640-5654.

Li YN, Tsujimura T, Kawamura S, Dowling JE (2012a) Bipolar cell-photoreceptor connectivity in the zebrafish (Danio rerio) retina. J Comp Neurol 520:3786-3802.

Li Z, Ptak D, Zhang L, Walls EK, Zhong W, Leung YF (2012b) Phenylthiourea specifically reduces zebrafish eye size. PLoS One 7:e40132.

Lister JA, Robertson CP, Lepage T, Johnson SL, Raible DW (1999) nacre encodes a zebrafish microphthalmia-related protein that regulates neural-crest-derived pigment cell fate. Development 126:3757-3767.

Lohmann C, Myhr KL, Wong RO (2002) Transmitter-evoked local calcium release stabilizes developing dendrites. Nature 418:177-181.

London M, Hausser M (2005) Dendritic computation. Annu Rev Neurosci 28:503-532.

Lowe AS, Nikolaou N, Hunter PR, Thompson ID, Meyer MP (2013) A systems-based dissection of retinal inputs to the zebrafish tectum reveals different rules for different functional classes during development. J Neurosci 33:13946-13956.

Luo L (2015) Wiring of the Nervous System. In: Principles of Neurobiology (Luo L, ed), pp 167-204. New York: Garland Science.

Luo L, Flanagan JG (2007) Development of continuous and discrete neural maps. Neuron 56:284-300.

MacNeil MA, Masland RH (1998) Extreme diversity among amacrine cells: implications for function. Neuron 20:971-982.

MacNeil MA, Heussy JK, Dacheux RF, Raviola E, Masland RH (1999) The shapes and numbers of amacrine cells: matching of photofilled with Golgi-stained cells in the rabbit retina and comparison with other mammalian species. J Comp Neurol 413:305-326.

Mangrum WI, Dowling JE, Cohen ED (2002) A morphological classification of ganglion cells in the zebrafish retina. Vis Neurosci 19:767-779.

Marr D, Ullman S, Poggio TA (2010) Vision: A Computational Investigation into the Human Representation and Processing of Visual Information: MIT Press.

Marshel JH, Kaye AP, Nauhaus I, Callaway EM (2012) Anterior-posterior direction opponency in the superficial mouse lateral geniculate nucleus. Neuron 76:713-720.

Masland RH (2001) Neuronal diversity in the retina. Curr Opin Neurobiol 11:431-436.

Masland RH (2012a) The neuronal organization of the retina. Neuron 76:266-280.

Masland RH (2012b) The tasks of amacrine cells. Vis Neurosci 29:3-9.

Matsuoka RL, Nguyen-Ba-Charvet KT, Parray A, Badea TC, Chedotal A, Kolodkin AL (2011a) Transmembrane semaphorin signalling controls laminar stratification in the mammalian retina. Nature 470:259-263.

Matsuoka RL, Jiang Z, Samuels IS, Nguyen-Ba-Charvet KT, Sun LO, Peachey NS, Chedotal A, Yau KW, Kolodkin AL (2012) Guidance-cue control of horizontal cell morphology, lamination, and synapse formation in the mammalian outer retina. J Neurosci 32:6859-6868.

Matsuoka RL, Chivatakarn O, Badea TC, Samuels IS, Cahill H, Katayama K, Kumar SR, Suto F, Chedotal A, Peachey NS, Nathans J, Yoshida Y, Giger RJ, Kolodkin AL (2011b) Class 5 transmembrane semaphorins control selective Mammalian retinal lamination and function. Neuron 71:460-473.

McLaughlin T, O'Leary DD (2005) Molecular gradients and development of retinotopic maps. Annu Rev Neurosci 28:327-355.

Meek J (1983) Functional anatomy of the tectum mesencephali of the goldfish. An explorative analysis of the functional implications of the laminar structural organization of the tectum. Brain Res 287:247-297.

Mehta V, Sernagor E (2006) Early neural activity and dendritic growth in turtle retinal ganglion cells. Eur J Neurosci 24:773-786.

Merlin S, Horng S, Marotte LR, Sur M, Sawatari A, Leamey CA (2013) Deletion of Ten-m3 induces the formation of eye dominance domains in mouse visual cortex. Cereb Cortex 23:763-774.

Meyer MP, Smith SJ (2006) Evidence from in vivo imaging that synaptogenesis guides the growth and branching of axonal arbors by two distinct mechanisms. J Neurosci 26:3604-3614.

Mieda M, Kikuchi Y, Hirate Y, Aoki M, Okamoto H (1999) Compartmentalized expression of zebrafish ten-m3 and ten-m4, homologues of the Drosophila ten(m)/odd Oz gene, in the central nervous system. Mech Dev 87:223-227.

Minet AD, Chiquet-Ehrismann R (2000) Phylogenetic analysis of teneurin genes and comparison to the rearrangement hot spot elements of E. coli. Gene 257:87-97.

Minet AD, Rubin BP, Tucker RP, Baumgartner S, Chiquet-Ehrismann R (1999) Teneurin-1, a vertebrate homologue of the Drosophila pair-rule gene ten-m, is a neuronal protein with a novel type of heparin-binding domain. J Cell Sci 112 (Pt 12):2019-2032.

Missaire M, Hindges R (2015) The role of cell adhesion molecules in visual circuit formation: from neurite outgrowth to maps and synaptic specificity. Dev Neurobiol 75:569-583.

Morgan JL, Soto F, Wong RO, Kerschensteiner D (2011) Development of cell type-specific connectivity patterns of converging excitatory axons in the retina. Neuron 71:1014-1021.

Morrie RD, Feller MB (2015) An Asymmetric Increase in Inhibitory Synapse Number Underlies the Development of a Direction Selective Circuit in the Retina. J Neurosci 35:9281-9286.

Morrie RD, Feller MB (2016) Development of synaptic connectivity in the retinal direction selective circuit. Curr Opin Neurobiol 40:45-52.

Mosca TJ (2015) On the Teneurin track: a new synaptic organization molecule emerges. Front Cell Neurosci 9:204.

Mosca TJ, Luo L (2014) Synaptic organization of the Drosophila antennal lobe and its regulation by the Teneurins. Elife 3:e03726.

Mosca TJ, Hong W, Dani VS, Favaloro V, Luo L (2012) Trans-synaptic Teneurin signalling in neuromuscular synapse organization and target choice. Nature 484:237-241.

Mueller KP, Schnaedelbach OD, Russig HD, Neuhauss SC (2011) VisioTracker, an innovative automated approach to oculomotor analysis. J Vis Exp 10.3791/3556.

Mumm JS, Williams PR, Godinho L, Koerber A, Pittman AJ, Roeser T, Chien CB, Baier H, Wong RO (2006) In vivo imaging reveals dendritic targeting of laminated afferents by zebrafish retinal ganglion cells. Neuron 52:609-621.

Munch TA, da Silveira RA, Siegert S, Viney TJ, Awatramani GB, Roska B (2009) Approach sensitivity in the retina processed by a multifunctional neural circuit. Nat Neurosci 12:1308-1316.

Murphy-Baum BL, Taylor WR (2015) The Synaptic and Morphological Basis of Orientation Selectivity in a Polyaxonal Amacrine Cell of the Rabbit Retina. J Neurosci 35:13336-13350.

Nath A, Schwartz GW (2016) Cardinal Orientation Selectivity Is Represented by Two Distinct Ganglion Cell Types in Mouse Retina. J Neurosci 36:3208-3221.

Neuhauss SC, Biehlmaier O, Seeliger MW, Das T, Kohler K, Harris WA, Baier H (1999) Genetic disorders of vision revealed by a behavioral screen of 400 essential loci in zebrafish. J Neurosci 19:8603-8615.

Nevin LM, Taylor MR, Baier H (2008) Hardwiring of fine synaptic layers in the zebrafish visual pathway. Neural Dev 3:36.

Nevin LM, Robles E, Baier H, Scott EK (2010) Focusing on optic tectum circuitry through the lens of genetics. BMC Biol 8:126.

Niell CM (2013) Vision: more than expected in the early visual system. Curr Biol 23:R681-684.

Niell CM, Stryker MP (2008) Highly selective receptive fields in mouse visual cortex. J Neurosci 28:7520-7536.

Nikolaev A, Leung KM, Odermatt B, Lagnado L (2013) Synaptic mechanisms of adaptation and sensitization in the retina. Nat Neurosci 16:934-941.

Nikolaou N, Meyer MP (2015) Lamination Speeds the Functional Development of Visual Circuits. Neuron 88:999-1013.

Nikolaou N, Lowe AS, Walker AS, Abbas F, Hunter PR, Thompson ID, Meyer MP (2012) Parametric functional maps of visual inputs to the tectum. Neuron 76:317-324.

Nunes SM, Ferralli J, Choi K, Brown-Luedi M, Minet AD, Chiquet-Ehrismann R (2005) The intracellular domain of teneurin-1 interacts with MBD1 and CAP/ponsin resulting in subcellular codistribution and translocation to the nuclear matrix. Exp Cell Res 305:122-132.

O'Sullivan ML, Martini F, von Daake S, Comoletti D, Ghosh A (2014) LPHN3, a presynaptic adhesion-GPCR implicated in ADHD, regulates the strength of neocortical layer 2/3 synaptic input to layer 5. Neural Dev 9:7.

O'Sullivan ML, de Wit J, Savas JN, Comoletti D, Otto-Hitt S, Yates JR, 3rd, Ghosh A (2012) FLRT proteins are endogenous latrophilin ligands and regulate excitatory synapse development. Neuron 73:903-910.

Odermatt B, Nikolaev A, Lagnado L (2012) Encoding of luminance and contrast by linear and nonlinear synapses in the retina. Neuron 73:758-773.

Oesch N, Euler T, Taylor WR (2005) Direction-selective dendritic action potentials in rabbit retina. Neuron 47:739-750.

Okawa H, Della Santina L, Schwartz GW, Rieke F, Wong RO (2014a) Interplay of cell-autonomous and nonautonomous mechanisms tailors synaptic connectivity of converging axons in vivo. Neuron 82:125-137.

Okawa H, Hoon M, Yoshimatsu T, Della Santina L, Wong RO (2014b) Illuminating the multifaceted roles of neurotransmission in shaping neuronal circuitry. Neuron 83:1303-1318.

Olshausen BA, Field DJ (1996) Emergence of simple-cell receptive field properties by learning a sparse code for natural images. Nature 381:607-609.

Olveczky BP, Baccus SA, Meister M (2003) Segregation of object and background motion in the retina. Nature 423:401-408.

Olveczky BP, Baccus SA, Meister M (2007) Retinal adaptation to object motion. Neuron 56:689-700.

Omori Y, Araki F, Chaya T, Kajimura N, Irie S, Terada K, Muranishi Y, Tsujii T, Ueno S, Koyasu T, Tamaki Y, Kondo M, Amano S, Furukawa T (2012) Presynaptic dystroglycan-pikachurin complex regulates the proper synaptic connection between retinal photoreceptor and bipolar cells. J Neurosci 32:6126-6137.

Oohashi T, Zhou XH, Feng K, Richter B, Morgelin M, Perez MT, Su WD, Chiquet-Ehrismann R, Rauch U, Fassler R (1999) Mouse ten-m/Odz is a new family of dimeric type II transmembrane proteins expressed in many tissues. J Cell Biol 145:563-577.

Orger MB, Gahtan E, Muto A, Page-McCaw P, Smear MC, Baier H (2004) Behavioral screening assays in zebrafish. Methods Cell Biol 77:53-68.

Osterhout JA, El-Danaf RN, Nguyen PL, Huberman AD (2014) Birthdate and outgrowth timing predict cellular mechanisms of axon target matching in the developing visual pathway. Cell Rep 8:1006-1017.

Osterhout JA, Stafford BK, Nguyen PL, Yoshihara Y, Huberman AD (2015) Contactin-4 mediates axon-target specificity and functional development of the accessory optic system. Neuron 86:985-999.

Osterhout JA, Josten N, Yamada J, Pan F, Wu SW, Nguyen PL, Panagiotakos G, Inoue YU, Egusa SF, Volgyi B, Inoue T, Bloomfield SA, Barres BA, Berson DM, Feldheim DA, Huberman AD (2011) Cadherin-6 mediates axon-target matching in a non-image-forming visual circuit. Neuron 71:632-639.

Otaki JM, Firestein S (1999) Neurestin: putative transmembrane molecule implicated in neuronal development. Dev Biol 212:165-181.

Page-McCaw PS, Chung SC, Muto A, Roeser T, Staub W, Finger-Baier KC, Korenbrot JI, Baier H (2004) Retinal network adaptation to bright light requires tyrosinase. Nat Neurosci 7:1329-1336.

Pang JJ, Gao F, Wu SM (2002) Segregation and integration of visual channels: layer-by-layer computation of ON-OFF signals by amacrine cell dendrites. J Neurosci 22:4693-4701.

Park SJ, Kim IJ, Looger LL, Demb JB, Borghuis BG (2014) Excitatory synaptic inputs to mouse on-off direction-selective retinal ganglion cells lack direction tuning. J Neurosci 34:3976-3981.

Parker MO, Brock AJ, Millington ME, Brennan CH (2013) Behavioural phenotyping of casper mutant and 1-pheny-2-thiourea treated adult zebrafish. Zebrafish 10:466-471.

Passaglia CL, Troy JB, Ruttiger L, Lee BB (2002) Orientation sensitivity of ganglion cells in primate retina. Vision Res 42:683-694.

Pawley JB (2005) Handbook of biological confocal microscopy. New York, NY: Springer.

Pearson JT, Kerschensteiner D (2015) Ambient illumination switches contrast preference of specific retinal processing streams. J Neurophysiol 114:540-550.

Pei Z, Chen Q, Koren D, Giammarinaro B, Acaron Ledesma H, Wei W (2015) Conditional Knock-Out of Vesicular GABA Transporter Gene from Starburst Amacrine Cells Reveals the Contributions of Multiple Synaptic Mechanisms Underlying Direction Selectivity in the Retina. J Neurosci 35:13219-13232.

Peirce JW (2008) Generating Stimuli for Neuroscience Using PsychoPy. Front Neuroinform 2:10.

Piscopo DM, El-Danaf RN, Huberman AD, Niell CM (2013) Diverse visual features encoded in mouse lateral geniculate nucleus. J Neurosci 33:4642-4656.

Preuss SJ, Trivedi CA, vom Berg-Maurer CM, Ryu S, Bollmann JH (2014) Classification of object size in retinotectal microcircuits. Curr Biol 24:2376-2385.

Randlett O, Poggi L, Zolessi FR, Harris WA (2011) The oriented emergence of axons from retinal ganglion cells is directed by laminin contact in vivo. Neuron 70:266-280.

Randlett O, MacDonald RB, Yoshimatsu T, Almeida AD, Suzuki SC, Wong RO, Harris WA (2013) Cellular requirements for building a retinal neuropil. Cell Rep 3:282-290.

Ren JQ, McCarthy WR, Zhang H, Adolph AR, Li L (2002) Behavioral visual responses of wild-type and hypopigmented zebrafish. Vision Res 42:293-299.

Reyon D, Khayter C, Regan MR, Joung JK, Sander JD (2012) Engineering designer transcription activator-like effector nucleases (TALENs) by REAL or REAL-Fast assembly. Curr Protoc Mol Biol Chapter 12:Unit 12.15.

Richardson DS, Lichtman JW (2015) Clarifying Tissue Clearing. Cell 162:246-257.

Robles E, Filosa A, Baier H (2013) Precise lamination of retinal axons generates multiple parallel input pathways in the tectum. J Neurosci 33:5027-5039.

Robles E, Laurell E, Baier H (2014) The retinal projectome reveals brain-area-specific visual representations generated by ganglion cell diversity. Curr Biol 24:2085-2096.

Rodieck RW (1998) The First Steps in Seeing: Sinauer Associates.

Roska B, Werblin F (2001) Vertical interactions across ten parallel, stacked representations in the mammalian retina. Nature 410:583-587.

Rubin BP, Tucker RP, Martin D, Chiquet-Ehrismann R (1999) Teneurins: a novel family of neuronal cell surface proteins in vertebrates, homologous to the Drosophila pair-rule gene product Ten-m. Dev Biol 216:195-209.

Rubin BP, Tucker RP, Brown-Luedi M, Martin D, Chiquet-Ehrismann R (2002) Teneurin 2 is expressed by the neurons of the thalamofugal visual system in situ and promotes homophilic cell-cell adhesion in vitro. Development 129:4697-4705.

Ryazanova AD, Alekseev AA, Slepneva IA (2012) The phenylthiourea is a competitive inhibitor of the enzymatic oxidation of DOPA by phenoloxidase. J Enzyme Inhib Med Chem 27:78-83.

Sander JD, Maeder ML, Reyon D, Voytas DF, Joung JK, Dobbs D (2010) ZiFiT (Zinc Finger Targeter): an updated zinc finger engineering tool. Nucleic Acids Res 38:W462-468.

Sander JD, Cade L, Khayter C, Reyon D, Peterson RT, Joung JK, Yeh JR (2011) Targeted gene disruption in somatic zebrafish cells using engineered TALENs. Nat Biotechnol 29:697-698.

Sanes JR, Yamagata M (2009) Many paths to synaptic specificity. Annu Rev Cell Dev Biol 25:161-195.

Sanes JR, Zipursky SL (2010) Design principles of insect and vertebrate visual systems. Neuron 66:15-36.

Sanes JR, Masland RH (2015) The types of retinal ganglion cells: current status and implications for neuronal classification. Annu Rev Neurosci 38:221-246.

Sato S, Omori Y, Katoh K, Kondo M, Kanagawa M, Miyata K, Funabiki K, Koyasu T, Kajimura N, Miyoshi T, Sawai H, Kobayashi K, Tani A, Toda T, Usukura J, Tano Y, Fujikado T, Furukawa T (2008) Pikachurin, a dystroglycan ligand, is essential for photoreceptor ribbon synapse formation. Nat Neurosci 11:923-931.

Schindelin J, Arganda-Carreras I, Frise E, Kaynig V, Longair M, Pietzsch T, Preibisch S, Rueden C, Saalfeld S, Schmid B, Tinevez JY, White DJ, Hartenstein V, Eliceiri K, Tomancak P, Cardona A (2012) Fiji: an open-source platform for biological-image analysis. Nat Methods 9:676-682.

Schmitt EA, Dowling JE (1999) Early retinal development in the zebrafish, Danio rerio: light and electron microscopic analyses. J Comp Neurol 404:515-536.

Schneider CA, Rasband WS, Eliceiri KW (2012) NIH Image to ImageJ: 25 years of image analysis. Nat Methods 9:671-675.

Scholer J, Ferralli J, Thiry S, Chiquet-Ehrismann R (2015) The intracellular domain of teneurin-1 induces the activity of microphthalmia-associated transcription factor (MITF) by binding to transcriptional repressor HINT1. J Biol Chem 290:8154-8165.

Schreiner D, Weiner JA (2010) Combinatorial homophilic interaction between gamma-protocadherin multimers greatly expands the molecular diversity of cell adhesion. Proc Natl Acad Sci U S A 107:14893-14898.

Schubert T, Hoon M, Euler T, Lukasiewicz PD, Wong RO (2013) Developmental regulation and activity-dependent maintenance of GABAergic presynaptic inhibition onto rod bipolar cell axonal terminals. Neuron 78:124-137.

Semmelhack JL, Donovan JC, Thiele TR, Kuehn E, Laurell E, Baier H (2014) A dedicated visual pathway for prey detection in larval zebrafish. Elife 3.

Sernagor E, Grzywacz NM (1995) Emergence of complex receptive field properties of ganglion cells in the developing turtle retina. J Neurophysiol 73:1355-1364.

Sernagor E, Grzywacz NM (1996) Influence of spontaneous activity and visual experience on developing retinal receptive fields. Curr Biol 6:1503-1508.

Sethuramanujam S, McLaughlin AJ, deRosenroll G, Hoggarth A, Schwab DJ, Awatramani GB (2016) A Central Role for Mixed Acetylcholine/GABA Transmission in Direction Coding in the Retina. Neuron 90:1243-1256.

Seung HS, Sumbul U (2014) Neuronal cell types and connectivity: lessons from the retina. Neuron 83:1262-1272.

Shapiro L, Love J, Colman DR (2007) Adhesion molecules in the nervous system: structural insights into function and diversity. Annu Rev Neurosci 30:451-474.

Shekhar K, Lapan SW, Whitney IE, Tran NM, Macosko EZ, Kowalczyk M, Adiconis X, Levin JZ, Nemesh J, Goldman M, McCarroll SA, Cepko CL, Regev A, Sanes JR (2016) Comprehensive Classification of Retinal Bipolar Neurons by Single-Cell Transcriptomics. Cell 166:1308-1323.e1330.

Shen K, Scheiffele P (2010) Genetics and cell biology of building specific synaptic connectivity. Annu Rev Neurosci 33:473-507.

Silva JP, Lelianova VG, Ermolyuk YS, Vysokov N, Hitchen PG, Berninghausen O, Rahman MA, Zangrandi A, Fidalgo S, Tonevitsky AG, Dell A, Volynski KE, Ushkaryov YA (2011) Latrophilin 1 and its endogenous ligand Lasso/teneurin-2 form a high-affinity transsynaptic receptor pair with signaling capabilities. Proc Natl Acad Sci U S A 108:12113-12118.

Singh AP, Nusslein-Volhard C (2015) Zebrafish stripes as a model for vertebrate colour pattern formation. Curr Biol 25:R81-92.

Sivyer B, Williams SR (2013) Direction selectivity is computed by active dendritic integration in retinal ganglion cells. Nat Neurosci 16:1848-1856.

Sklar P et al. (2011) Large-scale genome-wide association analysis of bipolar disorder identifies a new susceptibility locus near ODZ4. Nat Genet 43:977-983.

Soto F, Watkins KL, Johnson RE, Schottler F, Kerschensteiner D (2013) NGL-2 regulates pathway-specific neurite growth and lamination, synapse formation, and signal transmission in the retina. J Neurosci 33:11949-11959.

Soto F, Ma X, Cecil JL, Vo BQ, Culican SM, Kerschensteiner D (2012) Spontaneous activity promotes synapse formation in a cell-type-dependent manner in the developing retina. J Neurosci 32:5426-5439.

Storey E, Bahlo M, Fahey M, Sisson O, Lueck CJ, Gardner RJ (2009) A new dominantly inherited pure cerebellar ataxia, SCA 30. J Neurol Neurosurg Psychiatry 80:408-411.

Streisinger G, Singer F, Walker C, Knauber D, Dower N (1986) Segregation analyses and gene-centromere distances in zebrafish. Genetics 112:311-319.

Sun L, Han X, He S (2011) Direction-selective circuitry in rat retina develops independently of GABAergic, cholinergic and action potential activity. PLoS One 6:e19477.

Sun LO, Jiang Z, Rivlin-Etzion M, Hand R, Brady CM, Matsuoka RL, Yau KW, Feller MB, Kolodkin AL (2013) On and off retinal circuit assembly by divergent molecular mechanisms. Science 342:1241974.

Sun LO, Brady CM, Cahill H, Al-Khindi T, Sakuta H, Dhande OS, Noda M, Huberman AD, Nathans J, Kolodkin AL (2015) Functional assembly of accessory optic system circuitry critical for compensatory eye movements. Neuron 86:971-984.

Suzuki N, Fukushi M, Kosaki K, Doyle AD, de Vega S, Yoshizaki K, Akazawa C, Arikawa-Hirasawa E, Yamada Y (2012) Teneurin-4 is a novel regulator of oligodendrocyte differentiation and myelination of small-diameter axons in the CNS. J Neurosci 32:11586-11599.

Suzuki N, Numakawa T, Chou J, de Vega S, Mizuniwa C, Sekimoto K, Adachi N, Kunugi H, Arikawa-Hirasawa E, Yamada Y, Akazawa C (2014) Teneurin-4 promotes cellular protrusion formation and neurite outgrowth through focal adhesion kinase signaling. Faseb j 28:1386-1397.

Suzuki SC, Bleckert A, Williams PR, Takechi M, Kawamura S, Wong RO (2013) Cone photoreceptor types in zebrafish are generated by symmetric terminal divisions of dedicated precursors. Proc Natl Acad Sci U S A 110:15109-15114.

Swindale NV (1998) Orientation tuning curves: empirical description and estimation of parameters. Biol Cybern 78:45-56.

Tachibana M, Kaneko A (1988) Retinal bipolar cells receive negative feedback input from GABAergic amacrine cells. Vis Neurosci 1:297-305.

Tagawa Y, Sawai H, Ueda Y, Tauchi M, Nakanishi S (1999) Immunohistological studies of metabotropic glutamate receptor subtype 6-deficient mice show no abnormality of retinal cell organization and ganglion cell maturation. J Neurosci 19:2568-2579.

Tan LA, Chand D, De Almeida R, Xu M, De Lannoy L, Lovejoy DA (2012) Modulation of neuroplastic changes and corticotropin-releasing factor-associated behavior by a phylogenetically ancient and conserved peptide family. Gen Comp Endocrinol 176:309-313.

Taylor WR, Smith RG (2011) Trigger features and excitation in the retina. Curr Opin Neurobiol 21:672-678.

Taylor WR, Smith RG (2012) The role of starburst amacrine cells in visual signal processing. Vis Neurosci 29:73-81.

Teh C, Chudakov DM, Poon KL, Mamedov IZ, Sek JY, Shidlovsky K, Lukyanov S, Korzh V (2010) Optogenetic in vivo cell manipulation in KillerRed-expressing zebrafish transgenics. BMC Dev Biol 10:110.

Temizer I, Donovan JC, Baier H, Semmelhack JL (2015) A Visual Pathway for Looming-Evoked Escape in Larval Zebrafish. Curr Biol 25:1823-1834.

Thisse B, Pflumio S, Fürthauer M, Loppin B, Heyer V, Degrave A, Woehl R, Lux A, Steffan T, Charbonnier XQ, Thisse C (2001) Expression of the zebrafish genome during embryogenesis (NIH R01 RR15402). ZFIN Direct Data Submission http://zfin.org/action/figure/all-figure-view/ZDB-PUB-010810-1?probeZdbID=ZDB-EST-020923-1.

Thisse C, Thisse B (2008) High-resolution in situ hybridization to whole-mount zebrafish embryos. Nat Protoc 3:59-69.

Thu CA, Chen WV, Rubinstein R, Chevee M, Wolcott HN, Felsovalyi KO, Tapia JC, Shapiro L, Honig B, Maniatis T (2014) Single-cell identity generated by combinatorial homophilic interactions between alpha, beta, and gamma protocadherins. Cell 158:1045-1059.

Tian N (2008) Synaptic activity, visual experience and the maturation of retinal synaptic circuitry. J Physiol 586:4347-4355.

Tian N, Copenhagen DR (2001) Visual deprivation alters development of synaptic function in inner retina after eye opening. Neuron 32:439-449.

Tian N, Copenhagen DR (2003) Visual stimulation is required for refinement of ON and OFF pathways in postnatal retina. Neuron 39:85-96.

Tikidji-Hamburyan A, Reinhard K, Seitter H, Hovhannisyan A, Procyk CA, Allen AE, Schenk M, Lucas RJ, Münch TA (2015) Retinal output changes qualitatively with every change in ambient illuminance. Nature neuroscience 18:66-74.

Tomer R, Lovett-Barron M, Kauvar I, Andalman A, Burns VM, Sankaran S, Grosenick L, Broxton M, Yang S, Deisseroth K (2015) SPED Light Sheet Microscopy: Fast Mapping of Biological System Structure and Function. Cell 163:1796-1806.

Tomita K, Moriyoshi K, Nakanishi S, Guillemot F, Kageyama R (2000) Mammalian achaete-scute and atonal homologs regulate neuronal versus glial fate determination in the central nervous system. Embo j 19:5460-5472.

Trenholm S, Johnson K, Li X, Smith RG, Awatramani GB (2011) Parallel mechanisms encode direction in the retina. Neuron 71:683-694.

Tucker RP, Chiquet-Ehrismann R (2006) Teneurins: a conserved family of transmembrane proteins involved in intercellular signaling during development. Dev Biol 290:237-245.

Tucker RP, Martin D, Kos R, Chiquet-Ehrismann R (2000) The expression of teneurin-4 in the avian embryo. Mech Dev 98:187-191.

Tucker RP, Kenzelmann D, Trzebiatowska A, Chiquet-Ehrismann R (2007) Teneurins: transmembrane proteins with fundamental roles in development. Int J Biochem Cell Biol 39:292-297.

Tucker RP, Beckmann J, Leachman NT, Scholer J, Chiquet-Ehrismann R (2012) Phylogenetic analysis of the teneurins: conserved features and premetazoan ancestry. Mol Biol Evol 29:1019-1029.

van Strien NM, Cappaert NL, Witter MP (2009) The anatomy of memory: an interactive overview of the parahippocampal-hippocampal network. Nat Rev Neurosci 10:272-282.

van Wyk M, Taylor WR, Vaney DI (2006) Local edge detectors: a substrate for fine spatial vision at low temporal frequencies in rabbit retina. J Neurosci 26:13250-13263.

Vaney DI, Sivyer B, Taylor WR (2012) Direction selectivity in the retina: symmetry and asymmetry in structure and function. Nat Rev Neurosci 13:194-208.

Venkataramani S, Taylor WR (2010) Orientation selectivity in rabbit retinal ganglion cells is mediated by presynaptic inhibition. J Neurosci 30:15664-15676.

Venkataramani S, Taylor WR (2016) Synaptic Mechanisms Generating Orientation Selectivity in the ON Pathway of the Rabbit Retina. J Neurosci 36:3336-3349.

Vihtelic TS, Hyde DR (2000) Light-induced rod and cone cell death and regeneration in the adult albino zebrafish (Danio rerio) retina. J Neurobiol 44:289-307.

Visser JJ, Cheng Y, Perry SC, Chastain AB, Parsa B, Masri SS, Ray TA, Kay JN, Wojtowicz WM (2015) An extracellular biochemical screen reveals that FLRTs and Unc5s mediate neuronal subtype recognition in the retina. Elife 4:e08149.

Vladimirov N, Mu Y, Kawashima T, Bennett DV, Yang CT, Looger LL, Keller PJ, Freeman J, Ahrens MB (2014) Light-sheet functional imaging in fictively behaving zebrafish. Nat Methods 11:883-884.

Vlasits AL, Morrie RD, Tran-Van-Minh A, Bleckert A, Gainer CF, DiGregorio DA, Feller MB (2016) A Role for Synaptic Input Distribution in a Dendritic Computation of Motion Direction in the Retina. Neuron 89:1317-1330.

Vysokov NV, Silva JP, Lelianova VG, Ho C, Djamgoz MB, Tonevitsky AG, Ushkaryov YA (2016) The Mechanism of Regulated Release of Lasso/Teneurin-2. Front Mol Neurosci 9:59.

Wang L, Sarnaik R, Rangarajan K, Liu X, Cang J (2010) Visual receptive field properties of neurons in the superficial superior colliculus of the mouse. J Neurosci 30:16573-16584.

Wassle H (2004) Parallel processing in the mammalian retina. Nat Rev Neurosci 5:747-757.

Wei W, Feller MB (2011) Organization and development of direction-selective circuits in the retina. Trends Neurosci 34:638-645.

Wei W, Hamby AM, Zhou K, Feller MB (2011) Development of asymmetric inhibition underlying direction selectivity in the retina. Nature 469:402-406.

Werblin FS (2011) The retinal hypercircuit: a repeating synaptic interactive motif underlying visual function. J Physiol 589:3691-3702.

White RM, Sessa A, Burke C, Bowman T, LeBlanc J, Ceol C, Bourque C, Dovey M, Goessling W, Burns CE, Zon LI (2008) Transparent adult zebrafish as a tool for in vivo transplantation analysis. Cell Stem Cell 2:183-189.

Whittaker JR (1966) An analysis of melanogenesis in differentiating pigment cells of ascidian embryos. Dev Biol 14:1-39.

Williams ME, de Wit J, Ghosh A (2010) Molecular mechanisms of synaptic specificity in developing neural circuits. Neuron 68:9-18.

Wolf S, Supatto W, Debregeas G, Mahou P, Kruglik SG, Sintes JM, Beaurepaire E, Candelier R (2015) Whole-brain functional imaging with two-photon light-sheet microscopy. Nat Methods 12:379-380.

Wong RO, Ghosh A (2002) Activity-dependent regulation of dendritic growth and patterning. Nat Rev Neurosci 3:803-812.

Wong RO, Herrmann K, Shatz CJ (1991) Remodeling of retinal ganglion cell dendrites in the absence of action potential activity. J Neurobiol 22:685-697.

Wong WT, Wong RO (2001) Changing specificity of neurotransmitter regulation of rapid dendritic remodeling during synaptogenesis. Nat Neurosci 4:351-352.

Wong WT, Faulkner-Jones BE, Sanes JR, Wong RO (2000) Rapid dendritic remodeling in the developing retina: dependence on neurotransmission and reciprocal regulation by Rac and Rho. J Neurosci 20:5024-5036.

Wyatt HJ, Day NW (1976) Specific effects of neurotransmitter antagonists on ganglion cells in rabbit retina. Science 191:204-205.

Xi Y, Yu M, Godoy R, Hatch G, Poitras L, Ekker M (2011) Transgenic zebrafish expressing green fluorescent protein in dopaminergic neurons of the ventral diencephalon. Dev Dyn 240:2539-2547.

Xiao T, Staub W, Robles E, Gosse NJ, Cole GJ, Baier H (2011) Assembly of lamina-specific neuronal connections by slit bound to type IV collagen. Cell 146:164-176.

Xu HP, Tian N (2007) Retinal ganglion cell dendrites undergo a visual activity-dependent redistribution after eye opening. J Comp Neurol 503:244-259.

Xu HP, Sun JH, Tian N (2014) A general principle governs vision-dependent dendritic patterning of retinal ganglion cells. J Comp Neurol 522:3403-3422.

Yamagata M, Sanes JR (2008) Dscam and Sidekick proteins direct lamina-specific synaptic connections in vertebrate retina. Nature 451:465-469.

Yamagata M, Sanes JR (2012) Expanding the Ig superfamily code for laminar specificity in retina: expression and role of contactins. J Neurosci 32:14402-14414.

Yamagata M, Weiner JA, Sanes JR (2002) Sidekicks: synaptic adhesion molecules that promote lamina-specific connectivity in the retina. Cell 110:649-660.

Yilmaz M, Meister M (2013) Rapid innate defensive responses of mice to looming visual stimuli. Curr Biol 23:2011-2015.

Yogev S, Shen K (2014) Cellular and molecular mechanisms of synaptic specificity. Annu Rev Cell Dev Biol 30:417-437.

Yonehara K, Balint K, Noda M, Nagel G, Bamberg E, Roska B (2011) Spatially asymmetric reorganization of inhibition establishes a motion-sensitive circuit. Nature 469:407-410.

Yonehara K, Farrow K, Ghanem A, Hillier D, Balint K, Teixeira M, Juttner J, Noda M, Neve RL, Conzelmann KK, Roska B (2013) The first stage of cardinal direction selectivity is localized to the dendrites of retinal ganglion cells. Neuron 79:1078-1085.

Yonehara K, Fiscella M, Drinnenberg A, Esposti F, Trenholm S, Krol J, Franke F, Scherf BG, Kusnyerik A, Muller J, Szabo A, Juttner J, Cordoba F, Reddy AP, Nemeth J, Nagy ZZ, Munier F, Hierlemann A, Roska B (2016) Congenital Nystagmus Gene FRMD7 Is Necessary for Establishing a Neuronal Circuit Asymmetry for Direction Selectivity. Neuron 89:177-193.

Yoshida K, Watanabe D, Ishikane H, Tachibana M, Pastan I, Nakanishi S (2001) A key role of starburst amacrine cells in originating retinal directional selectivity and optokinetic eye movement. Neuron 30:771-780.

Young TR, Leamey CA (2009) Teneurins: important regulators of neural circuitry. Int J Biochem Cell Biol 41:990-993.

Young TR, Bourke M, Zhou X, Oohashi T, Sawatari A, Fassler R, Leamey CA (2013) Ten-m2 Is Required for the Generation of Binocular Visual Circuits. J Neurosci 33:12490-12509.

Zhang C, McCall MA (2012) Receptor targets of amacrine cells. Vis Neurosci 29:11-29.

Zhang LI, Poo MM (2001) Electrical activity and development of neural circuits. Nat Neurosci 4 Suppl:1207-1214.

Zhang RW, Li XQ, Kawakami K, Du JL (2016) Stereotyped initiation of retinal waves by bipolar cells via presynaptic NMDA autoreceptors. Nat Commun 7:12650.

Zhang Y, Kim IJ, Sanes JR, Meister M (2012) The most numerous ganglion cell type of the mouse retina is a selective feature detector. Proc Natl Acad Sci U S A 109:E2391-2398.

Zhao X, Chen H, Liu X, Cang J (2013) Orientation-selective responses in the mouse lateral geniculate nucleus. J Neurosci 33:12751-12763.

Zheng L, Michelson Y, Freger V, Avraham Z, Venken KJ, Bellen HJ, Justice MJ, Wides R (2011) Drosophila Ten-m and filamin affect motor neuron growth cone guidance. PLoS One 6:e22956.

Zhou XH, Brandau O, Feng K, Oohashi T, Ninomiya Y, Rauch U, Fassler R (2003) The murine Ten-m/Odz genes show distinct but overlapping expression patterns during development and in adult brain. Gene Expr Patterns 3:397-405.

Zipursky SL, Sanes JR (2010) Chemoaffinity revisited: dscams, protocadherins, and neural circuit assembly. Cell 143:343-353.

Appendix

Citations are indicated as of 24/01/2017

Paper 1

Title: Teneurin-3 Specifies Morphological and Functional Connectivity of Retinal Ganglion Cells in the Vertebrate Visual System

Journal: Cell Reports

Year: 2013

Authors: Paride Antinucci[1], Nikolas Nikolaou[1], Martin P. Meyer[1], and Robert Hindges[1]*

[1]Centre for Developmental Neurobiology, King's College London, Guy's Campus, London SE1 1UL, UK
*Corresponding author

Citations: 21 (Google Scholar)

Contribution: Design of project and experiments, data collection and analysis, paper writing (primary writer)

PMID: 24183672

DOI: 10.1016/j.celrep.2013.09.045

This publication contains work presented in Chapter 4 and 5 of this thesis.

Cell Reports
Report

Teneurin-3 Specifies Morphological and Functional Connectivity of Retinal Ganglion Cells in the Vertebrate Visual System

Paride Antinucci,[1] Nikolas Nikolaou,[1] Martin P. Meyer,[1] and Robert Hindges[1,*]
[1]MRC Centre for Developmental Neurobiology, King's College London, Guy's Campus, London SE1 1UL, UK
*Correspondence: robert.hindges@kcl.ac.uk
http://dx.doi.org/10.1016/j.celrep.2013.09.045

SUMMARY

A striking feature of the CNS is the precise wiring of its neuronal connections. During vertebrate visual system development, different subtypes of retinal ganglion cells (RGCs) form specific connections with their corresponding synaptic partners. However, the underlying molecular mechanisms remain to be fully elucidated. Here, we report that the cell-adhesive transmembrane protein Teneurin-3 (Tenm3) is required by zebrafish RGCs for acquisition of their correct morphological and functional connectivity in vivo. Teneurin-3 is expressed by RGCs and their presynaptic amacrine and postsynaptic tectal cell targets. Knockdown of Teneurin-3 leads to RGC dendrite stratification defects within the inner plexiform layer, as well as mistargeting of dendritic processes into outer portions of the retina. Moreover, a subset of RGC axons exhibits tectal laminar arborization errors. Finally, functional analysis of RGCs targeting the tectum reveals a selective deficit in the development of orientation selectivity after Teneurin-3 knockdown. These results suggest that Teneurin-3 plays an instructive role in the functional wiring of the vertebrate visual system.

INTRODUCTION

In the vertebrate retina, retinal ganglion cells (RGCs) develop stereotypic dendritic arborization patterns and make specific synaptic connections with amacrine and bipolar cells in the inner plexiform layer (IPL) (Masland, 2012). The formation of such precise connections is critical for the processing of visual information and the generation of feature selectivity in RGCs (Gollisch and Meister, 2010; Wässle, 2004). A key structural characteristic of visual circuits is the organization of connections into precise laminae (Roska and Werblin, 2001; Sanes and Zipursky, 2010). Recent studies have shown that the assembly of neuropil strata in the IPL is regulated by both adhesive (Yamagata and Sanes, 2008) and repulsive transmembrane proteins (Matsuoka et al., 2011). Similarly, such attractive and repulsive cues are also crucial in establishing specific connectivity between RGC axons and their targets in the brain (Osterhout et al., 2011; Xiao et al., 2011). Our understanding of the molecular mechanisms that specify connections within the retina and between the retina and retinorecipient nuclei in the brain, however, is still far from complete.

Teneurins (Ten-m/Odz) are a phylogenetically conserved family of type II transmembrane proteins (Tucker et al., 2012; Tucker and Chiquet-Ehrismann, 2006). Their large extracellular domain contains eight epidermal growth factor (EGF)-like repeats, multiple tyrosine and aspartate (YD) repeats and five NHL (NCL-1, HT2A, and Lin-41) repeats, which mediate homophilic recognition and adhesion (Beckmann et al., 2013). In vertebrates, these proteins are encoded by four genes, *teneurin 1–4* (also called *odz1–4*), expressed in distinct and often interconnected regions of the nervous system (Tucker and Chiquet-Ehrismann, 2006). In *Drosophila*, the role of teneurins in synaptic partner matching and target choice has been elegantly shown in the olfactory system (Hong et al., 2012) and at the neuromuscular junction (Mosca et al., 2012). In mice, teneurins regulate the generation of binocular visual circuits by controlling the development of ipsilaterally projecting RGCs (Dharmaratne et al., 2012; Leamey et al., 2007; Young et al., 2013). However, a role for teneurins in mediating synapse-specific functional wiring in the vertebrate visual system has yet to be demonstrated.

Here, we investigate the role of *teneurin-3* (hereafter referred to as *tenm3*) in shaping the morphological and functional connectivity of RGCs in vivo using zebrafish. We report that *tenm3* is expressed in RGCs, amacrine cells, and the main retinorecipient target in the brain, the optic tectum. We show that *tenm3* knockdown induces stratification and targeting errors of both dendrites and axons in a subset of RGCs. In support of this, we provide evidence showing that orientation-selective, but not direction-selective, responses are impaired in *tenm3* morphants, suggesting that *tenm3* is involved in wiring subsets of functionally defined visual circuits.

RESULTS

Our study focused on time points between 2 days postfertilization (dpf) and 5 dpf, a period during which RGCs undergo a rapid

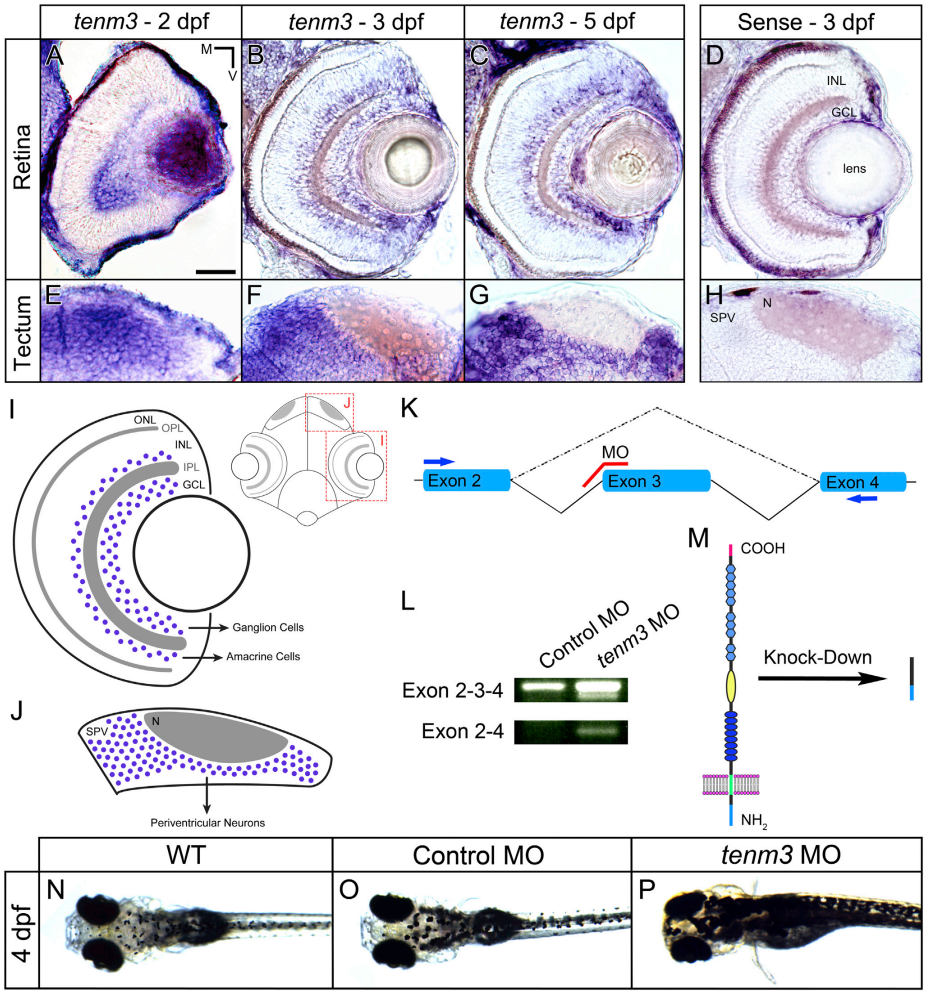

Figure 1. *Teneurin-3* Is Expressed in Interconnected Regions of the Zebrafish Visual System

(A–C) Retinal cryosections of whole-mount in situ hybridizations showing *tenm3* mRNA expression at 2, 3, and 5 dpf.

(D and H) Control in situ hybridizations using sense *tenm3* riboprobe.

(E–G) Tectal cryosections of whole-mount in situ hybridizations showing *tenm3* mRNA expression at 2, 3, and 5 dpf. All images are in transverse plane. Scale bar, 40 μm. N, neuropil; M, medial; V, ventral.

(I) Schematic showing the expression pattern of *tenm3* in the retina. *Tenm3*-positive cells are represented as blue circles. Neuropil layers are indicated in gray. Anatomical reference is reported on the right. IPL, inner plexiform layer; ONL, outer nuclear layer; OPL, outer plexiform layer.

(J) Schematic showing the expression pattern of *tenm3* in the optic tectum.

(K) Schematic detailing the targeting site of splice-blocking *tenm3* morpholino (MO), which is shown in red. Exons are represented in cyan. Solid lines indicate introns. The dashed line indicates exon 3 deletion caused by *tenm3* MO injections. Primers used for RT-PCR (L) are reported as blue arrows.

(legend continued on next page)

Cell PRESS
Open ACCESS

phase of morphological and functional development (Lowe et al., 2013; Meyer and Smith, 2006; Mumm et al., 2006).

Teneurin-3 Is Expressed in Interconnected Regions of the Developing Visual System

To reveal the expression pattern of *tenm3* in the developing zebrafish visual system, we carried out in situ hybridization analyses using a specific digoxigenin-labeled antisense riboprobe against *tenm3*. In the retina, *tenm3* is expressed in the ganglion cell layer (GCL) and the inner third of the inner nuclear layer (INL), where amacrine cells are located (Figures 1A–1C). Since in zebrafish only a very small number of displaced amacrine cells reside in the GCL (Connaughton et al., 1999), the majority of signal detected in this layer can be attributed to RGCs. At 2 dpf, *tenm3* is expressed more strongly in the ventral part of the retina (Figure 1A). At 3 and 5 dpf, *tenm3* acquires a sparse expression pattern, suggesting that at these stages of development only a subset of cells are *tenm3*-positive (Figures 1B and 1C). *Tenm3* is also expressed in the main target of RGC axons, the optic tectum (Figures 1E–1G). At 2 dpf, *tenm3* is highly expressed in the medial portion of the stratum periventriculare (SPV), where cell bodies of most tectal cells are located (Figure 1E). Between 3 and 5 dpf, this medial-to-lateral gradient gradually decreases (Figures 1F and 1G) and, at 5 dpf, *tenm3* shows a salt-and-pepper expression pattern (Figure 1G). In summary, *tenm3* is expressed by RGCs, amacrine cells, and tectal neurons (Figures 1I and 1J), consistent with a possible role of *tenm3* in instructing connectivity along the visual pathway.

Teneurin-3 Regulates RGC Dendritic Stratification in the IPL

To investigate the function of *tenm3* within the developing visual system, we used antisense morpholino oligonucleotides (MOs) to knock down *tenm3* expression levels. We designed a splice-blocking MO (Draper et al., 2001) targeting the boundary between intron 2 and exon 3 (hereafter referred to as *tenm3* MO; Figure 1K). Injection of *tenm3* MO into one-cell-stage zebrafish embryos produces the deletion of exon 3 (Figure 1L), which encodes part of the intracellular domain. This leads to a frameshift in exon 4 (transmembrane domain) and a subsequent early stop codon in exon 5, resulting in deletion of the transmembrane and extracellular domains (Figure 1M). To confirm results obtained with this *tenm3* MO, a second splice-blocking MO targeting a nonoverlapping region of *tenm3* mRNA (i.e., the boundary between exon 4 and intron 4) was also used (*tenm3* MO 2; see Figure S1). *Tenm3* morphants are viable and do not show any obvious morphological defect. However, 4 dpf *tenm3* MO-injected larvae fail to show a normal visually mediated background adaptation (VBA) and therefore appear darker compared to wild-type (WT) and control MO-injected larvae (Figures 1N–1P). Since the VBA is a neuroendocrine response dependent on the function of RGCs (Kay et al., 2001), we deduced that the knockdown of *tenm3* somehow impairs the normal development of the visual system.

In order to examine IPL organization in vivo, we used the Tg(*Isl2b:Gal4;UAS:Kaede*) transgenic zebrafish line (see Experimental Procedures), where the fluorescent protein Kaede is expressed in the majority of RGCs. At 5 dpf, when RGC dendrites exhibit clear stratification, four Kaede-positive strata are visible in the IPL of WT and control MO-injected larvae (Figures 2A and 2B). Fluorescence intensity measurements across the IPL of multiple larvae show that these strata are positioned at 5%, 33%, 66%, and 95% depth of the IPL (with 0% corresponding to GCL/IPL border and 100% to IPL/INL border), and thus were named S5, S33, S66, and S95, respectively (Figure 2E; WT n = 7 larvae, control MO n = 7). The presence of four dendritic strata in the IPL of 5 dpf zebrafish larvae is consistent with previous work using the Tg(*Brn3c:MGFP*) transgenic line, where approximately 50% of RGCs are labeled (Mumm et al., 2006). In 5 dpf *tenm3* morphants, by contrast, strata within the IPL are poorly defined (Figures 2C and 2D). The average fluorescence intensity profile reveals that only three Kaede-positive strata are present in the IPL of *tenm3* morphants (Figure 2E; n = 10 larvae). Specifically, only one irregularly laminated stratum is visible in the medial portion of the IPL, instead of the two middle strata (S33 and S66) found in WT and control MO retinae. Furthermore, the outermost stratum (S95) is not tightly stratified and appears thicker compared to control groups. No significant difference in IPL width was observed among the three groups (WT 15.2 ± 0.2 μm; control MO 15.0 ± 0.1 μm; *tenm3* MO 15.1 ± 0.2 μm; $F_{2,21} = 0.08$, $p = 0.92$, n = 24 larvae). In addition to these stratification abnormalities in the IPL, we detected ectopic RGC processes in the INL of *tenm3* morphants (Figures 2C′ and 2D′, cyan arrowheads; n = 19 out of 20 larvae), a phenomenon never observed in WT and control MO larvae, where all RGC dendrites are confined within the IPL (Figures 2A′ and 2B′; n = 10 larvae per group). Strikingly, in some cases, these processes reach the outer plexiform layer (OPL; Figure 2C′, yellow arrow). Ectopic RGC processes extending into the INL were also seen in *tenm3* morphant retinae at 3 dpf, when RGCs start to develop stratified dendritic arbors within the IPL (data not shown).

To resolve the changes in RGC dendritic morphology in greater detail, we mosaically labeled individual RGCs by coinjecting *Ath5:Gal4*, *UAS:GFP* and *UAS:tdTomato* DNA constructs into one-cell-stage embryos. The combinatorial expression of different fluorescent reporters in RGCs enabled us to distinguish between occasionally overlapping dendritic arbors of different cells. Using this approach, we were able to determine that the neurites mistargeting into outer layers of the retina observed in *tenm3* morphants originate from RGC dendrites (Figure 3A, cyan arrowheads) and that this phenotype is restricted to a

(L) RT-PCR analysis of *tenm3* mRNA structure in control MO- and *tenm3* MO-injected embryos. Two shorter splice variants are distinguished in *tenm3* morphants. cDNA sequence comparison revealed that the shortest splice variant lacks exon 3.
(M) Schematic detailing the effect of exon 3 deletion caused by the splice-blocking *tenm3* MO, resulting in the deletion of Tenm3 transmembrane and extracellular domains. The full-length protein is represented on the left. The N terminus is located intracellularly, whereas the C terminus is in the extracellular space.
(N–P) At 4 dpf, *tenm3* morphant larvae fail to visually adapt their skin pigmentation to the level of background illumination.
See also Figure S1.

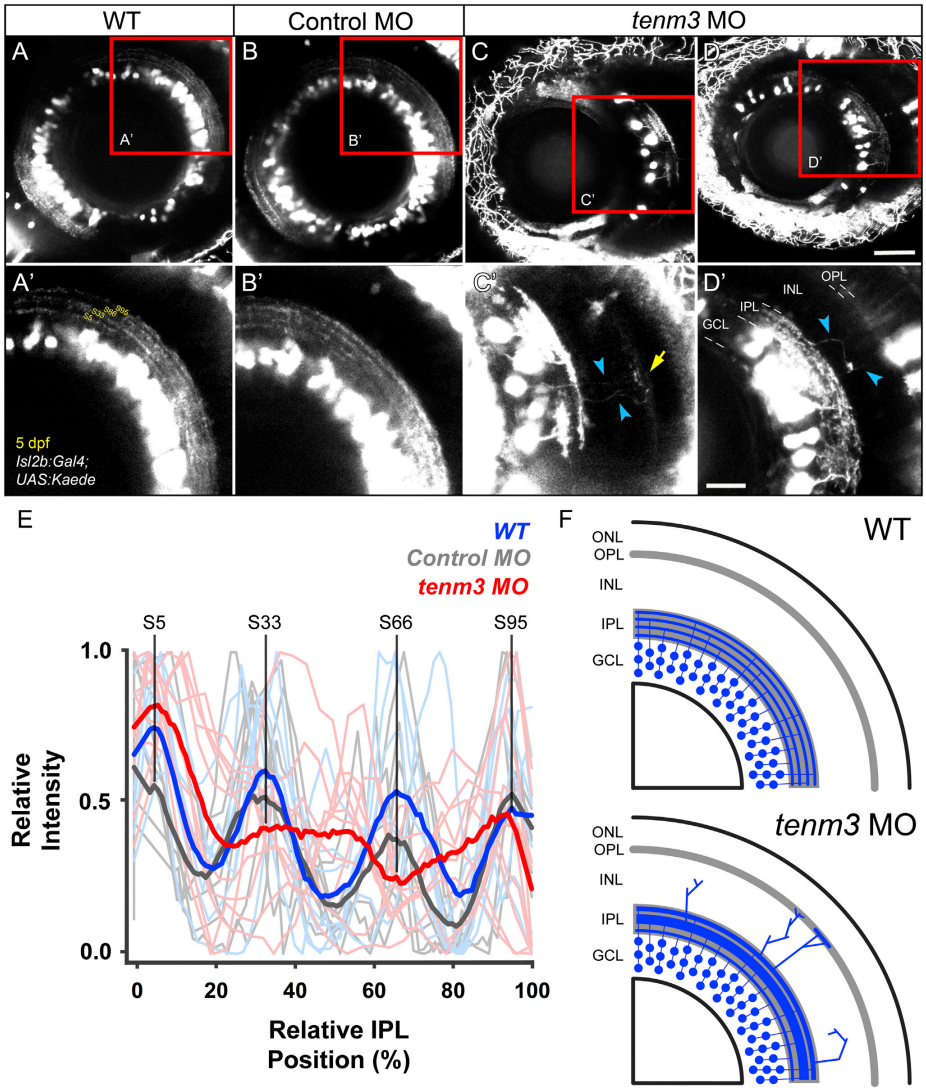

Figure 2. ***Teneurin-3*** **Is Required for Correct Stratification of RGC Dendrites**

(A–D) Kaede-expressing RGCs in the retina of 5 dpf WT, control MO-injected, and *tenm3* MO-injected larvae.

(A′–D′) Insets in (A)–(D) showing the dendritic stratification pattern of Kaede-positive RGCs. All images represent maximum intensity projections of ~20 μm confocal z stacks. Scale bars, 40 μm (A–D) and 20 μm in (A′–D′). GCL, ganglion cell layer; INL, inner nuclear layer; IPL, inner plexiform layer; OPL, outer plexiform layer.

(legend continued on next page)

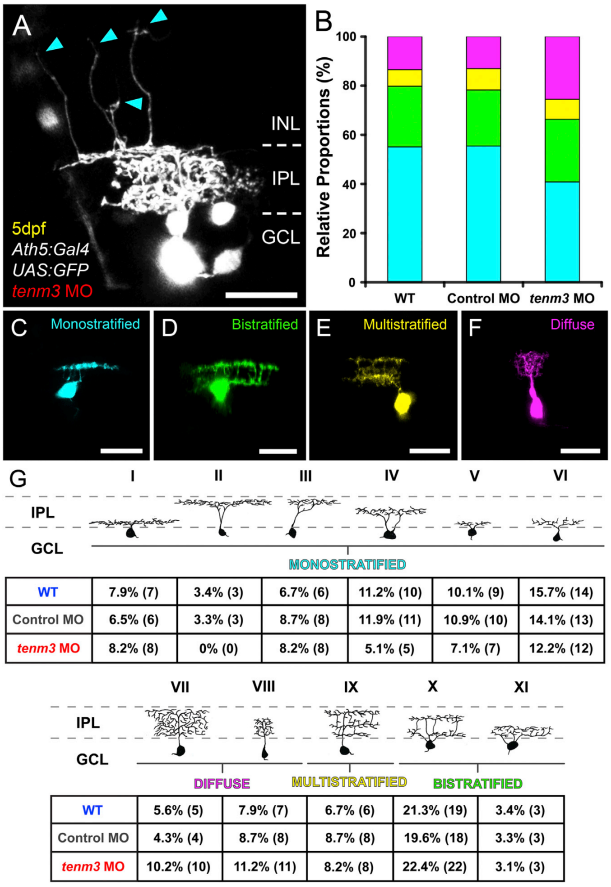

WT	7.9% (7)	3.4% (3)	6.7% (6)	11.2% (10)	10.1% (9)	15.7% (14)
Control MO	6.5% (6)	3.3% (3)	8.7% (8)	11.9% (11)	10.9% (10)	14.1% (13)
tenm3 MO	8.2% (8)	0% (0)	8.2% (8)	5.1% (5)	7.1% (7)	12.2% (12)

WT	5.6% (5)	7.9% (7)	6.7% (6)	21.3% (19)	3.4% (3)
Control MO	4.3% (4)	8.7% (8)	8.7% (8)	19.6% (18)	3.3% (3)
tenm3 MO	10.2% (10)	11.2% (11)	8.2% (8)	22.4% (22)	3.1% (3)

Figure 3. Higher Proportion of RGCs with Diffuse Dendritic Arbors in *teneurin-3* Morphants

(A) Lateral view of mosaically labeled RGCs in the retina of a 5 dpf *tenm3* MO-injected larva. Scale bar, 20 μm. GCL, ganglion cell layer; INL, inner nuclear layer; IPL, inner plexiform layer.

(B) Bar graph showing the proportions of 5 dpf RGCs possessing monostratified (cyan, C), bistratified (green, D), multistratified (yellow, E), and diffuse (magenta, F) dendritic arbors relative to the total number mosaically labeled RGCs within each animal group (WT n = 89 cells in 34 larvae; control MO n = 92 cells in 39 larvae; *tenm3* MO n = 98 cells in 49 larvae).

(C–F) Representative RGCs with monostratified (C), bistratified (D), multistratified (E), and diffuse (F) dendritic arbors. All images represent maximum intensity projections of ~30 μm confocal z stacks that have been pseudocolored and rotated to best show dendritic arborizations. Scale bars, 20 μm.

(G) Summary table showing the morphological classification and frequency of the 11 RGC types within each group (number of cells found per each type are reported in brackets). In *tenm3* morphants, four diffuse RGCs (4.1% of cells) showed dendritic arborization patterns that could not be classified in any of the 11 types and, hence, were not included in the table.

subset of cells (n = 5 cells out of 98 in 49 larvae). Moreover, mosaic labeling allowed us to visualize the precise IPL dendritic stratification patterns of single RGCs (Figures 3C–3F). Interestingly, 5 dpf *tenm3* morphants show a significantly higher proportion of RGCs possessing diffuse dendritic arbors (*tenm3* MO 25 diffuse versus 73 stratified cells in 49 larvae; WT 12 diffuse versus 77 stratified cells in 34 larvae; control MO 12 diffuse versus 80 stratified cells in 39 larvae; $\chi^2 = 6.596$, df = 2, p = 0.037). Looking at the relative proportions between monostratified, bistratified, multistratified, and diffuse RGCs, it appears that the increase in number of RGCs with diffuse dendritic arbors is exclusively at the expense of monostratified RGCs (Figure 3B; WT 55.1% monostratified, 24.7% bistratified, 6.7% multistratified, 13.5% diffuse; control MO 55.5% monostratified, 22.8% bistratified, 8.7% multistratified, 13% diffuse; *tenm3* MO 40.8% monostratified, 25.5% bistratified, 8.2% multistratified, 25.5% diffuse). Further identification and classification of the 11 RGC types previously reported in the adult zebrafish retina (Mangrum et al., 2002) revealed that the monostratified RGC types are not indiscriminately affected by *tenm3* knockdown. In fact, some RGC monostratified types decrease in frequency in *tenm3* morphants whereas others show frequencies comparable to those found in control animals (Figure 3G). Overall, these data show that *tenm3* knockdown causes structural irregularities in the developing

(E) Fluorescence profiles of IPL stratification in 5 dpf WT (blue), control MO-injected (gray), and *tenm3* MO-injected (red) larvae. Thin traces represent intensity profiles of IPLs of single larvae. Thick traces indicate average profiles (WT, n = 7 larvae; control MO, n = 7; *tenm3* MO, n = 10). Zero percent corresponds to the boundary between GCL and IPL, whereas 100% corresponds to the boundary between IPL and INL.

(F) Schematic summarizing the defects observed in *tenm3* morphant retinae. RGCs are indicated in blue. Neuropil layers are in gray. ONL, outer nuclear layer. See also Figure S4.

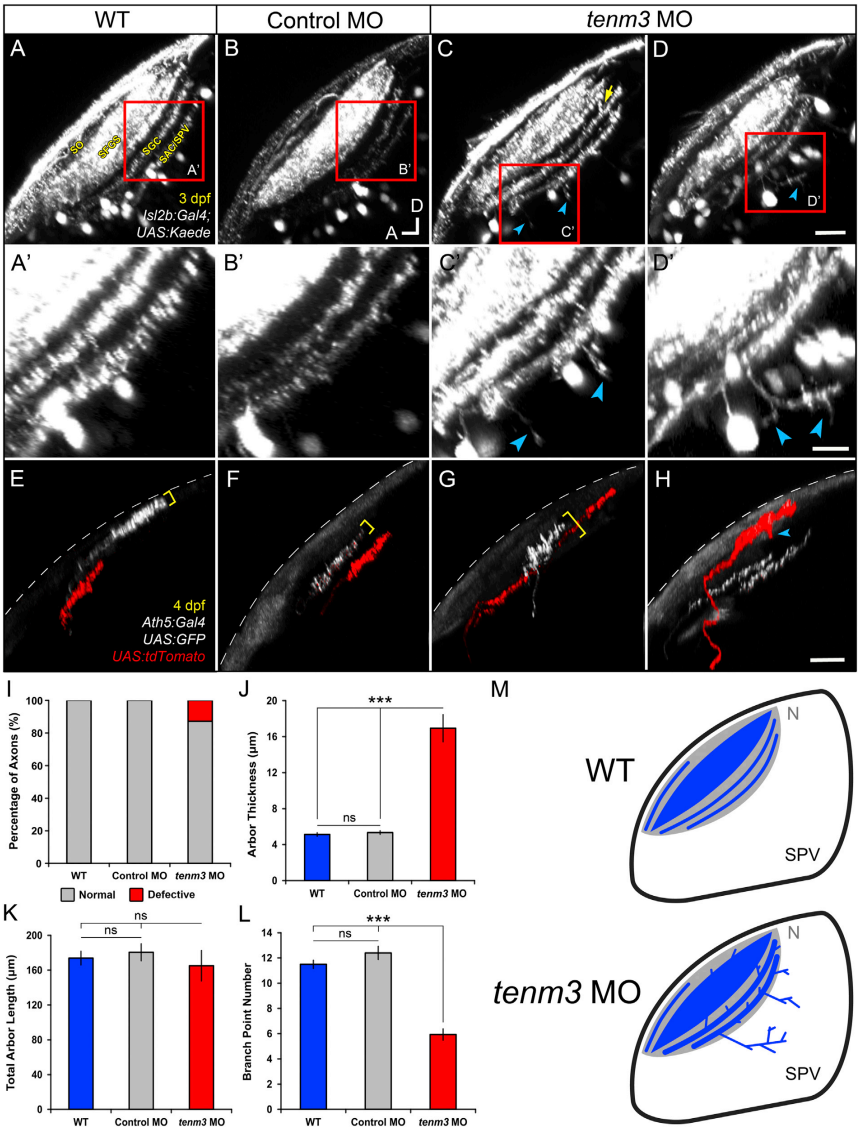

(legend on next page)

Cell PRESS Open ACCESS

retina (Figure 2F) and that changes in RGC dendritic stratification appear to be limited to specific RGC types.

Laminar Targeting Errors in a Subset of RGC Axons Upon Teneurin-3 Knockdown

We next examined RGC axonal arborization in the tectal neuropil. Similar to the IPL in the retina, this structure is characterized by a stereotypic lamination pattern (Xiao et al., 2011). Using the Tg(*Isl2b:Gal4;UAS:Kaede*) zebrafish line, we visualized the four main retinorecipient laminae of the tectum that, from the most superficial to the deepest, are named stratum opticum (SO), stratum fibrosum et griseum superficiale (SFGS), stratum griseum centrale (SGC), and lamina at the interface between the stratum album centrale and the stratum periventriculare (SAC/SPV; Figure 4A) (Nevin et al., 2010). In 3 dpf WT and control MO larvae, all RGC axons are restricted to these four laminae and no axons are found outside the neuropil region (Figures 4A and 4B; n = 15 larvae per group). In *tenm3* morphants, by contrast, we observed neurites projecting aberrantly into the SPV (Figures 4C and 4D, cyan arrowheads; n = 18 out of 23 larvae). 3D reconstruction and neurite tracing revealed that these processes arise principally from the deepest lamina (SAC/SPV) and, in some cases, are up to 30–40 μm long and possess several branches (Figure 4D′, cyan arrowheads). In addition, tectal laminae of *tenm3* morphants are less precisely delimited and axons aberrantly cross lamina borders (Figure 4C, yellow arrow).

To examine in more detail how the lamination defects seen at the population level arise, we labeled individual RGCs through mosaic expression of either GFP or tdTomato driven by the *ath5* promoter. As a rule, individual RGC axons arborize in a planar fashion within a single tectal lamina or sublamina (the SO and SFGS are further subdivided into 2 and 6 sublaminae, respectively) (Robles et al., 2013). This behavior was confirmed in 4 dpf control groups, where 100% of labeled axons (WT n = 102 axons in 50 larvae; control MO n = 94 axons in 45 larvae) showed planar arborization patterns (Figures 4E, 4F, 4I, and 4J; arbor thickness WT 5.1 ± 0.1 μm; control MO 5.3 ± 0.1 μm; n = 20 axons per group). In contrast, we found RGCs with abnormally laminated axonal arbors in *tenm3* morphants (Figures 4G and 4H). Intriguingly, these axons represent only a fraction of the total number of labeled RGCs (Figure 4I; 12.7%, n = 20 axons out of 157 in 80 larvae). They are characterized by possessing axonal processes projecting toward adjacent laminae (Figure 4H, cyan arrowhead) and significantly broader cross-sectional profiles (arbor thickness *tenm3* MO 16.9 ± 1.4 μm; $F_{2,57}$ = 57.97, $p < 0.0001$, n = 20 axons) than those observed in control animals (Figures 4G and 4J). The total arbor length of aberrant axons is comparable to that of control groups (Figure 4K; *tenm3* MO 165.1 ± 17.4 μm; WT 173.8 ± 7.7 μm; control MO 180.5 ± 9.7 μm; $F_{2,57}$ = 0.33, p = 0.72, n = 20 axons per group) but their number of branch points is significantly lower (Figure 4L; *tenm3* MO 5.9 ± 0.4; WT 11.5 ± 0.3; control MO 12.4 ± 0.5; $F_{2,57}$ = 48.86, $p < 0.0001$, n = 60), suggesting that *tenm3* knockdown impairs their capacity to either form or stabilize new branches, without affecting overall arbor length. Taken together, these results indicate that *tenm3* is required for the correct laminar targeting and arborization of a subset of RGC axons (Figure 4M).

Teneurin-3 Is Required for Functional Development of Orientation-Selective RGCs

To investigate the functional consequences of *tenm3* knockdown, we analyzed direction-selective (DS) and orientation-selective (OS) responses of RGC axon terminals innervating the tectal neuropil. Light or dark drifting bars moving in 12 directions were presented to one eye of 5 dpf Tg(*Isl2b:Gal4;UAS:SyGCaMP3*) transgenic larvae while functionally imaging the contralateral tectum (Figure 5A) (Nikolaou et al., 2012). Since SyGCaMP3 is based on the fusion between the synaptic vesicle protein synaptophysin and the genetically encoded calcium indicator GCaMP3, this transgenic line enables the targeting of the probe specifically to RGC presynaptic terminals and hence the functional analysis of RGCs within the tectal target. RGCs of all three animal groups respond to drifting bars (Movies S1, S2, and S3) and exhibit complex patterns of stimulus responses (Figure S2). In order to characterize and map visual response properties (i.e., direction and orientation selectivity) present in the retinal input to the tectum, we used a voxel-wise analysis strategy that is independent of cellular and neuropil morphology (Nikolaou et al., 2012). Only visually responsive voxels were subjected to further characterization. Direction- and orientation-selective indices (DSI and OSI) based on fitted von Mises profiles were calculated together with an estimate for their goodness of fit, R^2 (Lowe et al., 2013) (see Supplemental Experimental Procedures). For a voxel to be regarded as DS or OS, mutually exclusive criteria were employed: DS if $R^2 > 0.8$, DSI > 0.5, and OSI < 0.5; and OS if $R^2 > 0.8$, OSI > 0.5, and DSI < 0.5 (Figure 5B). Functional maps in which DS and OS voxels are color-coded, obtained from individual larvae, were spatially coregistered to generate parametric composite maps (Figures 5C–5E; WT n = 8 larvae; control MO n = 11; *tenm3* MO n = 20). Analyzing the

Figure 4. Axon Laminar Targeting Errors in a Subset of RGCs in *teneurin-3* Morphants

(A–D) The four main retinorecipient laminae of the tectum are visible in the Tg(*Isl2b:Gal4;UAS:Kaede*) zebrafish line at 3 dpf. SO, stratum opticum; SFGS, stratum fibrosum et griseum superficiale; SGC, stratum griseum centrale; SAC, stratum album centrale; SPV, stratum periventriculare.

(A′–D′) Insets in (A)–(D) showing RGC axon lamination in deep laminae of the tectal neuropil.

(E–H) Lateral view of mosaically labeled RGC axons at 4 dpf. Dashed lines indicate the skin overlaying the tectum. All images represent maximum intensity projections of ~50 μm confocal z stacks that have been rotated around the longitudinal axis to best show axonal lamination. Scale bars, 20 μm (A–H) and 10 μm in (A′–D′). A, anterior; D, dorsal.

(I) Quantification of axon laminar targeting behaviors in mosaically labeled RGCs (WT n = 102 axons in 50 larvae; control MO n = 94 axons in 45 larvae; *tenm3* MO n = 157 axons in 80 larvae).

(J–L) Bar graphs showing the measurements for arbor thickness (J), total arbor length (K), and branching point number (L) of single RGC axons (n = 20 axons per group). All graphs show mean values ± SEM. ***$p < 0.001$; ns, not significant by one-way ANOVA followed by Tukey's HSD test.

(M) Schematic summarizing the defects observed in the optic tecta of *tenm3* morphants. RGC axons are indicated in blue. Neuropil layers are in gray. N, neuropil. See also Figure S4.

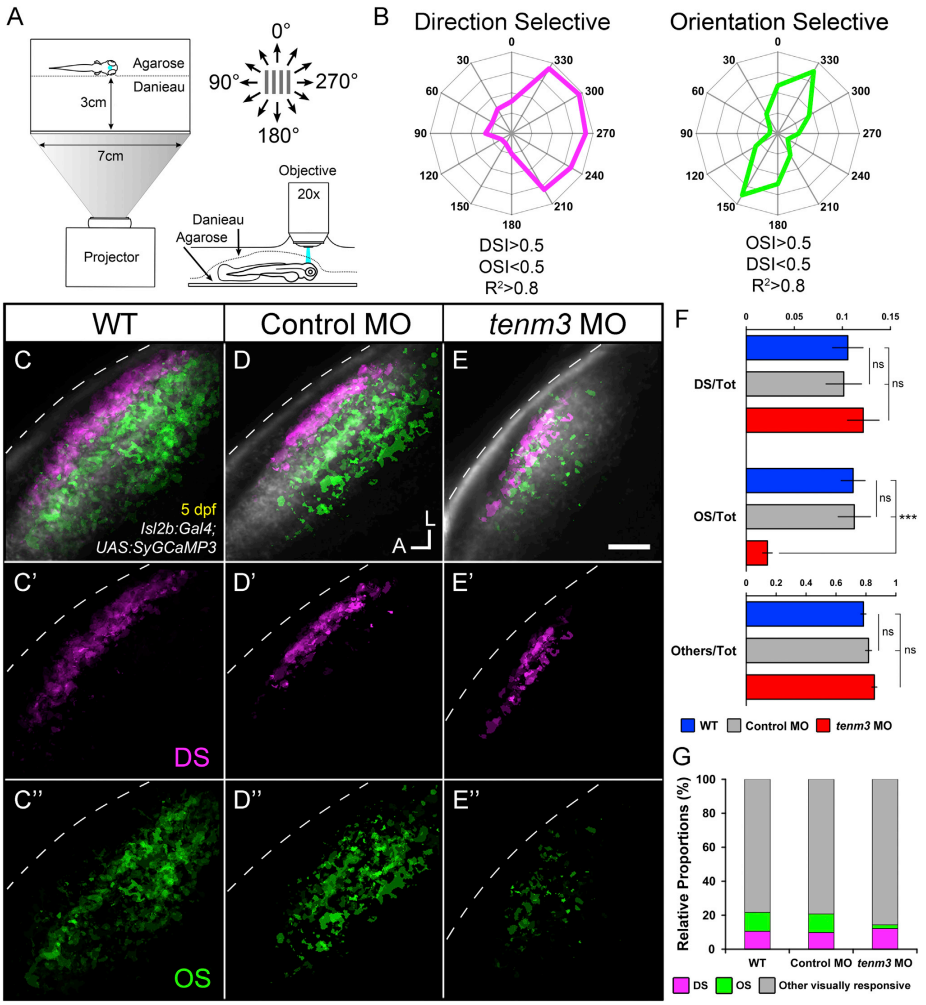

Figure 5. Impaired Development of Orientation-Selective RGCs Following *teneurin-3* Knockdown

(A) Schematic describing the experimental setup. Larvae were immobilized in agarose and placed with one eye facing a screen, where drifting bars moving in 12 directions were projected. Visually evoked SyGCaMP3 responses were recorded in the contralateral tectal neuropil.

(B) Polar plots of representative direction-selective (DS, magenta) and orientation-selective (OS, green) voxels showing relative integral responses to moving bars. Criteria employed to characterize the two classes of voxels are reported at the bottom.

(C–E) Composite parametric maps across multiple 5 dpf Tg(*Isl2b:Gal4;UAS:SyGCaMP3*) larvae representing the spatial distribution of DS (magenta) and OS (green) voxels within each group (WT n = 8 larvae; control MO n = 11; *tenm3* MO n = 20). Within individual parametric maps, voxel brightness is proportional to the summed incidence of each functional response across all larvae imaged. The standard space template image derived for each group (grayscale) provides an anatomical reference. Dashed lines indicate the skin overlaying the tectum. Scale bar, 20 μm. A, anterior; L, lateral.

(legend continued on next page)

Cell PRESS
Open ACCESS

DS RGC input to the tectum, we observed that in all three experimental groups DS responses are present (Figures 5C′–5E′). Moreover, the normal laminar organization of DS voxels within the superficial region of SFGS (Nikolaou et al., 2012) is preserved in *tenm3* morphants (Figures 5C′–5E′). Further analysis of DS RGC subtypes revealed that all three DS RGC populations—tuned to anterior (~260°), dorsoposterior (~40°), and ventroposterior (~150°) motion—found in control groups (Nikolaou et al., 2012) are also present in *tenm3* morphants (Figure S3). Overall, no difference between *tenm3* morphants and control groups was observed in the DS RGC input to the tectum.

In contrast, we found that the OS RGC input to the tectum is severely impaired upon *tenm3* knockdown. Specifically, the overall number of OS voxels is decreased in *tenm3* morphants (Figures 5C″–5E″). In addition, the OS RGC voxels that are typically found in deeper sublaminae of SFGS with little or no overlap with DS RGCs in control animals (Figures 5C and 5D) (Nikolaou et al., 2012) show a substantial degree of overlap with DS voxels in *tenm3* morphants (Figure 5E). To further confirm the OS RGC impairment, we analyzed the relative proportions of functional response classes within each experimental group. In *tenm3* morphants, we found a significant decrease in the ratio between OS voxels and the total population of visually responsive voxels (Figure 5F; OS/tot *tenm3* MO 0.022 ± 0.004, n = 20 larvae; WT 0.111 ± 0.012, n = 8; control MO 0.112 ± 0.016, n = 11; $F_{2,36}$ = 24.61, $p < 0.0001$), so the OS input becomes the smallest population of RGCs responding to drifting bars in this group (Figure 5G). The relative proportions of DS and non-DS/non-OS (classified as "others") voxel populations, however, were similar among the three animal groups (Figures 5F and 5G; DS/tot WT 0.105 ± 0.015, control MO 0.101 ± 0.018, *tenm3* MO 0.121 ± 0.016, $F_{2,36}$ = 0.42, p = 0.66; others/tot WT 0.783 ± 0.016, control MO 0.817 ± 0.019, *tenm3* MO 0.856 ± 0.016, $F_{2,36}$ = 3.06, p = 0.059, n = 39 larvae), suggesting no impairment by *tenm3* knockdown. These functional results indicate that visual responses of OS RGCs are affected by *tenm3* knockdown whereas DS RGCs develop normally, therefore reinforcing the possible role of *tenm3* in the assembly of specific visual circuits. All structural and functional phenotypes observed using *tenm3* MO were confirmed in larvae injected with a second splice-blocking MO against *tenm3* (*tenm3* MO 2; Figure S4), supporting the specificity of gene knockdown.

DISCUSSION

Recent studies in *Drosophila* showed that teneurins are involved in establishing specific synaptic circuits (Hong et al., 2012; Mosca et al., 2012). However, a similar role in vertebrate neural circuit wiring has not yet been demonstrated. Here, we report that Teneurin-3 is required for the correct structural and functional development of RGCs in zebrafish. RGCs and their pre- and postsynaptic cellular targets (i.e., amacrine cells and tectal neurons, respectively) express *tenm3* during the period of intense synapse formation (2–5 dpf), suggesting an instructive role in synaptic matching through homophilic interactions between neuronal partners along the visual pathway. *Tenm3* knockdown produces laminar targeting errors of RGC dendrites and axons, indicating that Tenm3 acts in both the IPL of the retina and the tectal neuropil. Intriguingly, these errors appear to be restricted to a subset of RGCs, hinting that Tenm3 acts in specific RGC subtypes and that Tenm3-negative cells are unaffected. Consistent with this hypothesis, when we examined the functional development of visual response properties conveyed by RGCs, we observed that the OS retinal input to the tectum is strongly impaired whereas direction selectivity is not affected in *tenm3* morphant larvae. This does not exclude, however, that additional RGC functional subtypes may be affected in *tenm3* morphants. Previous studies in mice showed that Teneurin-3 regulates the development of topography in the retinogeniculate (Leamey et al., 2007) and retinocollicular pathways (Dharmaratne et al., 2012), specifically for the ipsilaterally projecting RGC population. However, the fact that *teneurin-3* is not exclusively expressed in ipsilaterally projecting RGCs (Leamey et al., 2007) and is also found in the visual system of species where RGCs project contralaterally only, like chick (Kenzelmann-Broz et al., 2010) and zebrafish (Mieda et al., 1999; this study), clearly suggests additional functions in vertebrate visual system development.

Taken together, our findings support a role for Tenm3 in the establishment of functional cell subtype-specific wiring in vertebrates. What developmental mechanisms does Tenm3 regulate? It is generally accepted that molecules mediating homophilic cell-cell adhesion instruct the recognition between pre- and postsynaptic elements by triggering specific synapse formation/stabilization (Sanes and Yamagata, 2009; Williams et al., 2010). In addition, teneurin-mediated homophilic recognition and subsequent formation of cell-adhesion partners leads to inhibition of neurite outgrowth (Beckmann et al., 2013). Thus, the simplest hypothesis is that *tenm3* (by being expressed in RGCs, amacrine cells, and tectal neurons) controls the lamination of RGC neurites through stabilization of branches contacting neurites of *tenm3*-expressing cells. Homophilic adhesion has been extensively studied in the IPL of the chick retina, where different immunoglobulin superfamily adhesion molecules are expressed by specific subsets of cells and control the precise sublaminar matching of their neurites (Yamagata and Sanes, 2008, 2012). Interestingly, this matching mechanism appears to be conserved in higher visual targets. For example, evidence in mouse showed that Cadherin-6 mediates the axon-target recognition between a specific subset of RGCs and their target

(C′–E′) Parametric maps for DS voxels only.
(C″–E″) Parametric maps for OS voxels only.
(F) Bar graphs showing the ratios between defined voxel classes and total visually responsive voxels (Tot) within each group (WT n = 8 larvae; control MO n = 11; *tenm3* MO n = 20). Non-DS and non-OS voxels are classified as "others." All graphs show mean values ± SEM. ***$p < 0.001$; ns, not significant by one-way ANOVA followed by Tukey's HSD test.
(G) Bar graph showing the proportions of DS and OS voxel classes relative to visually responsive voxels within each group.
See also Figures S2–S4 and Movies S1, S2, and S3.

nuclei in the brain (Osterhout et al., 2011). An alternative mechanism that might regulate RGC neurite arborization is the neurite costratification between morphologically and functionally related cells expressing the same combination of adhesive proteins. This kind of interaction certainly occurs during IPL development. In studies where single or multiple retinal cell classes were selectively eliminated, the remaining cellular components could form a stratified IPL, therefore suggesting that no single pre- or postsynaptic retinal cell class is strictly essential for IPL formation (Kay et al., 2004; Randlett et al., 2013). Further experiments are needed to determine the exact mechanisms of action of Tenm3 and in which cell subtypes it is expressed. Meanwhile, our results presented here point toward an important role for teneurins in the development of vertebrate neural circuit specificity.

EXPERIMENTAL PROCEDURES

Transgenic Lines and Constructs

Transgenic lines Tg(*Isl2b:Gal4*) and Tg(*UAS:SyGCaMP3*) have been described previously (Ben Fredj et al., 2010; Nikolaou et al., 2012). Transgenic line Tg(*UAS:Kaede*) was a gift of Prof. Chi Bin-Chien. The *UAS:GFP* and *UAS:tdTomato* DNA constructs were described previously (Ben Fredj et al., 2010), and the *Ath5:Gal4* plasmid was a gift of Prof. Steve Wilson (UCL, UK). All animal procedures were approved by the local Animal Welfare and Ethics Review Body (King's College London) and were carried out in accordance with the Animals (Scientific Procedures) Act 1986, under license from the United Kingdom Home Office.

Functional Imaging

Confocal imaging was performed using an LSM 710 confocal microscope equipped with a spectral detection scan head and a 20×/1.0 NA water-immersion objective (Carl Zeiss). Functional time series of visually evoked SyGCaMP3 responses were acquired at a rate of 4.1 Hz and 0.415 × 0.415 μm resolution (256 × 256 pixels) and 1 AU pinhole aperture. Visual stimulation and voxel-wise analysis of functional data were performed as described previously (Nikolaou et al., 2012) (see Supplemental Experimental Procedures).

Statistical Analyses

The statistical significance of the differences between mean values and in the proportion of diffuse RGCs among groups was determined by one-way ANOVA followed by Tukey's HSD test and chi-square test, respectively, using SigmaPlot (Systat Software). The criterion for statistical significance was set at $p < 0.05$ and results are represented as mean ± SEM.

SUPPLEMENTAL INFORMATION

Supplemental Information includes Supplemental Experimental Procedures, four figures, and three movies and can be found with this article online at http://dx.doi.org/10.1016/j.celrep.2013.09.045.

ACKNOWLEDGMENTS

We thank L. Ward and J. Clarke for control morpholino, S. Wilson for *Ath5:Gal4* DNA construct, and A. Lowe for software design and instruction. We also thank N. Maiorano for comments on the manuscript and P. Hunter for practical help. This study was supported by a KCL investment grant to R.H. and a KCL Health Schools PhD studentship sponsored by the Medical Research Council (MRC) to P.A. M.P.M and N.N are supported by MRC project grants awarded to M.P.M (G0801242, G1100162).

Received: April 30, 2013
Revised: August 5, 2013
Accepted: September 30, 2013
Published: October 31, 2013

REFERENCES

Beckmann, J., Schubert, R., Chiquet-Ehrismann, R., and Müller, D.J. (2013). Deciphering teneurin domains that facilitate cellular recognition, cell-cell adhesion, and neurite outgrowth using atomic force microscopy-based single-cell force spectroscopy. Nano Lett. *13*, 2937–2946.

Ben Fredj, N., Hammond, S., Otsuna, H., Chien, C.B., Burrone, J., and Meyer, M.P. (2010). Synaptic activity and activity-dependent competition regulates axon arbor maturation, growth arrest, and territory in the retinotectal projection. J. Neurosci. *30*, 10939–10951.

Connaughton, V.P., Behar, T.N., Liu, W.L., and Massey, S.C. (1999). Immunocytochemical localization of excitatory and inhibitory neurotransmitters in the zebrafish retina. Vis. Neurosci. *16*, 483–490.

Dharmaratne, N., Glendining, K.A., Young, T.R., Tran, H., Sawatari, A., and Leamey, C.A. (2012). Ten-m3 is required for the development of topography in the ipsilateral retinocollicular pathway. PLoS ONE *7*, e43083.

Draper, B.W., Morcos, P.A., and Kimmel, C.B. (2001). Inhibition of zebrafish fgf8 pre-mRNA splicing with morpholino oligos: a quantifiable method for gene knockdown. Genesis *30*, 154–156.

Gollisch, T., and Meister, M. (2010). Eye smarter than scientists believed: neural computations in circuits of the retina. Neuron *65*, 150–164.

Hong, W., Mosca, T.J., and Luo, L. (2012). Teneurins instruct synaptic partner matching in an olfactory map. Nature *484*, 201–207.

Kay, J.N., Finger-Baier, K.C., Roeser, T., Staub, W., and Baier, H. (2001). Retinal ganglion cell genesis requires lakritz, a Zebrafish atonal Homolog. Neuron *30*, 725–736.

Kay, J.N., Roeser, T., Mumm, J.S., Godinho, L., Mrejeru, A., Wong, R.O., and Baier, H. (2004). Transient requirement for ganglion cells during assembly of retinal synaptic layers. Development *131*, 1331–1342.

Kenzelmann-Broz, D., Tucker, R.P., Leachman, N.T., and Chiquet-Ehrismann, R. (2010). The expression of teneurin-4 in the avian embryo: potential roles in patterning of the limb and nervous system. Int. J. Dev. Biol. *54*, 1509–1516.

Leamey, C.A., Merlin, S., Lattouf, P., Sawatari, A., Zhou, X., Demel, N., Glendining, K.A., Oohashi, T., Sur, M., and Fässler, R. (2007). Ten_m3 regulates eye-specific patterning in the mammalian visual pathway and is required for binocular vision. PLoS Biol. *5*, e241.

Lowe, A.S., Nikolaou, N., Hunter, P.R., Thompson, I.D., and Meyer, M.P. (2013). A systems-based dissection of retinal inputs to the zebrafish tectum reveals different rules for different functional classes during development. J. Neurosci. *33*, 13946–13956.

Mangrum, W.I., Dowling, J.E., and Cohen, E.D. (2002). A morphological classification of ganglion cells in the zebrafish retina. Vis. Neurosci. *19*, 767–779.

Masland, R.H. (2012). The neuronal organization of the retina. Neuron *76*, 266–280.

Matsuoka, R.L., Nguyen-Ba-Charvet, K.T., Parray, A., Badea, T.C., Chédotal, A., and Kolodkin, A.L. (2011). Transmembrane semaphorin signalling controls laminar stratification in the mammalian retina. Nature *470*, 259–263.

Meyer, M.P., and Smith, S.J. (2006). Evidence from in vivo imaging that synaptogenesis guides the growth and branching of axonal arbors by two distinct mechanisms. J. Neurosci. *26*, 3604–3614.

Mieda, M., Kikuchi, Y., Hirate, Y., Aoki, M., and Okamoto, H. (1999). Compartmentalized expression of zebrafish ten-m3 and ten-m4, homologues of the Drosophila ten(m)/odd Oz gene, in the central nervous system. Mech. Dev. *87*, 223–227.

Mosca, T.J., Hong, W., Dani, V.S., Favaloro, V., and Luo, L. (2012). Trans-synaptic Teneurin signalling in neuromuscular synapse organization and target choice. Nature *484*, 237–241.

Mumm, J.S., Williams, P.R., Godinho, L., Koerber, A., Pittman, A.J., Roeser, T., Chien, C.B., Baier, H., and Wong, R.O. (2006). In vivo imaging reveals dendritic targeting of laminated afferents by zebrafish retinal ganglion cells. Neuron *52*, 609–621.

Nevin, L.M., Robles, E., Baier, H., and Scott, E.K. (2010). Focusing on optic tectum circuitry through the lens of genetics. BMC Biol. *8*, 126.

Nikolaou, N., Lowe, A.S., Walker, A.S., Abbas, F., Hunter, P.R., Thompson, I.D., and Meyer, M.P. (2012). Parametric functional maps of visual inputs to the tectum. Neuron *76*, 317–324.

Osterhout, J.A., Josten, N., Yamada, J., Pan, F., Wu, S.W., Nguyen, P.L., Panagiotakos, G., Inoue, Y.U., Egusa, S.F., Volgyi, B., et al. (2011). Cadherin-6 mediates axon-target matching in a non-image-forming visual circuit. Neuron *71*, 632–639.

Randlett, O., MacDonald, R.B., Yoshimatsu, T., Almeida, A.D., Suzuki, S.C., Wong, R.O., and Harris, W.A. (2013). Cellular requirements for building a retinal neuropil. Cell Rep. *3*, 282–290.

Robles, E., Filosa, A., and Baier, H. (2013). Precise lamination of retinal axons generates multiple parallel input pathways in the tectum. J. Neurosci. *33*, 5027–5039.

Roska, B., and Werblin, F. (2001). Vertical interactions across ten parallel, stacked representations in the mammalian retina. Nature *410*, 583–587.

Sanes, J.R., and Yamagata, M. (2009). Many paths to synaptic specificity. Annu. Rev. Cell Dev. Biol. *25*, 161–195.

Sanes, J.R., and Zipursky, S.L. (2010). Design principles of insect and vertebrate visual systems. Neuron *66*, 15–36.

Tucker, R.P., and Chiquet-Ehrismann, R. (2006). Teneurins: a conserved family of transmembrane proteins involved in intercellular signaling during development. Dev. Biol. *290*, 237–245.

Tucker, R.P., Beckmann, J., Leachman, N.T., Schöler, J., and Chiquet-Ehrismann, R. (2012). Phylogenetic analysis of the teneurins: conserved features and premetazoan ancestry. Mol. Biol. Evol. *29*, 1019–1029.

Wässle, H. (2004). Parallel processing in the mammalian retina. Nat. Rev. Neurosci. *5*, 747–757.

Williams, M.E., de Wit, J., and Ghosh, A. (2010). Molecular mechanisms of synaptic specificity in developing neural circuits. Neuron *68*, 9–18.

Xiao, T., Staub, W., Robles, E., Gosse, N.J., Cole, G.J., and Baier, H. (2011). Assembly of lamina-specific neuronal connections by slit bound to type IV collagen. Cell *146*, 164–176.

Yamagata, M., and Sanes, J.R. (2008). Dscam and Sidekick proteins direct lamina-specific synaptic connections in vertebrate retina. Nature *451*, 465–469.

Yamagata, M., and Sanes, J.R. (2012). Expanding the Ig superfamily code for laminar specificity in retina: expression and role of contactins. J. Neurosci. *32*, 14402–14414.

Young, T.R., Bourke, M., Zhou, X., Oohashi, T., Sawatari, A., Fässler, R., and Leamey, C.A. (2013). Ten-m2 is required for the generation of binocular visual circuits. J. Neurosci. *33*, 12490–12509.

Paper 2

Title: Neural Mechanisms Generating Orientation Selectivity in the Retina

Journal: Current Biology

Year: 2016

Authors: Paride Antinucci[1], Oniz Suleyman, Clinton Monfries, and Robert Hindges[1]*

[1]Centre for Developmental Neurobiology, King's College London, Guy's Campus, London SE1 1UL, UK
*Corresponding author

Citations: 1 (Google Scholar)

Contribution: Design of project and experiments, data collection and analysis, paper writing (primary writer)

PMID: 27374343

DOI: 10.1016/j.cub.2016.05.035

This publication contains work presented in Chapter 4, 5 and 6 of this thesis.

Article

Current Biology

Neural Mechanisms Generating Orientation Selectivity in the Retina

Graphical Abstract

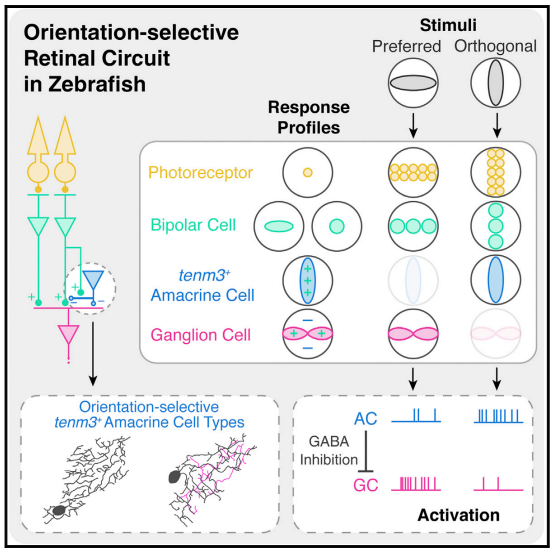

Authors

Paride Antinucci, Oniz Suleyman, Clinton Monfries, Robert Hindges

Correspondence

robert.hindges@kcl.ac.uk

In Brief

The neural mechanisms underlying orientation selectivity in the vertebrate retina are still poorly understood. Antinucci et al. identify a class of orientation-tuned amacrine cells characterized by elongated dendritic arbors that are essential for generating orientation selectivity in retinal ganglion cells.

Highlights

- We identify Tenm3$^+$ ACs with elongated dendritic arbors showing orientation tuning
- Tenm3$^+$ AC GABAergic inhibition is crucial for orientation-selective RGC tuning
- Orientation tuning is present also among some bipolar cell presynaptic terminals
- We propose a model of how orientation selectivity is generated in ganglion cells

Antinucci et al., 2016, Current Biology *26*, 1802–1815
July 25, 2016
http://dx.doi.org/10.1016/j.cub.2016.05.035

CellPress

CellPress

Current Biology
Article

Neural Mechanisms Generating Orientation Selectivity in the Retina

Paride Antinucci,[1] Oniz Suleyman,[1] Clinton Monfries,[1] and Robert Hindges[1,*]
[1]MRC Centre for Developmental Neurobiology, King's College London, Guy's Campus, London SE1 1UL, UK
*Correspondence: robert.hindges@kcl.ac.uk
http://dx.doi.org/10.1016/j.cub.2016.05.035

SUMMARY

The orientation of visual stimuli is a salient feature of visual scenes. In vertebrates, the first neural processing steps generating orientation selectivity take place in the retina. Here, we dissect an orientation-selective circuit in the larval zebrafish retina and describe its underlying synaptic, cellular, and molecular mechanisms. We genetically identify a class of amacrine cells (ACs) with elongated dendritic arbors that show orientation tuning. Both selective optogenetic ablation of ACs marked by the cell-adhesion molecule Teneurin-3 (Tenm3) and pharmacological interference with their function demonstrate that these cells are critical components for orientation selectivity in retinal ganglion cells (RGCs) by being a source of tuned GABAergic inhibition. Moreover, our morphological analyses reveal that Tenm3$^+$ ACs and orientation-selective RGCs co-stratify their dendrites in the inner plexiform layer, and that Tenm3$^+$ ACs require Tenm3 to acquire their correct dendritic stratification. Finally, we show that orientation tuning is present also among bipolar cell presynaptic terminals. Our results define a neural circuit underlying orientation selectivity in the vertebrate retina and characterize cellular and molecular requirements for its assembly.

INTRODUCTION

The detection of oriented visual stimuli is a key neural computation performed by visual systems of many animals. Neurons performing this task are known as orientation selective (OS) since they respond preferentially to elongated stimuli oriented along a specific axis in the visual field but respond weakly to stimuli oriented orthogonally to their preferred axis. Orientation selectivity was first discovered in cat primary visual cortex by Hubel and Wiesel over 50 years ago [1]. Since then, numerous studies described OS neurons in visual systems of vertebrates and invertebrates, including primates [2], rodents [3], fish [4], and insects [5]. Work in several vertebrate species identified OS cells in regions upstream of primary visual cortex, like the lateral geniculate nucleus [6–8] and the retina [9–12], suggesting that the first steps in the processing of oriented stimuli take place early along the vertebrate visual pathway. In the retina, orientation selectivity is present among retinal ganglion cells (RGCs) [10, 13], the sole retinal output neurons, and amacrine cells (ACs) [13, 14], a class of inhibitory neurons that modulate and shape RGC responses. However, it is presently unclear how orientation selectivity emerges in these cells and whether they form a distinct retinal circuit, partially due to the lack of specific molecular markers allowing targeted labeling and manipulations.

The vertebrate retina consists of more than 70 neuron types [15]. Its primary function is to detect light stimuli, convert them into electrochemical signals, and, subsequently, send the processed information to higher visual nuclei through parallel feature-specific neural pathways. Most of the information processing takes place in a layered neuropil structure called the inner plexiform layer (IPL) [16]. Essential neural substrates underlying the computations performed in the IPL are the specific and stereotypic synaptic connections between three classes of neurons, namely, bipolar cells (BCs), ACs, and RGCs (Figure 1A). Recent developmental studies have shown that cell-adhesion molecules selectively expressed in specific retinal cell types mediate the matching between defined pre- and postsynaptic partners to establish this complex wiring pattern [18–20]. While several cell types and molecules crucial for establishing direction selectivity in the retina have been identified [20, 21], the equivalents for orientation selectivity are largely unknown to date.

Teneurins are a family of transmembrane cell-adhesion proteins that play a synaptic matching role in the *Drosophila* olfactory system [22] and neuromuscular junction [23]. In vertebrates, teneurins are highly expressed in several interconnected regions of the brain, including the visual system [24, 25]. In vitro and in vivo data suggest that *trans*-synaptic interactions are possible both homophilically through their five NHL domains [22, 26], and heterophilically with the cell-adhesion G-protein-coupled receptors latrophilins [27, 28]. We previously showed that *teneurin-3* (*tenm3*) is expressed in zebrafish ACs and RGCs during a period of intense synaptic formation (Figure 1B) and that, when *tenm3* is knocked down, RGC dendrites fail to correctly stratify in the IPL [17]. We also reported a functional link between *tenm3* and RGC orientation selectivity.

Here, using *tenm3* as a marker, we identify crucial cellular players and mechanisms generating orientation selectivity in the larval zebrafish retina. First, we reveal that *tenm3*-expressing (*tenm3*$^+$) ACs co-stratify their neurites with orientation-selective RGC (OSGC) dendrites and that, upon *tenm3* knockout, they fail to correctly stratify their neurites in the IPL. Second, we show evidence suggesting that *tenm3*$^+$ ACs generate OSGC tuning by providing γ-aminobutyric acid (GABA) feedforward inhibitory input. Third, we identify and characterize orientation-tuned *tenm3*$^+$ AC types with elongated dendritic arbors. Fourth, we find

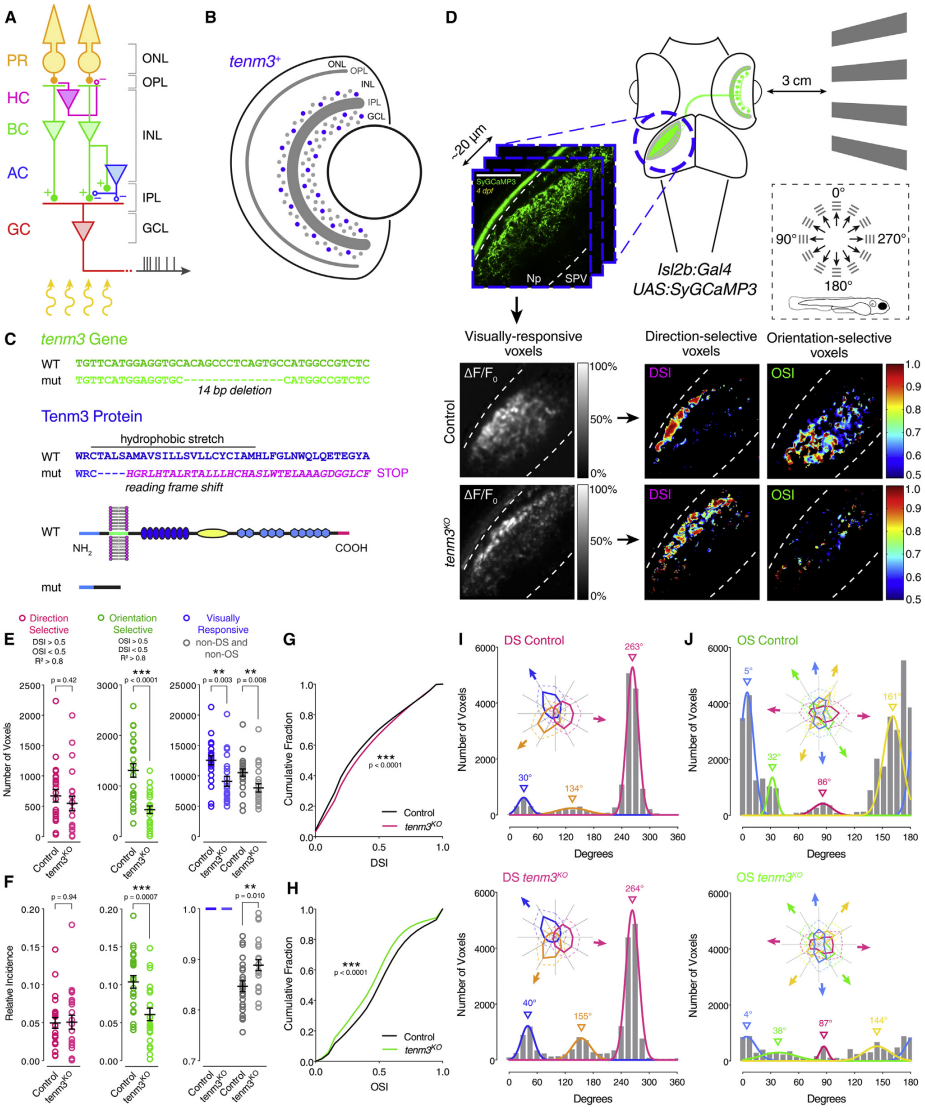

Figure 1. Tenm3 Is Required for RGC Orientation Selectivity

(A) Basic neural circuit structure of the vertebrate retina. Cell classes are represented in colors, whereas layers are shown in black. Excitatory synapses are indicated by "+" (filled circles), inhibitory synapses are labeled with "–" (empty circles). PR, photoreceptor; HC, horizontal cell; BC, bipolar cell; AC, amacrine cell; RGC, retinal ganglion cell; ONL, outer nuclear layer; INL, inner nuclear layer; GCL, ganglion cell layer; OPL, outer plexiform layer; IPL, inner plexiform layer.

(legend continued on next page)

that a fraction of BC presynaptic terminals show orientation tuning. Finally, we present a circuit model describing how OSGCs acquire their orientation selectivity by integrating tuned *tenm3*$^{+}$ ACs and BC inputs.

RESULTS

Generation of a Tenm3^{KO} Tool to Study Retinal Orientation Selectivity

Previous work using transient gene knockdown methods suggested that Tenm3 is involved in the development of orientation selectivity in zebrafish RGCs [17]. To confirm this role and, subsequently, use Tenm3 as a marker to identify cells generating RGC orientation selectivity, we generated a zebrafish *tenm3* knockout mutant (*tenm3*^{KO}) using Transcription Activator-Like Effector Nuclease (TALEN)-based genome editing (see Supplemental Experimental Procedures). In *tenm3*^{KO} mutants, a 14-bp deletion in the exon encoding the transmembrane domain of Tenm3 leads to a reading frameshift and, subsequently, to a premature stop codon causing the loss of the entire extracellular domain (Figures 1C and S1A–S1F). We then examined the retinal functional output of *tenm3*^{KO} mutants as previously described [4, 17]. Briefly, drifting bars moving in 12 different directions were presented to awake immobilized zebrafish larvae through a projection screen (Figure 1D). Using the RGC-specific transgenic line *Tg(isl2b:Gal4;UAS:SyGCaMP3)*, population visual responses were simultaneously recorded through calcium imaging of RGC axon terminals in the contralateral optic tectum (Movie S1). Voxel-wise analysis was then used to isolate visually responsive voxels and identify direction-selective (DS) and OS responses (Figures 1D and S1G) [29]. We found that 4 days post-fertilization (dpf) *tenm3*^{KO} mutants have a large decrease in both the number of OS voxels (Figure 1E) and the proportion of OSGC output relative to the whole population of responsive voxels (Figure 1F). As a consequence, the relative proportion of "non-tuned" (non-DS and non-OS) RGC output was increased in *tenm3*^{KO} mutants (Figure 1F). This impairment in the OSGC population is consistent with the lower degree of orientation selectivity, quantified by the orientation selectivity index (OSI), across visually responsive voxels in *tenm3*^{KO} mutants (Figure 1H). By contrast, the direction-selective RGC (DSGC) population of responses did not show any impairment in *tenm3*^{KO} mutants (Figures 1E–1G), suggesting that Tenm3 is not involved in the assembly of DS circuits. Equivalent results were obtained in 7-dpf *tenm3*^{KO} mutants (Figures S1H–S1K), indicating that the development of RGC orientation selectivity is not simply delayed. A modest but significant decrease in the number of visually responsive voxels was observed in *tenm3*^{KO} mutants at 4 dpf (Figure 1E), but not at 7 dpf (Figure S1H).

We next explored to what extent the subtypes of DSGCs and OSGCs previously described in zebrafish [29] were affected by Tenm3 loss of function. Different subpopulations of DSGC and OSGC responses were identified by fitting Gaussian distributions to the grouped population data of preferred angles [4, 29]. As expected, population sizes and relative proportions of the three subtypes of DSGCs were not altered in *tenm3*^{KO} mutants (Figures 1I and S1L), reinforcing the view that RGC direction selectivity develops through Tenm3-independent mechanisms. Interestingly, the decrease in OS responses in *tenm3*^{KO} mutants was not equally represented among the four OSGC subtypes, with the small OSGC subpopulation tuned to vertical bars moving along the horizontal axis being the least affected (magenta, Figures 1J and S1M). Overall, these results confirm and further elucidate the crucial role played by Tenm3 in generating RGC orientation selectivity during development [17]. Additionally, they provide a genetic access point to reveal the individual circuit components and mechanisms underlying retinal orientation selectivity.

Neurite Stratification Pattern of Tenm3^{+} ACs and OSGCs

Since *tenm3* is expressed not only in RGCs, but also in ACs [17], we asked whether the functional phenotype observed in *tenm3*^{KO} OSGCs results from structural defects in the presynaptic AC population. We thus generated a zebrafish bacterial artificial chromosome (BAC) transgenic line, *Tg(tenm3:Gal4)*, where Gal4FF is under transcriptional control of regulatory elements upstream and downstream of the *tenm3* start codon (Figure 2A) (see Supplemental Experimental Procedures). In this BAC line, Gal4 is expressed in brain regions where *tenm3* is endogenously expressed, including the retina and optic tectum (Figure S2) [17]. In the retina, the *Tg(tenm3:Gal4;UAS:tagRFP-CAAX)* line labels a subset of ACs (hereafter referred to as *tenm3*$^{+}$ ACs) but fails to drive expression in RGCs (Figures 2B and S2A–S2C; Movie S2), possibly due to a lack of RGC-specific regulatory elements

(B) Schematic showing *tenm3* mRNA expression in the retina of zebrafish larvae. Blue circles indicate *tenm3*$^{+}$ ACs and RGCs. Adapted from Antinucci et al. [17].
(C) TALEN-mediated *tenm3* gene knockout (top) and consequent structural changes in the Tenm3 protein (bottom).
(D) Functional calcium imaging of RGC axon terminals expressing SyGCaMP3 (green) in 4-dpf *Tg(isl2b:Gal4;UAS:SyGCaMP3)* larvae. Distance of right eye from projection screen is 3 cm. Recordings are performed from two to four Z-planes (approximately 20 μm total volume thickness) in the contralateral optic tectum. Dashed box shows the angles of moving bars relative to zebrafish larva orientation. Mean $\Delta F/F_0$ images of calcium recordings in control and *tenm3*^{KO} larvae followed by mapping of DS and OS voxels are displayed. Np, neuropil; SPV, stratum periventriculare; DSI, direction selectivity index; OSI, orientation selectivity index. Scale bar, 40 μm.
(E and F) Average number (E) and relative frequency (F) of DS, OS, visually responsive, and non-DS/non-OS voxels per Z-plane in control (n = 23 larvae) and *tenm3*^{KO} (n = 22 larvae) 4-dpf larvae. Criteria used to identify DS and OS voxels are reported at the top. Error bars, ±SEM. $^{**}p < 0.01$, $^{***}p < 0.001$, unpaired two-tailed Student's t test.
(G and H) Cumulative distributions of DSI values ($R^2 > 0$) across voxels with OSI < 0.5 (G) and OSI values ($R^2 > 0$) across voxels with DSI < 0.5 (H) in control and *tenm3*^{KO} larvae. $^{***}p < 0.001$, two-sample Kolmogorov-Smirnov test.
(I and J) Cumulative histograms summarizing the incidence of preferred angles for identified DS (I) and OS voxels (J) in control (n = 23; top) and *tenm3*^{KO} (n = 22; bottom) 4-dpf larvae. Overlaid curves are the fitted Gaussian distributions for each DS or OS subtype. Polar plots illustrate the mean (+1 SD) normalized response profiles for each DS or OS subtype.
See also Figure S1, Table S1, and Movie S1.

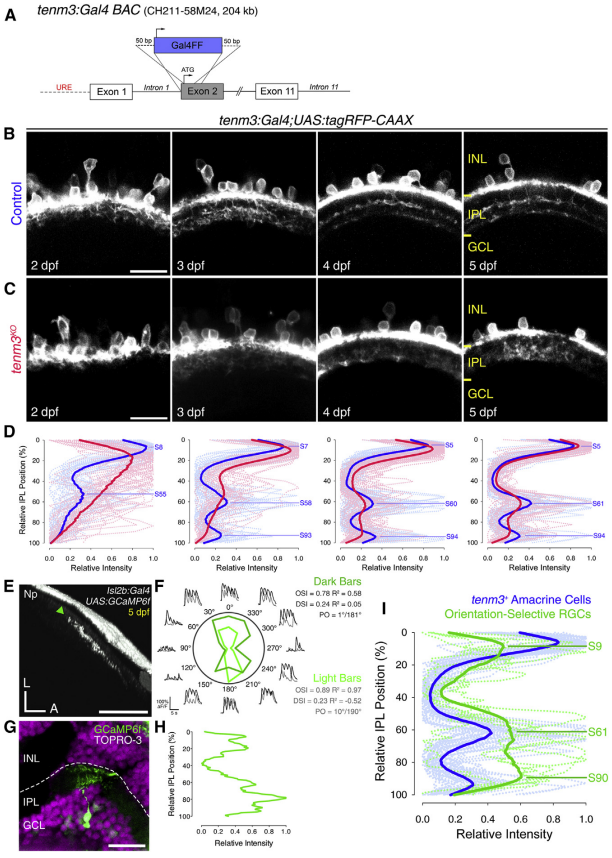

Figure 2. IPL Stratification Pattern of Tenm3$^+$ ACs and OSGCs

(A) Schematic of the bacterial artificial chromosome (BAC) DNA construct used to transgenically express Gal4FF in *tenm3*$^+$ cells. URE, upstream regulatory elements.

(B and C) Inner plexiform layer (IPL) stratification pattern of *tenm3*$^+$ AC neurites in control (B) and *tenm3*^{KO} (C) *Tg(tenm3:Gal4;UAS:tagRFP-CAAX)* larvae from 2 to 5 dpf. INL, inner nuclear layer; GCL, ganglion cell layer. Scale bars, 20 μm.

(D) IPL fluorescence intensity profiles of *tenm3*$^+$ AC neurites in control (blue; n = 13 larvae) and *tenm3*^{KO} larvae (red; n = 13 larvae) from 2 to 5 dpf. Thin traces represent individual IPL profiles, whereas thick traces indicate average IPL profiles. 0% corresponds to the INL/IPL boundary, whereas 100% corresponds to the IPL/GCL boundary. Fluorescence peaks indicating IPL strata in control larvae are labeled with the letter "S" followed by their relative IPL position.

(E and F) Visual responses to moving bars (F) recorded through calcium imaging of an individual orientation-selective RGC (OSGC) axon terminal expressing GCaMP6f (E, green arrowhead) in the optic tectum of a 5-dpf *UAS:GCaMP6f*-injected *Tg(isl2b:Gal4)* larva. Polar plots show the integral responses to moving dark and light bars (F; dark and light green, respectively). Black and gray traces represent the $\Delta F/F_0$ calcium responses to moving dark and light bars, respectively. Np, neuropil; L, lateral; A, anterior; PO, preferred orientation. Scale bar, 40 μm.

(G and H) Immunostaining for GCaMP6f (green) showing the dendritic morphology (G) of the functionally identified OSGC in (E) and the corresponding normalized IPL fluorescence intensity profile (H). Cell bodies are labeled with the nuclear stain TO-PRO-3 (magenta). Scale bar, 20 μm.

(I) IPL fluorescence intensity profiles of OSGCs (green; n = 5 cells) and *tenm3*$^+$ AC neurites (blue; n = 13 larvae) at 5 dpf. 12.8% of functionally imaged RGCs were OS (five out of 39 cells in 39 larvae). Thin traces represent individual IPL profiles, whereas thick traces indicate average IPL profiles. Fluorescence peaks indicating IPL strata formed by OSGC dendrites are labeled with the letter "S" followed by their relative IPL position. See also Figures S2 and S3 and Movie S2.

in the BAC construct used for transgenesis. We therefore used this line to selectively visualize the morphological development of *tenm3*$^+$ ACs from 2 to 5 dpf. During this period, *tenm3* is highly expressed in the retina [17], and, at 3 dpf, RGCs start to show orientation selectivity [29]. Interestingly, *tenm3*$^+$ ACs stratify their neurites in three precise IPL strata located at 5%, 61%, and 94% depth (0% corresponds to the inner nuclear layer (INL)/IPL border, 100% to the IPL/GCL border), which were named S5, S61, and S94, respectively (Figures 2B and 2D). This tri-laminar IPL stratification pattern is visible at 3 dpf and gradually refines over the following 2 developmental days. In *tenm3*^{KO} mutants, by contrast, *tenm3*$^+$ AC neurites do not stratify correctly in the IPL (Figure 2C). This is particularly striking at 3 dpf when they fail to target the two innermost IPL strata and instead stratify diffusely across the IPL (Figure 2D).

An indication of potential synaptic connections between *tenm3*$^+$ ACs and OSGCs would be their dendritic co-stratification in the IPL. Currently, no transgenic line exists to selectively label OSGCs and directly detect dendritic co-stratification with *tenm3*$^+$ ACs. Therefore, we sparsely expressed GCaMP6f [30] in individual RGCs and, after functionally identifying OSGCs, we performed post hoc immunostaining to analyze their IPL stratification pattern (Figures 2E–2G). Then, we averaged fluorescence intensity profiles of dendritic stratification from multiple OSGCs (Figures 2H and S3) and overlaid the resulting mean profile (green, Figure 2I) to the IPL stratification profile of *tenm3*$^+$ ACs (blue). We found that, as a population, OSGCs stratify their dendrites in three strata located at 9%, 61%, and 90% IPL depth and indeed show a high degree of overlap with *tenm3*$^+$ AC neurites (Figure 2I). These results, together with the functional impairment

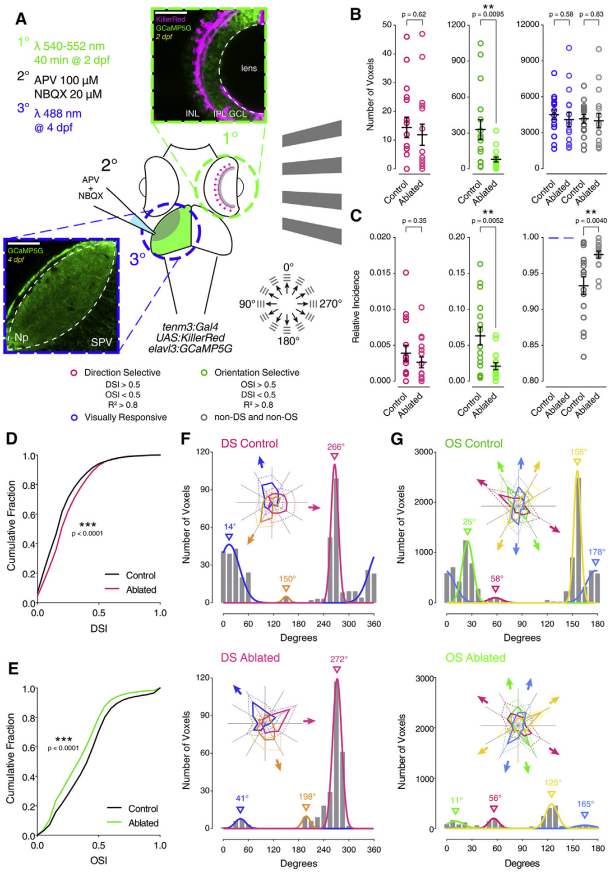

Figure 3. Tenm3⁺ ACs Generate Orientation Tuning in RGCs

(A) Summary of the experimental procedures used to record visual responses from larvae where *tenm3*⁺ ACs were optogenetically ablated. At 2 dpf, the eyes of *Tg(tenm3:Gal4;UAS:KillerRed; elavl3:GCaMP5G)* larvae, where KillerRed is selectively expressed in *tenm3*⁺ ACs only (magenta), are illuminated with green light (540–552 nm) for 40 min. Then, at 4 dpf, visual responses to moving bars are recorded through calcium imaging of RGC axon terminals (expressing GCaMP5G; green) in the optic tectum contralateral to the illuminated eye. Local application of the glutamate receptor antagonists APV and NBQX (100 and 20 μM, respectively) is used to isolate RGC axonal calcium responses from tectal cell dendritic responses. INL, inner nuclear layer; GCL, ganglion cell layer; IPL, inner plexiform layer; Np, neuropil; SPV, stratum periventriculare. Scale bars, 40 μm.

(B and C) Average number (B) and relative frequency (C) of DS, OS, visually responsive, and non-DS/non-OS voxels per Z-plane in control (n = 16 larvae) and *tenm3*⁺ AC ablated (n = 16 larvae) 4-dpf larvae. Error bars, ±SEM. **p < 0.01, unpaired two-tailed Student's t test.

(D and E) Cumulative distributions of DSI values ($R^2 > 0$) across voxels with OSI < 0.5 (D) and OSI values ($R^2 > 0$) across voxels with DSI < 0.5 (E) in control and *tenm3*⁺ AC ablated larvae. ***p < 0.001, two-sample Kolmogorov-Smirnov test.

(F and G) Cumulative histograms summarizing the incidence of preferred angles for identified DS (F) and OS voxels (G) in control (n = 16; top) and *tenm3*⁺ AC ablated (n = 16; bottom) 4-dpf larvae. Overlaid curves are the fitted Gaussian distributions for each DS or OS subtype. Polar plots illustrate the mean (+1 SD) normalized response profiles for each DS or OS subtype.

See also Figure S4, Table S1, and Movie S3.

in RGC orientation selectivity (Figure 1) and previously reported defects in RGC dendritic IPL stratification following Tenm3 loss of function [17] strongly suggest that *tenm3*⁺ ACs and OSGCs are part of the same circuit and that Tenm3 is involved in the morphological and functional development of these two neural populations.

Tenm3⁺ ACs Generate OSGC Tuning through GABAergic Inhibition

To investigate whether *tenm3*⁺ ACs play a role in the emergence of RGC orientation selectivity, we took advantage of the *Tg(tenm3:Gal4)* line to selectively ablate these cells and assess the functional consequences in RGCs. In the *Tg(tenm3:Gal4; UAS:KillerRed;elavl3:GCaMP5G)* line, the genetically encoded photosensitizer KillerRed [31] is expressed in *tenm3*⁺ ACs, whereas GCaMP5G is expressed pan-neuronally (Figure 3A) [32]. At 2 dpf, we optogenetically ablated *tenm3*⁺ ACs by illuminating the retina with intense green light (540–552 nm) for 40 min (Figure S4; see Supplemental Experimental Procedures). Subsequently, at 4 dpf, we recorded RGC visual responses to moving bars as described above (Movie S3). To isolate RGC axonal calcium responses from tectal cell dendritic responses, we locally applied the glutamate receptor antagonists APV and NBQX (100 and 20 μM, respectively) in the tectum [33]. Unlike KillerRed-positive larvae, control larvae subjected to the same procedures did not exhibit retinal cell death (Figure S4). Animals subjected to *tenm3*⁺ AC ablation showed a dramatic impairment in RGC orientation selectivity but no detrimental change in DSGC responses (Figures 3B–3E). The magnitude of the decrease in number of OS voxels, relative proportion of OSGC output and overall degree of RGC orientation selectivity was analogous to what we observed in *tenm3*^{KO} mutants. Moreover, the OSGC subpopulation tuned to vertical stimuli was the least affected by *tenm3*⁺ AC

ablation (magenta, Figure 3G), matching our Tenm3 KO results. Compared to data acquired using the *Tg(isl2b:Gal4;UAS:SyGCaMP3)* line (Figures 1I and 1J), we observed differences in the relative proportions of DSGC and OSGC subtypes as well as in their preferred directions or orientations both in control and *tenm3*$^+$ AC ablated groups (Figures 3F and 3G), likely resulting from the use of a different transgenic line or the pharmacological treatment used to isolate RGC responses.

The results obtained by ablating *tenm3*$^+$ ACs strongly support the idea that the output of *tenm3*$^+$ ACs is crucial in generating RGC orientation selectivity. We therefore aimed to reveal the role played by *tenm3*$^+$ AC neurotransmission in performing this neural computation. Immunohistochemical analyses showed that most *tenm3*$^+$ ACs are GABAergic and express the calcium-binding protein Parvalbumin (Figures 4A, 4B, and 4F). *Tenm3*$^+$ ACs also comprise dopaminergic ACs, which constitute a very small fraction of the whole AC population in zebrafish (Figure 4C) [34]. Negligible or no co-localization was observed between *tenm3*$^+$ ACs and cholinergic or glycinergic ACs, respectively (Figures 4D–4F). Cholinergic ACs correspond to starburst ACs (SACs), which are key cellular players in generating RGC direction selectivity [35], consistent with the observation that neither Tenm3 KO nor *tenm3*$^+$ AC ablation affected DSGC tuning. We next tested the role of GABA-mediated inhibition in producing OSGC tuning by blocking $GABA_A$ receptors through picrotoxin (100 μM). RGC visual responses were recorded from the same *Tg(isl2b:Gal4;UAS:SyGCaMP3)* larvae before and after drug application. Notably, OSGCs were severely affected by GABA inhibition block, with a decrease in both OS responses and overall degree of RGC orientation selectivity comparable to the effects seen in *tenm3*^{KO} mutants and after *tenm3*$^+$ AC ablation (Figures 4G, 4H, and 4J). Similarly to the knockout and ablation experiments, the small OSGC subpopulation tuned to vertical bars was the least affected by the pharmacological block (magenta, Figure 4L). As expected, RGC direction selectivity was also negatively impacted (Figures 4G–4I and 4K), since directionally tuned GABAergic inhibitory input from SACs plays an essential role in most DSGCs [35]. Compared to the impairments in RGC direction and orientation selectivity caused by blocking $GABA_A$ receptors, the effects produced by blocking glycine receptors using strychnine (70 μM) were minimal (Figures S5A–S5F). Taken together, these results demonstrate that OSGCs require GABAergic inhibitory input, likely from *tenm3*$^+$ ACs, to acquire their orientation tuning.

Single-Cell Morphologies of Tenm3$^+$ AC Types

To explore a possible link between the morphology of *tenm3*$^+$ ACs and the function they play in the OS circuit, we sparsely labeled *tenm3*$^+$ ACs by injecting *UAS:eGFP-CAAX* DNA constructs into 1-4 cell-stage *Tg(tenm3:Gal4)* embryos. We identified seven types of *tenm3*$^+$ ACs characterized by distinct morphological properties (Figures 5A–5F). These types differ in terms of their observed frequency, IPL dendritic stratification, dendritic field area (Figures 5I and 5J), and, interestingly, dendritic field elongation, quantified by calculating the eccentricity of their dendritic fields (Figures 5G and 5H). The most frequent *tenm3*$^+$ AC type (type I, 43% of *tenm3*$^+$ ACs) is a narrow-field AC with a dendritic arbor mono-stratified in S5 (Figure 5A). Type II and III *tenm3*$^+$ ACs (19% and 16% of *tenm3*$^+$ ACs, respectively) are medium-field ACs characterized by highly elongated dendritic fields (Figures 5B, 5C, and 5H). Their dendritic arbors stratify differently in the IPL with type II *tenm3*$^+$ ACs having mono-stratified neurites in S5, and type III *tenm3*$^+$ ACs showing a bi-stratified dendritic arbor in S5 and S61. Type IV-ON and IV-OFF *tenm3*$^+$ ACs (each 8% of *tenm3*$^+$ ACs) are mono-stratified medium-field ACs characterized by circular dendritic fields of similar area but different IPL stratification pattern, with the ON type stratifying in the innermost stratum (S94) and the OFF type in the outermost stratum (S5; Figures 5D and 5E). Finally, type V and VI *tenm3*$^+$ ACs are the least frequent *tenm3*$^+$ AC types (each 3% of *tenm3*$^+$ ACs) and possess wide-field dendritic arbors. Type V has extensive, radially arranged neurites covering most of the retina (Figure 5F). Type VI corresponds to the dopaminergic interplexiform AC previously described in goldfish (Figure 4C) [36]. Importantly, k-means clustering based on IPL stratification, dendritic field area, and dendritic field elongation support the notion that the different *tenm3*$^+$ ACs identified here are indeed defined AC types (Figures 5L and 5M; type V and VI ACs were not included in the clustering). Moreover, several lines of evidence suggest that type I–IV *tenm3*$^+$ ACs are arranged in mosaics tiling the retina with a coverage factor close to 1: (1) their frequency scales quadratically as a function of their dendritic field area (Figure 5K); (2) their observed frequency does not differ significantly from the frequency estimated assuming a retinal coverage factor of 1 (Figure 5N). Interestingly, the high dendritic field elongation of type II and III *tenm3*$^+$ ACs (Figures 5B, 5C, and 5H) is a feature previously described also in rabbit orientation-sensitive ACs [13, 14]. This led us to hypothesize that type II and III *tenm3*$^+$ ACs could produce OS responses when stimulating the retina with elongated stimuli oriented along particular axes in the visual field and, consequently, constitute cellular elements underlying the emergence of retinal orientation selectivity.

Tenm3$^+$ ACs Show Orientation Tuning

To analyze tuning in the *tenm3*$^+$ AC population, we performed in vivo two-photon calcium imaging in the retinae of *Tg(tenm3:Gal4;UAS:SyGCaMP3)* larvae (Figure 6A; see Supplemental Experimental Procedures). We found that *tenm3*$^+$ ACs show stimulus-locked responses to moving square-wave gratings (Movie S4). Notably, analyses using different metrics of orientation selectivity (i.e., OSI and circular variance) and progressively higher tuning stringency levels revealed a large fraction of *tenm3*$^+$ ACs tuned to elongated stimuli (Figures S6A–S6D). The distribution of preferred stimulus orientations across *tenm3*$^+$ ACs indicated the presence of four subpopulations of OS responses tuned to gratings oriented along the cardinal (13°, 90°) and diagonal axes (40°, 145°; Figure 6B), similar to what we observed in OSGCs (Figure 1J). Compared to RGCs, however, *tenm3*$^+$ ACs exhibited a higher degree of orientation selectivity (Figures 6C–6E). If activation of *tenm3*$^+$ ACs along a particular axis in the visual field leads to inhibition of OSGC responses along that axis, one would expect that the relationship between their population distributions is inversely correlated. We therefore analyzed the frequency distribution of the four OS subpopulations in *tenm3*$^+$ ACs and RGCs (Figures 6I and 6J). We found that they are indeed anti-correlated (Figure 6K), suggesting that the OS inhibitory input provided by *tenm3*$^+$ ACs to OSGCs is

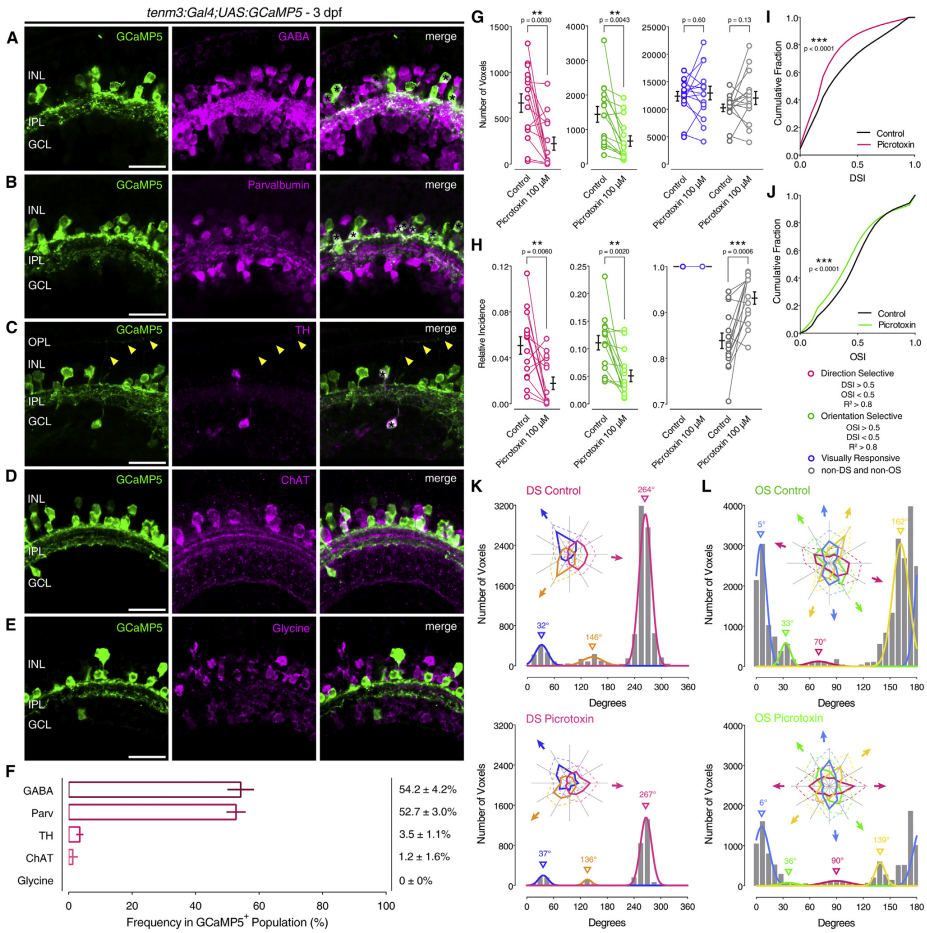

Figure 4. Role of Tenm3$^+$ AC GABAergic Inhibition in RGC Orientation Selectivity

(A–E) Immunostaining showing the expression of γ-aminobutyric acid (GABA; A), parvalbumin (B), tyrosine hydroxylase (TH; C), choline acetyltransferase (ChAT; D), and glycine (E) (all in magenta) in 3-dpf *Tg(tenm3:Gal4;UAS:GCaMP5)* larvae, where *tenm3*$^+$ ACs are labeled with GCaMP5 (green). Yellow arrowheads indicate neurites of TH$^+$ interplexiform ACs (C). INL, inner nuclear layer; GCL, ganglion cell layer; OPL, outer plexiform layer; IPL, inner plexiform layer. Scale bars, 20 μm.

(F) Percentage of GCaMP5$^+$ cells co-localizing with antigen$^+$ cells (mean ± SD). GABA, n = 13 retinae; Parvalbumin, n = 10 retinae; TH, n = 9 retinae; ChAT, n = 10 retinae; glycine, n = 5 retinae.

(G and H) Average number (G) and relative frequency (H) of DS, OS, visually responsive, and non-DS/non-OS voxels per Z-plane in 4-dpf *Tg(isl2b:Gal4;UAS:SyGCaMP3)* larvae (n = 15 larvae) before (control) and after (picrotoxin) the application of picrotoxin (100 μM). Error bars, ±SEM. $^{**}p < 0.01$, $^{***}p < 0.001$, paired two-tailed Student's t test.

(I and J) Cumulative distributions of DSI values ($R^2 > 0$) across voxels with OSI < 0.5 (I) and OSI values ($R^2 > 0$) across voxels with DSI < 0.5 (J) before (control) and after (picrotoxin) the application of picrotoxin (100 μM). $^{***}p < 0.001$, two-sample Kolmogorov-Smirnov test.

(K and L) Cumulative histograms summarizing the incidence of preferred angles for identified DS (K) and OS voxels (L) in 4-dpf larvae (n = 15 larvae) before (control) and after (picrotoxin) the application of picrotoxin (100 μM). Overlaid curves are the fitted Gaussian distributions for each DS or OS subtype. Polar plots illustrate the mean (+1 SD) normalized response profiles for each DS or OS subtype.

See also Figure S5 and Table S1.

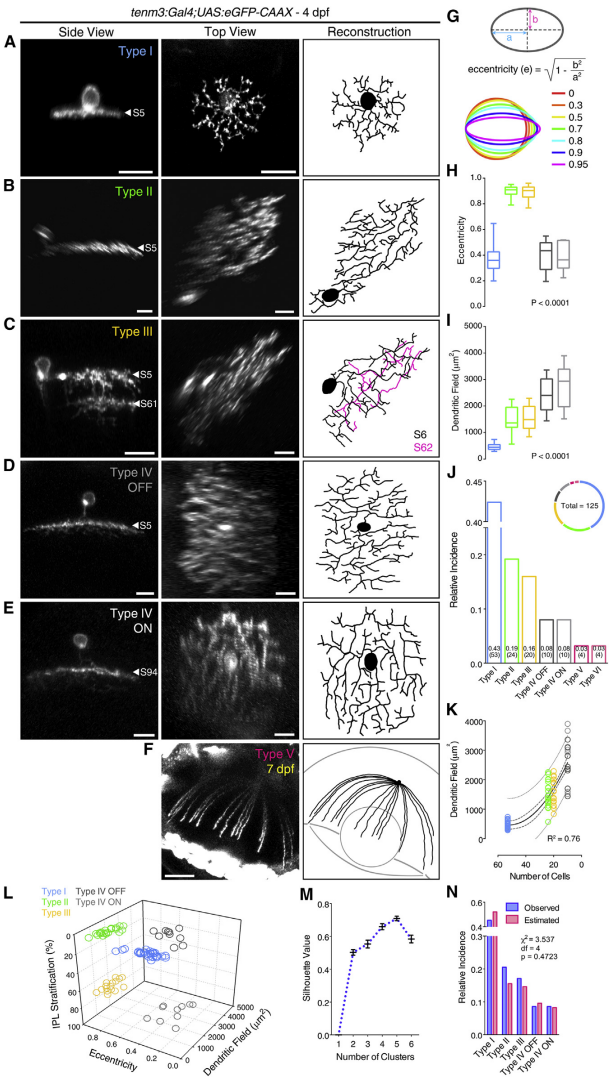

Figure 5. Morphological Diversity of Individual Tenm3⁺ AC Types

(A–F) Morphologies of single *tenm3*⁺ ACs expressing eGFP-CAAX in 4-dpf *UAS:eGFP-CAAX*-injected *Tg(tenm3:Gal4)* larvae. The side views (left), top views (middle), and top view 3D reconstructions (right) are shown. IPL strata location of *tenm3*⁺ AC neurites is indicated by the letter "S" followed by the relative IPL position. The 3D reconstructed neurites of the bi-stratified type III *tenm3*⁺ AC are color-coded according to the stratum they are located. Note that the type V *tenm3*⁺ AC shown in (F) is from a 7-dpf larva. Scale bars, 10 µm in (A)–(E) and 40 µm in (F).

(G) Diagram illustrating the quantification of dendritic field elongation by calculating the eccentricity of dendritic arbor profiles following ellipse fitting. "a" is the length of the semi-major axis, and "b" is the length of the semi-minor axis.

(H–J) Dendritic field elongation (i.e., eccentricity; H), dendritic field area (I), and relative frequency (J) of identified *tenm3*⁺ AC types (n = 125 cells from 65 larvae). The number of observed cells for each *tenm3*⁺ AC type is reported in brackets (J). Boxplots indicate interquartile ranges (boxes), medians (lines in boxes), and ranges (min-max, whiskers). p values are the results of one-way ANOVA.

(K) Relationship between dendritic field area of type I–IV *tenm3*⁺ ACs and their observed frequency (in number of cells). The continuous curve shows the nonlinear regression of the data with a second order polynomial function indicating a quadratic relationship between the two variables. Thick and thin dashed curves report the 95% confidence and prediction bands of the nonlinear fit, respectively. Goodness of fit value (R^2) is reported at the bottom-right corner.

(L and M) k-means clustering of type I–IV *tenm3*⁺ ACs based on their IPL stratification, dendritic field area, and dendritic field elongation. Individual cell data points are color coded according to which *tenm3*⁺ AC type they have been classified (L). Analysis of mean silhouette values for increasing number of clusters indicates that five clusters best describe the dataset (M). Importantly, the five cell clusters obtained by k-means are consistent with the classification of the most frequent *tenm3*⁺ ACs into five different types. Error bars, ±SEM.

(N) Observed (blue) and estimated (red; assuming a retinal coverage factor of 1) relative frequencies of type I–IV *tenm3*⁺ ACs. Results of the two-tailed chi-square test are reported.

See also Table S1.

orthogonally tuned (i.e., tuned to the orientation orthogonal to the OSGC-preferred orientation).

Given the presence of different *tenm3*⁺ AC types (Figure 5), we asked which ones display high orientation selectivity. We thus performed functional imaging of individually GCaMP6f-labeled *tenm3*⁺ ACs, followed by analyses of their tuning and dendritic field morphology (Figure S7A). Strikingly, the only *tenm3*⁺ ACs that showed stimulus-locked visual responses characterized by high orientation tuning were type II or III ACs (Figure 6F). Their degree of orientation selectivity was correlated with the elongation of their dendritic fields (Figure 6G), and the angular difference between their preferred stimulus orientation and dendritic field orientation was close to zero

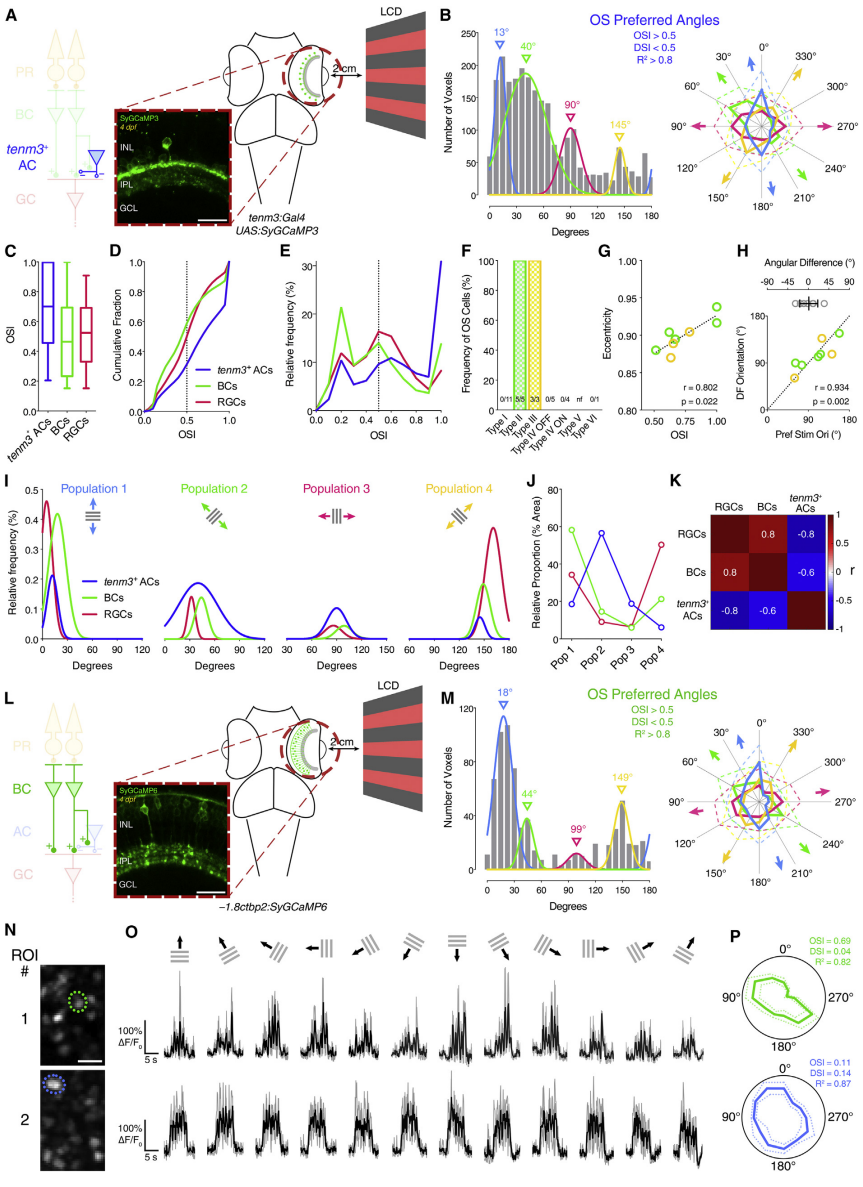

(legend on next page)

(Figure 6H), indicating that type II and III *tenm3*$^+$ ACs respond maximally when the stimulus orientation coincides with the orientation of their dendritic fields. Additionally, the distribution of dendritic field orientations across sparsely eGFP-labeled type II and III *tenm3*$^+$ ACs revealed that they fully cover the orientation space (Figures S7B and S7C). Since blocking $GABA_A$ receptors leads to impaired RGC orientation selectivity (Figures 4G–4L), we investigated whether these two AC types are GABAergic by performing anti-GABA immunostaining of sparsely eGFP-labeled *tenm3*$^+$ ACs. We observed that both type II and III *tenm3*$^+$ ACs do indeed express the neurotransmitter GABA (Figures S7D and S7E), consistent with the results in Figure 4. Together, these data show that type II and III *tenm3*$^+$ ACs constitute a source of orientation-tuned GABAergic inhibition in the retina.

Orientation-Selective Responses in Bipolar Cell Presynaptic Terminals

Since ACs have been shown to modulate BC output at the level of individual presynaptic terminals [37], tuned inhibitory input from type II and III *tenm3*$^+$ ACs could potentially generate orientation tuning in BC presynaptic terminals. We started investigating this idea by performing calcium imaging in the retinae of *Tg(−1.8ctbp2:SyGCaMP6)* larvae, where BC ribbon synapses are selectively labeled with SyGCaMP6 (Figure 6L; Movie S5) [38]. Interestingly, we observed that a fraction of BC responses (~5% of visually responsive voxels) is indeed highly orientation selective (OSI > 0.5, DSI < 0.5, R^2 > 0.8; Figures 6N–6P and S6E–S6H). Similarly to OSGCs and *tenm3*$^+$ ACs, the preferred stimulus orientations of OS responses fall into four subpopulations tuned to gratings oriented along the cardinal (18°, 99°) and diagonal axes (44°, 149°; Figure 6M). The degree of orientation selectivity across the whole population of BC terminals appeared to be more similar to RGCs than *tenm3*$^+$ ACs (Figures 6C–6E). Furthermore, the frequency distribution of the four OS BC subpopulations is highly correlated with that of OSGCs but inversely correlated with *tenm3*$^+$ ACs (Figures 6I–6K). This therefore suggests that orientation selectivity in BC terminals could be generated by orthogonal orientation-tuned inhibitory input from *tenm3*$^+$ ACs, similarly to OSGCs.

DISCUSSION

The vertebrate retina extracts information from visual scenes and sends it to higher brain areas through feature-specific neural pathways. Crucial neural substrates underlying this information processing in the retina are the stereotypic synaptic connections between defined neural cell types. How specific elements of the retinal circuit perform computations is, however, largely unknown. The data presented here define cellular and molecular building blocks of a circuit in the larval zebrafish retina capable of detecting the orientation of elongated visual stimuli. In particular, we take advantage of the functional link between RGC orientation selectivity and the cell-adhesion molecule Tenm3 to genetically identify a class of ACs with elongated dendritic arbors that show orientation tuning. We reveal that these *tenm3*$^+$ ACs and their GABAergic inhibitory output are crucial for the tuning of orientation-selective RGCs. Moreover, we show that Tenm3 is a key molecular player in both the morphological and functional development of the circuit, and that

Figure 6. Orientation Selectivity in Tenm3$^+$ ACs and BC Terminals

(A) Two-photon functional calcium imaging of *tenm3*$^+$ AC synaptic terminals expressing SyGCaMP3 (green) in 4-dpf *Tg(tenm3:Gal4;UAS:SyGCaMP3)* larvae. Distance of the eye from LCD screen is 2 cm. Recordings are performed from two to four Z-planes (approximately 20 μm total volume thickness). INL, inner nuclear layer; GCL, ganglion cell layer; IPL, inner plexiform layer. Scale bar, 20 μm.

(B) Cumulative histogram summarizing the incidence of preferred angles for identified *tenm3*$^+$ AC OS voxels in 4-dpf larvae (n = 20 larvae). Overlaid curves are the fitted Gaussian distributions for each OS subtype. Polar plots illustrate the mean (+1 SD) normalized response profiles for each OS subtype.

(C–E) Degree of orientation selectivity (quantified by the OSI) across voxels with DSI < 0.5 and R^2 > 0 in *tenm3*$^+$ ACs (blue, n = 20 larvae), BCs (green, n = 20 larvae), and RGCs (red, n = 23 larvae; data from Figure 1H). Boxplots in (C) indicate interquartile ranges (boxes), medians (lines in boxes), and 10–90 percentiles (whiskers). The black dotted lines in (D) and (E) indicate the OSI threshold used to identify OS responses (OSI > 0.5).

(F) Bar histogram summarizing the frequency of OS cells among *tenm3*$^+$ ACs in 4-dpf *Tg(tenm3:Gal4)* larvae injected with *UAS:GCaMP6f* DNA constructs (n = 29 cells from 27 larvae). The number of observed OS cells for each *tenm3*$^+$ AC type is reported at the bottom. nf, not found.

(G) Scatterplot representing the relationship between OSI and dendritic field eccentricity of OS type II and III *tenm3*$^+$ ACs (II, n = 5 cells; III, n = 3 cell). Spearman's correlation coefficient (r) with the corresponding p value is reported. Dotted line represents the linear regression fit to the data.

(H) Scatterplot representing the relationship between preferred stimulus orientation and dendritic field orientation of OS type II and III *tenm3*$^+$ ACs (II, n = 5 cells; III, n = 3 cell). Spearman's correlation coefficient (r) with the corresponding p value is reported. Dotted reference line indicates x = y. Top graph shows the angular difference between preferred stimulus orientation and dendritic field orientation (mean ± SD).

(I) Normalized frequency distributions of preferred stimulus orientations in OS *tenm3*$^+$ ACs (blue, n = 20 larvae), BCs (green, n = 20 larvae), and RGCs (red, n = 23 larvae; data from Figure 1J). The Gaussian distributions of the four different OS subpopulations are reported in separate graphs.

(J) Relative proportions of the four different OS subpopulations (Pop 1–4) in *tenm3*$^+$ ACs (blue), BCs (green), and RGCs (red). Values are obtained by calculating the relative proportion (%) of the area under the normalized Gaussian curves in (I).

(K) Correlation matrix showing Spearman's correlation coefficients (r) between the frequency distribution of the four OS subpopulations in *tenm3*$^+$ ACs, BCs, and RGCs.

(L) Two-photon functional calcium imaging of BC ribbon synapses expressing SyGCaMP6 (green) in 4-dpf *Tg(−1.8ctbp2:SyGCaMP6)* larvae. Distance of the eye from LCD screen is 2 cm. Recordings are performed from two to four Z-planes (approximately 20 μm total volume thickness). Scale bar, 20 μm.

(M) Cumulative histogram summarizing the incidence of preferred angles for identified BC OS voxels in 4-dpf larvae (n = 20 larvae). Overlaid curves are the fitted Gaussian distributions for each OS subtype. Polar plots illustrate the mean (+1 SD) normalized response profiles for each OS subtype.

(N–P) Examples of visual responses to moving gratings from two BC terminals. Images showing the mean fluorescence across tuning experiments with identified regions of interest (ROIs) are reported in (N). (O) shows calcium responses of the two ROIs in (N) with black traces representing the average responses across three trials (gray traces) for each stimulus epoch. Polar plots in (P) illustrate the mean response profile (±SD, dotted lines) of each ROI with corresponding OSI, DSI, and R^2 values. Note that ROI #1 shows orientation selectivity. Scale bar, 5 μm.

See also Figures S6 and S7, Table S1, and Movies S4 and S5.

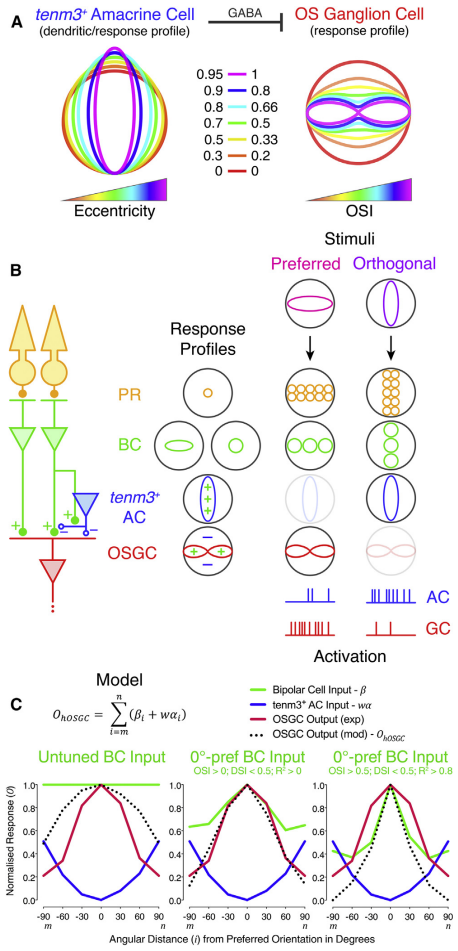

Figure 7. Circuit Model of Orientation Selectivity in the Retina

(A) Hypothesized principles underlying the emergence of orientation selectivity in the retina. The high dendritic field elongation (quantified by the eccentricity of fitted elliptic profiles) of defined *tenm3*$^+$ AC types is at the basis of their high orientation tuning (left). Maximal activation of tuned AC types is obtained when the orientation of elongated visual stimuli coincides with the orientation of their dendritic fields. As a result, these tuned *tenm3*$^+$ AC types generate orientation selectivity in RGCs (quantified by the OSI, right) by providing orthogonal orientation-tuned GABAergic inhibitory input. The color code describes the different levels of dendritic field elongation (left) and orientation selectivity (right).

(B) Examples of retinal OS circuit activation patterns for horizontal orientation-tuned OSGC preferred (magenta) and orthogonal (purple) stimuli. Excitatory input is indicated by "+" (full circles), whereas inhibitory input is indicated by "–" (empty circles). Putative synapses between OS *tenm3*$^+$ ACs and BC terminals are also represented. Tuning profiles of example photoreceptor (PR), bipolar cells (BCs), OS *tenm3*$^+$ amacrine cell (AC), and orientation-selective ganglion cell (OSGC) are also reported.

(C) Simulation of the OSGC tuning profile (O_{hOSGC}, black dotted line) using experimentally observed average response profiles of orthogonally tuned OS *tenm3*$^+$ ACs (α, blue line; n = 20 larvae) and BC terminals (β, green line; n = 20 larvae). Three different orientation-tuning levels of excitatory BC input were used: untuned (left), weakly tuned to preferred orientation (middle) and highly tuned to preferred orientation (right). The experimentally observed average response profile of OSGCs (n = 23 larvae) is shown in red. The algorithm used for the simulation is reported at the top with the related legend. Note that, since the OS *tenm3*$^+$ AC input (α) is inhibitory, a negative synaptic weight factor (*w*) is used in the algorithm. The orientation space ranges from "*m*" to "*n*", which are negative (−90°) and positive (90°) angles orthogonal to the preferred orientation (0°), respectively. Exp, experimental; mod, model; pref, preferred.

See also Figure S5.

orientation selectivity is also present among bipolar cell presynaptic terminals. Our study represents, to our knowledge, the most extensive characterization of the retinal orientation-selective circuit in a single tractable system. By collecting functional and structural data from amacrine, bipolar, and ganglion cells at cellular and population levels, we provide a mechanistic explanation of how defined neural cell types in the retina generate a fundamental property of visual perception—i.e., orientation selectivity. Additionally, our results elucidate the functional role of two novel AC types, therefore shedding some light on the most diverse and least understood retinal cell class [39].

A Circuit Model of Orientation Selectivity in the Retina

To integrate our data into a general framework describing the computation of orientation selectivity in RGCs, we outlined a model of the retinal OS circuit. The model is based on the following principles: (1) the highly elongated dendritic fields of type II and III *tenm3*$^+$ ACs identified in this study (Figure 5) underlie their orientation tuning (Figures 6 and 7A). Specifically, these defined AC types respond maximally when the orientation of elongated visual stimuli coincides with the orientation of their dendritic fields. Interestingly, ACs characterized by elongated dendritic fields and orientation selectivity have been found also in the rabbit retina, although their genetic identity is still unknown [13, 14]. (2) Type II and III *tenm3*$^+$ ACs provide orthogonal orientation-tuned inhibitory input to OSGCs and, potentially, BC presynaptic terminals (Figures 6I–6K). This feedforward inhibition is mediated by GABA and generates orientation selectivity in OSGCs (Figures 3, 4, and 7A). Interestingly, pharmacological block of synaptic inhibition onto zebrafish BC terminals indicates that orientation selectivity in BC ribbon synapses is generated through AC inhibitory input (J. Johnston and L. Lagnado, personal communication), therefore supporting the idea that the OS inhibitory output of type II and III *tenm3*$^+$ ACs could be at the basis of orientation selectivity in both BCs and OSGCs. Studies in the rabbit and mouse retina showed that OSGCs receive preferred orientation-tuned excitatory input and orthogonal orientation-tuned inhibitory input and, in rabbit, presynaptic GABAergic inhibition plays a pivotal role in the emergence of these OS inputs [9, 40]. Recent findings in *Drosophila* showed an analogous requirement of GABA signaling for orientation

selectivity [5], revealing strikingly similar mechanisms between vertebrates and invertebrates. (3) Stimulus orientation, not the axis of stimulus movement, is the visual feature OSGCs are selective to. This is supported by our observation that static gratings, even though less effective in eliciting RGC responses, produce results analogous to those obtained using moving gratings (Figures S5G–S5J). Again, such property has been observed in rabbit and mouse OSGCs as well [10, 40]. Additional mechanisms to those described here may contribute to the emergence of RGC orientation selectivity.

In a schematic example of our model (Figure 7B), when the retina is stimulated with the OSGC-preferred stimulus orientation, the orthogonally tuned *tenm3*$^+$ AC is weakly activated, therefore allowing the OSGC to fire action potentials. When the orthogonal stimulus orientation is presented, instead, the orthogonally tuned *tenm3*$^+$ AC is strongly activated, and, consequently, OSGC firing is inhibited. To further evaluate our model, we implemented the basic principles described above into a simple simulation of OSGC output (Figure 7C). To simulate the OSGC tuning profile (black dotted line), we used our experimentally observed average response profiles of OS *tenm3*$^+$ ACs (blue line) and BC presynaptic terminals (green line). We assumed the OS inhibitory input provided by *tenm3*$^+$ ACs has a subtractive effect on OSGC output and tested three different orientation-tuning levels of excitatory BC input. Interestingly, we found that the average OSGC response profile observed experimentally (red line) was best reproduced when linearly integrating highly OS (OSI > 0.5, DSI < 0.5, R^2 > 0.8) orthogonal orientation-tuned inhibitory input from *tenm3*$^+$ ACs and weakly OS (OSI > 0, DSI < 0.5, R^2 > 0) preferred orientation-tuned excitatory input from BCs (Figure 7C), indicating that OSGCs may receive BC input characterized by a substantial degree of heterogeneity in orientation tuning. This simulation also implies that OSGCs potentially integrate tuned input from both ACs and BCs to obtain the orientation selectivity observed in vivo. Our results show that the tuned GABAergic inhibitory output of *tenm3*$^+$ ACs is necessary to generate normal RGC orientation selectivity. However, further experiments are needed to precisely determine the relative contribution played by inhibitory AC versus excitatory BC tuned inputs in OSGCs. The strong similarities found between the OS circuit we characterize in the zebrafish retina and previous descriptions of orientation selectivity in mammalian retinae [9, 13, 40] suggest that our model can be generalized to other vertebrate species.

Functional Significance of Orientation Selectivity

The widespread presence of orientation-selective cells in visual systems of many animals highlights the prominent functional role of orientation selectivity in visual perception. Studies on the statistical properties of natural scenes indicate that natural images can be described by local, oriented filters similar to the receptive fields of OS cells found in visual systems [41]. One striking example in humans is the key role played by horizontal visual information in the identification of faces [42]. However, a central question is, where does orientation selectivity emerge in visual circuits? Interestingly, both in vertebrates and invertebrates the detection of elongated visual stimuli takes place early in visual processing [5, 10]. Even in mammalian species, including mice and monkeys, where for long time it was thought that orientation selectivity is an emergent property generated in primary visual cortex [1, 43], OS cells have been found in non-cortical areas such as the lateral geniculate nucleus [6–8] and superior colliculus [44], as well as in the retina [11, 12, 40, 45].

In our study, we found orientation selectivity in presynaptic terminals of BCs and ACs (Figures 6 and S6), which are neurons only one and two synapses away from photoreceptors, respectively. Additionally, we observed OS responses in these cells as early as 4 dpf, when zebrafish larvae start performing visually guided behaviors, such as the optokinetic reflex. Importantly, our data show that the cells and mechanisms underlying RGC orientation selectivity are different from those generating direction selectivity, in line with the notion that parallel retinal circuits process these two distinct visual features. This idea is further supported by the fact that zebrafish OSGC and DSGC axonal projections terminate in different, non-overlapping neuropil laminae of the optic tectum [4, 29].

Role of Teneurins in Neural Circuit Wiring

Teneurins are phylogenetically conserved type II transmembrane proteins with large extracellular domains that are highly expressed in neural tissues [24, 25]. In vertebrates, the teneurin family comprises four members, Tenm1–4, whereas in invertebrates fewer members have been identified (one in *C. elegans*, two in *Drosophila*). In both vertebrate and invertebrate species, teneurins interact in *trans* through both homo- and heterophilic mechanisms [22, 23, 26, 27]. Notably, these trans-interactions are crucial in mediating cell-cell recognition and adhesion. Elegant studies in *Drosophila* demonstrated that teneurins play an instructive role in the synaptic matching between specific pre- and postsynaptic cells [22, 23]. In addition, teneurins regulate other fine-scale neural wiring processes in vivo, such as cell-type-specific dendrite morphogenesis [17, 46], synapse organization [23, 47], and axon projection topography and lamination [17, 48]. The precise roles played by homo- versus heterophilic trans-interactions during these wiring events are still unclear. However, it appears that homophilic interactions are crucial for the initial recognition and matching between specific subsets of neurons [22, 26], whereas heterophilic interactions are involved in subsequent steps of synapse adhesion and organization [27, 28, 47]. Since teneurins can control these distinct processes even between the same sets of neurons [22, 47], sophisticated genetic manipulations will be required to disentangle the contribution of homo- versus heterophilic trans-interactions in neurons where a given teneurin and its heterophilic binding partners are simultaneously expressed.

Our data suggest that Tenm3 specifies the correct development of functionally and morphologically defined subsets of ACs and RGCs forming a circuit underlying retinal orientation selectivity. Even though our results are suggestive of direct synaptic matching between *tenm3*$^+$ ACs and OSGCs, the technical limitations of our study do not allow to unequivocally demonstrate the physical synaptic connections between these two neural populations, and, therefore, future experiments will be required to further elucidate this point. Given that Tenm3 is expressed in both ACs and RGCs (Figures S1C–S1F, S2B, and S2C) [17] and that Tenm3 loss of function leads to defects in *tenm3*$^+$ AC neurite IPL stratification (Figures 2B–2D) as well as specific morphological and functional impairments in RGCs

(Figures 1 and S1) [17], one possible explanation of Tenm3 mechanism of action could be through *trans*-synaptic homophilic interactions. However, loss of selective trans-interactions with other cell-adhesion molecules known to bind heterophilically with teneurins, such as latrophilins [27, 28], may as well explain the phenotypes we observed in *tenm3*^{KO} mutants. Interestingly, some latrophilins are expressed in the zebrafish eye at larval and adult stages, although it is not clear whether they exhibit a cell-type-specific expression pattern [49, 50]. Thus, the retinal orientation-selective circuit characterized in this study represents a tractable in vivo vertebrate system to test the specific roles played by teneurin homo- and heterophilic trans-interactions during neural circuit wiring.

In conclusion, our findings constitute a significant advancement in the understanding of how orientation selectivity emerges in the vertebrate retina, bringing together molecular markers, cell morphologies, pharmacology, and function. Moreover, the in vivo system and relative genetic tools established in this study will allow investigations of the precise functional role played by retinal orientation selectivity in higher visual areas of the brain as well as its role in performing visually guided behaviors.

EXPERIMENTAL PROCEDURES

Statistical test results are reported in the figures and figure legends. Statistical analyses and tests were carried out using Prism 6 (GraphPad), SigmaPlot 11 (Systat Software), or MATLAB R2014b (MathWorks). A comprehensive description of the statistical analyses and tests performed in this study can be found in Table S1. Before performing statistical tests, descriptive statistics (e.g., normality tests to see whether values come from a Gaussian distribution or F-test to compare variances) were used to choose the appropriate statistical test (reported in Table S1). The criterion for statistical significance was set at $p < 0.05$. In order to quantitatively measure and assess the effects of treatments or genetic manipulations between animal groups, the effect size (Cohen's *d*) and its 95% confidence interval were also calculated (see Table S1). See Supplemental Experimental Procedures for detailed methods and zebrafish lines used in this study. All animal procedures were approved by the local Animal Welfare and Ethics Review Body (King's College London) and were carried out in accordance with the Animals (Scientific Procedures) Act 1986 under license from the United Kingdom Home Office.

SUPPLEMENTAL INFORMATION

Supplemental Information includes seven figures, Supplemental Experimental Procedures, one table, and five movies and can be found with this article online at http://dx.doi.org/10.1016/j.cub.2016.05.035.

AUTHOR CONTRIBUTIONS

P.A. and R.H. designed the study. P.A. performed the experiments and analyzed the data. O.S. and C.M. generated the TALEN mutant zebrafish. P.A. and R.H. wrote the manuscript.

ACKNOWLEDGMENTS

We would like to thank Martin Meyer and Leon Lagnado for providing zebrafish transgenic lines, Oscar Marín and Martin Meyer for comments on the manuscript, and Andrew Lowe for analysis tools. We thank the Nikon Imaging Centre at King's College London for support and instrumentation. This study was supported by a BBSRC grant (BB/M000664/1) awarded to R.H. and a King's College London Health Schools PhD studentship awarded to P.A., sponsored by the Medical Research Council (1413592). O.S. and C.M. are part of a Genome Editing Team funded by a Wellcome Trust Technology Development Grant (WT093389) to Corinne Houart, Jon Clarke, Uwe Drescher, Simon Hughes, and R.H.

Received: March 22, 2016
Revised: April 21, 2016
Accepted: May 12, 2016
Published: June 30, 2016

REFERENCES

1. Hubel, D.H., and Wiesel, T.N. (1962). Receptive fields, binocular interaction and functional architecture in the cat's visual cortex. J. Physiol. *160*, 106–154.
2. Hubel, D.H., and Wiesel, T.N. (1968). Receptive fields and functional architecture of monkey striate cortex. J. Physiol. *195*, 215–243.
3. Niell, C.M., and Stryker, M.P. (2008). Highly selective receptive fields in mouse visual cortex. J. Neurosci. *28*, 7520–7536.
4. Nikolaou, N., Lowe, A.S., Walker, A.S., Abbas, F., Hunter, P.R., Thompson, I.D., and Meyer, M.P. (2012). Parametric functional maps of visual inputs to the tectum. Neuron *76*, 317–324.
5. Fisher, Y.E., Silies, M., and Clandinin, T.R. (2015). Orientation selectivity sharpens motion detection in *Drosophila*. Neuron *88*, 390–402.
6. Cheong, S.K., Tailby, C., Solomon, S.G., and Martin, P.R. (2013). Cortical-like receptive fields in the lateral geniculate nucleus of marmoset monkeys. J. Neurosci. *33*, 6864–6876.
7. Piscopo, D.M., El-Danaf, R.N., Huberman, A.D., and Niell, C.M. (2013). Diverse visual features encoded in mouse lateral geniculate nucleus. J. Neurosci. *33*, 4642–4656.
8. Marshel, J.H., Kaye, A.P., Nauhaus, I., and Callaway, E.M. (2012). Anterior-posterior direction opponency in the superficial mouse lateral geniculate nucleus. Neuron *76*, 713–720.
9. Venkataramani, S., and Taylor, W.R. (2010). Orientation selectivity in rabbit retinal ganglion cells is mediated by presynaptic inhibition. J. Neurosci. *30*, 15664–15676.
10. Levick, W.R. (1967). Receptive fields and trigger features of ganglion cells in the visual streak of the rabbits retina. J. Physiol. *188*, 285–307.
11. Zhao, X., Chen, H., Liu, X., and Cang, J. (2013). Orientation-selective responses in the mouse lateral geniculate nucleus. J. Neurosci. *33*, 12751–12763.
12. Baden, T., Berens, P., Franke, K., Román Rosón, M., Bethge, M., and Euler, T. (2016). The functional diversity of retinal ganglion cells in the mouse. Nature *529*, 345–350.
13. Bloomfield, S.A. (1994). Orientation-sensitive amacrine and ganglion cells in the rabbit retina. J. Neurophysiol. *71*, 1672–1691.
14. Murphy-Baum, B.L., and Taylor, W.R. (2015). The synaptic and morphological basis of orientation selectivity in a polyaxonal amacrine cell of the rabbit retina. J. Neurosci. *35*, 13336–13350.
15. Masland, R.H. (2012). The neuronal organization of the retina. Neuron *76*, 266–280.
16. Roska, B., and Werblin, F. (2001). Vertical interactions across ten parallel, stacked representations in the mammalian retina. Nature *410*, 583–587.
17. Antinucci, P., Nikolaou, N., Meyer, M.P., and Hindges, R. (2013). Teneurin-3 specifies morphological and functional connectivity of retinal ganglion cells in the vertebrate visual system. Cell Rep. *5*, 582–592.
18. Yamagata, M., and Sanes, J.R. (2008). Dscam and Sidekick proteins direct lamina-specific synaptic connections in vertebrate retina. Nature *451*, 465–469.
19. Krishnaswamy, A., Yamagata, M., Duan, X., Hong, Y.K., and Sanes, J.R. (2015). Sidekick 2 directs formation of a retinal circuit that detects differential motion. Nature *524*, 466–470.
20. Duan, X., Krishnaswamy, A., De la Huerta, I., and Sanes, J.R. (2014). Type II cadherins guide assembly of a direction-selective retinal circuit. Cell *158*, 793–807.

21. Sun, L.O., Jiang, Z., Rivlin-Etzion, M., Hand, R., Brady, C.M., Matsuoka, R.L., Yau, K.W., Feller, M.B., and Kolodkin, A.L. (2013). On and off retinal circuit assembly by divergent molecular mechanisms. Science *342*, 1241974.
22. Hong, W., Mosca, T.J., and Luo, L. (2012). Teneurins instruct synaptic partner matching in an olfactory map. Nature *484*, 201–207.
23. Mosca, T.J., Hong, W., Dani, V.S., Favaloro, V., and Luo, L. (2012). Trans-synaptic Teneurin signalling in neuromuscular synapse organization and target choice. Nature *484*, 237–241.
24. Tucker, R.P., and Chiquet-Ehrismann, R. (2006). Teneurins: a conserved family of transmembrane proteins involved in intercellular signaling during development. Dev. Biol. *290*, 237–245.
25. Mosca, T.J. (2015). On the Teneurin track: a new synaptic organization molecule emerges. Front. Cell. Neurosci. *9*, 204.
26. Beckmann, J., Schubert, R., Chiquet-Ehrismann, R., and Müller, D.J. (2013). Deciphering teneurin domains that facilitate cellular recognition, cell-cell adhesion, and neurite outgrowth using atomic force microscopy-based single-cell force spectroscopy. Nano Lett. *13*, 2937–2946.
27. Boucard, A.A., Maxeiner, S., and Südhof, T.C. (2014). Latrophilins function as heterophilic cell-adhesion molecules by binding to teneurins: regulation by alternative splicing. J. Biol. Chem. *289*, 387–402.
28. Silva, J.P., Lelianova, V.G., Ermolyuk, Y.S., Vysokov, N., Hitchen, P.G., Berninghausen, O., Rahman, M.A., Zangrandi, A., Fidalgo, S., Tonevitsky, A.G., et al. (2011). Latrophilin 1 and its endogenous ligand Lasso/teneurin-2 form a high-affinity transsynaptic receptor pair with signaling capabilities. Proc. Natl. Acad. Sci. USA *108*, 12113–12118.
29. Lowe, A.S., Nikolaou, N., Hunter, P.R., Thompson, I.D., and Meyer, M.P. (2013). A systems-based dissection of retinal inputs to the zebrafish tectum reveals different rules for different functional classes during development. J. Neurosci. *33*, 13946–13956.
30. Chen, T.W., Wardill, T.J., Sun, Y., Pulver, S.R., Renninger, S.L., Baohan, A., Schreiter, E.R., Kerr, R.A., Orger, M.B., Jayaraman, V., et al. (2013). Ultrasensitive fluorescent proteins for imaging neuronal activity. Nature *499*, 295–300.
31. Bulina, M.E., Chudakov, D.M., Britanova, O.V., Yanushevich, Y.G., Staroverov, D.B., Chepurnykh, T.V., Merzlyak, E.M., Shkrob, M.A., Lukyanov, S., and Lukyanov, K.A. (2006). A genetically encoded photosensitizer. Nat. Biotechnol. *24*, 95–99.
32. Ahrens, M.B., Orger, M.B., Robson, D.N., Li, J.M., and Keller, P.J. (2013). Whole-brain functional imaging at cellular resolution using light-sheet microscopy. Nat. Methods *10*, 413–420.
33. Hunter, P.R., Lowe, A.S., Thompson, I.D., and Meyer, M.P. (2013). Emergent properties of the optic tectum revealed by population analysis of direction and orientation selectivity. J. Neurosci. *33*, 13940–13945.
34. Xi, Y., Yu, M., Godoy, R., Hatch, G., Poitras, L., and Ekker, M. (2011). Transgenic zebrafish expressing green fluorescent protein in dopaminergic neurons of the ventral diencephalon. Dev. Dyn. *240*, 2539–2547.
35. Vaney, D.I., Sivyer, B., and Taylor, W.R. (2012). Direction selectivity in the retina: symmetry and asymmetry in structure and function. Nat. Rev. Neurosci. *13*, 194–208.
36. Dowling, J.E., and Ehinger, B. (1978). The interplexiform cell system. I. Synapses of the dopaminergic neurons of the goldfish retina. Proc. R. Soc. Lond. B Biol. Sci. *201*, 7–26.
37. Asari, H., and Meister, M. (2012). Divergence of visual channels in the inner retina. Nat. Neurosci. *15*, 1581–1589.
38. Johnston, J., Ding, H., Seibel, S.H., Esposti, F., and Lagnado, L. (2014). Rapid mapping of visual receptive fields by filtered back projection: application to multi-neuronal electrophysiology and imaging. J. Physiol. *592*, 4839–4854.
39. MacNeil, M.A., Heussy, J.K., Dacheux, R.F., Raviola, E., and Masland, R.H. (1999). The shapes and numbers of amacrine cells: matching of photofilled with Golgi-stained cells in the rabbit retina and comparison with other mammalian species. J. Comp. Neurol. *413*, 305–326.
40. Nath, A., and Schwartz, G.W. (2016). Cardinal orientation selectivity is represented by two distinct ganglion cell types in mouse retina. J. Neurosci. *36*, 3208–3221.
41. Olshausen, B.A., and Field, D.J. (1996). Emergence of simple-cell receptive field properties by learning a sparse code for natural images. Nature *381*, 607–609.
42. Dakin, S.C., and Watt, R.J. (2009). Biological "bar codes" in human faces. J Vis *9*, 2.1–10.
43. Niell, C.M. (2013). Vision: more than expected in the early visual system. Curr. Biol. *23*, R681–R684.
44. Wang, L., Sarnaik, R., Rangarajan, K., Liu, X., and Cang, J. (2010). Visual receptive field properties of neurons in the superficial superior colliculus of the mouse. J. Neurosci. *30*, 16573–16584.
45. Passaglia, C.L., Troy, J.B., Rüttiger, L., and Lee, B.B. (2002). Orientation sensitivity of ganglion cells in primate retina. Vision Res. *42*, 683–694.
46. Hattori, Y., Usui, T., Satoh, D., Moriyama, S., Shimono, K., Itoh, T., Shirahige, K., and Uemura, T. (2013). Sensory-neuron subtype-specific transcriptional programs controlling dendrite morphogenesis: genome-wide analysis of Abrupt and Knot/Collier. Dev. Cell *27*, 530–544.
47. Mosca, T.J., and Luo, L. (2014). Synaptic organization of the *Drosophila* antennal lobe and its regulation by the Teneurins. eLife *3*, e03726.
48. Dharmaratne, N., Glendining, K.A., Young, T.R., Tran, H., Sawatari, A., and Leamey, C.A. (2012). Ten-m3 is required for the development of topography in the ipsilateral retinocollicular pathway. PLoS ONE *7*, e43083.
49. Harty, B.L., Krishnan, A., Sanchez, N.E., Schiöth, H.B., and Monk, K.R. (2015). Defining the gene repertoire and spatiotemporal expression profiles of adhesion G protein-coupled receptors in zebrafish. BMC Genomics *16*, 62.
50. Lange, M., Norton, W., Coolen, M., Chaminade, M., Merker, S., Proft, F., Schmitt, A., Vernier, P., Lesch, K.P., and Bally-Cuif, L. (2012). The ADHD-susceptibility gene lphn3.1 modulates dopaminergic neuron formation and locomotor activity during zebrafish development. Mol. Psychiatry *17*, 946–954.

Paper 3

Title: A *crystal*-clear zebrafish for *in vivo* imaging

Journal: Scientific Reports

Year: 2016

Authors: Paride Antinucci[1]*, and Robert Hindges[1]*

[1]Centre for Developmental Neurobiology, King's College London, Guy's Campus, London SE1 1UL, UK
*Co-corresponding authors

Citations: 1 (Google Scholar)

Contribution: Design of project and experiments, data collection and analysis, paper writing (primary writer)

PMID: 27381182

DOI: 10.1038/srep29490

This publication contains work presented in Chapter 3 of this thesis.

www.nature.com/scientificreports

SCIENTIFIC REPORTS

OPEN

A *crystal*-clear zebrafish for *in vivo* imaging

Paride Antinucci & Robert Hindges

Received: 11 March 2016
Accepted: 17 June 2016
Published: 06 July 2016

The larval zebrafish (*Danio rerio*) is an excellent vertebrate model for *in vivo* imaging of biological phenomena at subcellular, cellular and systems levels. However, the optical accessibility of highly pigmented tissues, like the eyes, is limited even in this animal model. Typical strategies to improve the transparency of zebrafish larvae require the use of either highly toxic chemical compounds (e.g. 1-phenyl-2-thiourea, PTU) or pigmentation mutant strains (e.g. *casper* mutant). To date none of these strategies produce normally behaving larvae that are transparent in both the body and the eyes. Here we present *crystal*, an optically clear zebrafish mutant obtained by combining different viable mutations affecting skin pigmentation. Compared to the previously described combinatorial mutant *casper*, the *crystal* mutant lacks pigmentation also in the retinal pigment epithelium, therefore enabling optical access to the eyes. Unlike PTU-treated animals, *crystal* larvae are able to perform visually guided behaviours, such as the optomotor response, as efficiently as wild type larvae. To validate the *in vivo* application of *crystal* larvae, we performed whole-brain light-sheet imaging and two-photon calcium imaging of neural activity in the retina. In conclusion, this novel combinatorial pigmentation mutant represents an ideal vertebrate tool for completely unobstructed structural and functional *in vivo* investigations of biological processes, particularly when imaging tissues inside or between the eyes.

In order to understand complex biological phenomena, structural and functional information has to be extracted from intact animal systems at different spatial scales. Optical transparency of animals is a highly desirable feature to study these biological processes *in vivo*. Pigment molecules, such as melanin, haemoglobin and myoglobin, are the main sources of visible light absorption in biological tissues[1,2]. Lipids and collagen, on the other hand, constitute the primary molecules responsible for light scattering. Recently, several tissue clearing techniques have been developed to reduce light scattering in fixed biological tissues by selectively removing lipids in a non-destructive way[3]. However, the only molecules that can be removed from living systems without dramatically impairing their viability are pigment molecules localised in defined tissues, such as melanin present in the skin. Here, we used a combinatorial genetic approach to generate a viable, fully transparent zebrafish mutant, which we name *crystal*, lacking the vast majority of skin pigmentation. Compared to the previously described combinatorial pigmentation mutant *casper* that has pigmented eyes[4], the *crystal* mutant constitutes a significant improvement for *in vivo* imaging of tissues inside or between the eyes.

In zebrafish, multiple populations of cells produce pigments that ultimately restrict the optical accessibility of tissues[5,6]. The three main kinds of pigment cells (or chromatophores) are the melanophores (black appearance), iridophores (silvery or blue) and xanthophores (yellow) (Fig. 1a). In addition to these three populations, which in zebrafish larvae derive from neural crest cells, there is another population of pigment cells forming the retinal pigment epithelium (RPE), which originates from optic lobe neuroepithelial cells (Fig. 1a)[7]. Common strategies to reduce zebrafish skin pigmentation can be grouped in two categories: 1) use of chemical compounds interfering with the synthesis of melanin, the most popular one being 1-phenyl-2-thiourea (PTU)[8]; 2) use of pigmentation mutants in which genes controlling either pigment formation, chromatophore formation or interactions between chromatophores have been inactivated[4,6,9]. The first strategy, despite being straightforward (i.e., embryos can be simply raised in medium containing 200 μM PTU), is associated with toxic side effects that impair morphogenesis, behaviour and survival. For example, PTU has been shown to interfere not only with tyrosinase (the enzyme that catalyses the production of melanin)[10,11], but also with other enzymes, such as thyroid peroxidase[12] and dopamine beta-hydroxylase[13]. Therefore, the poor selectivity of this drug results in severe consequences including reduced thyroid hormone synthesis[14], decreased eye size[12], abnormal cranial neural crest and extraocular muscle development[15], impaired retinal light adaptation[16], as well as anxiety[17] and reduced mobility, hatching and

MRC Centre for Developmental Neurobiology, King's College London, Guy's Campus, London SE1 1UL, UK. Correspondence and requests for materials should be addressed to P.A. (email: paride.antinucci@kcl.ac.uk) or R.H. (email: robert.hindges@kcl.ac.uk)

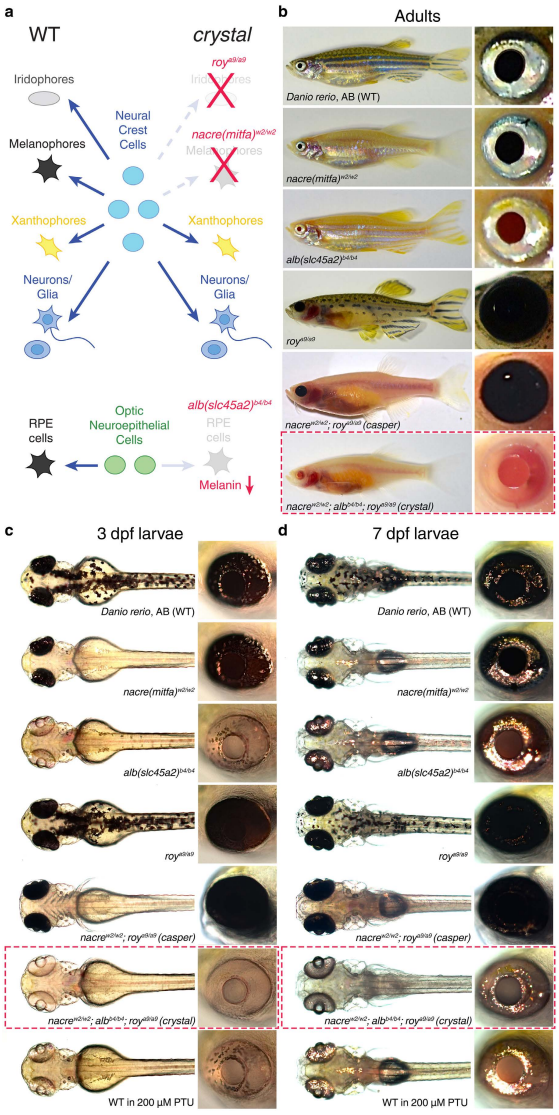

Figure 1. Generation of *crystal*, a fully transparent combinatorial pigmentation mutant. (**a**) Left: schematic diagram of the main populations of pigment cells in wild type (WT) zebrafish. Centre: cell lineages generating the different populations of pigment cells. Right: mutations affecting genes controlling either pigment cell formation ($nacre^{w2/w2}$ and $roy^{a9/a9}$) or melanin production ($alb^{b4/b4}$) used to generate the *crystal* mutant. RPE, retinal pigment epithelium. (**b–d**) Pigmentation phenotypes of wild type, single mutant, *casper* and *crystal* zebrafish at adult (>3 month old, (**b**)), embryonic (3 dpf, (**c**)) and larval (7 dpf, (**d**)) stages. Red dashed boxes indicate *crystal* mutants. Insets on the right display eye pigmentation phenotypes. 3 dpf and 7 dpf zebrafish treated with 200 µM PTU are shown at the bottom of (**c**,**d**). Note that the optical transparency of *crystal* fish is higher than that of wild type, single mutant, *casper* and PTU-treated fish.

survival[8] (see also Results and Discussion). In contrast, the second strategy is considerably less disruptive since it takes advantage of viable mutations affecting the function of genes expressed in specific subsets of cells where they are involved in defined processes of pigment production[5]. Since the formation of each pigment type is controlled independently of the others, the combination of different mutations is required to produce fully transparent zebrafish. This strategy has been previously implemented to generate the double mutant *casper*, which lacks all melanophores and iridophores[4]. Here, we further develop this strategy to generate a fully optically clear combinatorial mutant (*crystal*) that not only lacks all melanophores and iridophores, but also has a non-pigmented RPE. This particular feature makes *crystal* larvae especially suited for imaging tissues inside or between the eyes while avoiding the use of chemical pigmentation blockers. Importantly, *crystal* mutants show no behavioural or viability deficits as compared to wild type animals. We also validate the *in vivo* application of this novel mutant by performing whole-brain light-sheet imaging and two-photon functional recordings of neural activity in the retinae of *crystal* larvae.

Results and Discussion

Generation of *crystal*: a fully transparent zebrafish for *in vivo* imaging. To generate optically clear zebrafish lacking the vast majority of skin pigmentation without using chemical compounds inhibiting pigment formation, we undertook a combinatorial genetic approach. Three previously described viable mutations affecting different populations of chromatophores (Fig. 1a) were selected and combined through crossbreeding (Fig. 1b): 1) the $nacre^{w2/w2}$ mutant lacks all melanophores due to a mutation in the *mitfa* gene[9]. Since the *nacre* mutation does not affect the population of cells forming the RPE, this structure is still pigmented in this single mutant. 2) The *albino* ($alb^{b4/b4}$) mutant is characterised by a general deficiency in the production of melanin due to a mutation in the *slc45a2* gene[18]. 3) The *roy orbison* ($roy^{a9/a9}$) mutant shows a complete lack of iridophores[4]. The gene responsible for this mutant phenotype is currently unknown. The resulting combinatorial triple mutant ($nacre^{w2/w2}$;$alb^{b4/b4}$;$roy^{a9/a9}$; red boxes in Fig. 1b–d), which we name *crystal*, lacks the vast majority of dark and reflective pigments normally present at the cutaneous level and, as a consequence, appears optically clear. The internal organs are clearly visible in adult (>3 months old) *crystal* mutants as opposed to wild type and single mutant fish (Fig. 1b). Compared to the previously described double mutant *casper* ($nacre^{w2/w2}$;$roy^{a9/a9}$)[4], where internal organs are also visible, the triple mutant *crystal* ($nacre^{w2/w2}$;$alb^{b4/b4}$;$roy^{a9/a9}$) lacks melanin in the RPE (Fig. 1b). Consequently, the eyes of *crystal* fish are considerably less pigmented than wild type, single mutant and *casper* fish, therefore resulting easily accessible to optical investigation (see right insets in Fig. 1b–d). The pigmentation phenotype of *crystal* fish is already evident at embryonic (e.g., 3 dpf, Fig. 1c) and larval (e.g., 7 dpf, Fig. 1d) stages. Importantly, the optical clarity of *crystal* larvae is even superior to that of larvae treated with 200 μM PTU (Fig. 1c,d), since PTU inhibits melanin production but does not interfere with iridophore function[8]. Moreover, unlike PTU-treated animals, adult *crystal* mutants are viable and produce normal numbers of offspring. Heterozygous fish ($nacre^{w2/+}$; $alb^{b4/+}$;$roy^{a9/+}$) do not exhibit any visible phenotype (data not shown). Overall, the *crystal* mutant constitutes a significant improvement in the optical accessibility of both larval and adult zebrafish, even superior to the previously described combinatorial mutant *casper*[4], which is characterised by black-pigmented eyes.

***Crystal* zebrafish larvae exhibit normal visual behaviour.** An ideal system for *in vivo* imaging has to be characterised not only by optical clarity but also by normal functional and behavioural viability. The use of PTU to quickly obtain transparent zebrafish larvae is widespread across the research community. However, numerous studies reported severe morphological and behavioural side effects caused by the toxicity of PTU treatment (see Introduction). We thus wanted to compare the behavioural viability of *crystal* larvae to wild type larvae and to larvae raised in medium containing 200 μM PTU. As a representative visually guided behaviour we tested the ability of 5 dpf larvae to perform the optomotor response. During optomotor response assays, freely swimming zebrafish larvae respond to whole-field moving stimuli (e.g., dark and light bars) by swimming in the same direction of stimulus motion (Fig. 2a)[16]. They do so to compensate for the optic flow-induced perception of apparent involuntary displacement, and therefore regain the desired course of locomotion. Individual larvae were tested five times in total and scored according to the number of trials they responded to (i.e., fish turns and swims in the direction of the moving stimulus). Notably, *crystal* larvae exhibited a response rate equivalent to wild type larvae as opposed to PTU-treated larvae, which instead showed a dramatic behavioural impairment (Fig. 2b).

Given the observed behavioural consequences of PTU treatment, we further investigated whether PTU has any effect on zebrafish visual system function. We did so by recording visually induced neural responses in the optic tectum, which in zebrafish is the main retinorecipient brain area. The zebrafish optic tectum receives inputs from all functional types of retinal ganglion cells[19], the sole output neurons of the retina, including ganglion cells tuned to stimulus direction of motion (direction-selective cells) or stimulus orientation (orientation-selective cells)[20]. Using a transgenic fish line where the genetically encoded calcium indicator GCaMP5G is expressed pan-neuronally[21], we analysed visual responses to moving dark and light bars in both the tectal neuropil and periventricular neurons through *in vivo* calcium imaging, as previously described (Fig. 2c and Supplementary Video 1)[22,23]. Compared to untreated *Tg(elavl3:GCaMP5G)* larvae, 4 dpf PTU-treated larvae (treatment from 1 dpf to 3 dpf) showed a large decrease in visual responses with direction- and orientation-selective neural responses being absent or severely impaired, respectively (Fig. 2c). From these data, we conclude that PTU can cause deleterious consequences on both zebrafish behaviour and neural function, and should be therefore avoided whenever these two biological processes are under investigation. Since PTU is a highly non-selective drug (see Introduction) and is generally applied at the whole-animal level, it is difficult to attribute any of the detrimental effects we observed to a specific biochemical pathway.

Whole-brain light-sheet imaging of *crystal* larvae. We next aimed to validate the *in vivo* application of *crystal* larvae by performing whole-brain light-sheet imaging[24]. Light-sheet microscopy has recently

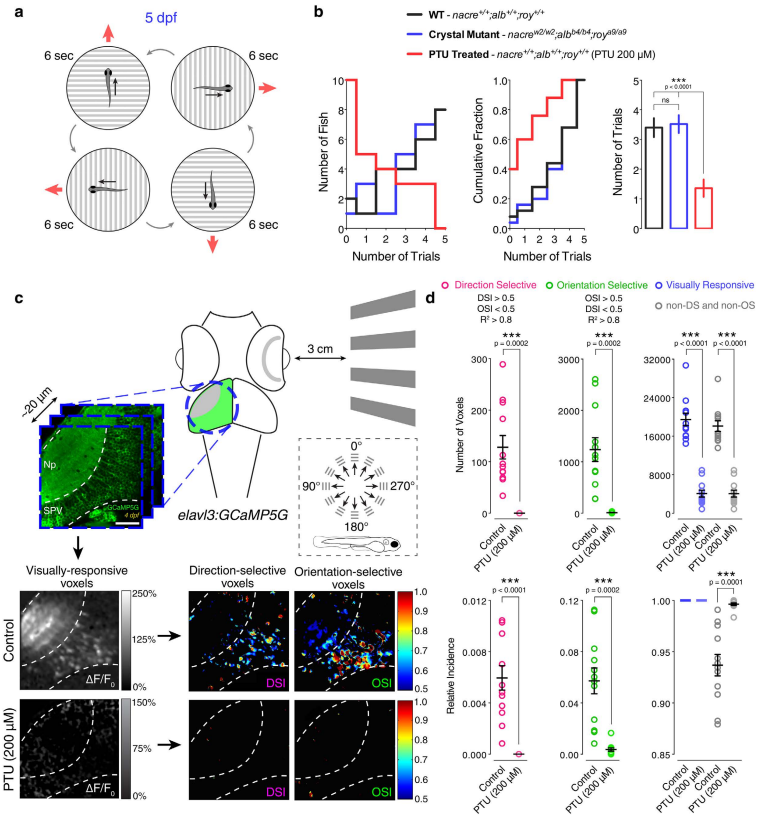

Figure 2. PTU impairs zebrafish behaviour and visual system function. (**a**) Schematic diagram illustrating the optomotor response behavioural assay. Individual 5 dpf larvae were positioned in a petri dish containing Danieau solution. An LCD screen controlled by a computer was used to display black and white square-wave gratings moving in 4 directions (red arrows) at the bottom of the petri dish. Each larva was tested 5 times in total (each trial lasted 6 seconds) and scored according to the trials it responded to (i.e., fish turns and swims in the direction of the moving gratings). (**b**) Quantification of the optomotor response assays for 5 dpf wild type (WT, black), *crystal* (blue) and PTU-treated (red) larvae (n = 25 larvae in each group). The frequency distribution (left), cumulative frequency distribution (centre) and mean ± SEM (right) of number of responsive trials per larva are reported. Note that PTU-treated larvae show a significant decrease in the number of trials they respond to. ns, non-significant; ***$p < 0.001$; one-way ANOVA with post-hoc Tukey's HSD test. (**c**) Functional calcium imaging of tectal cells and retinal ganglion cell axons expressing GCaMP5G (green) in 4 dpf *Tg(elavl3:GCaMP5G)* larvae. Distance of right eye from projection screen is 3 cm. Recordings are performed from 3 Z-planes (approximately 20 µm total volume thickness) in the contralateral optic tectum at 4 Hz image acquisition rate. Dashed box shows the angles of moving bars relative to zebrafish larva orientation. Mean $\Delta F/F_0$ images of calcium recordings in untreated (control) and PTU-treated larvae followed by mapping of direction-selective (DS) and orientation-selective (OS) voxels are displayed. Np, neuropil; SPV, stratum periventriculare; DSI, direction selectivity index; OSI, orientation selectivity index. Scale bar is 40 µm. (**d**) Average number (top) and relative frequency (bottom) of DS, OS, visually responsive and non-DS/non-OS voxels per Z-plane in control and PTU-treated 4 dpf larvae (n = 12 larvae in each group). Criteria used to identify DS and OS voxels are reported at the top. Note the dramatic reduction in visually responsive, DS and OS voxels following 200 µM PTU treatment. Error bars are ± SEM. ***$p < 0.001$, unpaired two-tailed Student's t test.

experienced a series of significant technological advancements and is generally used to study nervous system activity and development with cellular resolution at the whole-animal level[21,25–27]. In typical zebrafish light-sheet

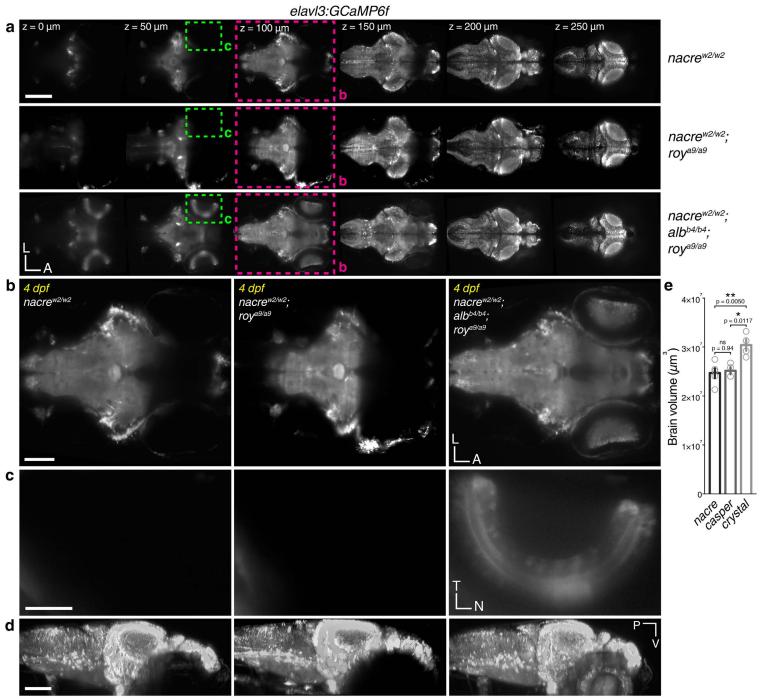

Figure 3. Improved optical accessibility of zebrafish larvae in whole-brain light-sheet imaging using *crystal*. (**a**) Volumetric imaging of the larval zebrafish brain with light-sheet microscopy in 4 dpf *nacre* (top), *casper* (middle) and *crystal* (bottom) *Tg(elavl3:GCaMP6f)* larvae (n = 4–5 larvae in each group). Six different volume sections per larva out of 450 (total xyz volume of 798 × 623 × 283 µm^3) are displayed. L, left; A, anterior. Scale bar is 200 µm. (**b**) Single volume sections of the brain (100 µm Z plane depth) in *nacre* (left), *casper* (middle) and *crystal* (right) larvae. Note the dark region between the eyes of *nacre* and *casper* larvae due to the excitation light being absorbed or reflected by pigments present on the surface of the eyes. L, left; A, anterior. Scale bar is 100 µm. (**c**) Insets showing the labelling of amacrine and ganglion cells in the left retina of the *crystal* larva (right) compared to *nacre* (left) and *casper* (middle) larvae, where no GCaMP6f fluorescence is detected in the eyes. T, temporal; N, nasal. Scale bar is 50 µm. (**d**) 3D reconstructions of the brain (lateral view) of *nacre* (left), *casper* (middle) and *crystal* (right) *Tg(elavl3:GCaMP6f)* larvae shown in (**a**). Note the improved optical accessibility (~18% of brain volume) allowed by *crystal*. P, posterior; V, ventral. Scale bar is 100 µm. (**e**) Average imaged brain volume in *nacre*, *casper* and *crystal* 4 dpf *Tg(elavl3:GCaMP6f)* larvae. Error bars are ± SEM. ns, non-significant; *p < 0.05; **p < 0.01; one-way ANOVA with post-hoc Tukey's HSD test.

preparations, the excitation light is provided laterally and fluorophore emission light is collected through an objective positioned orthogonally to the illumination plane. However, due to the strong pigmentation of the eyes, imaging of areas inside or between these structures is normally problematic. We therefore compared the optical accessibility of the nervous system between *crystal, nacre* and *casper* larvae at 4 dpf using the pan-neuronal *Tg(elavl3:GCaMP6f)* line[28] (Fig. 3a and Supplementary Video 2). In our setup, the sheet of laser light (488 nm) is generated by two objectives positioned on the lateral sides of the larva. In *crystal* larvae, the excitation light can easily reach deep (i.e., ventral) regions of the brain (Fig. 3b) as well as the retinae (Fig. 3c) without being absorbed or reflected by pigments normally present on the surface of the eyes, like in *nacre* or *casper* larvae (note the dark regions in the left and middle panels of Fig. 3b,c). Therefore, *crystal* allows a fully unobstructed optical access of the larval zebrafish brain in its entirety (i.e., including the eyes), as opposed to *nacre* and *casper* mutants where a substantial portion of the nervous system (~18%) is not accessible through standard light-sheet imaging (Fig. 3a,d,e; mean volume ± SEM, *crystal* 3.04 ± 0.12 × 10^7 µm^3, n = 4; *casper* 2.51 ± 0.07 × 10^7 µm^3, n = 4; *nacre* 2.47 ± 0.10 × 10^7 µm^3, n = 5; p = 0.0040, $F_{2,10} = 10.09$, one-way ANOVA with post-hoc Tukey's HSD test). Even though the optical accessibility of crystal larvae through light-sheet imaging is significantly higher than *nacre* and *casper* mutants, it is noteworthy that the spatial definition of brain regions between the eyes appears lower than

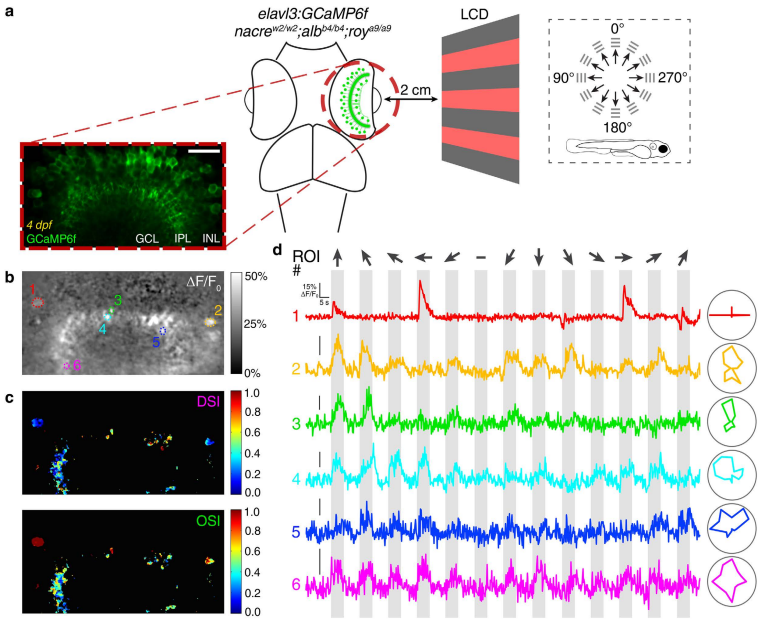

Figure 4. Calcium imaging of visually evoked neural activity in the retina using *crystal*. (**a**) Two-photon functional calcium imaging of amacrine cells and ganglion cell dendrites expressing GCaMP6f (green) in 4 dpf *crystal Tg(elavl3:GCaMP6f)* larvae (n = 8 larvae). Distance of the eye from LCD screen is 2 cm. Recordings are performed from 2–4 Z-planes (approximately 20 μm total volume thickness) at 4 Hz image acquisition rate. Dashed box shows the angles of moving gratings relative to zebrafish larva orientation. INL, inner nuclear layer; GCL, ganglion cell layer; IPL, inner plexiform layer. Scale bar is 20 μm. (**b,c**) Mean $\Delta F/F_0$ image of a representative calcium recording (**b**) followed by voxel-wise analysis of direction and orientation selectivity of visual responses (**c**). DSI, direction selectivity index; OSI, orientation selectivity index. (**d**) $\Delta F/F_0$ calcium traces during a representative tuning experiment from the 6 selected regions of interest (ROIs) shown in (**b**). Polar plots showing the tuning profiles (i.e., integral $\Delta F/F_0$ responses to different stimuli) of individual ROIs are reported on the right. Stimulus epochs are shown in grey. Dark arrows indicate the different directions of gratings motion. The blank-screen null condition is indicated by a '–' sign.

other regions of the brain, likely due to scattering of excitation light by the lenses. Despite this fact, the light-sheet signal detected from these regions in *crystal* mutants is still many-fold higher than in the other animal groups (Fig. 3a,b).

Two-photon calcium imaging in the intact retina using *crystal*. To further assess the *in vivo* application of *crystal* larvae we performed two-photon functional imaging of neural activity in the retina (Fig. 4a), a brain region that is not optically accessible in wild type, single pigmentation mutant or *casper* larvae (Fig. 1) unless embryos are raised in medium containing PTU[29,30]. The retina is a sensory neural circuit formed by multiple classes of excitatory cells (photoreceptors, bipolar and ganglion cells) and inhibitory cells (horizontal and amacrine cells)[31]. Its primary function is to detect and process light stimuli and, subsequently, send the processed visual information to higher brain areas through different types of functionally specialised ganglion cells[32]. To record visual responses in the larval retina through calcium imaging, 4 dpf *Tg(elavl3:GCaMP6f) crystal* larvae were immobilised in 2% low melting point agarose with one eye facing an LCD screen where square-wave gratings moving in 12 different directions were displayed (n = 8 larvae). Visually evoked calcium transients were recorded from amacrine and ganglion cells at 4 Hz using near-infrared (930 nm) two-photon laser excitation (Supplementary Video 3). Voxel-wise analysis was then used to identify visually responsive voxels (Fig. 4b) and quantify direction and orientation selectivity of visual responses at subcellular resolution (0.248 × 0.248 μm voxel XY size, Fig. 4c) as previously described[22,33]. $\Delta F/F_0$ calcium traces from 6 selected regions of interest (ROIs, Fig. 4b) are displayed as examples (Fig. 4d). Interestingly, not only we could record stimulus-locked responses, but also we observed the presence of direction-selective (direction selectivity index (DSI) > 0.5, ROI# 4 and 5) and orientation-selective (orientation selectivity index (OSI) > 0.5, ROI# 1–3) responses (Fig. 4c,d), indicating that

the retina is functional in *crystal* larvae. A previous study has reported that adult zebrafish mutants with hypopigmented eyes show deficits in performing visual escape assays under defined luminance conditions[34]. Thus, even though our visual behaviour assays demonstrated that *crystal* larvae perform the optomotor response as well as wild type larvae (Fig. 2a,b), we cannot exclude that *crystal* mutants might show abnormal retinal responses under certain luminance conditions. However, given the deleterious effects caused by PTU treatment (Fig. 2c,d; see Introduction), the *crystal* mutant represents, to the best of our knowledge, the most viable strategy to perform *in vivo* functional imaging in the intact retina of larval zebrafish.

Conclusions

In this study, we generated a viable, optically transparent combinatorial pigmentation mutant zebrafish, named *crystal*, which constitutes an ideal tool for completely unobstructed *in vivo* imaging of biological phenomena. More specifically, compared to *casper* mutants[4], *crystal* fish are superior in terms of optical transparency when imaging inside or between the eyes. We validated the viability and *in vivo* application of *crystal* larvae through the optomotor response assay, whole-brain light-sheet imaging and two-photon functional imaging of neural activity in the intact retina. Importantly, *crystal* larvae show a higher viability than larvae treated with the chemical pigmentation blocker PTU. We envisage that *crystal* will be an invaluable tool for other *in vivo* applications, such as one-photon[21] or two-photon[27] volumetric calcium imaging of neural activity across the entire brain in semi-restrained behaving[35] or paralysed fictively swimming[36] zebrafish larvae, as well as to study the wiring, function and plasticity of neural circuits in normally highly pigmented, optically inaccessible structures like the eyes[30,37,38].

Methods

Animals. Zebrafish were maintained at 28.5 °C on a 14 hr ON/10 hr OFF light cycle in Danieau solution [58 mM NaCl, 0.7 mM KCl, 0.4 mM $MgSO_4$, 0.6 mM $Ca(NO_3)_2$ 5.0 mM HEPES, pH 7.6]. The combinatorial *crystal* mutant (*alb*$^{b4/b4}$;*nacre*$^{w2/w2}$;*roy*$^{a9/a9}$) was generated by sequentially crossbreeding three different single mutant strains, namely *nacre*$^{w2/w2}$ (ref. 9), *roy*$^{a9/a9}$ (ref. 4) and *alb*$^{b4/b4}$ (ref. 18) mutants. Importantly, both larvae and adult *crystal* zebrafish are viable and do not display visible morphological, functional or behavioural abnormalities other than the pigmentation phenotype. The *casper* mutant was obtained by crossing *nacre*$^{w2/w2}$ and *roy*$^{a9/a9}$ mutants, as previously described[4]. The *AB* line was used to obtain wild type zebrafish. Transgenic lines used in this study include *Tg(elavl3:GCaMP5G)*[21] and *Tg(elavl3:GCaMP6f)*[28]. Confocal functional imaging experiments were performed in the *nacre* mutant. Light-sheet imaging experiments were performed in *nacre*, *casper* and *crystal* mutants. Two-photon functional imaging experiments were performed in *crystal* larvae. To treat zebrafish larvae with PTU we followed standard procedures[8], specifically larvae were raised in 200 μM PTU (Sigma) in Danieau solution from 24 hours post fertilisation (hpf). *Tg(elavl3:GCaMP5G)* larvae used for confocal functional imaging of visually evoked neural activity in the optic tectum were treated with 200 μM PTU from 24 hpf to 3 dpf and imaged at 4 dpf. This work was approved by the local Animal Welfare and Ethical Review Body (King's College London), and was carried out in accordance with the *Animals (Scientific Procedures) Act 1986*, under license from the United Kingdom Home Office (PPL70/8057).

Imaging. *Whole-animal in vivo microscopy.* Whole-animal images of adult zebrafish were taken with a Nikon D7000 digital SLR camera equipped with a Sigma 150 mm macro lens. Adult zebrafish were anesthetized with 0.2% tricaine (MS222, Sigma) in fish facility water and placed in a 90 mm petri dish containing fish facility water. Imaging of larvae was performed using a ZEISS Axioskop microscope connected to EXi Blue CCD cameras (Retiga) and Volocity acquisition software (PerkinElmer). Larval zebrafish were anesthetized with 0.02% tricaine in Danieau solution and immobilized in 1% low melting point agarose (Sigma) on glass slides.

Confocal calcium imaging. Imaging was performed using a ZEISS LSM 710 confocal microscope equipped with a spectral detection scan head and a 20X/1.0 NA water-immersion objective (Carl Zeiss). Functional time-series of visually evoked calcium responses in retinal ganglion cells (RGCs) were acquired at a rate of 4.1 Hz and 0.415×0.415 μm resolution (256×256 pixels), and 1 AU pinhole aperture. Excitation light was provided by a 488 nm multi-line laser. Non-anaesthetised *Tg(elavl3:GCaMP5G)* larvae were immobilized in 2% low melting point agarose (Sigma) prepared in Danieau solution and mounted dorsal side up on a raised glass platform that was placed in a custom-made Danieau-filled chamber. The agarose was sufficient to restrain the larvae so that anaesthesia was not required. Imaging was performed in the afternoon (1–8 pm).

Light-sheet imaging. Whole-brain light-sheet imaging was performed using a ZEISS Lightsheet Z.1 microscope equipped with two 10X/0.2 NA illumination objectives and one 20X/1.0 NA water-immersion detection objective (Carl Zeiss). 488 nm laser excitation light was used to elicit GCaMP6f fluorescence and a 505–545 BP filter was used for emitted light detection. The pivot scanner (Carl Zeiss) was used to deliver homogeneous illumination and, therefore, avoid shadows along the illumination axis. The thickness of the light sheet was 5.39 μm at the centre and 10.8 μm at the edges of the field of view. Exposure time was 29.97 ms. The size of volumetric images was $623 \times 798 \times 283\ \mu m^3$ ($1500 \times 1920 \times 490$ pixels) with a resolution of $0.415 \times 0.415 \times 0.631$ μm. 4 dpf *nacre*, *casper* and *crystal Tg(elavl3:GCaMP6f)* larvae were first paralysed for 10–15 minutes in α-bungarotoxin (1 mg/ml; Biotium) prepared in Danieau solution. Subsequently, larvae were immobilized in 2% low melting point agarose (Sigma) and placed inside a glass capillary (20 μl volume, 701904; Brand). We subsequently extruded the section of the agarose cylinder containing the head of the larva from the capillary, and oriented the larvae so that the dorsal side of the head was facing the detection objective and the eyes were facing the two illumination objectives. Whole-brain light-sheet imaging of *casper* mutant larvae was performed using a custom-made

light-sheet microscope built by Dr Martin Meyer (King's College London) and equipped with a 20X/1.0 NA water-immersion XLUMPlanFLN detection objective (Olympus).

Two-photon calcium imaging. Two-photon functional imaging in the retina was performed using a Nikon A1R MP microscope equipped with a 4-channel GaAsP NDD and an Apochromat 25X/1.1 NA water-immersion objective (Nikon). Excitation was provided by a Chameleon Ultra II Mode-locked titanium-sapphire laser (Coherent) tuned to 930 nm. Time-series of visually evoked calcium responses were acquired at a rate of 4 Hz and $0.248 \times 0.248\,\mu m$ resolution (512×256 pixels). Following activation of the laser scanning, we waited 60 seconds before starting the visual stimulation to ensure the retina adapted to the background light level caused by the multi-photon laser. 4 dpf *crystal Tg(elavl3:GCaMP6f)* larvae were first paralysed for 10–15 minutes in α-bungarotoxin (1 mg/ml; Biotium) prepared in Danieau solution. Subsequently, larvae were immobilized in 2% low melting point agarose (Sigma) and mounted on a raised custom-made glass platform with the dorsal side up (45° angle tilt) and one eye facing an LCD screen (see Visual stimulation) that was placed underneath a custom-made Danieau-filled chamber. Imaging was performed in the afternoon (1–8 pm).

Visual stimulation. *Moving bars in confocal preparation.* Moving bars stimuli were generated as previously described[22,33]. A diffusion filter (3026, Rosco) was bonded to one side of the chamber to serve as a projection screen. The agarose in front of the eye facing the projection screen was removed, allowing an unobstructed view of the projected image on the side of the chamber. Larvae were positioned 3 cm away from the screen and the projected image filled a visual field of ~97° × 63°. Visual stimuli consisted of light (56 cd/m^2) or dark bars (8 cd/m^2) (175% and 25% of mean luminance, respectively) on a mean grey background (32 cd/m^2). As no qualitative differences between light and dark bars were noted, data obtained using the two stimuli were combined. Each bar was 10° in width moving at a speed of 20°/s and separated from the preceding bar by 30°, enabling more than one bar on the screen at any one time. The long axes of the bars were orthogonal to the direction of motion. Each of the 12 directions of motion was presented once (3 seconds) in a pseudo-random order unique to each slice in every animal imaged. Each inter-epoch interval was 10 seconds to enable GCaMP5G signals to return to baseline. A blank-screen null condition of 2 seconds was also interleaved. Visual experiments were generated and controlled using custom-written Labview and MATLAB code (MathWorks), implemented on a ViSaGe stimulus presenter (Cambridge Research Systems) and delivered via a DLP Pico Projector (Optoma).

Moving gratings in two-photon preparation. Moving gratings stimuli in the two-photon preparation were generated and controlled using PsychoPy[39], and delivered through an LCD screen (SKD5VA-3, GoodWell Technology) positioned underneath a custom-made Perspex chamber. A long-pass red glass filter (FGL610, Thorlabs) was positioned between the LCD screen and the chamber to allow for simultaneous imaging and visual stimulation. Larvae were positioned 2 cm away from the screen and the image on the LCD screen filled a visual field of ~140° × 100° (mean background luminance 30.4 cd/m^2). Visual stimuli consisted of square-wave gratings (100% contrast, spatial frequency 1.66 cycles/cm, temporal frequency 1 cycles/s). Each grating bar was 8.5° in width and the long axes of the bars were orthogonal to the direction of motion. Each of the 12 directions of motion was presented once (6 seconds) with and inter-epoch interval of 10 seconds to enable GCaMP6f signals to return to baseline. A blank-screen null condition of 6 seconds was also interleaved. TTL triggers (0-5-0 Volts) to record epoch time events where generated through a LabJack USB DAQ device (U3-LV, LabJack Corporation). Following activation of the laser scanning, we waited 60 seconds before starting the visual stimulation to ensure the retina adapted to the background light level caused by the multi-photon laser.

Optomotor response assay. Individual 5 dpf larvae were positioned in a 35 mm petri dish containing Danieau solution. The LCD screen of an iPhone 5 (Apple) controlled by a MacBook Pro (Apple) through Duet Display (Kairos Technologies) was used to display black and white square-wave gratings (85% contrast, spatial frequency 0.33 cycles/mm, temporal frequency 3.5 cycles/s) moving in 4 directions (90° angular distance) at the bottom of the petri dish. Visual stimuli were generated in Keynote (Apple). Each larva was tested 5 times in total (each trial lasted 6 s followed by 10 s of static gratings) and scored according to the trials it responded to (i.e., fish turns and swims in the direction of the moving gratings). The behaviour of larvae was visually monitored using an M165 FC stereomicroscope (Leica).

Analysis. *Functional Analyses.* *In vivo* calcium imaging data were analysed as previously described[22,33]. In summary, functional time-series were processed before analysis as follows: time-series images from each experiment were corrected for motion with a rigid-body algorithm (SPM12; http://www.fil.ion.ucl.ac.uk/spm/), median filtered with a kernel size of 1 voxel to remove dark and shot noise, and spatially smoothed with a 2D Gaussian kernel = 2 voxels to improve signal-to-noise. A baseline (B) that corrects for low-frequency drifts was determined using a cubic-spline algorithm extrapolating between knots averaged from 5 s of the inter-epoch interval data. Both relative signal intensity changes ($\Delta F = F\text{-}B$; where F = raw fluorescence) and normalised signal intensity changes [$\%\Delta F/F_0 = (F\text{-}B)/B$] were calculated at each voxel. ΔF was used for population functional data (voxel-wise analysis), whereas $\%\Delta F/F_0$ was used for manually defined regions of interest (ROIs). For each voxel or ROI the integral response over the epoch-interval was calculated to provide a single response metric of each presented direction of stimulus motion. The integral within each epoch window is a summary metric more resistant to saturation effects of the calcium probe than maximum signal change. A threshold for each voxel within an acquisition image sequence was determined from the variance of ΔF changes during the inter-epoch intervals and null condition, threshold = 5 × SDs. All voxels that were supra-threshold within at least two visual presentation epochs were regarded as visually responsive and subjected to further characterization.

To analyse the direction and orientation selectivity of visually responsive voxels direction- and orientation-selective indices (DSI and OSI)[40], based on fitted von-Mises or Gaussian profiles[41], were calculated together with an estimate for their goodness of fit, R^2. The DSI was defined as $(R_{pref}-R_{null})/(R_{pref}+R_{null})$, where R_{pref}, the response to the preferred direction, was the integral response over the preferred direction epoch-interval. R_{null} was similarly calculated as the integral response evoked by the direction opposite to the preferred direction. The OSI was defined as $(R_{pref}-R_{orth})/(R_{pref}+R_{orth})$, where R_{pref}, the response to the preferred orientation, was the integral response over the preferred orientation epoch-interval. R_{orth} was similarly calculated as the integral response evoked by the orthogonal orientation. To minimize cross talk and over-fitting associated with DSI and OSI metrics, a stringent approach was undertaken. For a voxel to be regarded as direction-selective (DS) or orientation-selective (OS), mutually exclusive criteria were used: DS if DSI >0.5 and OSI <0.5; and OS if OSI >0.5 and DSI <0.5. In both cases, the goodness of fit (R_2) for DSI and OSI, respectively, had to be >0.8; thus, the fitted curves explained at least 80% of the integral responses. A single von-Mises distribution was used to fit responses of DS voxels and estimate their preferred direction of motion angle from the centre of the fitted curve. The sum of two von-Mises (180° angular distance apart) was used to fit responses of OS voxels and estimate their preferred orientation of motion angles from the centres of the fitted curves. Circular variance was also calculated for comparison as an alternative metric of orientation selectivity (Circular variance <0.4)[41].

Morphological Analyses. To determine the brain volume imaged in 4 dpf *nacre*, *casper* and *crystal Tg(elavl3:GCaMP6f)* larvae, we calculated the number of $GCaMP6f^{+}$ voxels in each volumetric image by applying the adjust>threshold function followed by the analyse>histogram>list command in ImageJ[42]. Subsequently, the obtained values were multiplied by the volume of a single voxel ($0.415\times0.415\times0.631\,\mu m^3=1.086\times10^{-1}\,\mu m^3$).

Statistical Analyses. Statistical test results are reported in Figures and Figure legends. Statistical analyses and tests were carried out using Prism 6 (GraphPad) or MATLAB R2014b (MathWorks). Before performing statistical tests, descriptive statistics (e.g., normality tests to see whether values come from a Gaussian distribution or F-test to compare variances) were used to choose the appropriate statistical test (reported in Figure legends together with test results). The criterion for statistical significance was set at $p<0.05$.

References

1. Jacques, S. L. Optical properties of biological tissues: a review. *Phys Med Biol* **58,** R37–R61 (2013).
2. Pawley, J. B. *Handbook of biological confocal microscopy*. (Springer, 2005).
3. Richardson, D. S. & Lichtman, J. W. Clarifying Tissue Clearing. *Cell* **162,** 246–257 (2015).
4. White, R. M. *et al.* Transparent adult zebrafish as a tool for *in vivo* transplantation analysis. *Cell Stem Cell* **2,** 183–189 (2008).
5. Singh, A. P. & Nusslein-Volhard, C. Zebrafish stripes as a model for vertebrate colour pattern formation. *Curr Biol* **25,** R81–R92 (2015).
6. Kelsh, R. N. *et al.* Zebrafish pigmentation mutations and the processes of neural crest development. *Development* **123,** 369–389 (1996).
7. Bharti, K., Nguyen, M. T., Skuntz, S., Bertuzzi, S. & Arnheiter, H. The other pigment cell: specification and development of the pigmented epithelium of the vertebrate eye. *Pigment Cell Res* **19,** 380–394 (2006).
8. Karlsson, J., von Hofsten, J. & Olsson, P. E. Generating transparent zebrafish: a refined method to improve detection of gene expression during embryonic development. *Mar Biotechnol* (*NY*) **3,** 522–527 (2001).
9. Lister, J. A., Robertson, C. P., Lepage, T., Johnson, S. L. & Raible, D. W. Nacre encodes a zebrafish microphthalmia-related protein that regulates neural-crest-derived pigment cell fate. *Development* **126,** 3757–3767 (1999).
10. Whittaker, J. R. An analysis of melanogenesis in differentiating pigment cells of ascidian embryos. *Dev Biol* **14,** 1–39 (1966).
11. Ryazanova, A. D., Alekseev, A. A. & Slepneva, I. A. The phenylthiourea is a competitive inhibitor of the enzymatic oxidation of DOPA by phenoloxidase. *J Enzyme Inhib Med Chem* **27,** 78–83 (2012).
12. Li, Z. *et al.* Phenylthiourea specifically reduces zebrafish eye size. *PLoS One* **7,** e40132 (2012).
13. Johnson, G. A., Boukma, S. J. & Kim, E. G. *In vivo* inhibition of dopamine beta-hydroxylase by 1-phenyl-3-(2-thiazolyl)-2-thiourea (U-14,624). *J Pharmacol Exp Ther* **171,** 80–87 (1970).
14. Elsalini, O. A. & Rohr, K. B. Phenylthiourea disrupts thyroid function in developing zebrafish. *Dev Genes Evol* **212,** 593–598 (2003).
15. Bohnsack, B. L., Gallina, D. & Kahana, A. Phenothiourea sensitizes zebrafish cranial neural crest and extraocular muscle development to changes in retinoic acid and IGF signaling. *PLoS One* **6,** e22991 (2011).
16. Orger, M. B. *et al.* Behavioral screening assays in zebrafish. *Methods Cell Biol* **77,** 53–68 (2004).
17. Parker, M. O., Brock, A. J., Millington, M. E. & Brennan, C. H. Behavioural phenotyping of casper mutant and 1-pheny-2-thiourea treated adult zebrafish. *Zebrafish* **10,** 466–471 (2013).
18. Streisinger, G., Singer, F., Walker, C., Knauber, D. & Dower, N. Segregation analyses and gene-centromere distances in zebrafish. *Genetics* **112,** 311–319 (1986).
19. Robles, E., Laurell, E. & Baier, H. The retinal projectome reveals brain-area-specific visual representations generated by ganglion cell diversity. *Curr Biol* **24,** 2085–2096 (2014).
20. Nikolaou, N. *et al.* Parametric functional maps of visual inputs to the tectum. *Neuron* **76,** 317–324 (2012).
21. Ahrens, M. B., Orger, M. B., Robson, D. N., Li, J. M. & Keller, P. J. Whole-brain functional imaging at cellular resolution using light-sheet microscopy. *Nat Methods* **10,** 413–420 (2013).
22. Antinucci, P., Nikolaou, N., Meyer, M. P. & Hindges, R. Teneurin-3 specifies morphological and functional connectivity of retinal ganglion cells in the vertebrate visual system. *Cell Rep* **5,** 582–592 (2013).
23. Nikolaou, N. & Meyer, M. P. Lamination Speeds the Functional Development of Visual Circuits. *Neuron* **88,** 999–1013 (2015).
24. Keller, P. J. & Ahrens, M. B. Visualizing whole-brain activity and development at the single-cell level using light-sheet microscopy. *Neuron* **85,** 462–483 (2015).
25. Tomer, R. *et al.* SPED Light Sheet Microscopy: Fast Mapping of Biological System Structure and Function. *Cell* **163,** 1796–1806 (2015).
26. Chhetri, R. K., Amat, F., Wan, Y., Hockendorf, B. & Lemon, W. C. Whole-animal functional and developmental imaging with isotropic spatial resolution. *Nat Methods* **12,** 1171–1178 (2015).
27. Wolf, S. *et al.* Whole-brain functional imaging with two-photon light-sheet microscopy. *Nat Methods* **12,** 379–380 (2015).
28. Dunn, T. W. *et al.* Brain-wide mapping of neural activity controlling zebrafish exploratory locomotion. *Elife* **5** (2016).
29. Odermatt, B., Nikolaev, A. & Lagnado, L. Encoding of luminance and contrast by linear and nonlinear synapses in the retina. *Neuron* **73,** 758–773 (2012).

30. Nikolaev, A., Leung, K. M., Odermatt, B. & Lagnado, L. Synaptic mechanisms of adaptation and sensitization in the retina. *Nat Neurosci* **16,** 934–941 (2013).
31. Masland, R. H. The neuronal organization of the retina. *Neuron* **76,** 266–280 (2012).
32. Baden, T. *et al.* The functional diversity of retinal ganglion cells in the mouse. *Nature* **529,** 345–350 (2016).
33. Lowe, A. S., Nikolaou, N., Hunter, P. R., Thompson, I. D. & Meyer, M. P. A systems-based dissection of retinal inputs to the zebrafish tectum reveals different rules for different functional classes during development. *J Neurosci* **33,** 13946–13956 (2013).
34. Ren, J. Q., McCarthy, W. R., Zhang, H., Adolph, A. R. & Li, L. Behavioral visual responses of wild-type and hypopigmented zebrafish. *Vision Res* **42,** 293–299 (2002).
35. Bianco, I. H. & Engert, F. Visuomotor transformations underlying hunting behavior in zebrafish. *Curr Biol* **25,** 831–846 (2015).
36. Vladimirov, N. *et al.* Light-sheet functional imaging in fictively behaving zebrafish. *Nat Methods* **11,** 883–884 (2014).
37. Randlett, O. *et al.* Cellular requirements for building a retinal neuropil. *Cell Rep* **3,** 282–290 (2013).
38. Antinucci, P., Suleyman, O., Monfries, C. & Hindges, R. Neural mechanisms generating orientation selectivity in the retina. *Current Biology*, http://dx.doi.org/10.1016/j.cub.2016.05.035 (2016).
39. Peirce, J. W. Generating Stimuli for Neuroscience Using PsychoPy. *Front Neuroinform* **2,** 10 (2008).
40. Niell, C. M. & Stryker, M. P. Highly selective receptive fields in mouse visual cortex. *J Neurosci* **28,** 7520–7536 (2008).
41. Swindale, N. V. Orientation tuning curves: empirical description and estimation of parameters. *Biol Cybern* **78,** 45–56 (1998).
42. Schneider, C. A., Rasband, W. S. & Eliceiri, K. W. NIH Image to ImageJ: 25 years of image analysis. *Nat Methods* **9,** 671–675 (2012).

Acknowledgements
We would like to thank Andrew Lowe for analysis tools, Vladimir Grigoriev for providing the Nikon D7000 digital SLR camera, and Martin Meyer for providing zebrafish transgenic lines, the custom-made light-sheet microscope and comments on the manuscript. We are grateful to ZEISS (Ben Ewins) for providing the Lightsheet Z.1 microscope. We thank the Nikon Imaging Centre at King's College London for additional support and instrumentation. This work was supported by the Biotechnology and Biological Sciences Research Council (BB/M000664/1 to R.H.) and by the Medical Research Council (1413592 to P.A.).

Author Contributions
P.A. and R.H. designed the study. P.A. performed the experiments and analysed the data. P.A. and R.H. wrote the manuscript.

Additional Information
Supplementary information accompanies this paper at http://www.nature.com/srep

Competing financial interests: The authors declare no competing financial interests.

How to cite this article: Antinucci, P. and Hindges, R. A *crystal*-clear zebrafish for *in vivo* imaging. *Sci. Rep.* **6**, 29490; doi: 10.1038/srep29490 (2016).

Paper 4

Title: Orientation Selectivity in the Retina: ON Cell Types and Mechanisms (*Review*)

Journal: Journal of Neuroscience

Year: 2016

Authors: Paride Antinucci[1]*, Fatima Abbas[1], and Paul R. Hunter[1]*

[1]Centre for Developmental Neurobiology, King's College London, Guy's Campus, London SE1 1UL, UK
*Co-corresponding authors

Citations: 0 (Google Scholar)

Contribution: Critical paper review, and paper writing

PMID: 27488626

DOI: 10.1523/JNEUROSCI.1527-16.2016

8064 • The Journal of Neuroscience, August 3, 2016 • 36(31):8064 – 8066

Journal Club

Editor's Note: These short, critical reviews of recent papers in the *Journal*, written exclusively by graduate students or postdoctoral fellows, are intended to summarize the important findings of the paper and provide additional insight and commentary. For more information on the format and purpose of the Journal Club, please see http://www.jneurosci.org/misc/ifa_features.shtml.

Orientation Selectivity in the Retina: ON Cell Types and Mechanisms

Paride Antinucci, Fatima Abbas, and Paul R. Hunter
Centre for Developmental Neurobiology, King's College London, Guy's Campus, London SE1 1UL, United Kingdom
Review of Nath and Schwartz and of Venkataramani and Taylor

Orientation selectivity was first described in cat primary visual cortex by Hubel and Wiesel (1962) as the selectivity of neuronal firing for elongated visual stimuli oriented along a specific axis. Shortly afterward, Levick (1967) identified orientation-selective ganglion cells (OSGCs) in the rabbit retina, suggesting that orientation-specific information is already evident in the output neurons of the retina. Since then, orientation-selective cells have been described in many vertebrate and invertebrate visual systems, including primates (Hubel and Wiesel, 1968), rodents (Niell and Stryker, 2008), fish (Nikolaou et al., 2012), and insects (Fisher et al., 2015). Notably, orientation selectivity has also been characterized even earlier in visual processing, in amacrine cells (Bloomfield, 1994; Murphy-Baum and Taylor, 2015), a class of inhibitory retinal neurons modulating ganglion cell responses. In addition to their preferred angular selectivity, orientation-selective cells are classified by their luminance polarity. For example, OFF-OSGCs have been described in the rabbit retina due to their response preference for dark (negative contrast, or "OFF") stimuli and suppression by light (positive contrast, or "ON") stimuli (Venkataramani and Taylor, 2010).

Providing a mechanistic understanding of the circuitry that generates neuronal feature selectivity is a core goal for visual neuroscientists. Such focus has provided an exquisitely detailed picture of the circuit and synaptic mechanisms generating direction selectivity (selectivity to motion of a stimulus in a particular direction) in the mouse retina and fly optic lobe (for review, see Borst and Helmstaedter, 2015). By comparison, our understanding of the mechanisms generating orientation selectivity in the retina is still rudimentary, largely due to the lack of specific molecular markers. Additionally, there is a drive to characterize the diversity of ganglion cell types, or feature channels, based on their functional, morphological, and genetic profiles (Baden et al., 2016). To date, how many OSGC types are present in the retina and how evolutionarily conserved they are across species remains unclear.

To start addressing these gaps in our understanding, two publications in *The Journal of Neuroscience* have undertaken large-scale single-cell analyses to examine the electrophysiological, morphological, and pharmacological signatures of newly identified ON-OSGCs in mouse (Nath and Schwartz, 2016) and rabbit (Venkataramani and Taylor, 2016) retinae. In particular, the ON-OSGCs characterized by the authors fall into the following two morphologically and physiologically distinct categories: cells tuned to horizontally oriented bars (found in both mouse and rabbit retinae); and cells tuned to vertically oriented bars (observed in mouse only). A summary of these results is presented in Figure 1.

One property that might underlie ganglion cell receptive field properties is dendritic morphology, including stratification and spatial organization within the inner plexiform layer (IPL). For example, the alignment of dendrites along a preferred direction has a role in generating direction selectivity in some ganglion cells (Kim et al., 2008). To describe the dendritic morphology of ON-OSGCs and assess its potential role in generating orientation tuning, Nath and Schwartz (2016) and Venkataramani and Taylor (2016) filled functionally identified ON-OSGCs with fluorescent dyes. In the mouse, the dendrites of both vertical and horizontal ON-OSGCs stratified in both the ON and OFF IPL layers, while in the rabbit, the dendrites of horizontal ON-OSGCs stratified exclusively in the ON layer (Fig. 1*A*). The seemingly functionally irrelevant wiring in the OFF layer of mouse ON-OSGCs suggests an unexplored complexity in the receptive field properties of these cells. Strikingly, both research groups found that horizontal ON-OSGCs cells have elongated dendritic arbors oriented according to their stimulus orientation selectivity (i.e., horizontally oriented). Although this morphological bias could contribute to the tuning of horizontal ON-OSGCs, the extent to which this feature is necessary to generate orientation selectivity is unclear, because no significant bias was detected for vertically tuned cells.

Received May 10, 2016; revised June 16, 2016; accepted June 21, 2016.
This work was supported by a King's College London Health Schools PhD studentship sponsored by Medical Research Council Grant 1413592 (P.A.), and a Biotechnology and Biological Sciences Research Council project grant BB/L004992/1 (P.R.H.). We thank Drs. Martin Meyer and Federico Grillo for helpful discussions and critical reading of the manuscript.
The authors declare no competing financial interests.
Correspondence should be addressed to either Paride Antinucci or Paul R. Hunter, 4th Floor, New Hunt's House, London SE1 1UL, UK, E-mail: paride.antinucci@kcl.ac.uk or paul.hunter@kcl.ac.uk.
DOI:10.1523/JNEUROSCI.1527-16.2016
 0270-6474/16/368064-03$15.00/0

Presynaptic mechanisms could also produce orientation selectivity in ON-OSGCs. Therefore, to reveal the synaptic inputs received by these cells, Nath and Schwartz (2016) and Venkataramani and Taylor (2016) used whole-cell voltage-clamp recordings to isolate excitatory and inhibitory conductances. Notably, mouse and rabbit horizontal ON-OSGCs appeared to receive similar synaptic inputs. In particular, they received excitatory inputs tuned to the preferred orientation (i.e., horizontal) and inhibitory inputs tuned to the orthogonal orientation [i.e., vertical (90° angular distance); Fig. 1*B*]. Mouse vertical ON-OSGCs also received excitatory inputs tuned to the preferred orientation (i.e., vertical), but, unlike horizontal ON-OSGCs, they received variable inhibitory inputs. Although individual vertical ON-OSGCs did receive tuned inhibitory inputs, these inputs were not orthogonal to the preferred orientation in all cases (Nath and Schwartz, 2016, their Fig. 7*D*,*F*). Consequently, when data were pooled from the whole population of vertical ON-OSGCs, it appeared that inhibitory inputs have an untuned response profile (Nath and Schwartz, 2016, their Fig. 6*G*).

To further determine the precise contribution of inhibition to ON-OSGC orientation tuning, both groups pharmacologically blocked inhibitory neurotransmission. Venkataramani and Taylor (2016) demonstrated that the spiking of rabbit horizontal ON-OSGCs was rendered orientation selective through GABA-mediated mechanisms (Venkataramani and Taylor, 2016, their Fig. 7*A*,*B*). The main effect of blocking $GABA_A$ receptors was a dramatic loss of orientation selectivity in the inhibitory inputs (Venkataramani and Taylor, 2016, their Fig. 7*O*), indicating a crucial role played by inhibition from amacrine cells. In particular, the authors proposed a circuit mechanism whereby inhibitory inputs are suppressed during preferred orientation stimulation, possibly through disinhibition from a preferred orientation-selective GABAergic amacrine cell that inhibits another amacrine cell synapsing directly onto the horizontal ON-OSGC (Venkataramani and Taylor, 2016, their Fig. 11). As mentioned above, orientation-selective amacrine cell types have previously been described in the rabbit retina (Bloomfield, 1994; Murphy-Baum and Taylor, 2015), but the extent to which their outputs contribute to OSGC tuning remains unclear.

Nath and Schwartz (2016) did not show the effects of blocking inhibition on the spiking of mouse ON-OSGCs. They instead focused on the changes in excitatory and inhibitory conductances upon inhibition block. Individually blocking either glycine or $GABA_A$ receptors changed the peak amplitude of excitatory and inhibitory inputs but, surprisingly, did not produce any significant change in their orientation tuning (Nath and Schwartz, 2016, their Fig. 8*F*–*H*). When blocked simultaneously, the tuning of excitatory inputs remained unaffected, but the tuning of inhibitory inputs was abolished as a consequence of the total loss of inhibitory currents (Nath and Schwartz, 2016, their Fig. 8*A*,*C*). Overall, these results in the mouse suggest that there is a substantial level of redundancy among glycinergic and GABAergic mechanisms, and that orientation selectivity in mouse ON-OSGCs could be generated through both tuned excitatory inputs independent of inhibition and, at least in horizontal ON-OSGCs, a combination of tuned inhibitory inputs from different classes of amacrine cells. It is intriguing that the tuning of vertical ON-OSGCs, which do not possess elongated dendritic fields, seems to result almost exclusively from inhibition-independent tuned excitatory inputs. Future experiments will be required to precisely determine how the tuning of mouse ON-OSGC spiking is modulated by amacrine cell inhibition, and to what extent tuned excitatory inputs alone can generate the orientation selectivity of ON-OSGC spiking.

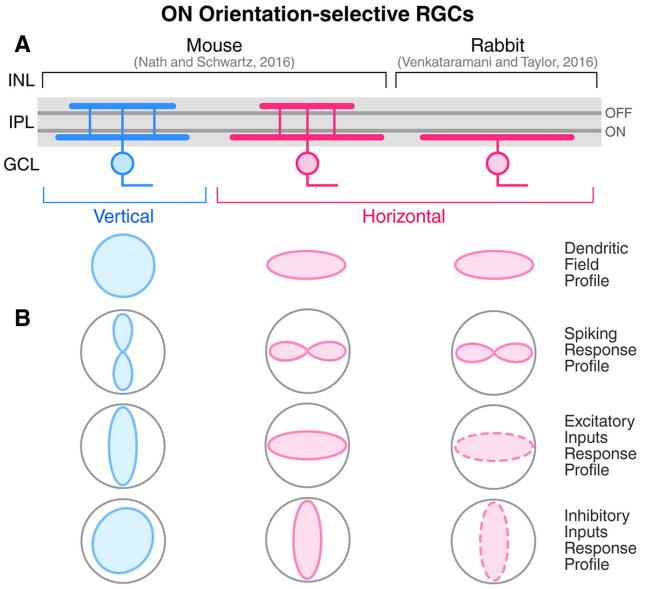

Figure 1. ***A***, ***B***, Schematic summarizing the morphological (***A***) and physiological (***B***) properties of ON-OSGCs in mouse (Nath and Schwartz, 2016) and rabbit (Venkataramani and Taylor, 2016) retinae. ***A***, Dendritic stratification (top) in the IPL and dendritic field profiles (bottom) of ON-OSGCs. Dark gray lines in the IPL indicate OFF and ON choline acetyltransferase (ChAT) strata. INL, Inner nuclear layer; GCL, ganglion cell layer. ***B***, Response profiles of ON-OSGC spiking (top), excitatory inputs (middle), and inhibitory inputs (bottom). Dashed lines of excitatory and inhibitory input response profiles in rabbit horizontal ON-OSGCs indicate the estimated profiles from responses recorded during preferred vs orthogonal orientation stimulation. Note the high degree of morphological and physiological homology between mouse and rabbit horizontal ON-OSGCs (magenta).

Together, these studies demonstrate the presence of novel morphologically and physiologically defined ON orientation-selective ganglion cell types in both mouse and rabbit retinae. The substantial degree of homology between horizontal ON-OSGCs in these two species suggests that conserved features and mechanisms might underlie retinal orientation selectivity across mammalian species. However, there are clear differences, such as the key requirement of GABAergic inhibition for rabbit ON-OSGC tuning not observed in the mouse and the dendritic stratification in the OFF IPL strata of mouse ON-OSGCs that is not present in the rabbit, that would suggest different mechanisms between species.

The morphological bias of horizontal ON-OSGCs not found in mouse vertical ON-OSGCs raises the question, what is the

advantage of generating this bias if it is not essential for tuning? The following two possible scenarios could explain this dichotomy: (1) these two ON-OSGCs have different, more complex receptive field properties, not revealed by the stimulus set used, that would allow classification into distinct functional groups; and (2) they use the same mechanisms to generate orientation selectivity and differ only in their preferred stimulus orientation. If scenario (2) is correct, the difference in their dendritic morphology is coincidental, not causative of orientation selectivity. Experiments mapping presynaptic inputs using 3D electron microscopy tracing (Briggman et al., 2011), high-resolution immunohistochemistry (Sigal et al., 2015), or neurotransmitter sensors/uncaging (Yonehara et al., 2013; Vlasits et al., 2016) would provide evidence on whether orientation selectivity is a consequence of a bias in the distribution of inputs on their dendritic arbors.

These studies also highlight the diversity of OSGC subtypes and the fraction of the overall retinal output they represent. In a previous study, Venkataramani and Taylor (2010) described two types of rabbit cardinal axes-tuned OFF-OSGCs, and in Venkataramani and Taylor (2016) they conclude that, collectively, OSGCs account for ~5% of all rabbit ganglion cells. In a comprehensive functional classification of mouse ganglion cells, Baden et al. (2016) identified ON, OFF, and ON-OFF OSGCs comprising different cardinally and obliquely tuned types, which collectively represent ~15% of the retinal output. Given the striking abundance of OSGCs in these two mammalian species, as well as reports of OSGCs in primates (Passaglia et al., 2002), it is likely that these cells directly contribute to orientation selectivity in higher visual centers. In line with this idea, several studies in rodents and primates have identified orientation-selective neurons in noncortical areas, such as the dorsal lateral geniculate nucleus (dLGN; Cheong et al., 2013; Piscopo et al., 2013) and superior colliculus (Wang et al., 2010). Further supporting this possibility, recent studies have shown that mouse dLGN axonal projections provide orientation-selective inputs to primary visual cortex (Sun et al., 2016) and that inactivating primary visual cortex does not change the orientation tuning of dLGN neurons (Zhao et al., 2013). The identification of genetic markers allowing the selective labeling or ablation of OSGC types as well as trans-synaptic tracing to their brain targets (Cruz-Martín et al., 2014) will provide crucial information regarding the extent that OSGCs contribute to orientation selectivity in higher visual centers. Such genetic markers will also be essential to dissect the presynaptic cellular components and mechanisms underlying the emergence of orientation selectivity in OSGCs.

References

Baden T, Berens P, Franke K, Román Rosón M, Bethge M, Euler T (2016) The functional diversity of retinal ganglion cells in the mouse. Nature 529:345–350. CrossRef Medline

Bloomfield SA (1994) Orientation-sensitive amacrine and ganglion cells in the rabbit retina. J Neurophysiol 71:1672–1691. Medline

Borst A, Helmstaedter M (2015) Common circuit design in fly and mammalian motion vision. Nat Neurosci 18:1067–1076. CrossRef Medline

Briggman KL, Helmstaedter M, Denk W (2011) Wiring specificity in the direction-selectivity circuit of the retina. Nature 471:183–188. CrossRef Medline

Cheong SK, Tailby C, Solomon SG, Martin PR (2013) Cortical-like receptive fields in the lateral geniculate nucleus of marmoset monkeys. J Neurosci 33:6864–6876. CrossRef Medline

Cruz-Martín A, El-Danaf RN, Osakada F, Sriram B, Dhande OS, Nguyen PL, Callaway EM, Ghosh A, Huberman AD (2014) A dedicated circuit links direction-selective retinal ganglion cells to the primary visual cortex. Nature 507:358–361. CrossRef Medline

Fisher YE, Silies M, Clandinin TR (2015) Orientation selectivity sharpens motion detection in Drosophila. Neuron 88:390–402. CrossRef Medline

Hubel DH, Wiesel TN (1962) Receptive fields, binocular interaction and functional architecture in the cat's visual cortex. J Physiol 160:106–154. CrossRef Medline

Hubel DH, Wiesel TN (1968) Receptive fields and functional architecture of monkey striate cortex. J Physiol 195:215–243. CrossRef Medline

Kim IJ, Zhang Y, Yamagata M, Meister M, Sanes JR (2008) Molecular identification of a retinal cell type that responds to upward motion. Nature 452:478–482. CrossRef Medline

Levick WR (1967) Receptive fields and trigger features of ganglion cells in the visual streak of the rabbits retina. J Physiol 188:285–307. CrossRef Medline

Murphy-Baum BL, Taylor WR (2015) The synaptic and morphological basis of orientation selectivity in a polyaxonal amacrine cell of the rabbit retina. J Neurosci 35:13336–13350. CrossRef Medline

Nath A, Schwartz GW (2016) Cardinal orientation selectivity is represented by two distinct ganglion cell types in mouse retina. J Neurosci 36:3208–3221. CrossRef Medline

Niell CM, Stryker MP (2008) Highly selective receptive fields in mouse visual cortex. J Neurosci 28:7520–7536. CrossRef Medline

Nikolaou N, Lowe AS, Walker AS, Abbas F, Hunter PR, Thompson ID, Meyer MP (2012) Parametric functional maps of visual inputs to the tectum. Neuron 76:317–324. CrossRef Medline

Passaglia CL, Troy JB, Rüttiger L, Lee BB (2002) Orientation sensitivity of ganglion cells in primate retina. Vision Res 42:683–694. CrossRef Medline

Piscopo DM, El-Danaf RN, Huberman AD, Niell CM (2013) Diverse visual features encoded in mouse lateral geniculate nucleus. J Neurosci 33:4642–4656. CrossRef Medline

Sigal YM, Speer CM, Babcock HP, Zhuang X (2015) Mapping synaptic input fields of neurons with super-resolution imaging. Cell 163:493–505. CrossRef Medline

Sun W, Tan Z, Mensh BD, Ji N (2016) Thalamus provides layer 4 of primary visual cortex with orientation- and direction-tuned inputs. Nat Neurosci 19:308–315. CrossRef Medline

Venkataramani S, Taylor WR (2010) Orientation selectivity in rabbit retinal ganglion cells is mediated by presynaptic inhibition. J Neurosci 30:15664–15676. CrossRef Medline

Venkataramani S, Taylor WR (2016) Synaptic mechanisms generating orientation selectivity in the ON pathway of the rabbit retina. J Neurosci 36:3336–3349. CrossRef Medline

Vlasits AL, Morrie RD, Tran-Van-Minh A, Bleckert A, Gainer CF, DiGregorio DA, Feller MB (2016) A role for synaptic input distribution in a dendritic computation of motion direction in the retina. Neuron 89:1317–1330. CrossRef Medline

Wang L, Sarnaik R, Rangarajan K, Liu X, Cang J (2010) Visual receptive field properties of neurons in the superficial superior colliculus of the mouse. J Neurosci 30:16573–16584. CrossRef Medline

Yonehara K, Farrow K, Ghanem A, Hillier D, Balint K, Teixeira M, Jüttner J, Noda M, Neve RL, Conzelmann KK, Roska B (2013) The first stage of cardinal direction selectivity is localized to the dendrites of retinal ganglion cells. Neuron 79:1078–1085. CrossRef Medline

Zhao X, Chen H, Liu X, Cang J (2013) Orientation-selective responses in the mouse lateral geniculate nucleus. J Neurosci 33:12751–12763. CrossRef Medline